Andreev quantum dot chains in indium antimonide nanowires

by

Hao Wu

Bachelor of Science, Nanjing University, 2014

Submitted to the Graduate Faculty of

the Kenneth P. Dietrich School of Arts and Sciences in partial fulfillment

of the requirements for the degree of

Doctor of Philosophy

University of Pittsburgh

2021

UNIVERSITY OF PITTSBURGH

KENNETH P. DIETRICH SCHOOL OF ARTS AND SCIENCES

This dissertation was presented

by

Hao Wu

It was defended on

Oct 26th 2021

and approved by

Sergey Frolov, Associate Professor, Department of Physics and Astronomy

Michael Hatridge, Assistant Professor, Department of Physics and Astronomy

Roger Mong, Associate Professor, Department of Physics and Astronomy

Joseph Boudreau, Professor, Department of Physics and Astronomy

Benjamin Hunt, Associate Professor, Department of Physics, Carnegie Mellon University

Andreev quantum dot chains in indium antimonide nanowires

Hao Wu, PhD

University of Pittsburgh, 2021

Kitaev chain is a theoretical model of a one-dimensional topological superconductor with Majorana zero modes at the two ends of the chain. Intending to emulate Kitaev chain, we build a tight-binding model of a 3-site quantum dot chain. Simulations of the energy spectrum and transport suggest partial-separated Majorana zero modes localize at two end sites within a narrow parameter window. Theory indicates that the triple-dot states acquire Majorana polarization in the fine-tuned regime (Kitaev regime) when Andreev states in all three dots reach zero-energy in a narrow range of magnetic field. A zero-bias peak extends in magnetic field would appear. We build a chain of three Andreev quantum dots in a semiconductor InSb nanowire. We observe Andreev bound states in each of the three dots, study their magnetic field and gate voltage dependence, and observe dot-dependent zero-bias conductance peaks in magneto-transport spectroscopy. We interpret zero-bias peaks as Andreev states along the triple-dot chain crossing zero-energy at finite magnetic fields. In our device, transport is dominated by one of the quantum dots in the chain, which has a zero-bias crossing at lower magnetic field than the other two dots, placing the Kitaev regime with Majorana end modes out of reach. The device geometry is suitable for studying the correlation of two end states with non-local measurements. A hard induced superconducting gap surviving to higher magnetic fields is desired. Devices with greater uniformity or independent control over superconductor-semiconductor coupling should realize the Kitaev chain with a high yield.

We characterize hybrid InSb nanowire/Sn shell devices fabricated with in-situ shadow technique and observe a hard induced superconducting gap that persists up to 4 T in magnetic field. The two-electron charging effect, a hallmark of charge parity stability, is observed in a small island of Sn/InSb. We also study a double quantum dot in a hybrid InAs nanowire/Al shell device and demonstrate Andreev blockade.

Due to its overall tunability and design flexibility, the quantum dot system remains

promising for quantum simulation of interesting models and particularly for modular topological quantum devices.

Table of contents

List of tables

List of figures

1.0 Introduction

1.1 Quantum computation and quantum simulation with quantum dots

In classical computers, the basic unit of information is a binary digit (bit). In quantum computing, the basic unit of information is called a quantum bit (qubit). A qubit is a controllable 2-level quantum mechanical system. There are various choices to physically implement qubits: charges and spins in semiconductor quantum dots [1], photons, trapped ions in optical lattices, nitrogen-vacancy centers in diamond, and superconducting circuits [2].

Quantum dot systems are versatile platforms for quantum information processing. In quantum dot-based spin qubits, initialization, manipulation, logic gate control and readout of spin states, and qubit entanglement have been demonstrated [3, 4, 5, 6, 7]. With high measurement and control fidelity [8], quantum dot-based qubit becomes a great candidate for scaling up quantum computation above the fault-tolerance threshold [9, 10].

The idea of quantum simulation is to solve complex many-body quantum problems by encoding quantum properties into the hardware.

Quantum simulation can provide valuable insights into complex and significant quantum problems with strong interactions that cannot be numerically calculated with classical computers. We can build a quantum system that is simple, controllable, easy to manipulate to simulate and study a more complex quantum system. If both systems can be described by the same Hamiltonian and the same equations, they will have the same solutions and behave similarly. One actively studied problem is quantum simulation of the Fermi-Hubbard model in ultracold atoms trapped by laser beams in optical lattices. It is motivated by the strong connection of the doped antiferromagnetic Fermi-Hubbard model and high Tc (critical temperature) superconductivity in cuprates.

Since electrons confined to artificial atom lattice sites (quantum dots) are governed by the same physics as those in crystalline lattices, semiconductor quantum dots in a chain or array are suitable for simulating 1D or 2D Hamiltonians of complex many-body states. Many properties of quantum dots can be engineered, including size, shape, confinement strength,

and energy spectra. By designing a semiconductor quantum dot array with desired charging energy and gate-tunable inter-dot tunnel coupling, it can mimic the quantum behavior of electrons in materials with exotic electronic and magnetic properties and provide insights into the underlying physics. Several models have been simulated by semiconductor quantum dots, including the strongly correlated Fermi-Hubbard model [11], Nagaoka ferromagnetism [12], and antiferromagnetic Heisenberg chain [13]. Furthermore, quantum dots can be constructed in semiconducting materials with intrinsic properties such as strong spin-orbit interaction, and large g-factor. Magnetism or superconductivity can also be induced into the quantum dots through the proximity effect [14], which expands the variety of problems that quantum dot systems can simulate.

1.2 Majorana fermions and topological quantum computing

Issues of decoherence and scalability obstruct the realization of practical quantum computation. To accomplish error correction in quantum computing, many physical qubits are needed to create one logical qubit [15, 16]. Topological quantum computing is an approach to circumvent the harsh requirements for logical qubits and scale up to realize fault-tolerant quantum computation [17, 18, 19]. Topological quantum computation is carried out by performing braiding operations on non-Abelian anyons, which are stable and resilient to decoherence [20, 21].

According to the spin-statistics theorem, in 3+1 space-time dimensions, elementary particles can be categorized into two kinds depending on their spin being half-integer or integer. Fermions, such as electrons, have half-integer spin. When we swap two fermions, the wavefunction of the system changes sign. On the other hand, bosons, such as photons, have integer spin. The wavefunction remains the same under the exchange of bosons.

In 2+1 space-time dimensions, anyons are quasiparticles which are neither fermions nor bosons. When we exchange two anyons, wavefunction has a phase shift other than 0 or π (0 is for bosons, π is for fermions). For example, in the fractional quantum Hall effect, fractionally charged quasiparticle excitations of Laughlin states are anyons [22]. Non-Abelian anyon is

one kind of anyons that exhibit non-Abelian exchange statistics. Majorana fermions are an example of non-Abelian anyons. Exchanging Majorana fermions, a process called braiding, can lead to changes in the system's state while keeping the same energy as the initial state. Changing the exchange order in a sequence of braiding operations will change the final state, which is one unique property of non-Abelian anyons.

Majorana fermions are predicted to exist in a type of exotic phase of matter, topological superconductor. Several platforms are considered to host Majorana fermions, including unconventional p-wave superconductors [23] and topological insulator in proximity to s-wave superconductor [24]. When a semiconductor nanowire with strong spin-orbit interaction, is coupled to an s-wave superconductor, in the presence of magnetic field, Majorana fermions can emerge as quasiparticle excitations (Majorana zero modes) at endpoints of the wire [25, 26]. Although its non-Abelian exchange statistics has not been confirmed in experiments yet, Majorana zero modes in hybrid superconductor-semiconductor nanowires have become one of the most promising candidates for topological qubits [27, 28, 29]. Semiconductor nanowire system has the advantage in performing braiding operations and demonstrating non-Abelian statistics in the future [30]. Experimentally demonstrating non-Abelian exchange statistics of Majorana zero modes would be a milestone towards the application of topological quantum computing.

1.3 Layout of the thesis

The content of this thesis is as follow:

Chapter 2 introduces the theory and background of the Kitaev chain model and Majorana zero modes in hybrid semiconductor/superconductor nanowire devices.

Chapter 3 describes the materials, device fabrication techniques, and measurement setups used in the thesis.

Chapter 4 shows a theoretical model of a three-site Andreev quantum dot chain.

Chapter 5 studies triple Andreev quantum dot chains in Indium Antimonide nanowires.

Chapter 6 presents a characterization study of Indium Antimonide nanowires with tin

shells.

Chapter 7 demonstrates the Andreev blockade phenomenon of double quantum dot chains in Indium Arsenide nanowires.

Chapter 8 concludes the thesis with a summary and outlook.

2.0 Theory

2.1 The Kitaev model

The Kitaev model is a tight-binding chain of N fermionic sites [31]. It describes one-dimensional spinless p-wave superconductor, where unpaired Majorana fermions are expected to emerge at the chain's ends. All proposals to realize Majorana fermions in a 1D quantum wire are based on this model [25, 26].

The Kitaev chain has the following Hamiltonian:

$$H_{chain} = -\mu \sum_{i=1}^{N} (c_i^\dagger c_i - \frac{1}{2}) - t \sum_{i=1}^{N-1} (c_{i+1}^\dagger c_i + h.c.) + \Delta \sum_{i=1}^{N-1} (c_i c_{i+1} + h.c.) \tag{2.1}$$

in which μ is onsite chemical potential, t is the hopping amplitude between two neighboring sites, Δ is the superconducting gap. $c_i^\dagger$ and c_i are the fermionic creation and annihilation operators on site i. Note that the above Hamiltonian does not contain spin indices, so the electrons are effectively spinless. Due to the Pauli exclusion principle, each fermionic site can only be occupied by one of such spinless electrons. P-wave superconductivity pairs electrons with the same spin from two neighboring sites.

We introduce Majorana operators γ_1 and γ_2 by splitting fermionic creation and annihilation operators $c^\dagger$ and c into their real and imaginary parts:

$$\begin{aligned} c &= \frac{1}{2}(\gamma_1 + i\gamma_2) \\ c^\dagger &= \frac{1}{2}(\gamma_1 - i\gamma_2) \end{aligned} \tag{2.2}$$

By inverting the above transformations, we can write Majorana operators in the following way:

$$\begin{aligned} \gamma_1 &= c^\dagger + c \\ \gamma_2 &= i(c^\dagger - c) \end{aligned} \tag{2.3}$$

It is simple to verify that $\gamma_1 = \gamma_1^\dagger$ and $\gamma_2 = \gamma_2^\dagger$: Majorana creation and annihilation operators are equal to themselves. Such quasiparticle γ is its own anti-particle, fits the

definition of a Majorana fermion. Similar to fermionic operators, Majorana operators anti-commute:

$$\{\gamma_i, \gamma_j\} = 2\delta_{ij} \tag{2.4}$$

A fermionic operator can always be expressed as a pair of Majorana operators. We substitute Majorana operators for fermionic operators and apply the anticommutation relation Eq. 2.4. We have the Kitaev chain Hamiltonian in the following form:

$$H_{chain} = \frac{i}{2}\sum_{i=1}^{N}(-\mu\gamma_{i,1}\gamma_{i,2}) + \frac{i}{2}\sum_{i=1}^{N-1}[(t+\Delta)\gamma_{i,2}\gamma_{i+1,1} + (-t+\Delta)\gamma_{i,1}\gamma_{i+1,2}] \tag{2.5}$$

To fully solve this Hamiltonian is complicated. However, two special cases represent two different phases and capture the essence of the model.

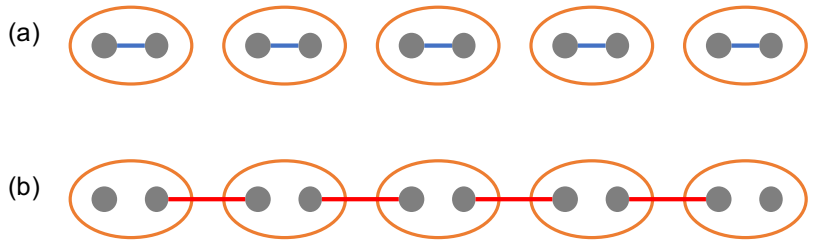

Figure 2.1: Schematic of a 5-site Kitaev chain in (a) topological trivial phase and (b) topological non-trivial phase. Each fermionic site is indicated by an orange circle enclosing two Majorana operators (grey dots). (a) shows the chain in the trivial case where Majorana operators from the same site pair up (blue line). (b) shows the chain in the topological non-trivial phase where Majorana operators from neighboring sites pair up (red line) and leave an unpaired Majorana operator at each end of the chain.

1. $\Delta = t = 0$ and $\mu < 0$.

   The Hamiltonian becomes:

$$H_{chain} = -\frac{i}{2}\mu\sum_{i=1}^{N}\gamma_{i,1}\gamma_{i,2} = -\mu\sum_{i=1}^{N}(c_i^\dagger c_i - \frac{1}{2}) \tag{2.6}$$

   In this case, two Majorana operators from the same site are paired, equivalent to a fermionic operator. Each site is occupied by one spinless electron. Fig. 2.1 (a) depicts this trivial case.

2. $\Delta = t$ and $\mu = 0$.

   The Hamiltonian becomes:

$$H_{chain} = it \sum_{i=1}^{N-1} \gamma_{i,2}\gamma_{i+1,1} \tag{2.7}$$

   It describes the case where paired Majorana operators $\gamma_{i,2}$ and $\gamma_{i+1,1}$ are from neighboring sites. In this situation, two Majorana operators $\gamma_{1,1}$ and $\gamma_{N,2}$ at the chain's two ends are left unpaired, shown in Fig. 2.1(b). Majorana operators $\gamma_{1,1}$ and $\gamma_{N,2}$ do not show up in the Hamiltonian Eq. 2.7, indicates the two Majoranas at the ends must be of zero energy.

We can define the paired Majorana operators in Eq. 2.7 as a new set of fermionic operators:

$$\begin{aligned} \tilde{c}_i &= \frac{1}{2}(\gamma_{i+1,1} + i\gamma_{i,2}) \\ \tilde{c}_i^\dagger &= \frac{1}{2}(\gamma_{i+1,1} - i\gamma_{i,2}) \end{aligned} \tag{2.8}$$

Obviously, they satisfy the anti-commutation rule as fermionic operators. The Hamiltonian now becomes:

$$H_{chain} = 2t \sum_{i=1}^{N-1} (\tilde{c}_i^\dagger \tilde{c}_i - \frac{1}{2}) \tag{2.9}$$

In this expression, $N-1$ fermionic sites each contribute $2t$ to the energy. The two non-local Majorana operators $\gamma_{1,1}$ and $\gamma_{N,2}$, which are absent from Eq. 2.7 can be combined as a non-local fermionic operator:

$$\begin{aligned} \tilde{c}_M &= \frac{1}{2}(\gamma_{1,1} + i\gamma_{N,2}) \\ \tilde{c}_M^\dagger &= \frac{1}{2}(\gamma_{1,1} - i\gamma_{N,2}) \end{aligned} \tag{2.10}$$

$\tilde{c}_M$ or $\tilde{c}_M^\dagger$ does not show up in Eq. 2.10, means that add or remove this non-local fermion M costs zero energy. $\tilde{c}_M^\dagger \tilde{c}_M$ can be either 0 or 1. It implies two degenerate ground states with different parity. The ground state degeneracy is a key property of non-Abelian anyons. An energy gap well separates the ground states from other excitations such that the ground

state degeneracy is robust against local perturbations. Note that this kind of pairing and existence of unpaired Majorana end modes occurs for a larger parameter space of μ.

As edge excitations, the existence of unpaired Majorana end modes can be derived through the bulk-edge correspondence. In momentum space, fermionic operators are:

$$\begin{aligned} c_i &= \frac{1}{\sqrt{N}} \sum_{n=1}^{N} e^{-ikn} c_k \\ c_i^\dagger &= \frac{1}{\sqrt{N}} \sum_{n=1}^{N} e^{ikn} c_k^\dagger \end{aligned} \tag{2.11}$$

Kitaev chain (Eq. 2.1) can be written in a canonical form through Bogoliubov-de Gennes transformation:

$$H = \frac{1}{2} \sum_k \psi_k^\dagger H_{BdG} \psi_k \tag{2.12}$$

in which, ψ_k is the Nambu spinor of particle-hole space:

$$\psi_k = \begin{pmatrix} c_k \\ c_{-k}^\dagger \end{pmatrix} \tag{2.13}$$

and H_{BdG} is the Bogoliubov-de Gennes Hamiltonian:

$$H_{BdG} = (-\mu - 2t\cos k)\tau_z + 2\Delta \sin k \tau_y = \begin{pmatrix} -\mu - 2t\cos k & -2i\Delta \sin k \\ 2i\Delta \sin k & \mu + 2t\cos k \end{pmatrix} \tag{2.14}$$

For very large N (infinite chain), k is continuous within Brillouin zone $[-\pi, \pi]$. The excitation spectrum is given by:

$$E(k) = \pm\sqrt{(\mu + 2t\cos k)^2 + 4\Delta^2 \sin^2 k} \tag{2.15}$$

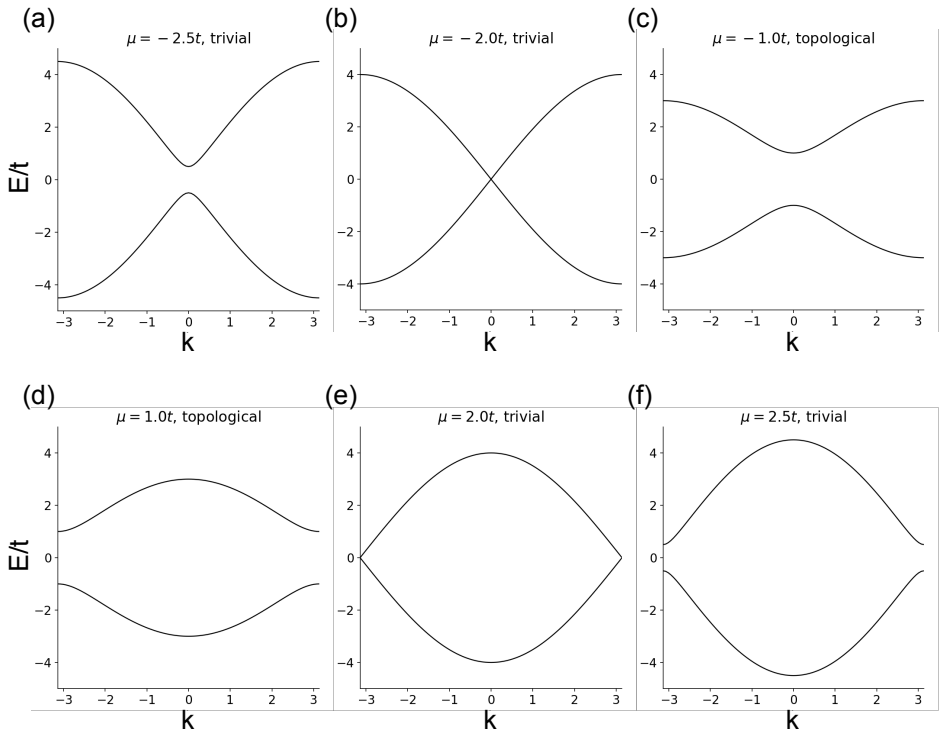

Figure 2.2: Band structures given by Eq. 2.15 at different μ. (a) $\mu = -2.5t$, energy spectrum is gapped at all k. (b) $\mu = -2t$, band gap closing at $k = 0$. (c) $\mu = -t$, band gap is inverted and topological phase with Majorana modes are expected. (d) $\mu = t$, band gap is inverted and topological phase with Majoranas are expected. (e) $\mu = 2t$, band gap closing at $k = \pm\pi$. (f) $\mu = 2.5t$, trivial phase without Majorana modes.

Fig. 2.2 shows the energy spectrum of an infinite Kitaev chain at different μ. For $\Delta \neq 0$, the spectrum remains gapped for most of the cases. The energy gap closes at $k = 0, \mu = -2t$ and $k = \pm\pi, \mu = 2t$. These are the boundaries separating two different phases corresponding to the above two special cases in Eq. 2.6 and Eq. 2.7. For $2|t| < |\mu|$, the phase is topologically trivial. For $2|t| > |\mu|$, the phase is topologically non-trivial with unpaired Majorana modes localized at the chain's ends. The special point ($\Delta = t$ and $\mu = 0$) is within the topologically non-trivial phase.

The solution of the energy spectrum in Eq. 2.15 is exact for an infinitely long chain. For a chain with finite length L, Majorana modes will not perfectly localize at the two end sites due

to weak interactions between the two boundary modes. The two Majorana wavefunctions exponentially decay into the bulk of the chain and have a non-zero overlap. This overlap of two Majorana wavefunctions can result in an energy splitting and lift the 2-fold ground state degeneracy.

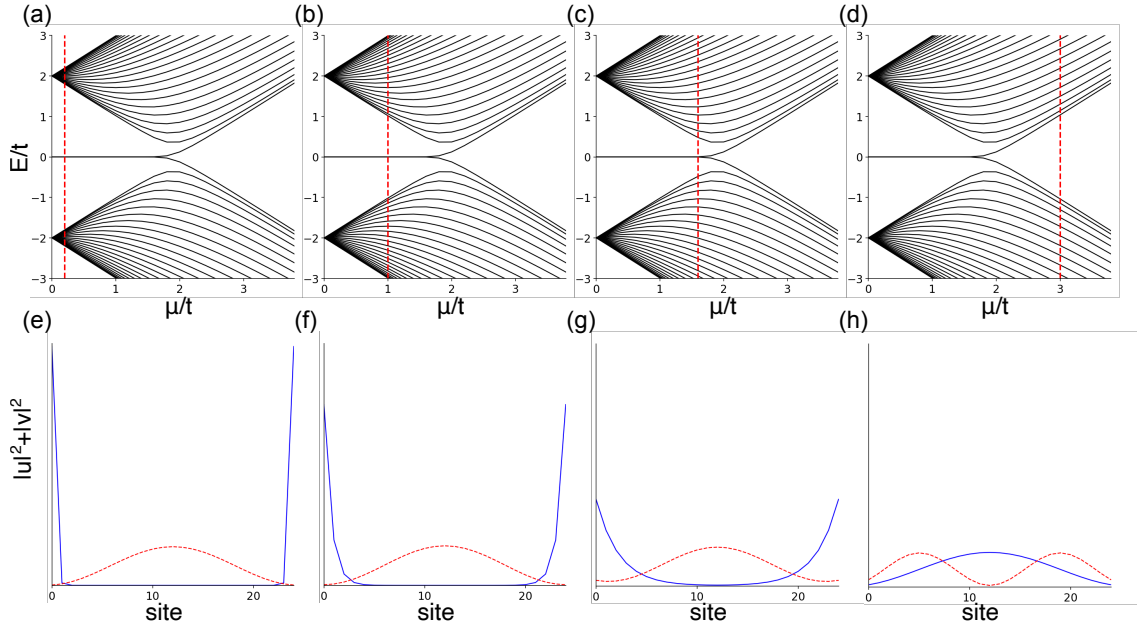

Figure 2.3: Topological protection of the Majorana end modes in a Kitaev chain of 25 sites. (a)-(d) Energy spectrum as a function of μ. Two states at zero energy start to split near $\mu = 2t$. $\Delta = t$. Red dotted lines show different μ values in (e)-(f). (e)-(f) Wavefunctions of the states correspond to Majorana modes along the chain. Blue lines show the ground state, and red lines show the first excited state. In (e), the energy gap between zero energy states and the first excited state is large, and the wavefunctions of Majorana modes localize at two ends of the chain. In (f) and (g), as the energy gap between zero energy states and the first excited state shrinks, the wavefunctions of Majorana modes are less well localized at two ends. In (h), the ground states split from zero energy, the gap between ground states and excited states are no longer present, the wavefunctions of Majorana modes overlap. (e) $\mu = 0.2$, (f) $\mu = 1$, (g) $\mu = 1.6$, (h) $\mu = 3$.

Fig. 2.1 shows the topological protection of the Majorana end modes at different μ

and the spatial distribution of the Majorana wavefunctions along the chain. At $\mu = 0$, two zero energy states corresponding to two Majorana modes localize at two ends. The Majorana modes are spatially separated by a gapped bulk. No other states are close to zero energy. Moving a single quasi-particle excitation (Majorana zero mode) away from zero energy is impossible because, with particle-hole symmetry, the excitation spectrum has to be symmetric about zero energy. The zero-energy Majorana states can lose their degeneracy when higher energy excitations in the bulk spectrum come close to zero energy to interact with them (closing of the bulk gap makes the boundary conditions for hosting unpaired Majorana modes no longer valid), shown in Fig. 2.1 as μ increases. As long as the bulk energy gap exists, the two Majorana states are protected.

Spectrum simulations of Kitaev model are generated by source code in [32].

2.2 Majorana bound states in 1D nanowires

The Kitaev chain model is simple in concept but difficult to realize. As a critical ingredient of the model, the existence of p-wave superconductivity is still controversial. Fortunately, theory suggests p-wave pairing can be effectively engineered by conventional materials [25, 26]. We combine one-dimensional semiconductor nanowire with strong Rashba spin-orbit interaction, proximity induced s-wave superconductivity, and Zeeman effect, under certain circumstances, it is similar to a 1D p-wave superconductor with triplet pairing.

We write the Kitaev chain Hamiltonian (Eq. 2.1) in a continuum limit:

$$H = \int dx[\Psi_x^\dagger(\frac{p_x^2}{2m} - \mu)\Psi_x + \Psi_x \Delta e^{i\phi} p_x \Psi_x + h.c.] \tag{2.16}$$

in which $\Psi_x^\dagger$ and Ψ_x are the fermionic creation and annihilation field operators, the spin indices are omitted since this model describes spinless electrons. p_x is the momentum operator in the x direction (assuming the chain is along the x direction). m is effective mass. μ is the chemical potential. Δ is the superconducting gap, and ϕ is the phase.

We modify the Hamiltonian to describe a one-dimensional semiconductor nanowire with Rashba spin-orbit interaction, in proximity with an s-wave superconductor, and in the presence of magnetic field:

$$H = \int dx[\Psi_x^\dagger(\frac{\hbar^2 k_x^2}{2m} - \mu - \alpha_{SO} k_x \sigma_y + \frac{1}{2} g\mu_B B\sigma_z)\Psi_x + \Psi_x \Delta e^{i\phi}\Psi_x + h.c.] \tag{2.17}$$

The nanowire is along the x direction. $(-\alpha_{SO} k_x \sigma_y)$ is the Rashba spin-orbit interaction term, assuming effective electric field is along the z direction and perpendicular to the direction of motion, x. α_{SO} is the spin-orbit strength. $(\frac{1}{2} g\mu_B B\sigma_z)$ is the Zeeman energy term. Applied external magnetic field B is aligned with the x direction. g is the Landé g-factor. μ_B is Bohr magneton.

To understand the physics of such a complex model, we will take a gradual approach. We will start with a simple quantum wire, solve the Hamiltonian and plot the energy spectrum. We will then add these components (spin-orbit interaction, magnetic field, and superconductivity) into the model one by one and see how the spectrum changes.

For a single subband quantum wire along the x direction, $\alpha_{SO} = B = \Delta = 0$,

$$H_{1D} = \frac{\hbar^2 k_x^2}{2m} - \mu \tag{2.18}$$

The corresponding energy spectrum is a parabola given by:

$$E = \frac{\hbar^2 k_x^2}{2m} - \mu \tag{2.19}$$

Fig. 2.4 shows the energy spectrum of a 1D wire.

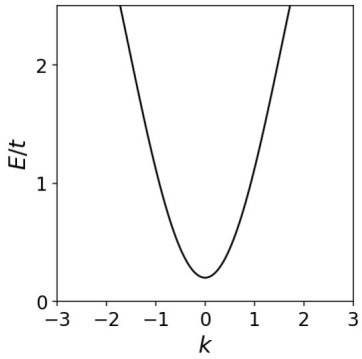

Figure 2.4: Energy spectrum of a single subband quantum wire given by Eq. 2.19 is a parabola. $\mu = -0.2t$.

We add spin-orbit term, the Hamiltonian is:

$$H_{1D+SO} = \frac{\hbar^2 k_x^2}{2m} - \mu - \alpha_{SO} k_x \sigma_y \tag{2.20}$$

Spin-orbit interaction lifts the spin degeneracy. In energy spectrum, the parabola of spin degenerate states are shifted to the left and right by $k_{SO} = \frac{m\alpha_{SO}}{\hbar^2}$ along the momentum axis and down in energy by $2E_{SO}$, where $E_{SO} = E(k = k_{SO}) = \frac{m\alpha^2}{2\hbar^2}$ is the spin-orbit energy. The energy of dispersion is given by:

$$E_{\pm} = \frac{\hbar^2 k_x^2}{2m} - \mu \pm \alpha_{SO} k_x \tag{2.21}$$

Now spin and momentum are correlated. Spins at opposite momentum have opposite signs. Fig. 2.5 shows the energy spectrum of a 1D wire with spin-orbit interaction.

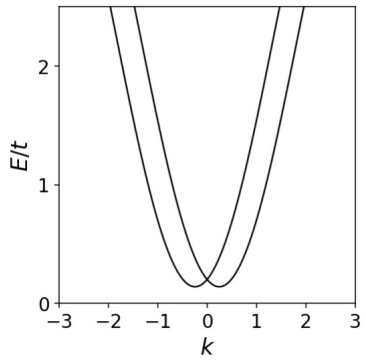

Figure 2.5: Energy spectrum of a quantum wire with spin-orbit interaction is given by Eq. 2.21. $\alpha = 0.5$. $\mu = -0.2t$. Spin-orbit term $\alpha_{SO} k_x \sigma_y$ results in a shift of $\pm k_{SO}$ of two parabolas with opposite spins and a shift of $2E_{SO}$ in energy.

Next, we add Zeeman term, and the external magnetic field is applied along the x direction:

$$H_{1D+SO+Zeeman} = \frac{\hbar^2 k_x^2}{2m} - \mu - \alpha_{SO} k_x \sigma_y + \frac{1}{2} g \mu_B B \sigma_z \tag{2.22}$$

The energy spectrum is given by:

$$E_{\pm} = \frac{\hbar^2 k_x^2}{2m} - \mu \pm \sqrt{(\alpha_{SO} k_x)^2 + (\frac{g\mu_B B}{2})^2} \tag{2.23}$$

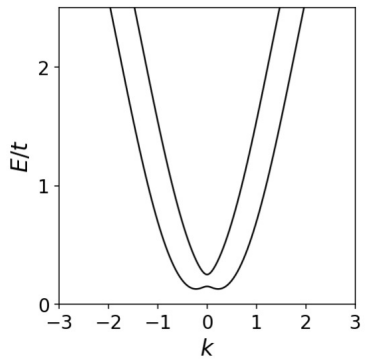

Figure 2.6: Energy spectrum of a quantum wire with spin-orbit interaction in a parallel magnetic field is given by Eq. 2.23. $B = 0.05$. $\mu = -0.2t$.

Fig. 2.6 shows the energy spectrum of a 1D wire with spin-orbit interaction in parallel magnetic field. Spin-orbit term $-\alpha_{SO}k_x\sigma_y$ can be written as $-\frac{\hbar}{2}B_{SO}\sigma_y$, where $B_{SO} = \frac{2\alpha_{SO}}{\hbar}k_x$ is effective B field along the y direction caused by spin-orbit interaction. Because B_{SO} is along the y direction and the applied external Zeeman field B is along the x direction, mixture between spin polarization along σ_x and σ_y occurs. At k=0, the spin-orbit term is zero. Spins are polarized along σ_x, a gap of $2E_Z = g\mu_B B$ is opened. When chemical potential μ is within the Zeeman gap, the spectrum is non-degenerate, only states at large positive and negative momentum contribute to transport. Spin degree of freedom is locked to momentum: only one possible spin direction for states propagating along one certain direction.

Finally, we add s-wave superconductivity and get the Majorana wire Hamiltonian:

$$H_{1D+SO+Zeeman+SC} = \int dx[\Psi_x^\dagger(\frac{\hbar^2k_x^2}{2m} - \mu - \alpha_{SO}k_x\sigma_y + \frac{1}{2}g\mu_B B\sigma_z)\Psi_x + \Psi_x\Delta e^{i\phi}\Psi_x + h.c.] \quad (2.24)$$

In Bogoliubov-de Gennes formalism, the Hamiltonian is given by:

$$H_{BdG} = \begin{pmatrix} H_0 & \mathbf{\Delta} \\ \mathbf{\Delta}^* & -\mathcal{T}H_0\mathcal{T}^{-1} \end{pmatrix} \quad (2.25)$$

where

$$H_0 = \begin{pmatrix} \frac{\hbar^2k_x^2}{2m} - \mu & \frac{1}{2}g\mu_B B + i\alpha_{SO}k_x \\ \frac{1}{2}g\mu_B B - i\alpha_{SO}k_x & \frac{\hbar^2k_x^2}{2m} - \mu \end{pmatrix} \quad (2.26)$$

and

$$\mathbf{\Delta} = \begin{pmatrix} 0 & e^{i\phi}\Delta \\ -e^{i\phi}\Delta & 0 \end{pmatrix} \tag{2.27}$$

$\mathcal{T}$ is time reversal operator:

$$-\mathcal{T}H_0\mathcal{T}^{-1} = \begin{pmatrix} -\frac{\hbar^2 k_x^2}{2m} + \mu & -\frac{1}{2}g\mu_B B - i\alpha_{SO}k_x \\ -\frac{1}{2}g\mu_B B + i\alpha_{SO}k_x & -\frac{\hbar^2 k_x^2}{2m} + \mu \end{pmatrix} \tag{2.28}$$

After introducing superconductivity into the system, near the Fermi level, states with opposite momentum $+k_x$ and $-k_x$ are paired up as Cooper pairs. At B=0, pairing is purely s-wave since states of opposite momentum have opposite spins and form a singlet. As increasing applied B field, a triplet component starts to emerge in the pair of states at $+k_x$ and $-k_x$, and resulting in a p-wave contribution to the superconductivity. The p-wave component increases as increasing B field. When B is above a critical field, the superconducting state becomes more p-wave like than s-wave like, and the state transitions from a topological trivial to non-trivial phase. Since the pairing originates from an s-wave superconductor, we can never have a pure p-wave superconducting phase where all spins are fully polarized and form triplet states, because spin-orbit interaction is present in the system and full spin polarization would suppress superconductivity.

When a significant fraction of the pairing becomes p-wave like, we can think of the system as an effectively p-wave superconductor in 1D. $\mu = 0$ is at the middle of the Zeeman gap. When B is large ($E_Z \gg E_{SO}$), only the lowermost band needs to be considered. In this limit, the fermionic operators ($\Psi_{\uparrow x}$ and $\Psi_{\downarrow x}$) can be approximated as:

$$\begin{aligned} \Psi_{\uparrow x} &\approx \frac{\alpha_{SO}k_x}{2E_Z}\Psi_x \\ \Psi_{\downarrow x} &\approx \Psi_x \end{aligned} \tag{2.29}$$

Furthermore, the effective Hamiltonian for the lower band is given by:

$$H_{eff} = \int dx[\Psi_x^\dagger(\frac{\hbar^2 k_x^2}{2m} - \mu_{eff})\Psi_x + e^{i\phi}\Delta_{eff}\hbar k_x \Psi_x \Psi_x + h.c.] \tag{2.30}$$

$\mu_{eff} = \mu + E_Z$ is the effective chemical potential, and $\Delta_{eff} = \frac{\alpha_{SO}\Delta}{2E_Z}$ is the effective superconducting pairing strength. Note that this Hamiltonian is the same as the Kitaev chain of a 1d spinless p-wave superconductor in Eq. 2.16.

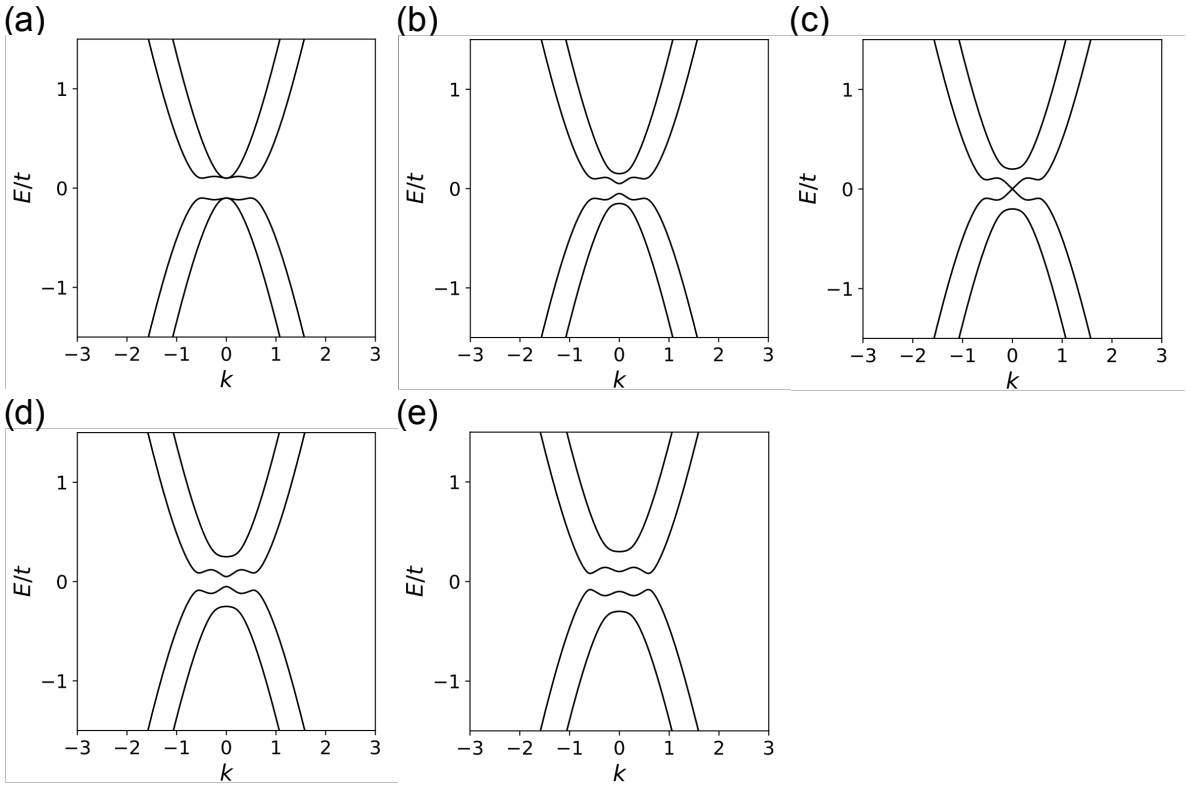

Figure 2.7: Energy spectrum of a Majorana wire given by Eq. 2.24 at different B. $\mu = 0$, $\Delta = 0.1$, $\alpha = 0.5$. (a) $B = 0$, $E_z = 0$, trivial phase. Gap E_1 at $k_x = 0$ and gap E_2 at finite k are of the same energy. The spectrum is degenerate at $k_x = 0$. (b) $B = 0.05$, $E_z < \sqrt{\Delta^2 + \mu^2}$, trivial phase. Gap E_1 at $k_x = 0$ is closing linearly, while gap E_2 at finite k closes slowly in B. (c) $B = 0.1$, $E_z = \sqrt{\Delta^2 + \mu^2}$, topological phase transition occurs at critical field. (d) $B = 0.15$, $E_z > \sqrt{\Delta^2 + \mu^2}$, non-trivial phase. Gap E_1 reopens at $k_x = 0$. (e) $B = 0.2$, $E_z > \sqrt{\Delta^2 + \mu^2}$, non-trivial phase.

In the spectrum of Majorana wire (Fig. 2.7), two energy gaps are present. E_1 at $k_x = 0$ and E_2 at finite $k_x = 2k_{SO}$.

At $k_x = 0$,

$$E_1 = \sqrt{\Delta^2 + \mu^2} - E_Z \tag{2.31}$$

Increase B from 0, the gap at $k_x = 0$ closes at $E_Z = \sqrt{\Delta^2 + \mu^2}$, when the topological phase transition happens and non-degenerate Majorana quasi-particles are about to emerge. Further increase B beyond this point, the gap $E_1 = \sqrt{\Delta^2 + \mu^2} - E_Z$ becomes negative and band inversion occurs, indicates transition into a topologically non-trivial phase.

For the gap at larger k, the solution can be simplified when $\mu = 0$, as:

$$E_2 = \frac{2\Delta E_{SO}}{\sqrt{E_{SO}(2E_{SO} + \sqrt{E_Z^2 + 4E_{SO}^2})}} \tag{2.32}$$

For $E_Z \ll E_{SO}$, $E_2 = \Delta$, the gap at finite k remains open. For $E_Z \gg E_{SO}$, $E_2 = 2\Delta\sqrt{\frac{E_{SO}}{E_Z}}$, the gap closes when system is no longer superconducting. For $\mu \neq 0$, spectrum can be more complex. The theory can be extended to multi-subband, one can also introduce disorder and consider finite length and width to better describe a real hybrid superconductor-semiconductor nanowire device.

Spectrum simulations of Majorana wire are generated by source code in [32].

2.3 Quantum dot coupled to superconducting leads

2.3.1 Quantum dot

A quantum dot is a system that can be filled with electrons or holes [33]. Two major effects influence the electronic properties of quantum dots. First, because of Coulomb repulsion between the electrons on the dots, an energy cost is required for adding an extra electron to the dot. Due to this charging energy, electron tunneling to the dot can be significantly suppressed at low temperatures. This phenomenon is known as the Coulomb blockade. Second, quantum confinement leads to a discrete energy spectrum.

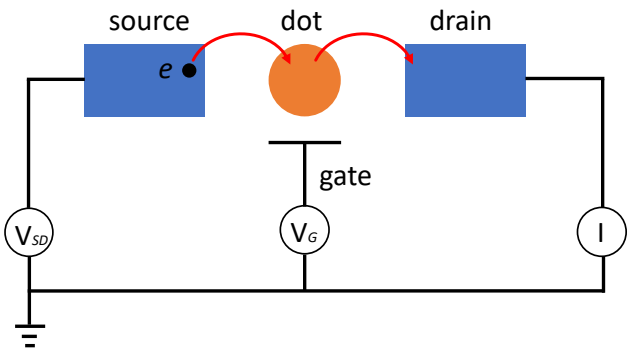

Figure 2.8: Schematic of a quantum dot. A quantum dot is connected to the source and the drain through tunnel barriers. Apply a bias voltage V_{SD} across the device, current I flow through the dot can be measured. A gate voltage V_G tunes the electrochemical potential of the dot.

Fig. 2.8 shows a quantum dot connected to the source and drain reservoirs through tunneling. To consider the above two effects, the minimal model to describe this system has two assumptions. First, it assumes the Coulomb interactions between electrons in the dot, and electrons between the dot and the environment can be characterized by a single, constant capacitance, C. C is the sum of capacitances between the dot and the source, C_S, the drain, C_D, and the gate, C_G: $C = C_S + C_D + C_G$. Second, the single-particle energy spectrum is independent of these interactions. The total energy $U(N)$ of a quantum dot with N electrons in the ground state is given by:

$$U(N) = \frac{[-|e|(N - N_0) + C_S V_S + C_D V_D + C_G V_G]^2}{2C} + \sum_{n=1}^{N} E_n \tag{2.33}$$

where $-|e|$ is the electron charge, N_0 is the background charge, E_n is the single energy level of the n-th electron, V_S, V_D, and V_G are the voltages applied on the source, drain, and gate, respectively.

The electrochemical potential $\mu(N)$ of the dot is defined as:

$$\mu(N) = U(N) - U(N-1) = (N - N_0 - \frac{1}{2})E_C - \frac{E_C}{|e|}(C_S V_S + C_D V_D + C_G V_G) + E_N \tag{2.34}$$

where $E_C = \frac{e^2}{C}$ is the charging energy. $\mu(N)$ represents the transition between the N-electron ground state and the $N-1$-electron ground state.

The electrochemical potential of the transitions between consecutive ground states are separated by the addition energy defined as:

$$E_{add}(N) = \mu(N+1) - \mu(N) = E_C + \Delta E \tag{2.35}$$

The addition energy contains an electrostatic part, the charging energy E_C, and energy spacing between two discrete levels, ΔE.

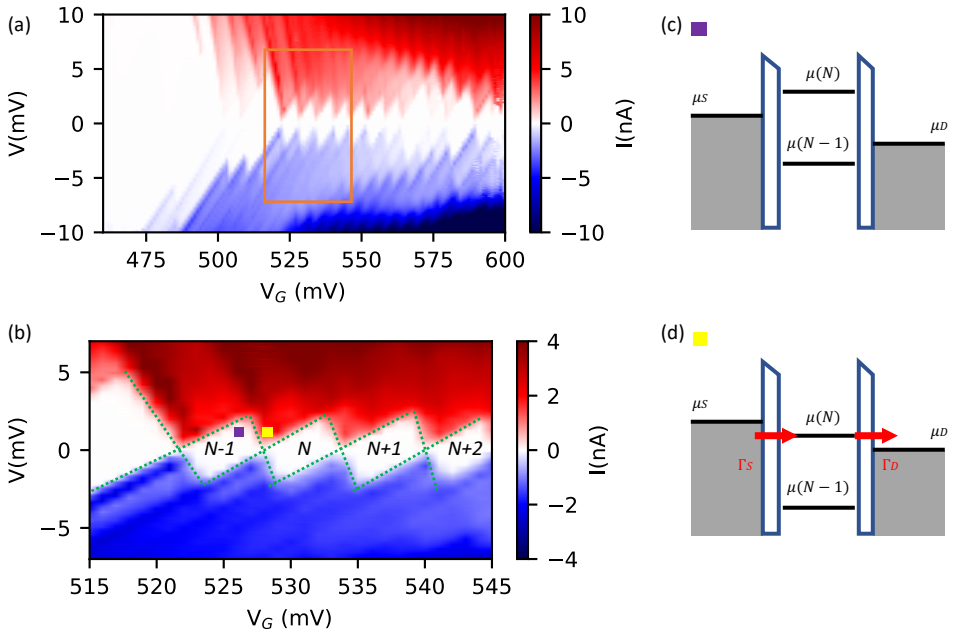

Figure 2.9: Electron transport through a quantum dot in an InSb nanowire. (a) Current through a quantum dot as a function of bias voltage and gate voltage. (b) Zoom-in of the scan in (a) shows Coulomb diamonds with electron numbers labeled. (c) Schematic of Coulomb blockade. No levels are within the bias window, and no electrons can flow through the dot. (d) Coulomb blockade is lifted when a more positive gate voltage is applied, as an energy level tuned into the bias window.

Fig. 2.9 shows electron transport through a quantum dot. Electron tunneling through the dot depends on the alignment of the electrochemical potential in the dot with respect to

the electrochemical potentials in the source, μ_S, and the drain, μ_D. In electrical transport measurements, a bias voltage, $V_{SD} = V_S - V_D$ can be applied across the source and drain reservoirs to open up an energy window (bias window), $\mu_S - \mu_D = -|e|V_{SD}$. For a quantum dot system in equilibrium, electron transport is only possible when a level corresponding to transport between ground states lies in the bias window, $\mu_S \geq \mu(N) \geq \mu_D$. If this condition is not met, Coulomb blockade will appear, as shown in Fig. 2.9(c). The number of electrons in the dot is fixed, no electron hops onto or out of the dot, and no current flows. Coulomb blockade can be lifted by changing gate voltage until the electrochemical potential $\mu(N)$ is tuned to be within the bias window, shown in Fig. 2.9(d). One electron can tunnel to the dot from the source electrode, increase the number of electrons from $N-1$ to N, and then tunnel to the drain. This transport cycle repeats, and current through the dot can be detected. Fig. 2.9(a-b) shows current as a function of the bias voltage and gate voltage. Within the diamond shape (enclosed by green dotted lines in Fig. 2.9(b)), the electron number is fixed, and the current is zero. These Coulomb blockaded regimes are known as the Coulomb diamonds. At low bias, by increasing the gate voltage V_G, the electrochemical potential $\mu(N)$ decreases, the ladder of the electrochemical potentials moves down in energy while the spacing between the levels remains the same. When $\mu(N)$ is within the bias window, electrons can flow outside the Coulomb diamond. Upon further increase of V_G, Coulomb blockade will appear again with $N + 1$ electrons in the dot.

2.3.2 Andreev reflection

Andreev reflection is a charge transferring process that occurs at the interface between a normal state material (N) and a superconductor (S). At the N-S interface, single-particle transmission is not allowed within the superconducting energy gap. Charge transfer occurs through the following process: at N-S interface, incident electron near Fermi level reflected as a hole with the same momentum returned to N, a charge of 2e transferred into superconducting condensate as a Cooper pair.

At low voltage bias, Andreev reflection is the only process responsible for electrical current at the N-S interface. The process transforms dissipative current in the normal

scattering region into supercurrent in the superconducting region.

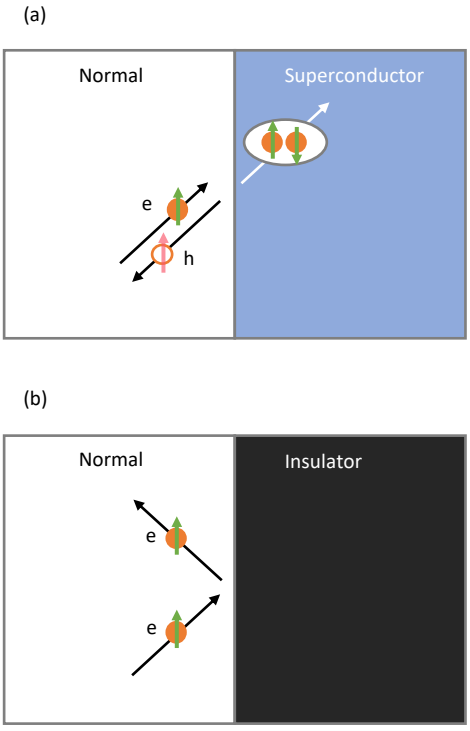

Figure 2.10: Schematic of (a) Andreev reflection at N-S interface, (b) normal reflection at N-I interface.

Fig. 2.10 (a) shows Andreev reflection at a N-S interface. Fig. 2.10 (b) depicts a normal reflection process at an interface of a normal state material (N) and an insulator (I). Compared to normal reflections, Andreev reflection has the following characteristics:

1. Andreev reflection converts an electron into a hole (with opposite charge). The disappearing 2e are absorbed by the superconductor as a Cooper pair.
2. Incident electron and reflected hole have opposite velocities.
3. The incident electron is of an excitation of energy ϵ above Fermi level, and the reflected hole is at energy ϵ below Fermi level. Andreev reflection is an elastic scattering process.
4. The reflected hole has a opposite spin as the incident electron.
5. Andreev reflection is a phase coherent process.

2.3.3 Anderson impurity model with superconducting leads

The Anderson impurity model is a Hamiltonian that is used to describe magnetic impurities embedded in metals. It can be applied to the description of a quantum dot coupled to superconducting leads. The effective Hamiltonian of the Anderson impurity model of a quantum dot coupled to superconducting leads is given by [34]:

$$H_{eff} = \sum_{\sigma}(\epsilon_d + \frac{U}{2})d_{\sigma}^{\dagger}d_{\sigma} + \frac{U}{2}(\sum_{\sigma} d_{\sigma}^{\dagger}d_{\sigma} - 1)^2 - \Gamma(\phi)(d_{\uparrow}^{\dagger}d_{\downarrow}^{\dagger} + h.c.) \tag{2.36}$$

where ϵ_d is the quantum dot energy level (orbital energy), U is the charging energy, d_{σ} is annihilation operator for an electron with spin σ, and Γ is the hybridization between the dot and the superconducting leads. The first two terms of Eq. 2.36 describe an isolated normal quantum dot with Coulomb interaction. The third term of Eq. 2.36 couples the quantum dot to the superconducting leads.

The effective Hamiltonian in Eq. 2.36 has four eigenstates:

$$\begin{aligned} |\uparrow\rangle \\ |\downarrow\rangle \\ |+\rangle = u\,|\uparrow\downarrow\rangle + v^*\,|0\rangle \\ |-\rangle = -v^*\,|\uparrow\downarrow\rangle + |0\rangle \end{aligned} \tag{2.37}$$

The $|\uparrow\rangle$ and $|\downarrow\rangle$ are the spin 1/2 states. They are degenerate when the magnetic field is absent and referred to as the magnetic doublet. The singlet $|+\rangle$ and $|-\rangle$ states are superpositions of the doubly occupied ($|\uparrow\downarrow\rangle$) and empty ($|0\rangle$) states. The coefficients are given by:

$$\begin{aligned} u &= \frac{1}{2}[1 + \frac{\epsilon_d + U/2}{\sqrt{(\epsilon_d + U/2)^2 + \Gamma(\phi)^2}}]^{1/2} \\ v &= \frac{1}{2}[1 - \frac{\epsilon_d + U/2}{\sqrt{(\epsilon_d + U/2)^2 + \Gamma(\phi)^2}}]^{1/2} \end{aligned} \tag{2.38}$$

The four eigenstates are the Andreev bound states of a single-level quantum dot with the following eigenenergies:

$$\begin{aligned} E_{\uparrow,\downarrow} &= \epsilon_d + U/2 \\ E_{\pm} &= \epsilon_d + U \pm \sqrt{(\epsilon_d + U/2)^2 + \Gamma(\phi)^2} \end{aligned} \tag{2.39}$$

The ground state of the quantum dot is either the magnetic doublet state ($|\uparrow\rangle$ or $|\downarrow\rangle$) or the lower energy singlet state $|-\rangle$. The parity of the ground state is determined by the competition between U, which favors an odd parity ground state (doublet state), and Γ, which prefers an even parity ground state (singlet state). The quantum phase transition between the singlet and doublet ground states occurs at a phase boundary described by:

$$(\epsilon_d + U/2)^2 + \Gamma(\phi)^2 = U^2/4, \tag{2.40}$$

The phase diagram of the singlet and doublet ground states with a phase boundary given by Eq. 2.40 is shown in Fig. 2.11 (a).

In the large charging energy limit (strongly interacting quantum dot), where $U > \Delta$, the quantum dot favors odd parity with magnetic doublet ground state. The magnetic doublet ground state of the quantum dot correlates with quasiparticles in the superconducting leads and forms a singlet state. This state is sometimes referred to as Yu-Shiba-Rusinov (YSR) singlet as the single spin in the quantum dot screened by quasiparticles from the superconducting leads resembles a magnetic impurity embedded in a superconductor [35, 36, 37].

However, in the large gap limit (weakly interacting quantum dot), where $\Delta > U$, i.e., the coupling between the quantum dot and superconducting leads is strong. The quantum dot energetically favors singlet ground state with even parity. Only the condensate of Cooper pairs are involved but not the continuous quasiparitcle spectrum. This regime can be confirmed in transport experiments with features including the lack of the Coulomb diamond resonances (negligible charging energy) and the absence of odd parity Andreev bound states (strong coupling to superconductor).

More detailed studies of the interplay between the quantum dot, the superconducting leads, and the Kondo effect can be found in [38, 39, 40, 34, 41, 42].

2.3.4 Sub-gap excitations: Andreev bound states

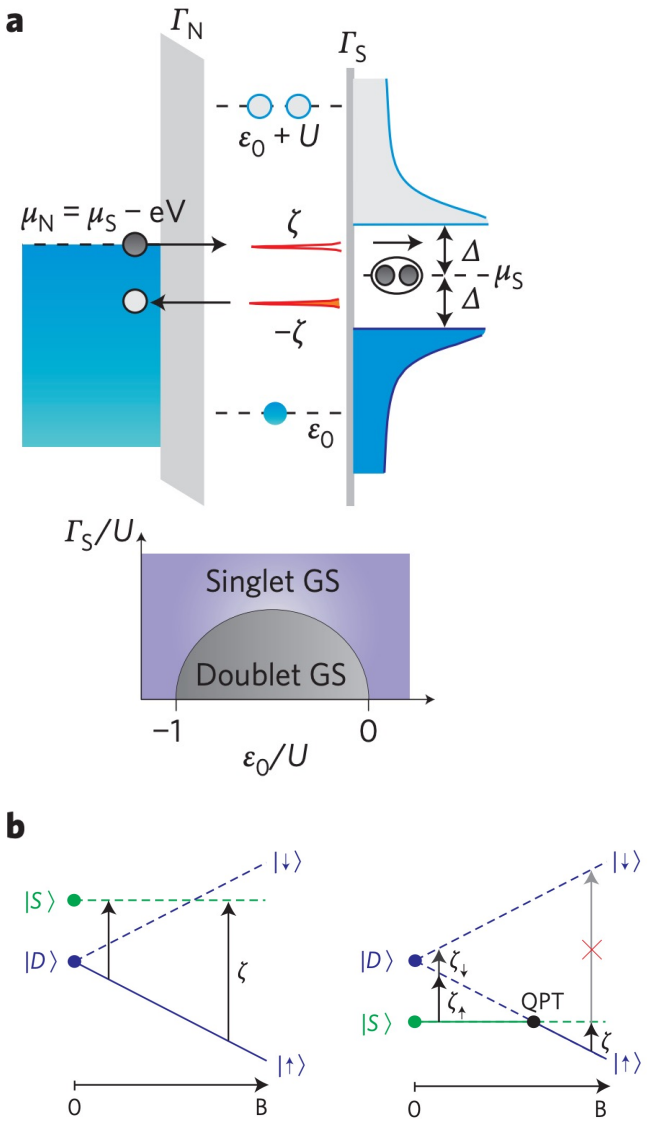

Figure 2.11: (a) Schematic of Andreev bound states in an N-QD-S system. (b) Low energy excitations and their magnetic field evolution. Figure adapted from [43].

Andreev bound states appear at normal scattering region of an S-N-S junction. The formation of Andreev bound states can be explained by Andreev reflections at both N-S interfaces. Consider an electron in the normal region, it Andreev reflects off the N-S interface on the right as a hole, and then Andreev reflects off the S-N interface on the left

again as an electron. Since an electron's momentum, energy, and spin are conserved during Andreev reflection, a standing wave can form as electrons Andreev reflect on both ends of the normal region. Andreev bound states were first studied in Josephson junctions, where the normal region does not have interactions. For a quantum dot coupled to superconductors (S-QD-S device), as long as the charging energy U is small compared to the superconducting gap Δ, the Andreev bound state picture should still be valid. Andreev bound states appear naturally when solving the Anderson impurity model with superconducting lead as discussed in section 2.3.3.

Fig. 2.11 (a) shows the schematic of Andreev bound states in an N-QD-S system. Γ_N and Γ_S are the tunneling couplings of the quantum dot to the normal lead and superconducting lead, respectively. Δ is the superconducting gap. U is the charging energy. ϵ_0 is the quantum dot energy level. μ_N and μ_S are the chemical potentials of the normal and superconducting lead. The sub-gap peaks located at $\pm\zeta$ represent transitions between ground and excited Andreev states with energy differences $\pm\zeta$. A bias voltage V is applied across the system. In tunneling measurements, when μ_N is aligned with ζ, an incident electron from the N lead Andreev reflects as a hole at the QD-S interface, and a Cooper pair is transported into the S lead. Resonances of transitions between Andreev ground state and excited state (2.11(b)) are observed as peaks in differential conductance. The phase diagram shows the stability of the doublet and the singlet ground states as a function of QD energy and the coupling to superconductor [34]. Fig. 2.11 (b) shows low-energy excitations and their magnetic field evolution. The left panel has the doublet state as the ground state at zero magnetic field. As applying a magnetic field, the degenerate doublet state Zeeman splits. The doublet $|\uparrow\rangle$ state becomes the ground state. Resonances correspond to the transitions between the doublet $|\uparrow\rangle$ ground state and the singlet excited state move up in energy. The right panel shows the magnetic field evolution of the singlet ground state. The excited doublet state Zeeman splits in a magnetic field. At quantum phase transition (QPT), the singlet state and the doublet $|\uparrow\rangle$ state are degenerate in energy. Further increasing magnetic field, the doublet $|\uparrow\rangle$ moves down in energy and becomes the ground state.

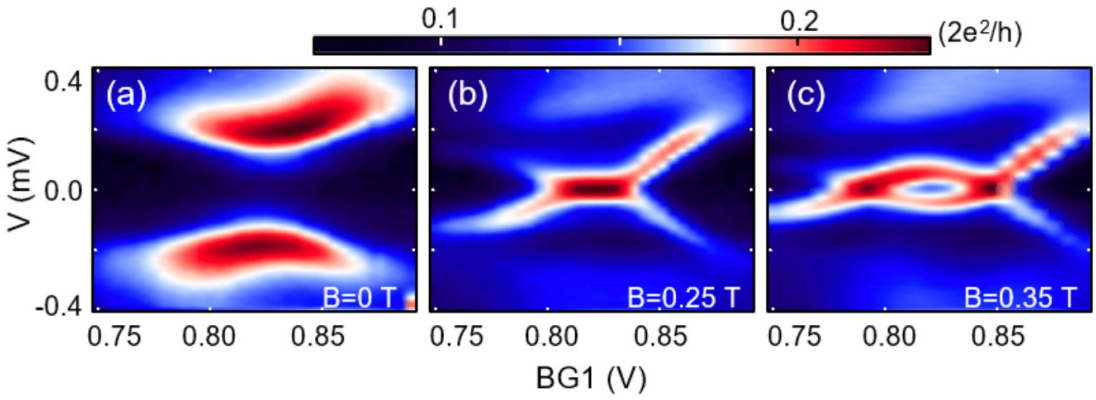

Figure 2.12: Andreev bound states with different couplings of the quantum dot to superconductor tuned by a gate voltage. (a) Singlet GS. (b) Quantum phase transition. (c) Doublet GS. Figure adapted from [44].

Fig. 2.12 shows the phase transition of the Andreev bound states from the singlet ground states with even parity to the doublet ground states with odd parity. Anti-crossing resonances in Fig. 2.12 (a) correspond to the transitions between the singlet Andreev ground state and the doublet Andreev excited state. When the magnetic field is applied, the doublet excited states Zeeman split, while the singlet ground state is not affected. The doublet $|\uparrow\rangle$ state moves down in energy. In Fig. 2.12 (b), Quantum phase transition occurs when the singlet state and the doublet $|\uparrow\rangle$ state are degenerate. A resonant peak at zero bias is observed ($\zeta = 0$). In higher magnetic fields, the doublet $|\uparrow\rangle$ state moves further down in energy and becomes the ground state. Fig. 2.12 (c) shows loop resonances that correspond to the transitions between the doublet $|\uparrow\rangle$ ground state and the singlet excited state.

Note that in a single-level QD, the zero-energy transitions only occur at the QPT. In tunneling spectroscopy, it should appear as a zero-energy crossing in magnetic fields. However, for a QD with multiple energy levels within the superconducting gap (that is, the large gap limit of the Anderson impurity model), level repulsion from higher energy states could result in an extended zero-bias peak in magnetic fields [43], which was previously considered as a Majorana signature.

Andreev dot is a quantum dot coupled to a superconductor with Andreev bound states.

It is the building block of the quantum dot chain experiments discussed in Chapter 5.

2.4 Implementation of the Kitaev model with quantum dot chain

Implementation of Kitaev model [31] in hybrid superconductor/semiconductor nanowire systems [25, 26] is by far the most promising approach to realize Majorana zero modes, which can be used as building blocks for topological quantum computation. However, the suppression of topological superconductivity by disorder and the inability to tune the chemical potential of a semiconductor nanowire in contact with a superconductor (the tunability of semiconductor reduced remarkably due to the screening effect) are the most significant challenges in the experimental realization of Majorana wire model. The tolerance for disorder in the continuous Majorana wire model [25, 26] is too low [45, 46]. The requirements for clean semiconductor nanowires and high spin-orbit coupling create difficulties in material synthesis and device fabrication.

Instead of extraordinary efforts to eliminate quantum dot states caused by disorder, quantum dots can be used in Majorana search. Theory suggests a robust topological superconducting phase can exist in a chain of quantum dots coupled to superconductors, as a discrete version of the Kitaev model [47, 48, 49].

Take the model from [47] as an example. A one-dimensional system is assembled with multiple dots coupled to superconductors, each with an Andreev bound state. Because sites are independently tunable, it helps to suppress and overcome the effect of disorder. As long as the electron can hop between neighboring quantum dots, the topological state can form in the chain. Quantum dots or superconductors can have local disorder and are not necessarily phase coherent. It is much easier to satisfy than to achieve ballistic transport in a nanowire. The quantum dot chain proposal provides a practical experimental system to realize Majorana zero modes.

Disorder in quantum dots and superconductors only affects and causes fluctuations in the spacing of dot levels δE_n. Chemical potential can be tuned by gate voltage such that a single level in each dot participates in transport through the chain. As long as there is

a single occupied spin-polarized level in each dot at zero chemical potential, the quantum dot/superconductor chain can be considered as equivalent to a 1D lattice model with a spin-polarized state per site.

A disordered Kitaev chain can be described by an effective Hamiltonian

$$H_{eff} = \sum_{n} -\mu_n \hat{\Psi}_n^\dagger \hat{\Psi}_n + t_n(\hat{\Psi}_{n+1}^\dagger \hat{\Psi}_n + h.c.) + \Delta_n(\hat{\Psi}_{n+1}^\dagger \hat{\Psi}_n^\dagger + h.c.) \tag{2.41}$$

where $\hat{\Psi}_n^\dagger$ is the creation operator in each dot, μ_n is the chemical potential in each dot, t_n is the normal tunneling amplitude between the dots, and Δ_n is the effective proximity-induced superconducting pairing amplitude. In a disordered chain, t_n and Δ_n can vary along the chain at each site, while μ_n can be tuned to near zero by gates. Time-reversal symmetry is broken by the Zeeman field. At $\mu_n = 0$, a single spin-polarized level in each dot participates in transport. Spin-orbit coupling allows a rotation of spin-polarization inside each dot, and the induced superconductivity pairs electrons from neighboring dots.

As simulation results demonstrated in [47], the spectrum of a disordered chain with only a few sites described by 2.41 shows zero modes protected by a robust gap.

In Ch. 4, we propose a model of Andreev quantum dot chain to realize the Kitaev model. In our model, superconductivity pairs electrons in the same dot. Andreev states in each dot has a singlet ground state at zero magnetic field. At finite magnetic fields, the Andreev ground states become spin-up doublet and pair along the chain.

3.0 Experimental methods

3.1 Nanowire growth

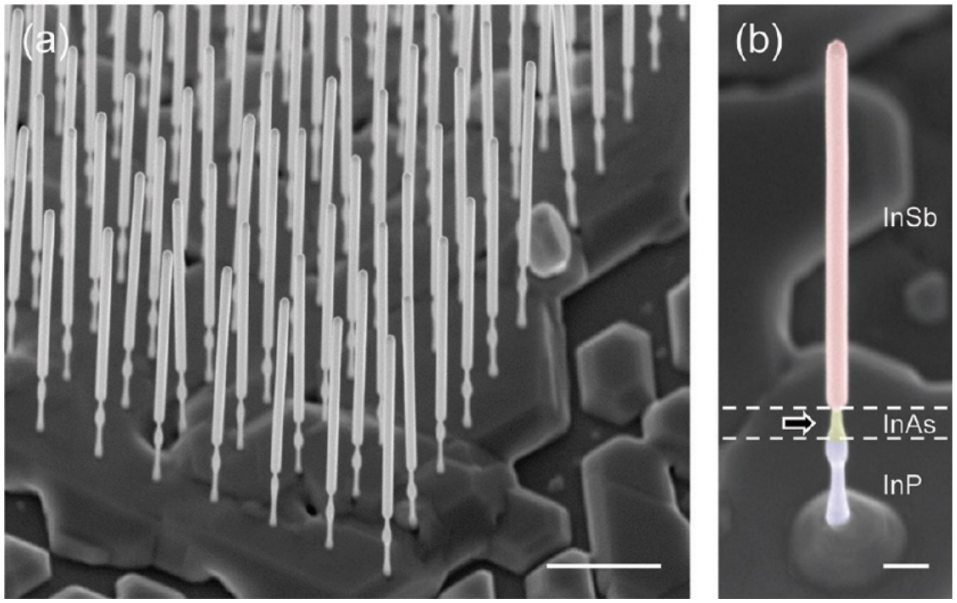

Figure 3.1: (a) SEM image of an array of InSb nanowires vertically grown on (111)B InP substrate. Scale bar corresponds to $1\mu m$. (b) Zoom-in image on a single InSb nanowire. The thin growth stem of InAs is where the nanowire easily breaks off from the growth chip when picking up and transferring to a device chip. Scale bar corresponds to $200nm$. Figure adapted from [50].

Bulk Indium Antimonide (InSb) has a small effective mass ($0.015m_e$), a small bandgap ($0.17eV$), and high electron mobility ($77000cm^2/Vs$). The growth of InSb nanowire is well established and can be optimized since a large set of temperatures, and III/V ratios are achievable [51].

InSb nanowires exhibit properties ideal for spin-based quantum dot devices and hybrid semiconductor-superconductor Majorana wire devices, including high electron mobility, which allows ballistic transport in the nanowire [52, 53], strong spin-orbit interaction [54, 55]

and large Landé g-factor [56, 57, 58]. Although due to details of confinement in the quasi one-dimensional nanowire, spin-orbit strength and g-factor may vary from device to device.

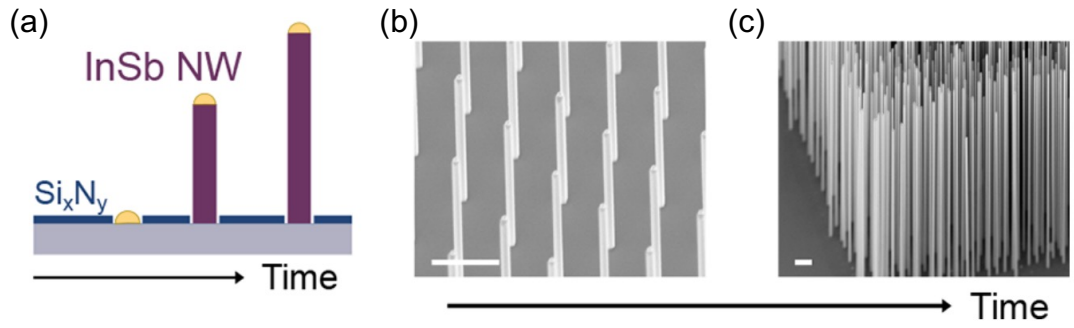

Figure 3.2: Stemless InSb nanowire growth via VLS mechanism on InSb(111)B substrate. Scale bars in (b) and (c) correspond to $1\mu m$. Figure adapted from [59].

InSb nanowires are grown by metal-organic vapor phase epitaxy (MOVPE) through vapor-liquid-solid (VLS) mechanism [60, 50]. The growth of InSb nanowires usually requires a stem of different materials for nucleation. In Fig. 3.1(b), InP stem is grown to facilitate uniform nucleation, and InAs stem is used to reduce the lattice mismatch with InSb. As arsenic evaporates during the growth of InSb, the InAs stem gets thinner and eventually breaks, which leaves the InSb nanowires to fall onto the substrate and they cannot be picked up. Such an InAs stem not only limits the length of the InSb nanowire ($1 - 3\mu m$), but its material mixes into the InSb segment and creates disorder in the nanowire. Using a selective-area mask, stemless InSb nanowires of a few to tens of microns long with high chemical purity and high electron mobility can grow directly from the substrate [59]. Fig. 3.2 (a) shows the stemless InSb nanowire growth process. Gold (Au) catalyst droplets are positioned within nano-openings of a selective-area mask of Silicon Nitride (Si_xN_y) on an InSb (111)B substrate. The presence of a selective-area mask prevents the spreading of the Au catalyst droplets and suppresses layer growth of InSb on the substrate, such that the growth of a stem is no longer needed. The InSb nanowires are grown with trimethyl-antimony (TMSb) and trimethyl-indium (TMIn). Stemless nanowires with high chemical purity and high electron mobility have less disorder. Longer nanowires are preferred for creating a robust topological

superconducting phase and establishing well separated Majorana zero modes.

Stemless nanowires are used in devices presented in Chapter 5. InSb nanowire growth is performed by S.R. Plissard, D. Car, S. Gazibegovic, G. Badawy in the research group of E.P.A.M Bakkers at Eindhoven University of Technology.

3.2 Device fabrication

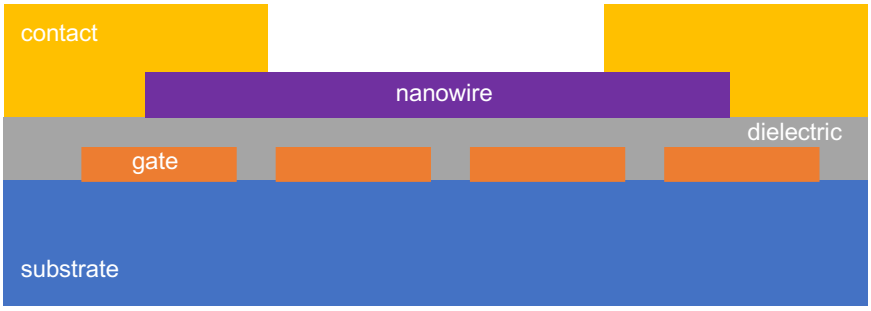

Figure 3.3: Schematic sideview of a two-terminal nanowire device on local electrostatic gates.

Different types of devices have been made for different projects and different purposes throughout our study. Here, we introduce the general steps of device fabrication. The simplest two terminal devices (illustrated in Fig. 3.3) are usually used to characterize the quality of nanowires and contacts at the stage of testing nanowire growth or improving fabrication recipes. More advanced devices with local electrostatic gates and multiple contacts (both superconducting and normal metal leads) follow this basic fabrication sequences while extra steps for defining and depositing local gates and contacts are required.

A general fabrication sequence includes the following steps:

1. **Fabrication of alignment markers, local gates, and bonding pads.** Alignment markers establish a coordinate system on a bare substrate. Local gates can control carrier density in a semiconductor nanowire. Details on alignment markers and gates are discussed in Sec. 3.2.2. Bonding pads are used to connect devices to electrical measurement circuits.

2. **Nanowire transferring and imaging.** Nanowires need to be transferred from a growth chip onto a device chip with pre-fabricated alignment markers, local gates, and bonding pads. Images of nanowires and nearby makers can precisely locate the nanowires on the device chip. More details on nanowire transferring are discussed in Sec. 3.2.3.
3. **Design and define contact patterns.** Based on each wire's location and orientation, desired patterns such as contacts and gate electrodes are designed and defined through a standard electron beam lithography (EBL) process. Details on lithography are discussed in Sec. 3.2.1.
4. **Oxide removal and surface cleaning.** Insulating native oxide layer on nanowire surface need to be removed and cleaned in order to reduce surface scattering processes and achieve Ohmic contacts. Both physical and chemical methods of surface cleaning are discussed in Sec. 3.2.4.
5. **Metal deposition and lift-off.** Materials of normal metals or superconductors are deposited. Resist is removed by lift-off process together with the deposited material covering it. More details in Sec. 3.2.5.
6. **Imaging and testing.** SEM images of devices and room temperature resistance measurements help to decide whether the devices are worth a cooldown or new devices need to be made.

A detailed fabrication recipe is included in the appendix.

3.2.1 Lithography

Standard optical lithography techniques are used to define large patterns (above $1\mu m$), such as bonding pads, which do not require the highest definition or great alignment accuracy. Traditional deep ultraviolet (DUV) optical lithography uses a pre-defined photomask with fixed patterns. It requires physical contact of the photomask and the wafer covered by the photoresist. A more advanced maskless aligner uses a spatial light modulator as a programmable mask, providing better pattern design flexibility. However, due to the wavelength of the DUV light, it is difficult to define submicron features with optical lithography. Electron beam lithography (EBL) is ideal for defining highly precise patterns, such as align-

ment markers and fine local gates, as narrow as tens of nanometer. Owing to its versatility, EBL is suitable for defining contacts of nanowire devices since the orientation and location of each nanowire transferred onto the gate chip are different.

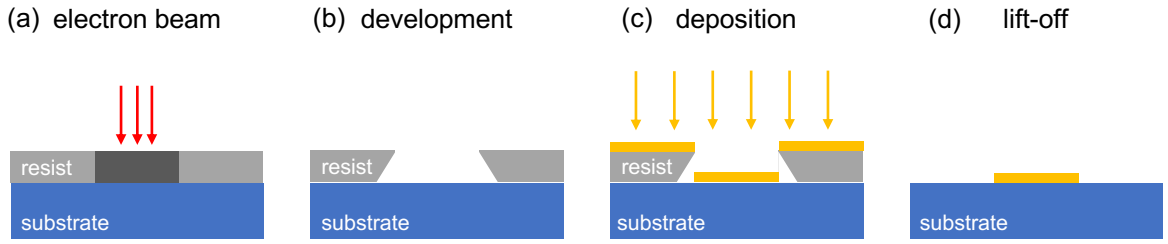

Figure 3.4: Schematic of lithography and metal deposition. (a) Exposure of electron beam. (b) Development. (c) Metal deposition. (d) Lift off.

Fig. 3.4 shows a schematic of a typical e-beam lithography process. (a) A substrate is coated with a thin layer of electron-sensitive resist. Polymethyl methacrylate (PMMA) is the most commonly used resist in our study. Exposure to electrons breaks the chemical bonds of the polymer and changes its solubility in developer, a solvent made of methyl isobutyl ketone (MIBK) and isopropanol (IPA). (b) During the development, the area of resist exposed to electron beam will be dissolved in the developer and removed, leaving the area uncovered. Resist in Fig. 3.4 (b) exhibits an undercut profile after development. An undercut profile is preferred since it is easy to lift off after material deposition. An undercut can be achieved by adjusting exposure electron dosage, developing time, e-beam energy (acceleration voltage), or using bi-layer resist. We found that even with enough dosage, there can still be resist residual in the exposed area after development which will reduce contact transparency. Before the deposition, a gentle oxygen plasma surface cleaning was added to the process to remove resist residual but not over-etch the finely patterned resist mask. (c) The patterned resist acts as a mask. Materials then can be deposit on the entire chip, covering both the resist mask and the exposed area where resist was removed in development. Thin films of normal metal, superconductor, or dielectric materials can be deposit through this process. (d) The rest of the resist and materials deposited on top will be removed by placing the sample in a solvent, usually acetone.

3.2.2 Alignment markers and gates

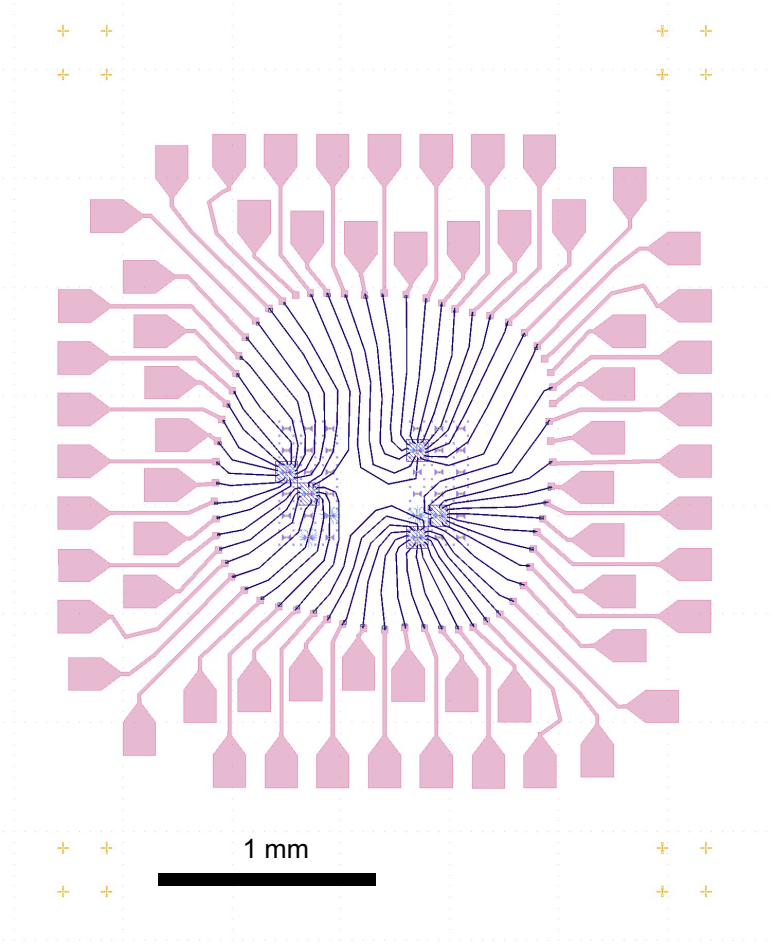

Figure 3.5: The layout of the device chip design. Pink patterns represent bonding pads. Yellow patterns are global alignment markers. Purple patterns are devices' source, drain, and gate electrodes.

Fig. 3.5 shows the layout of a chip design. Pink patterns of bonding pads are defined by optical lithography. Yellow patterns of global alignment markers at each corner of the chip and purple patterns of devices are defined by EBL. Global alignment markers are used to establish a coordinate system for the entire chip and reference the approximate locations of nanowires. Manually picking up a single nanowire from a growth chip and placing it onto a device chip is of high yield with practice. However, the location and orientation of nanowire landed onto the device chip are different for each transfer. Local alignment markers are

needed to reference the exact location and orientation of each wire.

For devices that do not require local control of chemical potentials, a global back gate is used. The global back gate consists of a p-doped Si substrate that voltage can be applied directly onto the back of the chip and a layer of $285nm$ thermally grown SiO_x as the dielectric.

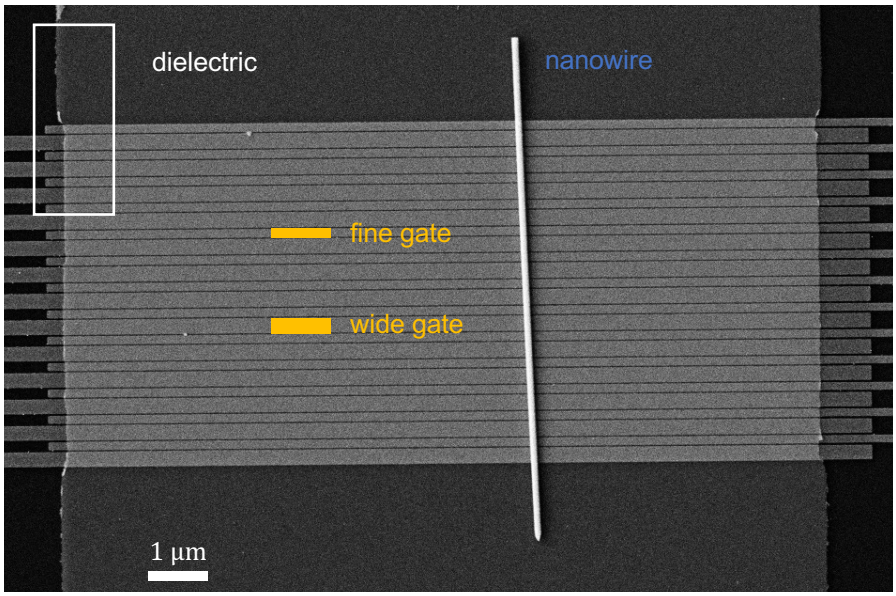

Figure 3.6: A nanowire on an array of local gates. The alternating narrow and wide gates are covered by dielectric.

For devices that require gate-controlled tunnel barriers, such as quantum dot devices, local gates are necessary. The design of local gates can be flexible to have desired width and pitch. Fig. 3.6 shows a nanowire on top of an array of alternating fine and wide local gates. Fine narrow gates are used to create sharp tunnel barriers to perform tunneling experiments or define quantum dots in the nanowire. Wide gates are used to control the chemical potentials of the wire segments uniformly. Above local gates, a thin dielectric layer is used to electrically separate gates and the nanowire. Patterning of the fine gates is performed by Jun Chen with a 100kV Elionix EBL system at Carnegie Mellon University.

Even though InSb has a small bandgap, it is difficult to tune the chemical potential of the InSb semiconductor nanowire segments covered by superconducting contacts due to the screening effect. A thin dielectric layer with a high dielectric constant κ can create a high

electric field and help control chemical potential with a relatively small voltage applied. A layer of $10nm$ HfO_x is deposit by the atomic layer deposition (ALD) at 120C. HfO_2 has a dielectric constant of 25, which is six times higher than that of SiO_2. We measured the breakdown voltage of our HfO_x layer as $\pm$ 9V.

3.2.3 Nanowire transferring and designing

InSb nanowires are transferred from a growth chip onto a sample substrate using a micromanipulator under an optical microscope. We built the nanowire deposition setup following [61]. A sharp tip (Indium or tungsten) is attached to the micromanipulator. Van der Waals forces can pick up a single nanowire when sweeping the tip gently against the end of the wire. By rotating the tip and tilting the arm of the manipulator, one can adjust the angle for the nanowire to land on the substrate. By moving the sample substrate under an optical microscope while lowering the tip and the nanowire, one can achieve precise alignment within 5 degrees. Wires are placed onto the substrate slowly and gently to avoid damage to the nanowire and the dielectric layer on top of local gates. Frequently adjusting the focus slightly with an optical microscope, it is obvious to notice when the end of the $5\mu m$ nanowire touches the sample substrate. At this moment, avoid moving the tip up and down, slowly move the stage towards the direction for desired wire orientation, the sample substrate will 'drag' the nanowire onto the substrate. Once the wire is deposited onto the substrate, despite its orientation, try not to move it with the tip if it scratches the dielectric layer.

After wire transfer but before imaging, we dip the chip into acetone and rinse, then rinse in isopropanol and blow-dry. This is necessary for the following purposes: 1, clean sample surface and remove organic debris. 2, remove nanowires that are not well attached to the substrate. Imaging and designing without removing these wires may result in misalignment of exposure since these wires may change positions and orientations while spin-coating e-beam resist.

A long nanowire ($10nm$) is easily bent and damaged when transferred onto pre-patterned gate chips. From our experiences, narrow wires ($\leq 100nm$) are unlikely to conduct at low temperatures. On the other hand, thick wires ($\geq 150nm$) are difficult to pinch off (tune to

tunneling regime with low carrier density). A typical stemless nanowire is $3-5\mu m$ in length with a diameter of $100-150nm$. We only design and fabricate devices with nanowires that look undamaged and of desired dimensions.

Scanning electron microscope (SEM) images of nanowires and nearby cross-shaped markers are inserted into computer-aided design (CAD) file, scaled, rotated, and distorted to match the layout of the alignment markers in the digital design. With fine alignment markers and high-quality SEM images, we know precisely where the nanowires are located and how they are oriented. Patterns of contacts and gate electrodes are drawn in the design file and defined by e-beam lithography.

3.2.4 Oxide removal and surface cleaning

The superconductor-semiconductor interface is the most crucial to the quality of a device. Defect-free InSb nanowires with minimum disorder and high electron mobility have an insulating layer of native oxide, containing compounds such as In_2O_3 and Sb_2O_5. This native oxide layer needs to be removed to make electrical contact with normal metal or superconductor. A transparent contact to a superconductor is important for the proximity effect to induce superconductivity into the nanowire. Complete removal of the native oxide is required. However, over-etch may damage the crystalline structure of the nanowire and create disorder. Disorder-induced Andreev bound states are commonly seen in hybrid nanowire devices, and they can mimic Majorana signatures in many aspects. So effective removal of the native oxide and gentle surface cleaning before the metal deposition is key to making transparent contact. Several methods of surface cleaning are used throughout our study.

3.2.4.1 Ar plasma etching

Argon RF plasma etching is a commonly used method to get rid of the oxide physically. Ar ions bombard the nanowire surface and kick out the atoms on the top layers. Ar plasma etching is efficient in removing the oxide, and it can be done in-situ before superconductor deposition without breaking the vacuum and avoid re-oxidation while transferring the sam-

ple. However, this method tends to etch the oxide non-uniformly. After Ar plasma cleaning, the nanowire exhibits a rough surface, which indicates the nanowire crystal lattice is damaged and disorder is created. The nanowire devices fabricated using this method show low mobility and a soft induced superconducting gap [62]. A soft gap refers to a weak suppression of the subgap density of states. A soft gap is undesirable in Majorana experiments since it limits the prominence of the subgap Majorana signatures in magnetic fields.

3.2.4.2 Sulfur passivation

Sulfur passivation is an ex-situ chemical wet etching process [63]. Sulfur passivation can etch the oxide uniformly and leave the nanowire surface smooth. This method is chemically selective. It etches the oxide while leaving the semiconductor nanowire crystal lattice intact. It is also a self-terminating process, leaving a thin layer of sulfur atoms on the nanowire surface, protecting the nanowire from re-oxidation while transferring the sample into the deposition chamber. The thin layer of sulfur may dope the nanowire surface. It is removed by a short and gentle in-situ Ar plasma cleaning before contact deposition. A detailed recipe for sulfur passivation is attached in the appendix.

As suggested in [64], before superconductor deposition, one can grow a thin layer of high-quality oxide or high bandgap semiconductor as a barrier in a controllable manner. This technique is developed to control the strength of the induced superconductivity, which provides another tunable parameter in engineering the topological phase.

3.2.5 Contact deposition

After oxide removal and surface cleaning, contact material (metallic, superconducting, or ferromagnetic) will be deposited. Normal contacts of gold (Au) or palladium (Pd) on top of a thin adhesion layer of titanium (Ti) are deposit by electron beam evaporation. The deposited film thickness should be larger than the nanowire thickness to cover fully and clamp down the nanowire to avoid disconnects in contacts due to stress. A thicker resist mask of slowly spin-coated PMMA, or a double layer PMMA, or a bi-layer of 495k PMMA/950k PMMA can be used to achieve an undercut for an easier lift off. Overheating may melt and

deform the resist mask and result in failed lift-off. During evaporation in deposition system without sample cooling, the electron beam current is monitored to ensure no overheating in the sample.

Sputtering can deposit materials with high melting points and alloys of different materials. NbTiN has a high critical temperature (13K measured in our lab) and high critical magnetic field (15T reported). NbTiN is easy to make contact with InSb and InAs nanowires, and it is stable against oxidation. Superconducting contacts of NbTiN are deposited in the AJA deposition system via DC sputtering from a target of NbTi alloy (Nb 70 wt% and Ti 30 wt%) with RF Ar plasma and nitrogen flow. Parameters including DC power, pressure, Ar/N2 flow, and distance between the target to the sample are optimized such that NbTiN thin film has the highest critical temperature. A wetting layer of NbTi is used to achieve a better induced superconducting gap [62]. In our recipe, Ar plasma was created in the vacuum chamber at a background pressure of a few mTorr. The energetic Ar ions from the plasma bombard the surface of the NbTi target. Rather than having ballistic trajectories, sputtered atoms ejected from the target have diffusive motion due to collisions with Ar ions in the plasma. Higher pressure results in more isotropic flow and conformal coating. Consequently, NbTiN deposited on the sidewall of the PMMA resist mask connects with the film deposited on top of the resist, causing difficulties in the lift-off process. Reducing film thickness could help with the lift-off issue. Sputter deposited NbTiN films have stress that may break the nanowire. To reduce the damage to the nanowire from the stressful NbTiN film, one can reduce the film thickness or reduce the contact area. However, thinner and smaller superconducting contact leads to a weaker proximity effect and a soft induced superconducting gap. Adjusting the nitrogen and argon flow to control the plasma pressure may help with solving the stress issue. However, it is a trade-off between high critical temperature and less stress. Further optimization and tests are needed to improve the fabrication recipe and achieve a hard induced superconducting gap in nanowires.

Evaporated superconducting vanadium (V) and aluminum (Al) have been tested. However, we failed to establish a hard induced superconducting gap in nanowires with V or Al at a high parallel magnetic field that may host topological phase.

3.2.6 Lift-off and imaging

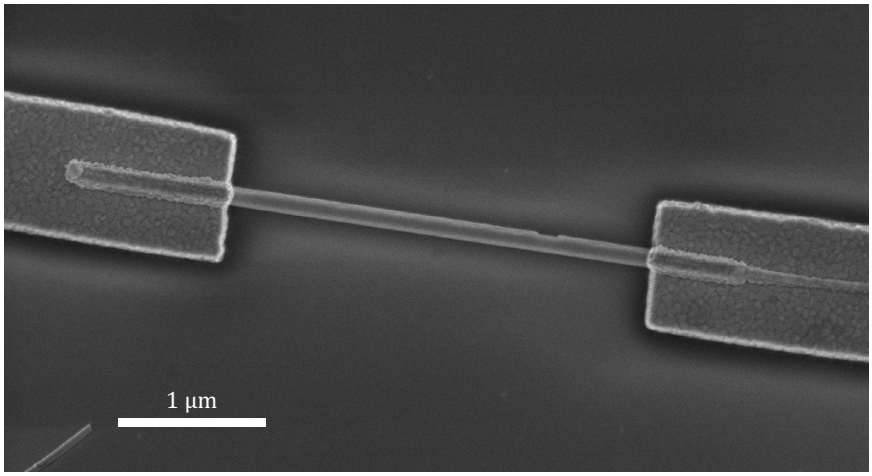

Figure 3.7: SEM image of a typical two-terminal InSb nanowire/Sn shell device with a shadow defined junction on a back gate.

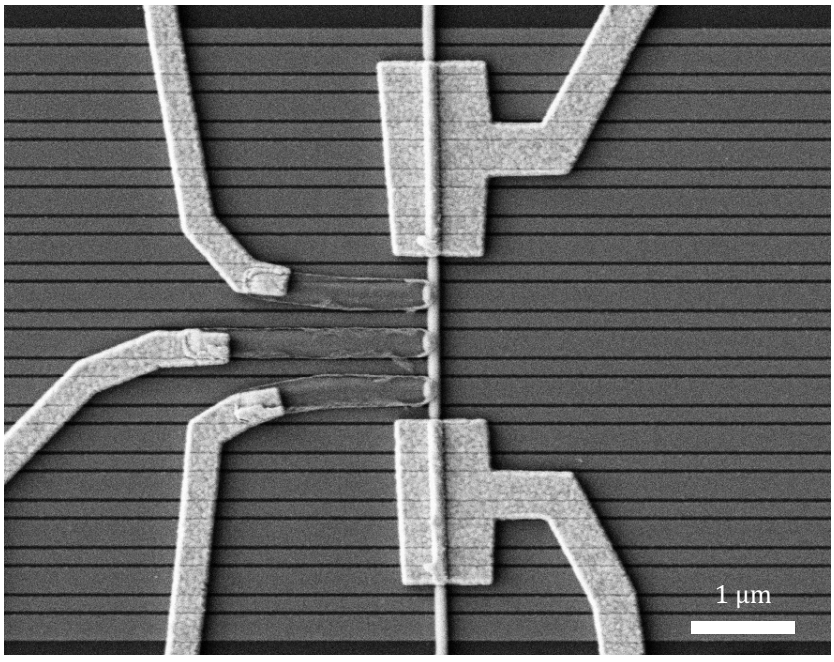

Figure 3.8: SEM image of a typical quantum dot chain device with two fully-covered normal contacts and three half-covered superconducting contacts on an array of local gates.

After contact deposition, the device chip is left in acetone to lift off. SEM images of devices are taken. Fig. 3.7 shows a typical two-terminal InSb nanowire device on a back gate. Fig. 3.8 shows a typical quantum dot chain device with multiple contacts on an array of fine local gates. Devices are tested at room temperature with a probe station. Selected devices will be loaded into a dilution refrigerator for low-temperature measurements.

3.3 Advances in nanowire growth and device fabrication

3.3.1 Epitaxial semiconductor/superconductor nanowire

As mentioned in Sec. 3.2.4, the semiconductor/superconductor interface quality is key to the induced superconducting gap and potential topological superconducting phase. The ex-situ methods of superconductor deposition discussed in Sec. 3.2.5 require removal of the oxidation layer grown on the nanowire surface due to exposure to air. With either physical dry etching (plasma etching) or chemical wet etching (sulfur passivation), damage to semiconductor nanowire is inevitable. Although with the optimization of the etching processes, the damage can be minimized. The disorder introduced to the interface by ex-situ etching results in the soft gap issue. Disorder-induced low-energy states complicate the interpretation of the experimental data and obscure the existence of Majorana zero modes in hybrid nanowire devices [65, 66].

In-situ growth of Indium Arsenide (InAs) semiconductor nanowires and Aluminum (Al) superconducting shell by molecular beam epitaxy (MBE) provides a new approach to electrical contacting nanowires and fabricating semiconductor/superconductor hybrid nanowire devices [64]. Fig. 3.9 shows a highly ordered epitaxial interface between the InAs nanowire and the Al shell, where both materials maintain crystallinity.

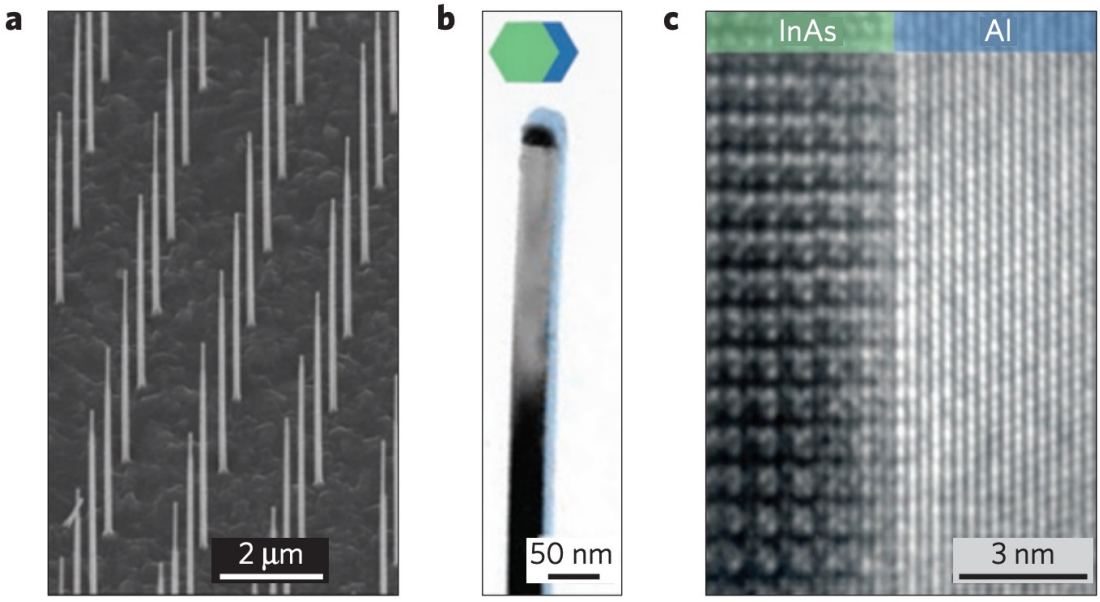

Figure 3.9: (a) SEM of an array of epitaxial InAs/Al nanowires grown on an InAs (111)B substrate. (b) Transmission electron microscope (TEM) image of an epitaxial InAs/Al nanowire. The 10nm Al shell covers two facets of the nanowire, highlighted in blue. (c) High-resolution TEM image of the InAs/Al interface. Figure adapted from [64].

With uniform InAs/Al interface and thin Al shell, a hard induced gap has been observed [67]. The hybrid InAs/Al epitaxial nanowires have strong spin-orbit coupling, high critical parallel magnetic fields, and gate tunable carrier density. Therefore, InAs/Al nanowires are suitable for Majorana study [28, 68, 69]. However, a reduced effective g factor suggests the superconducting density of states is distributed largely in the Al shell rather than in the semiconductor InAs nanowire [70]. The properties of large g factor and spin-orbit interaction of the InAs nanowire may be reduced in the hybrid InAs/Al epitaxial nanowire, which may lead to the topological phase being inaccessible beyond the critical parallel magnetic field of the Al thin shell.

Due to the screening effect, to perform tunneling experiments, segments of the Al shell need to be removed by chemical wet etching so that the exposed InAs nanowire segments can be gate tuned. The ex-situ etching can introduce disorder to the interface. To prevent

further oxidation and degradation of the interface quality, a capping layer can be deposited after the device is made.

Such InAs/Al core/shell nanowires are used in Andreev blockade experiments presented in Chapter 7. InAs/Al core/shell nanowire growth is performed by S. Khan in the research group of P. Krogstrup at Niels Bohr Institute, University of Copenhagen.

To avoid ex-situ etching, various shadow lithography techniques have been used [71, 72, 73]. Fig. 3.10 (a) shows the growth of hybrid InSb nanowire/Al superconducting islands with nanowires as shadow masks. The InSb nanowires are grown from accurately positioned Au particles (as a catalyst) via VLS mechanism on the inclined (111)B facets of the etched trenches on an InP (100) substrate. The nanowires on the two trenches grow towards each other. By adjusting the position and spacing of the Au particles, nanowires from two sides could grow into each other and form networks or close to each other but not merge. In MBE, apply Al flux parallel to the trenches. The front wire casts a shadow on the wire behind. Fig. 3.10 (b) shows InSb nanowires with shadow defined Al islands. EDX chemical composition of the nanowire shows an abrupt shadowed region separating two Al islands in Fig. 3.10 (c). Fig. 3.10 (d) shows the Al is covering two facets of the hexagonal nanowire, which allows gate tuning of the chemical potential. InSb nanowires are grown by MOVPE, and then nanowires are transferred ex-situ to an MBE chamber. Oxidation is removed by atomic hydrogen cleaning [74] before the deposition of superconducting Al. Fig. 3.10 (d) shows the oxidation is effectively removed, and no oxygen is observed at the interface.

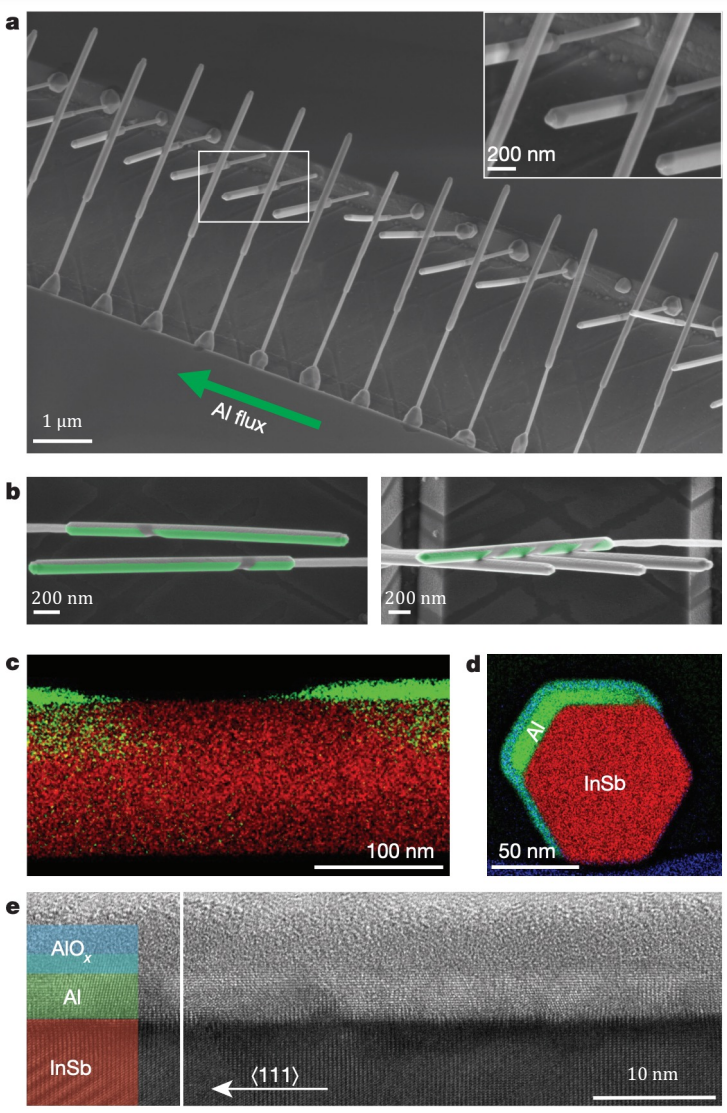

Figure 3.10: (a) SEM image of an array of InSb/Al nanowires. The green arrow indicates the direction of Al deposition. Each nanowire is shadowed by a wire in the front, leaving two Al islands separated by a shadowed region on the wire. (b) SEM images of InSb nanowires with two and four Al islands (false-colored green). (c) Scanning transmission electron microscopy (STEM) energy-dispersive X-ray spectroscopy (EDX) chemical composition of InSb nanowire (red) with Al islands (green) separated by an abrupt shadowed region free of Al. (d) EDX chemical composition of the hexagonal nanowire cross-section. Al covers two facets of the InSb nanowire. No oxidation layer formed at the interface. (e) High-resolution TEM image of the InSb/Al interface. A capping layer of AlOx is grown in-situ. Figure adapted from [71].

Al is deposited by MBE at a low temperature about 120K realized by active liquid nitrogen cooling. Growth of Al at a low temperature is crucial to realize a smooth thin film on the nanowire surface and to have a high critical parallel magnetic field. A capping layer of AlOx is grown in-situ in MBE to prevent oxidation of the Al islands and the shadowed junction. The capping layer also prevents the Al film from diffusion, resulting in uniformity of the film and a low critical parallel magnetic field. Fig. 3.10 (e) shows an epitaxial interface is established between InSb nanowire and Al. Note that the selectivity of chemical wet etching of Al on InSb is not very good. The method provided above is less invasive than defining the junction by etching.

The shadowed wire and the mask wire need to be close enough in order to realize an abrupt shadow. Using nanowire as a shadow mask limits the shadowed region's width to be similar to the nanowire diameter (100nm). It limits the variety of devices that can be made from these wires without further etching to extend the shadowed region. For example, the nanowire segment without superconductor needs to be 300nm wide such that a double quantum dot can be defined with fine local gates as in Fig. 7.1.

InSb nanowires with Sn islands using such nanowire shadow technique [71] are used in Chapter 6. InSb nanowire growth is performed by S. Gazibegovic, and G. Badawy in the research group of E.P.A.M Bakkers at Eindhoven University of Technology. Superconductor deposition of Sn is performed by M. Pendharkar in the research group of C.J. Palmstrom at University of California, Santa Barbara.

3.3.2 Seletive-area grown indium arsenide nanowires with shadow walls

In-plane selective-area growth (SAG) of semiconductors by chemical beam epitaxy (CBE) or molecular beam epitaxy (MBE) offers a scalable platform to realize complex devices and networks that are prerequisites for braiding Majorana modes and topological quantum computing [75, 76, 77].

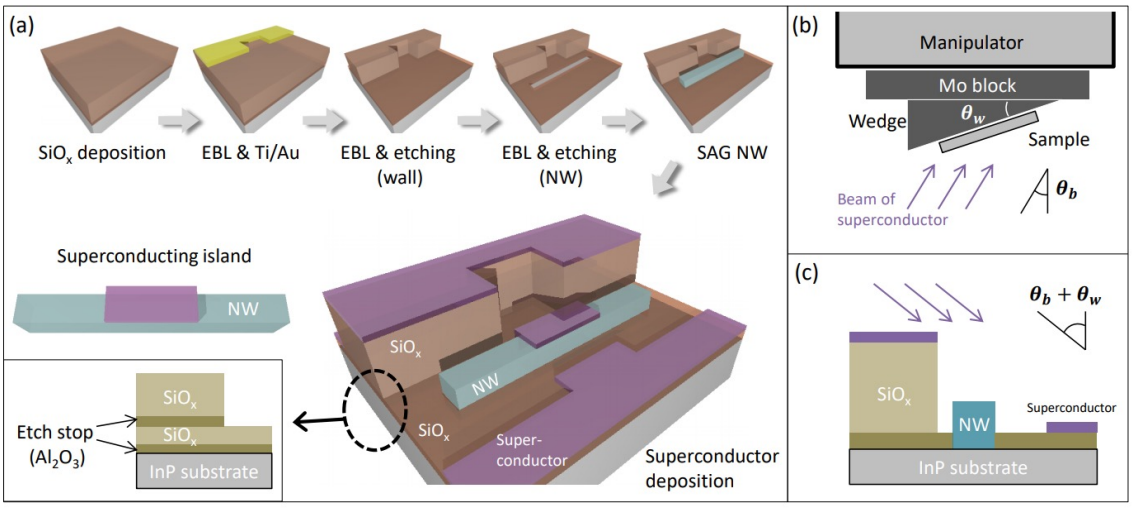

Figure 3.11: Schematic of the shadow wall structure. (a) Fabrication of the SiOx shadow wall mask, selective area growth of the nanowire, and superconductor deposition on SAG NW with the shadow wall structure. (b) In-situ angle deposition of superconductor. (c) A side view shows that the nanowire close to the shadow wall is not covered by a superconductor. Figure adapted from unpublished work of Joon Sue Lee.

Shadow technique combined with in-situ superconductor deposition is a novel approach to realize selective superconductor/semiconductor hybrids without the need of etching[78]. Therefore, the superconductor/semiconductor interface, crucial to the induced superconductivity, is intact throughout the device fabrication. Fig. 3.11 shows the schematic of how the shadow wall works.

By carefully controlling the SAG nanowire growth and incorporating different shapes of shadow walls, various semiconductor/superconductor hybrid geometries can be directly grown without breaking the vacuum.

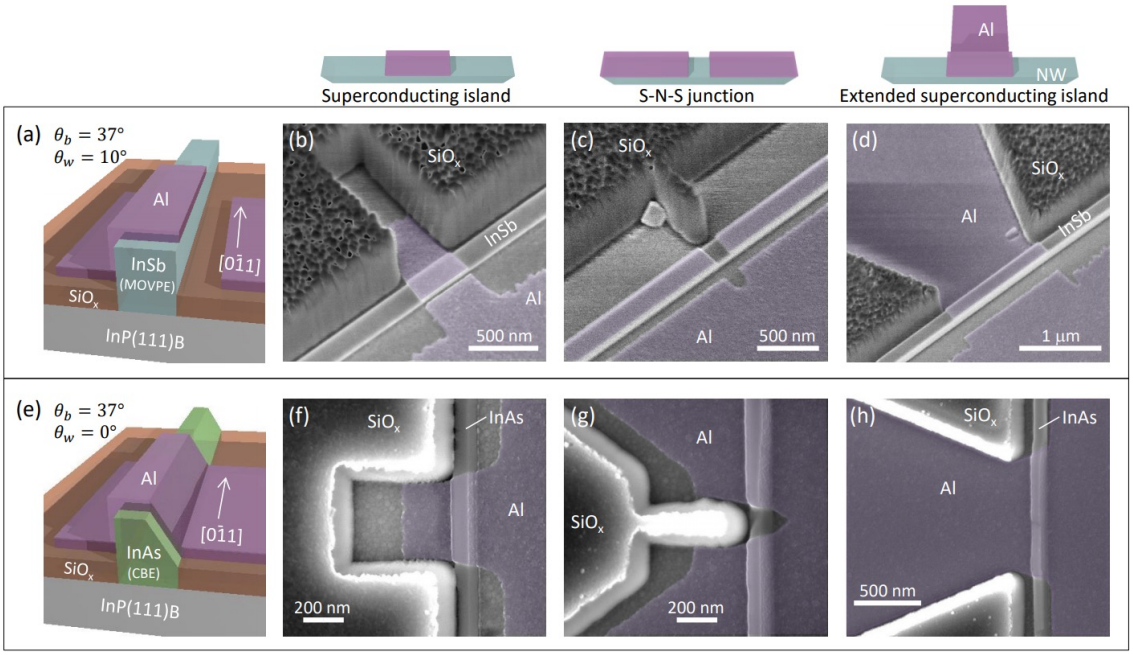

Figure 3.12: Different types of devices can be achieved by SAG NW with shadow wall structures. Figure adapted from unpublished work of Joon Sue Lee.

Figs. 3.12 (a,e) show that SAG nanowires with different crystallographic directions have different shapes of the cross-section. With angled deposition, the superconductor can fully cover or half cover the nanowire providing different strengths of proximity effect and tunability of the carrier density. Figs. 3.12 (b,f) show superconducting island geometry for Andreev quantum dot. Figs. 3.12 (c,g) show the Josephson junction geometry for supercurrent study. Figs. 3.12 (d,h) show the extended superconducting contact geometry suitable for Majorana wires.

We started the study of SAG InAs nanowires with shadow wall structures and (Al or Sn) superconducting islands. We have some initial results confirming hard induced superconductivity. SAG InAs/Al and SAG InAs/Sn nanowire growth are performed by J.S. Lee, A. Goswami, and M. Pendharkar in the research group of C.J. Palmstrom at University of California, Santa Barbara.

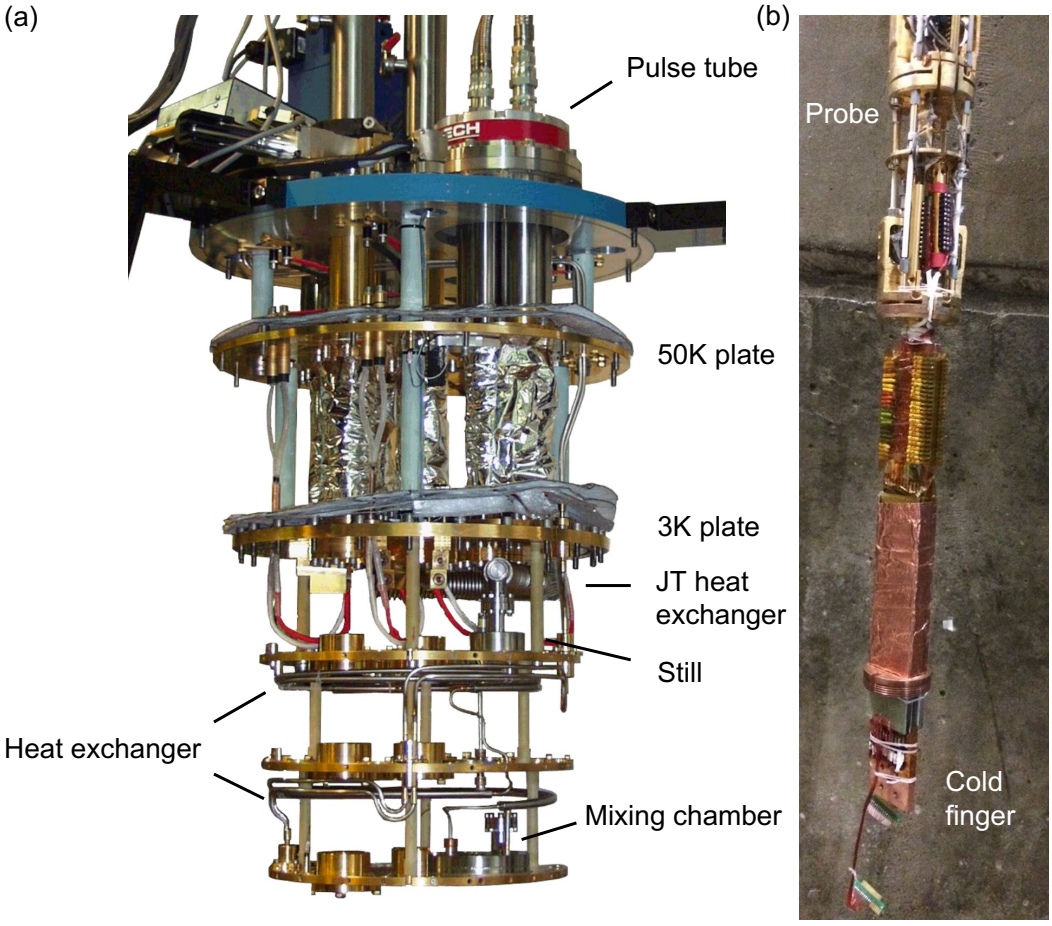

Figure 3.13: (a) Inside of a dilution refrigerator. (b) The measurement probe and the cold finger.

The subject of the thesis is Andreev quantum dots in nanowires, which consist of two main ingredients: semiconductor quantum dot and superconductivity. To observe the Coulomb blockade effect of quantum dots confined in nanowires, temperature below 1 Kelvin is mandatory. For studying the Josephson effect and proximity-induced superconductivity, a temperature well below the critical temperature is needed to suppress thermal excitation and quasiparticles in the superconductor. To suppress the thermal broadening of the states and resolve the tunneling spectroscopy of the sub-gap Andreev resonances, even lower tempera-

tures are preferred. Lower temperature results in a hard induced superconducting gap and sharp sub-gap resonances with prominence. Both are crucial to study low energy excitation states and further identify potential Majorana zero modes.

All transport measurements in this thesis are performed in a 3He/4He dilution refrigerator at a base temperature of 20-50 mK. We have two dilution refrigerators from Leiden cryogenics. They have top-loading measurement probes that enable quick cool-down from room temperature to base temperature less than 8 hours. One fridge has a solenoid magnet that goes up to 9T. The other has a vector magnet with a 6T/4T configuration. Fig. 3.13(a) shows the inside of the dilution refrigerator. There are multiple plates and cooling stages to isolate the sample from higher temperatures. The sample is wire bonded to a chip carrier and mounted on the cold finger of the probe, and is thermally connected to the mixing chamber plate at base temperature (Fig. 3.13(b)). The 3He/4He mixture undergoes spontaneous phase separation in the mixing chamber to form a 3He concentrated phase in equilibrium with a 3He diluted phase. Heat is absorbed when 3He is diluted as it flows from the concentrated phase through the phase boundary into the diluted phase. Heat is carried away by pumping 3He. Through circulating 3He in a closed cycle by pumping and compressing, continuous cooling is provided, and the base temperature is reached and maintained. Detailed discussion on the cooling mechanism and operation principles of 3He/4He dilution refrigerators can be found in [79]. The base temperature refers to the lattice temperature, or the temperature of the phonon bath, which could be as low as 10mK without the probe inserted. However, the wiring connecting the sample at low temperature and measurement instruments at room temperature is necessary to perform electrical measurements. Inevitably, extra heat load was introduced and resulting in a higher base temperature of around 40mK.

(a)

(b)

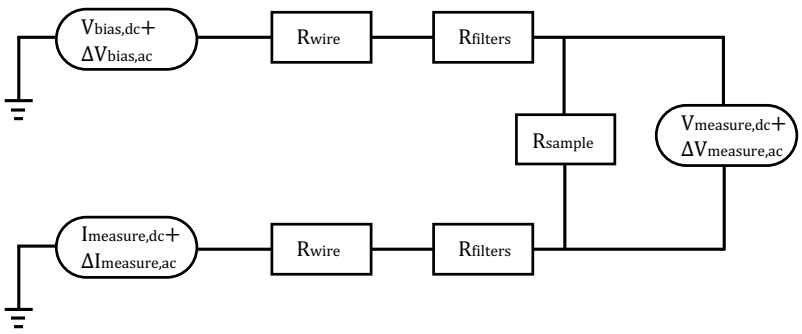

Figure 3.14: (a) IVVI-DAC rack. (b) Schematic of the measurement circuit. The voltage bias, current measurement, and voltage measurement is shown. Series resistance is the resistance of wires, filters, and amplifiers, which is in series with the sample. If the series resistance is comparable to the sample resistance, it can lead to a significant correction to the voltage bias across the sample.

The measurement setup and schematic of the measurement circuit are shown in Fig. 3.14 The IVVI-DAC rack contains voltage/current sources and current/voltage amplifiers, and 16 digital-to-analog converters (DACs) controlled by a computer through an optical fiber. DACs are used to apply voltage as control signals accurately. Current and voltage sources convert DAC signals to input measurement signals with amplification. The output signals from the device are amplified and converted into voltages and then measured with a standard digital multimeter and lockin amplifier. The voltage/current sources, current/voltage amplifiers, and DACs are designed and manufactured by TU Delft. More details on the IVVI source and measurement modules can be found in [80]. The measurement commands and data acquisition are performed by python scripts with QTlab [81].

Since the electrical current in the device is generated from and then detected by instruments at room temperature, the electron temperature in the device could be much higher than the lattice temperature. Multiple stages of filtering are used to reduce the electron thermal noises and enhance the electrical signals. At room temperature, the IVVI rack is powered by batteries, and the DACs are controlled by a computer via an optical fiber. It isolates the measurement setup from the power grid, where electrical interference could create considerable noise. With a π filter in each DC line, noise from 10MHz to 100MHz can be effectively filtered. Thermal anchoring of the wires is used at every plate on the measurement probe. Each plate on the probe is in thermal connection with a temperature stage of the refrigerator. Staged cooling of the wires reduces the thermal energy of electrons in the DC lines and the heat load on the mixing chamber. At low temperature, on the probe near the sample, each DC line passes through a copper powder filter in order to get rid of high-frequency noise in the GHz range. Next, each DC line passes through a low-pass RC filter with a cutoff frequency of 10kHz. The RC filters and the sample are mounted on the cold finger and shielded by a copper can acting as a Faraday cage.

4.0 Simulation of Andreev quantum dot chain

4.1 Introduction

Kitaev chain is a theoretical model of a one-dimensional topological superconductor with p-wave pairing, where unpaired Majorana zero modes exist at the two ends of the chain [31]. P-wave pairing, which is not readily available, can be effectively engineered, for instance, by combining one-dimensional semiconductor nanowires that have strong spin-orbit interaction, proximity-induced s-wave superconductivity, and Zeeman effect [25, 26]. This continuous Majorana wire model motivates the study of Majorana zero modes in hybrid superconductor/semiconductor heterostructures.

Following theory proposals of the continuous Majorana wire model [25, 26], zero-bias conductance peak, a signature of Majorana zero modes, has been observed in tunneling experiments of hybrid superconductor/semiconductor nanowire devices [27, 28, 82]. Zero-bias peaks are necessary but not sufficient to conclude Majorana.

Andreev bound states in quantum dots also produce zero-bias peaks and mimic signatures of Majorana zero modes, including quantized zero-bias peak, in the same devices [83, 84, 85]. Due to disorder or device geometry, Andreev bound states appear generically in superconductor/semiconductor nanowire systems [43, 86, 44, 87]. They have also been studied intentionally in semiconductor quantum dots coupled to superconductors [43, 88, 89, 90, 91, 92]. As an alternative interpretation to Majorana signatures, Andreev bound states have been considered as disturbing to unambiguous identification of Majorana zero modes [83, 85]. Future experiments will clearly distinguish the two phenomena by consistently demonstrating multiple Majorana signatures within the same nanowire.

Recent progress in studying Majorana zero modes in nanowires is mostly in material development and understanding other origins of the zero-bias peaks. Many fabrication techniques have been developed to improve device qualities to avoid quantum dots and Andreev bound states, such as the epitaxial growth of superconductors [64, 93], in-plane selective area nanowire growth [76, 77], and shadow lithography [71, 72, 73]. However, it is very

challenging to reach the disorder level required for the realization of Majorana zero modes and topological qubit in hybrid superconductor/semiconductor nanowire platforms [45, 46].

With the concern of the omnipresent Andreev bound states in hybrid superconductor/semiconductor nanowire devices, we take an alternative approach to implement the Kitaev chain other than the continuous Majorana wire model [25, 26]. Rather than trying to eliminate Andreev states, we take advantage of them in our Majorana search. Theory suggests a robust topological superconducting phase in chains of Andreev quantum dots [47, 48]. A one-dimensional system is assembled with multiple dots coupled to superconductors, each with an Andreev bound state. Because sites are independently tunable, it helps to suppress and overcome the effect of disorder. To study the discrete version of the Kitaev chain, we build a tight-binding model of a quantum dot chain containing three sites. We simulate the energy spectrum and transport of the triple-dot chain. For such a short chain, within a narrow parameter window, the probability distribution of Majorana wavefunctions indicates a partial separation of two Majorana zero modes localized at two end sites. For a longer quantum dot chain, the parameter space for the Kitaev regime should be larger, although it will be much harder to realize in experiments.

4.2 Model description

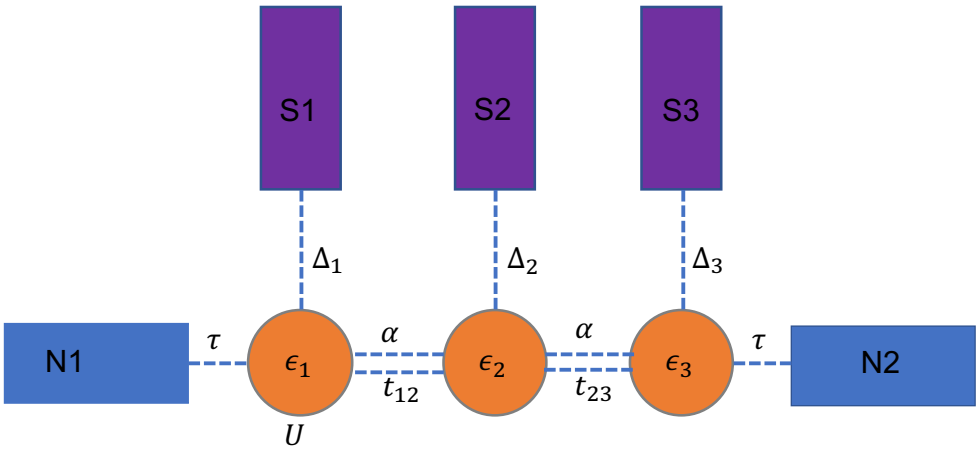

Figure 4.1: Schematic of the model containing three quantum dots, three superconducting leads, and two normal leads.

Fig. 4.1 shows the system described by a spinful Hamiltonian with nearest dot coupling t_i, dot potentials ϵ_i, an external magnetic field B, spin-orbit coupling α_i, induced superconductivity Δ_i, and electron interactions U_i.

$$\begin{aligned} H = &\sum_{i,\sigma} \epsilon_i \left(d^\dagger_{i,\sigma} d_{i,\sigma} - d_{i,\sigma} d^\dagger_{i,\sigma} \right) \\ &+ \sum_{i,\sigma} t_i \left(d^\dagger_{i+1,\sigma} d_{i,\sigma} + h.c \right) \\ &+ B \sum_i \left(d^\dagger_{i,\uparrow} d_{i,\downarrow} + h.c. \right) \\ &+ \sum_i \alpha_i \left(d^\dagger_{i,\uparrow} d_{i+1,\downarrow} - d^\dagger_{i,\downarrow} d_{i+1,\uparrow} + h.c. \right) \\ &+ \sum_i \Delta_i (d^\dagger_{i,\downarrow} d^\dagger_{i\uparrow} + h.c.) \\ &+ \sum_i U_i d^\dagger_{i,\uparrow} d_{i,\uparrow} d^\dagger_{i,\downarrow} d_{i,\downarrow} \end{aligned} \tag{4.1}$$

where $i \in \{1, 2, 3\}$ runs over the dots, $\sigma \in \{\uparrow, \downarrow\}$ runs over the spin and $d^\dagger_{i,\sigma}$ ($d_{i,\sigma}$) creates (destroys) an electron on dot i with spin σ. Let E_n and $|n\rangle$ denote the eigenvalues and eigenvectors of the Hamiltonian.

Majorana operators can be defined by

$$\begin{aligned} d^{\dagger}_{i,\sigma} &= \frac{1}{2}\left(\gamma_{x,i,\sigma} - i\gamma_{y,i,\sigma}\right) \\ d_{i,\sigma} &= \frac{1}{2}\left(\gamma_{x,i,\sigma} + i\gamma_{y,i,\sigma}\right) \end{aligned} \tag{4.2}$$

To calculate the current, we allow electrons to tunnel through the ends of the devices (i.e., to and from the leftmost and rightmost dots). We assume that the electron distribution in either lead is in equilibrium described by the Fermi-distribution $f(E)$ with a potential bias of eV on the left and $-eV$ on the right. We take the transition rates to be

$$\begin{aligned} \Gamma^{L,R}_{gain,nm} &= f(E_n - E_m \mp eV) \sum_{\sigma} t^2_{L,R} |\left\langle n\right| d^{\dagger}_{1,\sigma} \left|m\right\rangle|^2 \\ \Gamma^{L,R}_{loss,nm} &= (1 - f(E_n - E_m \mp eV)) \sum_{\sigma} t^2_{L,R} |\left\langle n\right| d_{1,\sigma} \left|m\right\rangle|^2 \end{aligned} \tag{4.3}$$

where t_L is the coupling to the left lead, t_R is the coupling to the right lead, and $\Gamma^{L,R}_{gain,nm}$ is the rate at which an electron comes into the system from the right lead R or left lead L and excites the system from the state $|m\rangle$ to the state $|n\rangle$, while $\Gamma^{L,R}_{loss,nm}$ is the rate at which an electron leaves the system going into the right R or left L lead causing decaying the system from $|m\rangle$ to $|n\rangle$. Notice that we have made no assumption about which state ($|m\rangle$ or $|n\rangle$) has more electrons. The total transition rate from $|m\rangle$ to $|n\rangle$ is then given by

$$\Gamma_{nm} = \Gamma^{L}_{gain,nm} + \Gamma^{L}_{loss,nm} + \Gamma^{R}_{gain,nm} + \Gamma^{R}_{loss,nm} \tag{4.4}$$

We assume the system is in a steady state so that the probabilities in each state is unchanging in time

$$0 = \frac{dP_n}{dt} = \sum_{m} M_{nm} P_m \tag{4.5}$$

where

$$M_{nm} = \Gamma_{nm} - \sum_{l} \delta_{nm} \Gamma_{ln} \tag{4.6}$$

Solving the set of linear equations in Eq. 4.5 and using the fact that $\sum_n P_n = 1$ allows us to solve for the probabilities. From here, we can calculate the current

$$I = \sum_{n} P_n \sum_{m} \left(\Gamma^{L}_{gain,mn} + \Gamma^{R}_{loss,mn} - \Gamma^{L}_{loss,mn} - \Gamma^{R}_{gain,mn}\right) \tag{4.7}$$

4.3 Simulations results

We plot simulations of the three-site quantum dot chain model, including the energy spectrum, differential conductance of the electron transport, and Majorana wavefunctions distribution, with various tunable parameters.

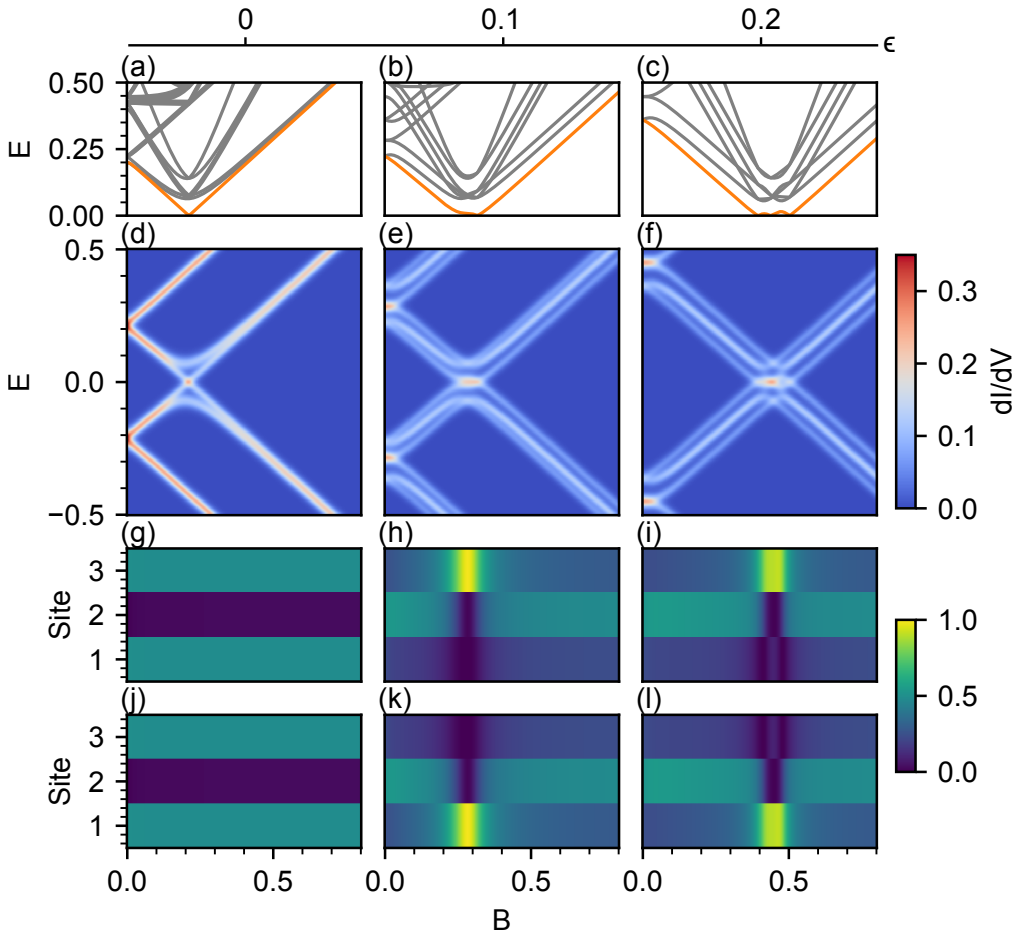

Figure 4.2: Simulation results for a chain of 3 identical dots at different dot potentials, $\epsilon = 0, 0.1, 0.2$. (a-c) Many-body spectra versus the magnetic field. The orange line is the first excited state. (d-f) Differential conductance in magnetic fields. (g-l) Evaluation of Majorana components (probability amplitudes) in different sites in magnetic fields. Other parameters used: $U = 0$, $\Delta = 0.2$, $\alpha = 0.05$, $t = 0.05$, $T = 0.01$.

Fig. 4.2 shows simulation results for a chain of 3 identical dots at different dot potentials,

$\epsilon = 0, 0.1, 0.2$. (a-c) Many-body spectra versus the magnetic field. The orange line is the first excited state. (d-f) Differential conductance in magnetic fields. (g-l) Evaluation of Majorana components (probability amplitudes) in different sites in magnetic fields. The color denotes $|\langle E|\gamma_{x,s,\uparrow}|G\rangle|^2+|\langle E|\gamma_{x,s,\downarrow}|G\rangle|^2$ in (g-i) and $|\langle E|\gamma_{y,s,\uparrow}|G\rangle|^2+|\langle E|\gamma_{y,s,\downarrow}|G\rangle|^2$ in (j-l), where $s = 1, 2, 3$ is the site, $|G\rangle$ is the ground state, $|E\rangle$ is the first excited state. In Figs. 4.2 (g,j), at $\epsilon = 0$, the system develops edge states, but there are no separated Majorana zero modes around the gap closing point. They are trivial bulk fermion states. In Figs. 4.2 (h,k) and Figs. 4.2 (i,l), as ϵ increases, two separated Majorana modes at site 1 and 3 appear near the gap closing point.

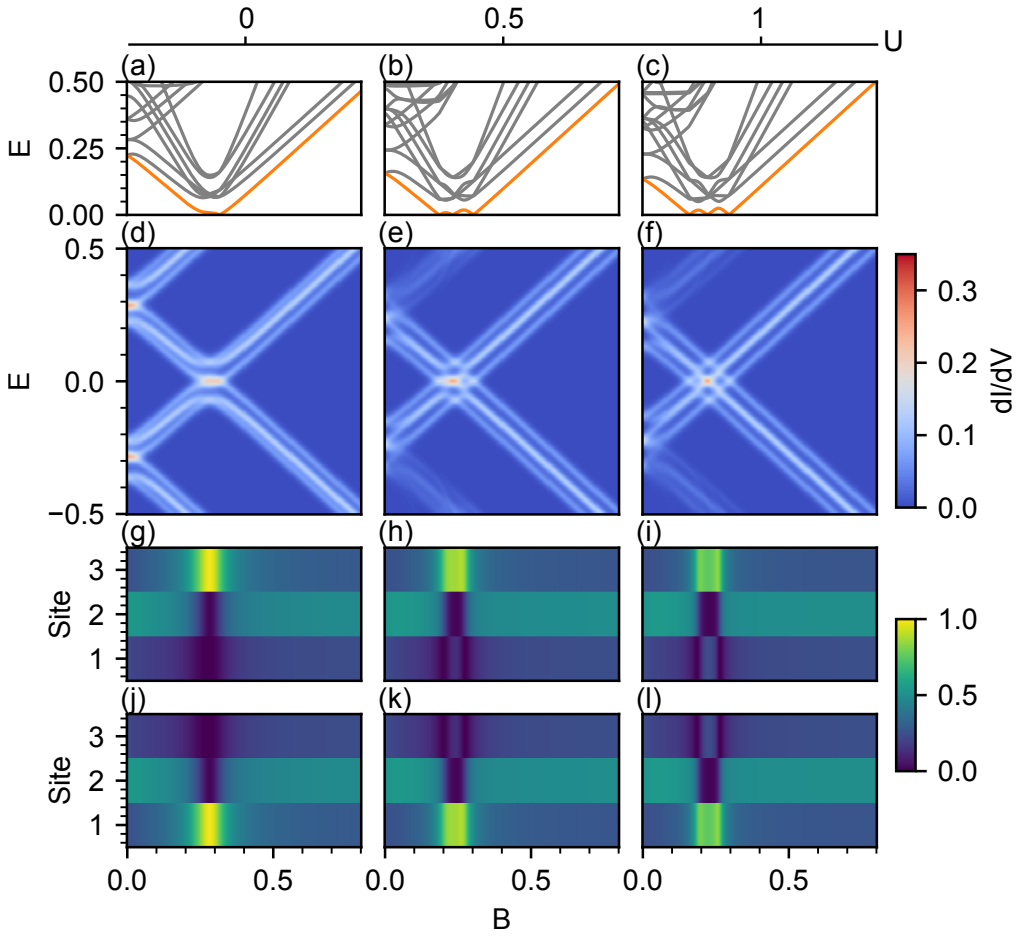

Figure 4.3: Simulation results for a chain of 3 identical dots with the Coulomb interaction, $U = 0, 0.5, 1$. (a-c) Many-body spectra versus the magnetic field. The orange line is the first excited state. (d-f) Differential conductance in magnetic fields. (g-l) Evaluation of Majorana components (probability amplitudes) in different sites in magnetic fields. Other parameters used: $\Delta = 0.2$, $\alpha = 0.05$, $t = 0.05$, $\epsilon = 0.1$, $T = 0.01$.

Fig. 4.3 shows simulation results for a chain of 3 identical dots with the Coulomb interaction, $U = 0, 0.5, 1$. (a-c) Many-body spectra versus the magnetic field. The orange line is the first excited state. (d-f) Differential conductance in magnetic fields. (g-l) Evaluation of Majorana components (probability amplitudes) in different sites in magnetic fields. The color denotes $|\langle E|\gamma_{x,s,\uparrow}|G\rangle|^2 + |\langle E|\gamma_{x,s,\downarrow}|G\rangle|^2$ in (g-i) and $|\langle E|\gamma_{y,s,\uparrow}|G\rangle|^2 + |\langle E|\gamma_{y,s,\downarrow}|G\rangle|^2$ in (j-l), where $s = 1, 2, 3$ is the site, $|G\rangle$ is the ground state, $|E\rangle$ is the first excited state. As

U increases, the extended zero-bias peak (in Fig. 4.3 (d)) develops into three crossings (in Fig. 4.3 (f)) and Majorana modes are no longer separated.

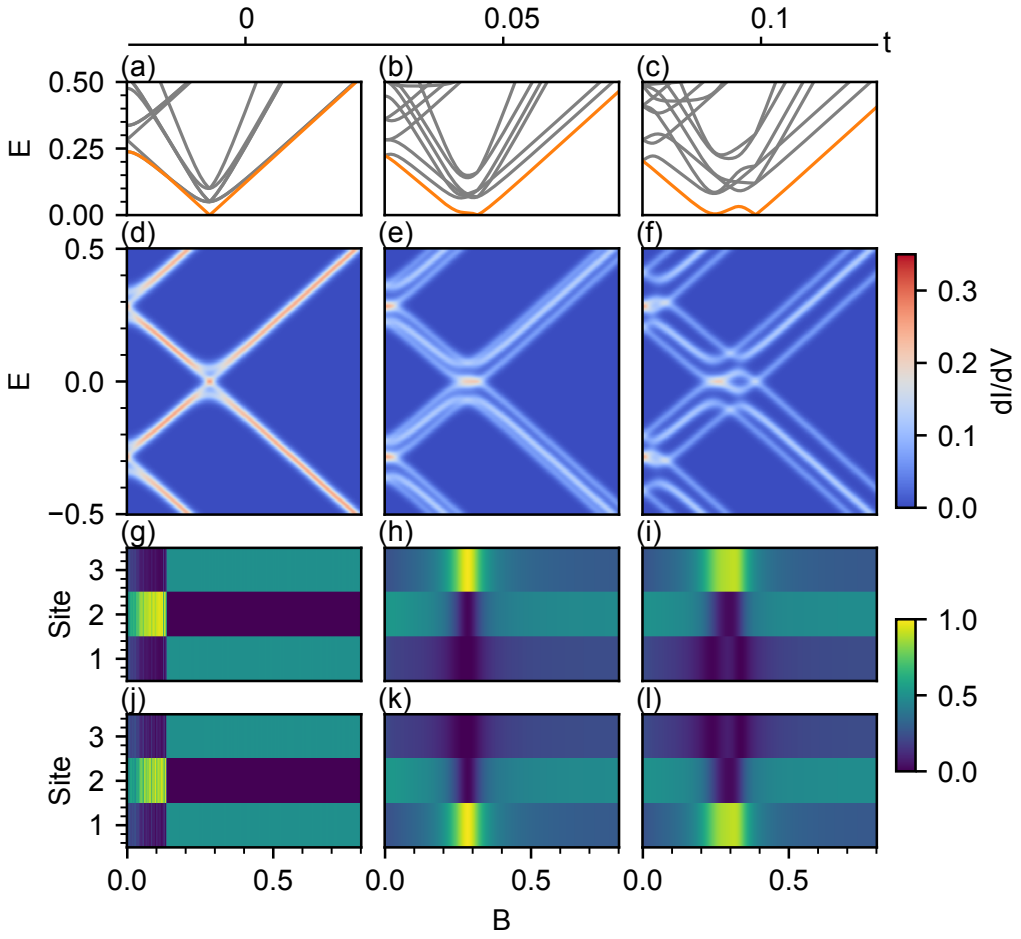

Figure 4.4: Simulation results for a chain of 3 identical dots with different inter-dot couplings, $t = 0, 0.05, 0.1$. (a-c) Many-body spectra versus the magnetic field. The orange line is the first excited state. (d-f) Differential conductance in magnetic fields. (g-l) Evaluation of Majorana components (probability amplitudes) in different sites in magnetic fields. Other parameters used: $U = 0$, $\Delta = 0.2$, $\alpha = 0.05$, $\epsilon = 0.1$, $T = 0.01$.

Fig. 4.4 shows simulation results for a chain of 3 identical dots with different inter-dot couplings, $t = 0, 0.05, 0.1$. (a-c) Many-body spectra versus the magnetic field. The orange line is the first excited state. (d-f) Differential conductance in magnetic field. (g-l) Evaluation of Majorana components (probability amplitudes) in different sites in magnetic field. The

color denotes $|\langle E|\gamma_{x,s,\uparrow}|G\rangle|^2+|\langle E|\gamma_{x,s,\downarrow}|G\rangle|^2$ in (g-i) and $|\langle E|\gamma_{y,s,\uparrow}|G\rangle|^2+|\langle E|\gamma_{y,s,\downarrow}|G\rangle|^2$ in (j-l), where $s=1,2,3$ is the site, $|G\rangle$ is the ground state, $|E\rangle$ is the first excited state. In Figs. 4.4 (g,j), at $t=0$, the system develops edge states in magnetic fields, but there are no separated Majorana zero modes around the gap closing point. In Figs. 4.4 (h,k), at $t=0.05$, two separated Majorana modes at site 1 and 3 appear near the gap closing point. In Figs. 4.4 (i,l), at $t=0.1$, although there are partial overlapping, two Majorana modes are still mostly localized at two end sites. In general, decrease the hopping term t equals having a longer chain, and more isolated Majorana modes should appear.

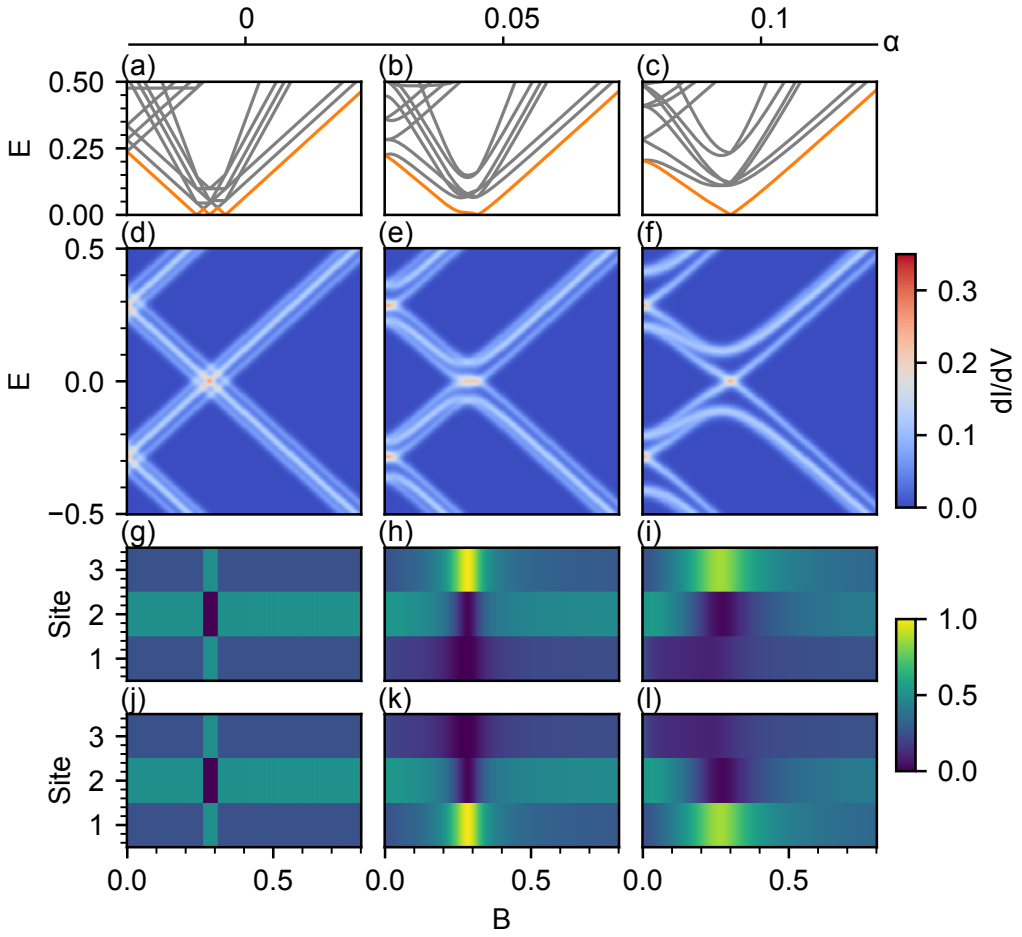

Figure 4.5: Simulation results for a chain of 3 identical dots with different spin-orbit couplings, $\alpha = 0, 0.05, 0.1$. (a-c) Many-body spectra versus the magnetic field. The orange line is the first excited state. (d-f) Differential conductance in magnetic fields. (g-l) Evaluation of Majorana components (probability amplitudes) in different sites in magnetic fields. Other parameters used: $U = 0$, $\Delta = 0.2$, $t = 0.05$, $\epsilon = 0.1$, $T = 0.01$.

Fig. 4.5 shows simulation results for a chain of 3 identical dots with different spin-orbit couplings, $\alpha = 0, 0.05, 0.1$. (a-c) Many-body spectra versus the magnetic field. The orange line is the first excited state. (d-f) Differential conductance in magnetic fields. (g-l) Evaluation of Majorana components (probability amplitudes) in different sites in magnetic fields. The color denotes $|\langle E|\gamma_{x,s,\uparrow}|G\rangle|^2 + |\langle E|\gamma_{x,s,\downarrow}|G\rangle|^2$ in (g-i) and $|\langle E|\gamma_{y,s,\uparrow}|G\rangle|^2 + |\langle E|\gamma_{y,s,\downarrow}|G\rangle|^2$ in (j-l), where $s = 1, 2, 3$ is the site, $|G\rangle$ is the ground state, $|E\rangle$ is the first

excited state. In Figs. 4.5 (g,j), at $\alpha = 0$, no separated Majorana zero modes around the gap closing point. They are trivial bulk fermion states. As α increases, two separated Majorana modes at site 1 and 3 appear near the gap closing point in Figs. 4.5(h,k,i,l).

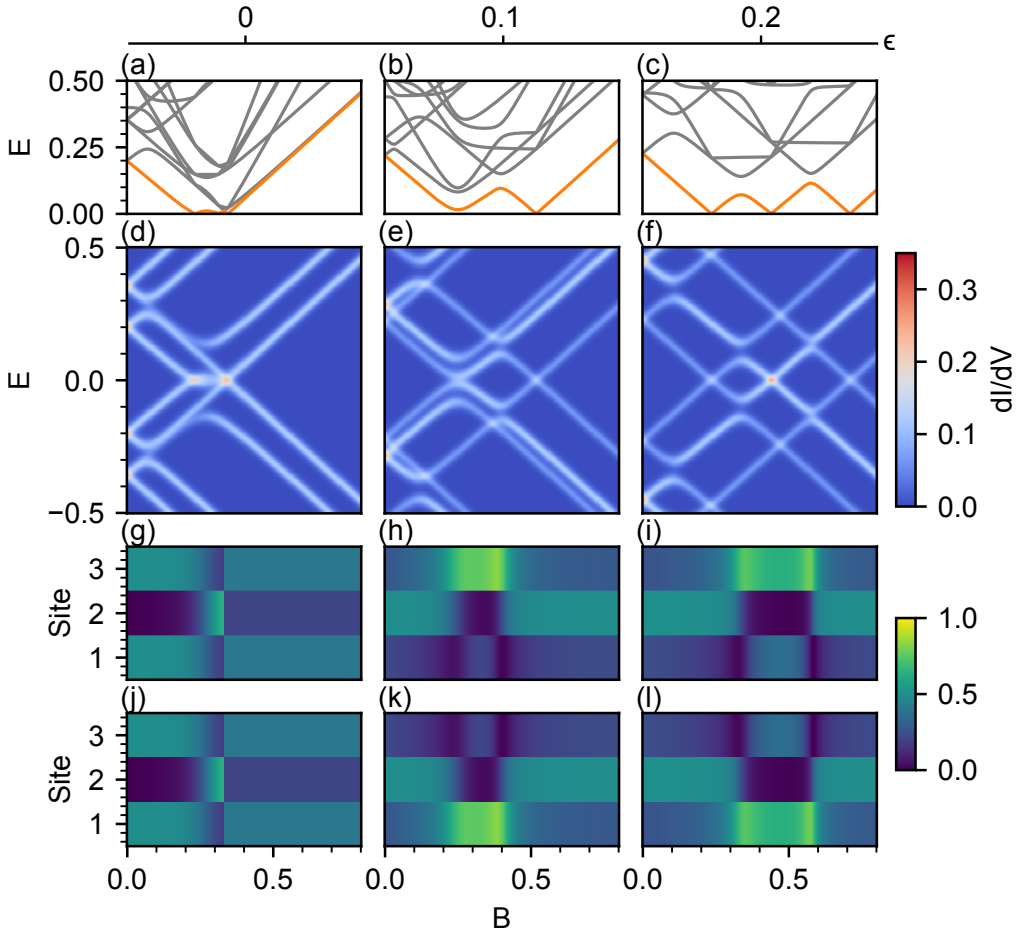

Figure 4.6: Simulation results for a chain of 3 identical dots at different dot potentials, $\epsilon = 0, 0.1, 0.2$. Inter-dot coupling $t = 0.2$ for a strongly coupled chain. (a-c) Many-body spectra versus the magnetic field. The orange line is the first excited state. (d-f) Differential conductance in magnetic fields. (g-l) Evaluation of Majorana components (probability amplitudes) in different sites in magnetic fields. Other parameters used: $U = 0$, $\Delta = 0.2$, $\alpha = 0.05$, $t = 0.2$, $T = 0.01$.

Fig. 4.6 shows simulation results for a chain of 3 identical dots at different dot potentials, $\epsilon = 0, 0.1, 0.2$. Inter-dot coupling $t = 0.2$ for a strongly coupled chain. (a-c) Many-body

spectra versus the magnetic field. The orange line is the first excited state. (d-f) Differential conductance in magnetic fields. (g-l) Evaluation of Majorana components (probability amplitudes) in different sites in magnetic fields. The color denotes $|\langle E|\gamma_{x,s,\uparrow}|G\rangle|^2 + |\langle E|\gamma_{x,s,\downarrow}|G\rangle|^2$ in (g-i) and $|\langle E|\gamma_{y,s,\uparrow}|G\rangle|^2 + |\langle E|\gamma_{y,s,\downarrow}|G\rangle|^2$ in (j-l), where $s = 1, 2, 3$ is the site, $|G\rangle$ is the ground state, $|E\rangle$ is the first excited state. In Fig. 4.6, as parameters increase, in energy spectrum (a-c) and transport (d-f), the region of zero energy crossings extends in a larger range of magnetic fields, which means in experiments, it is easier to observe a long zero-bias peak. However, the oscillations of low energy excitations near zero-energy (i.e., three zero energy crossings instead of a peak pinned to zero bias) result in partial overlapping of Majorana modes (g-l). Zero-bias peak oscillations are due to the finite size of the chain. Obviously, as the number of sites increase, in a longer chain, the number of zero energy crossings would increase, and the amplitude of the oscillations in energy would decrease. A long peak extending in a larger range of magnetic fields will be pinned to zero energy, and well-separated Majorana modes appear at two ends. Note that there can still be Majorana separation even for no crossing in differential conductance (e,f) (h,k,i,l).

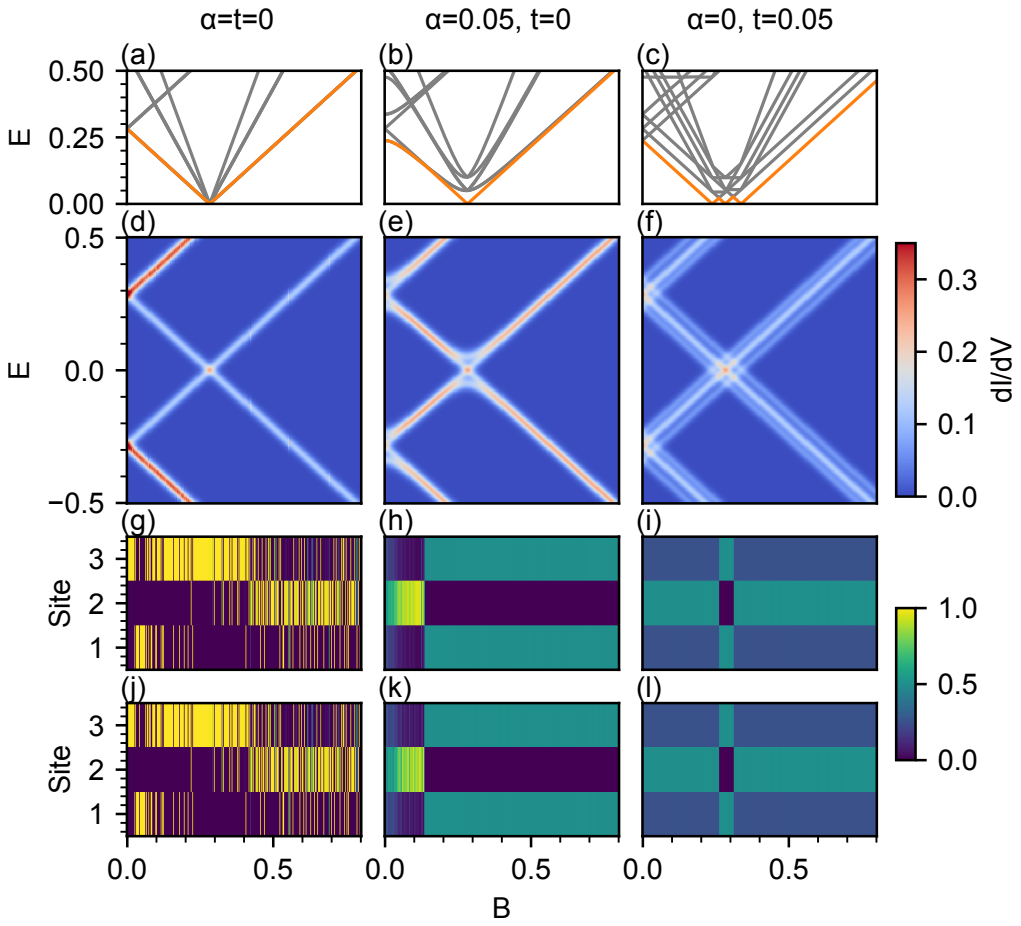

Figure 4.7: Simulation results for a chain of 3 identical dots with different α and t. (a-c) Many-body spectra versus the magnetic field. The orange line is the first excited state. (d-f) Differential conductance in magnetic fields. (g-l) Evaluation of Majorana components (probability amplitudes) in different sites in magnetic fields. Other parameters used: $U = 0$, $\Delta = 0.2$, $\epsilon = 0.1$, $T = 0.01$.

Fig. 4.7 shows simulation results for a chain of 3 identical dots with different α and t. (a-c) Many-body spectra versus the magnetic field. The orange line is the first excited state. (d-f) Differential conductance in magnetic fields. (g-l) Evaluation of Majorana components (probability amplitudes) in different sites in magnetic fields. The color denotes $|\langle E|\gamma_{x,s,\uparrow}|G\rangle|^2+|\langle E|\gamma_{x,s,\downarrow}|G\rangle|^2$ in (g-i) and $|\langle E|\gamma_{y,s,\uparrow}|G\rangle|^2+|\langle E|\gamma_{y,s,\downarrow}|G\rangle|^2$ in (j-l), where $s = 1, 2, 3$ is the site, $|G\rangle$ is the ground state, $|E\rangle$ is the first excited state. In Figs. 4.7 (a,d),

when both α and t are zero, it means the dots are decoupled. There is no tunneling between the dots. Such a chain of isolated dots is equivalent to a single dot. (g,j) show the unstable distribution of probabilities over the sites due to this reason. We need at least one parameter (α or t) to be non-zero to establish the chain of 3 dots. Both spin-orbit coupling and inter-dot couplings are crucial to the model. With only one parameter present (h,k and i,l), there is no Majorana separation.

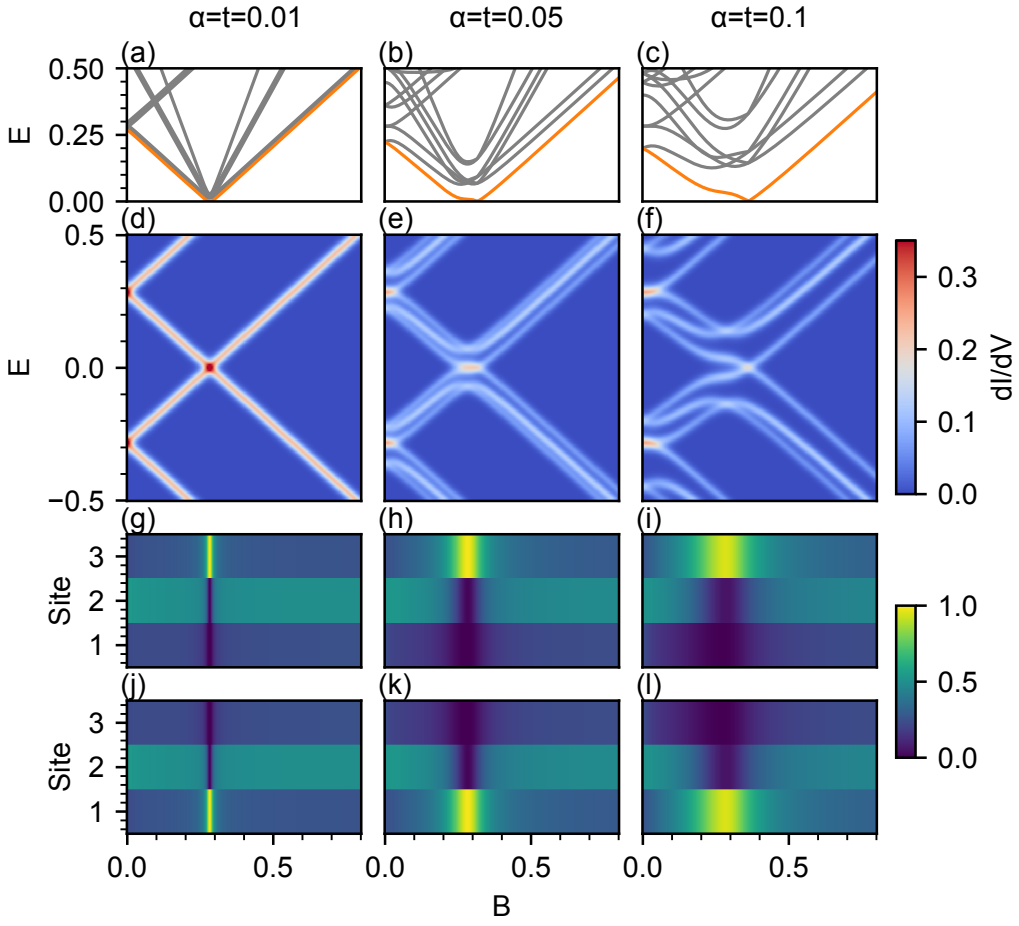

Figure 4.8: Simulation results for a chain of 3 identical dots with different α and t. (a-c) Many-body spectra versus the magnetic field. The orange line is the first excited state. (d-f) Differential conductance in magnetic fields. (g-l) Evaluation of Majorana components (probability amplitudes) in different sites in magnetic fields. Other parameters used: $U = 0$, $\Delta = 0.2$, $\epsilon = 0.1$, $T = 0.01$.

Fig. 4.8 shows simulation results for a chain of 3 identical dots with different α and t. (a-c) Many-body spectra versus the magnetic field. The orange line is the first excited state. (d-f) Differential conductance in magnetic fields. (g-l) Evaluation of Majorana components (probability amplitudes) in different sites in magnetic fields. The color denotes $|\langle E|\gamma_{x,s,\uparrow}|G\rangle|^2+|\langle E|\gamma_{x,s,\downarrow}|G\rangle|^2$ in (g-i) and $|\langle E|\gamma_{y,s,\uparrow}|G\rangle|^2+|\langle E|\gamma_{y,s,\downarrow}|G\rangle|^2$ in (j-l), where $s=1,2,3$ is the site, $|G\rangle$ is the ground state, $|E\rangle$ is the first excited state. In Figs. 4.8 (g,j), at $\alpha=t=0.01$, even though the parameters are of small values, two separated Majorana modes at site 1 and 3 appear at the gap closing point. In Figs. 4.8 (h,k) and (i,l), as parameters α and t increase, the magnetic field range in which Majorana modes are separated at two ends is expanding. Note that in Figs. 4.8 (c,f,i,l), there are separated Majorana modes at magnetic fields when resonances are not crossing zero energy. This means that when there are no long zero-bias peaks or even just a crossing, separated Majorana modes can still exist in a magnetic field range if the states are near zero-energy.

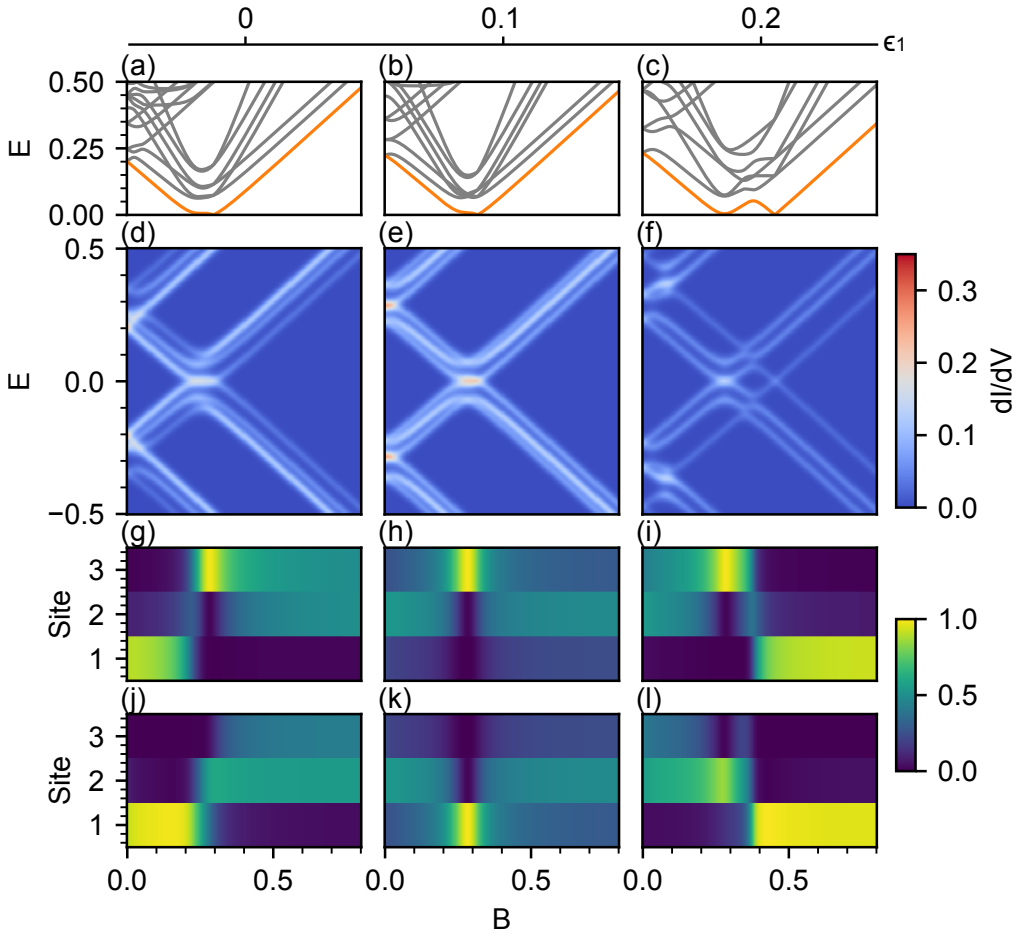

Figure 4.9: Simulation results for a chain of 3 dots with different dot1 potentials, $\epsilon_1 = 0, 0.1, 0.2$. (a-c) Many-body spectra versus the magnetic field. The orange line is the first excited state. (d-f) Differential conductance in magnetic fields. (g-l) Evaluation of Majorana components (probability amplitudes) in different sites in magnetic fields. Other parameters used: $U = 0$, $\Delta = 0.2$, $\alpha = 0.05$, $t = 0.05$, $\epsilon_2 = \epsilon_3 = 0.1$, $T = 0.01$.

Fig. 4.9 shows simulation results for a chain of 3 dots with different dot1 potentials, $\epsilon_1 = 0, 0.1, 0.2$. (a-c) Many-body spectra versus the magnetic field. The orange line is the first excited state. (d-f) Differential conductance in magnetic fields. (g-l) Evaluation of Majorana components (probability amplitudes) in different sites in magnetic fields. The color denotes $|\langle E|\gamma_{x,s,\uparrow}|G\rangle|^2 + |\langle E|\gamma_{x,s,\downarrow}|G\rangle|^2$ in (g-i) and $|\langle E|\gamma_{y,s,\uparrow}|G\rangle|^2 + |\langle E|\gamma_{y,s,\downarrow}|G\rangle|^2$ in (j-l), where $s = 1, 2, 3$ is the site, $|G\rangle$ is the ground state, $|E\rangle$ is the first excited state.

Since dot1 and dot3 are equivalent (they both have only one inter-dot coupling term), the study of varying dot1 potentials is the same as dot3. However, dot2 couples to both dot1 and dot3, vary dot2 potentials will be different. We will study the dependence on dot2 next. In Figs. 4.9 (g,j), at low magnetic fields before the zero energy crossing, two Majorana modes are highly overlapped and localized at site 1. No separated Majorana modes except for when dots are identical (h,k).

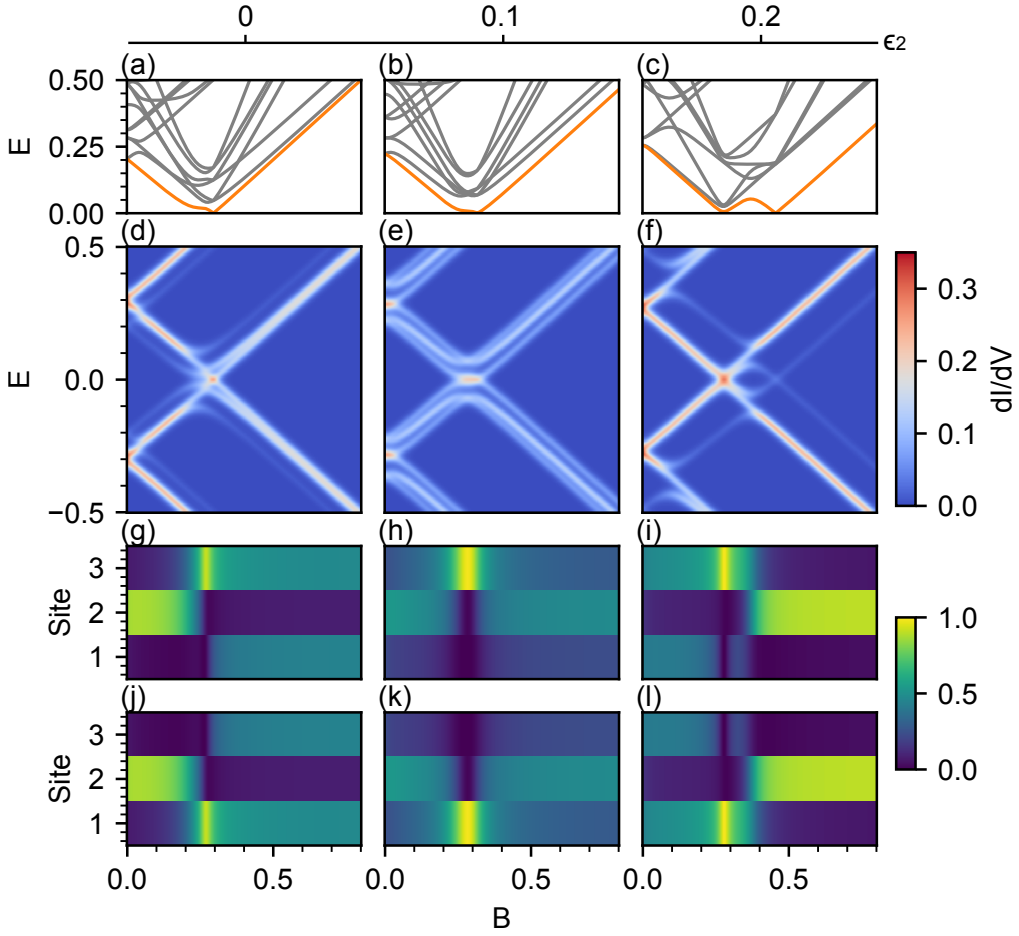

Figure 4.10: Simulation results for a chain of 3 dots with different dot2 potentials, $\epsilon_2 = 0, 0.1, 0.2$. (a-c) Many-body spectra versus the magnetic field. The orange line is the first excited state. (d-f) Differential conductance in magnetic fields. (g-l) Evaluation of Majorana components (probability amplitudes) in different sites in magnetic fields. Other parameters used: $U = 0$, $\Delta = 0.2$, $\alpha = 0.05$, $t = 0.05$, $\epsilon_1 = \epsilon_3 = 0.1$, $T = 0.01$.

Fig. 4.10 shows simulation results for a chain of 3 dots with different dot2 potentials, $\epsilon_2 = 0, 0.1, 0.2$. (a-c) Many-body spectra versus the magnetic field. The orange line is the first excited state. (d-f) Differential conductance in magnetic fields. (g-l) Evaluation of Majorana components (probability amplitudes) in different sites in magnetic fields. The color denotes $|\langle E|\gamma_{x,s,\uparrow}|G\rangle|^2 + |\langle E|\gamma_{x,s,\downarrow}|G\rangle|^2$ in (g-i) and $|\langle E|\gamma_{y,s,\uparrow}|G\rangle|^2 + |\langle E|\gamma_{y,s,\downarrow}|G\rangle|^2$ in (j-l), where $s = 1, 2, 3$ is the site, $|G\rangle$ is the ground state, $|E\rangle$ is the first excited state. Dot2 has less effect on Majorana separation. In Fig. 4.10, when tune dot2 potentials away from the identical dot chain (h,k), the separated Majorana modes at the gap closing remain in Figs. 4.10 (g,j,i,l). While near the zero energy crossing originates from dot2, two Majorana modes are overlapped and localized at site 2 in Figs. 4.10 (g,j,i,l).

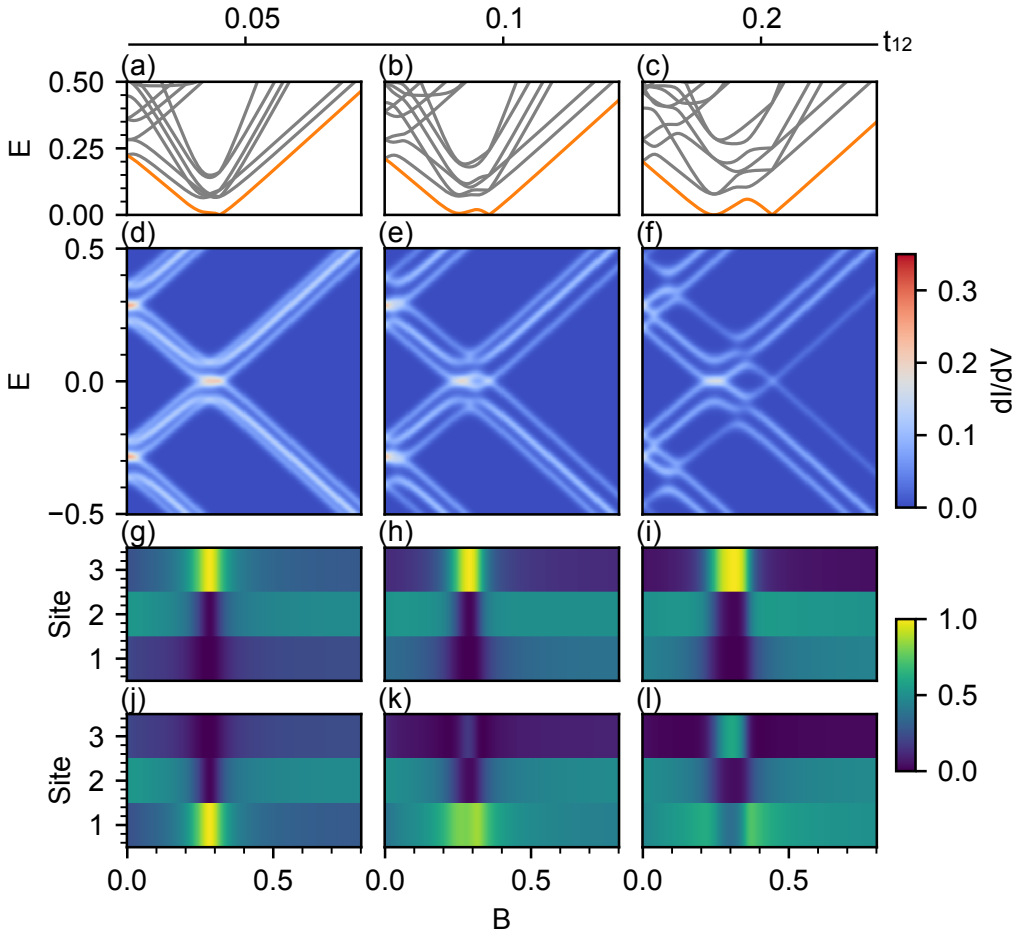

Figure 4.11: Simulation results for a chain of 3 dots with different dot1-dot2 couplings, $t_{12} = 0.05, 0.1, 0.2$. (a-c) Many-body spectra versus the magnetic field. The orange line is the first excited state. (d-f) Differential conductance in magnetic fields. (g-l) Evaluation of Majorana components (probability amplitudes) in different sites in magnetic fields. Other parameters used: $U = 0$, $\Delta = 0.2$, $\alpha = 0.05$, $t_{23} = 0.05$, $\epsilon = 0.1$, $T = 0.01$.

Fig. 4.11 shows simulation results for a chain of 3 dots with different dot1-dot2 couplings, $t_{12} = 0.05, 0.1, 0.2$. (a-c) Many-body spectra versus the magnetic field. The orange line is the first excited state. (d-f) Differential conductance in magnetic fields. (g-l) Evaluation of Majorana components (probability amplitudes) in different sites in magnetic fields. The color denotes $|\langle E|\gamma_{x,s,\uparrow}|G\rangle|^2 + |\langle E|\gamma_{x,s,\downarrow}|G\rangle|^2$ in (g-i) and $|\langle E|\gamma_{y,s,\uparrow}|G\rangle|^2 + |\langle E|\gamma_{y,s,\downarrow}|G\rangle|^2$ in (j-l), where $s = 1, 2, 3$ is the site, $|G\rangle$ is the ground state, $|E\rangle$ is the first excited state.

In Fig. 4.11, different inter-dot coupling strengths t_{12} and t_{23} are studied. When couplings t_{12} and t_{12} are the same, two Majorana wavefunctions are symmetric and localized at each end site at the gap closing (g,j). When increasing coupling of dot1 and dot2, t_{12} differs from t_{23}, Majorana modes are less well-separated. In (h,k), $t_{12} = 0.1$, Majorana modes are still mostly separated. While in (i,l), with even larger $t_{12} = 0.2$, near the zero energy crossings, Majorana modes are mostly overlapped and localized at site 3. Figs. 4.11 (f,i,l) show that at near zero-energy crossings or even seemingly extended zero-bias peaks, separated Majorana modes can still be absent. Since dot1 and dot3 are equivalent in this model, changing t_{23} will have similar effects on Majorana separation.

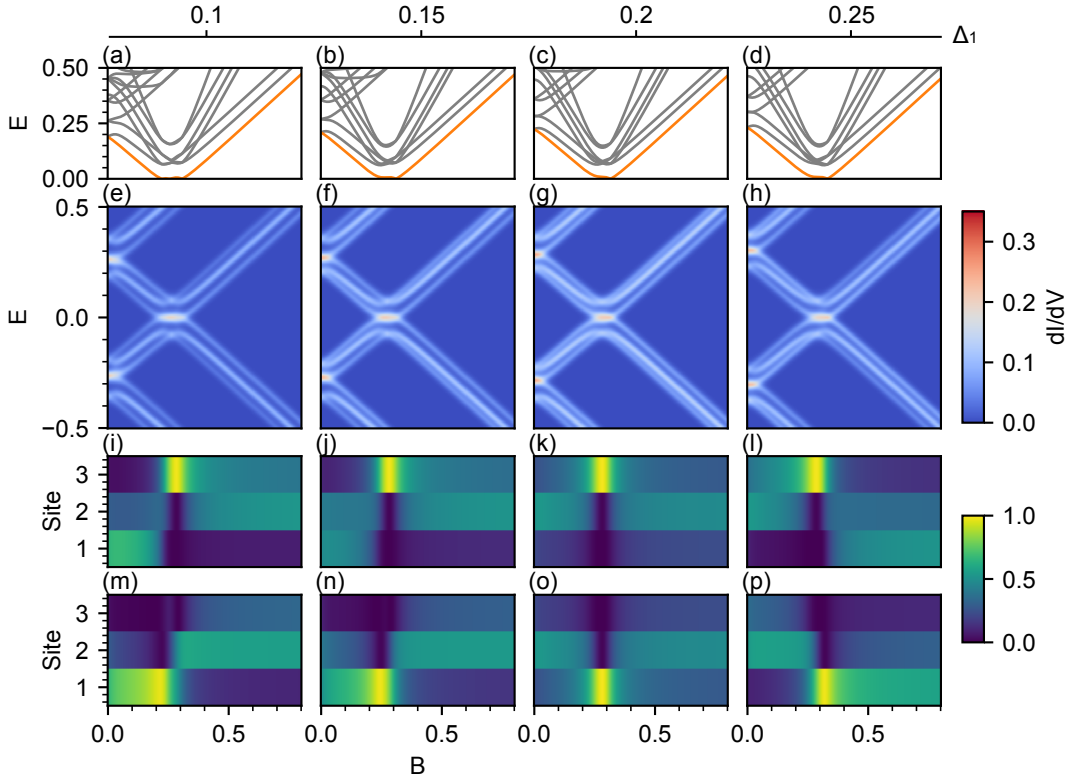

Figure 4.12: Simulation results for a chain of 3 dots with different induced superconducting gap in dot1, $\Delta_1 = 0.1, 0.15, 0.2, 0.25$. (a-d) Many-body spectra versus the magnetic field. The orange line is the first excited state. (e-h) Differential conductance in magnetic fields. (i-p) Evaluation of Majorana components (probability amplitudes) in different sites in magnetic fields. Other parameters used: $U = 0$, $\Delta_2 = \Delta_3 = 0.2$, $\alpha = 0.05$, $t = 0.05$, $\epsilon = 0.1$, $T = 0.01$.

Fig. 4.12 shows simulation results for a chain of 3 dots with different induced superconducting gap in dot1, $\Delta_1 = 0.1, 0.15, 0.2, 0.25$. (a-d) Many-body spectra versus the magnetic field. The orange line is the first excited state. (e-h) Differential conductance in magnetic fields. (i-p) Evaluation of Majorana components (probability amplitudes) in different sites in magnetic fields. The color denotes $|\langle E|\gamma_{x,s,\uparrow}|G\rangle|^2 + |\langle E|\gamma_{x,s,\downarrow}|G\rangle|^2$ in (i-l) and $|\langle E|\gamma_{y,s,\uparrow}|G\rangle|^2 + |\langle E|\gamma_{y,s,\downarrow}|G\rangle|^2$ in (m-p), where $s = 1, 2, 3$ is the site, $|G\rangle$ is the ground state, $|E\rangle$ is the first excited state. In Fig. 4.12, different induced superconducting gap strengths in dot1 are studied. When Δ_1 is similar to Δ_2 and Δ_3, $\Delta_1 = 0.15, 0.2, 0.25$ and $\Delta_2 = \Delta_3 = 0.2$, separated Majorana modes are still present in Figs. 4.12 (j,n,k,o,l,p). However, when $\Delta_1 = 0.1$ and $\Delta_2 = \Delta_3 = 0.2$, separated Majorana modes no longer exist.

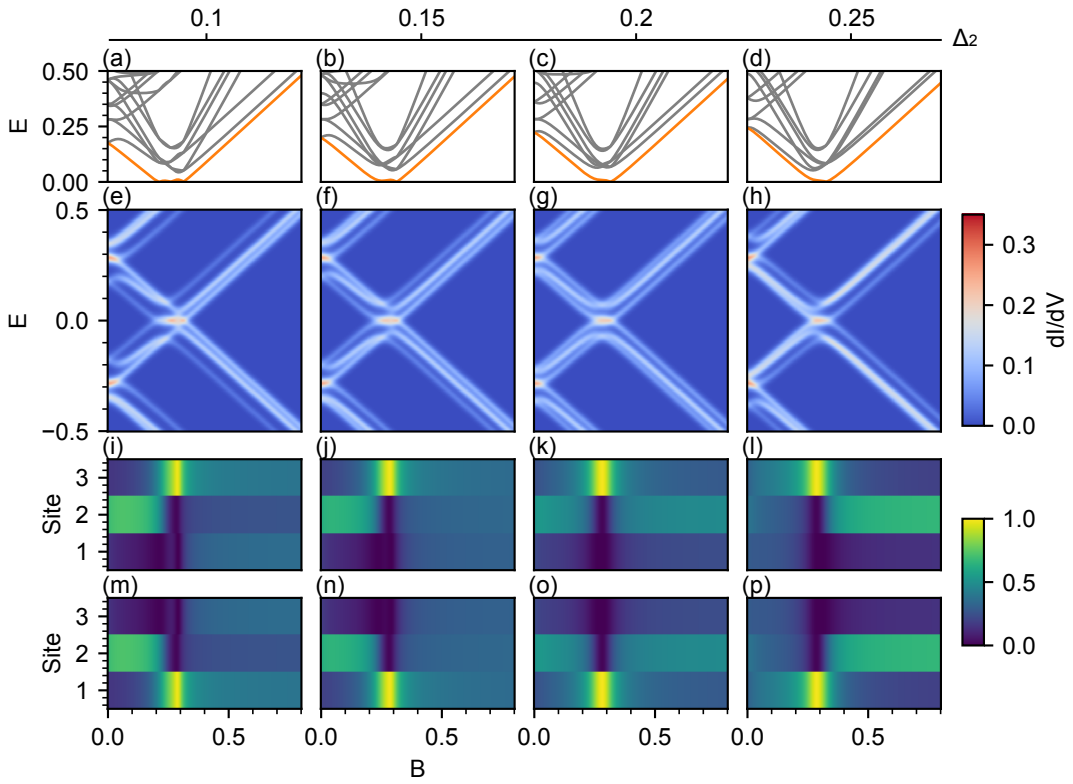

Figure 4.13: Simulation results for a chain of 3 dots with different induced superconducting gap in dot2, $\Delta_2 = 0.1, 0.15, 0.2, 0.25$. (a-d) Many-body spectra versus the magnetic field. The orange line is the first excited state. (e-h) Differential conductance in magnetic fields. (i-p) Evaluation of Majorana components (probability amplitudes) in different sites in magnetic fields. Other parameters used: $U = 0$, $\Delta_1 = \Delta_3 = 0.2$, $\alpha = 0.05$, $t = 0.05$, $\epsilon = 0.1$, $T = 0.01$.

Fig. 4.13 shows simulation results for a chain of 3 dots with different induced superconducting gap in dot2, $\Delta_2 = 0.1, 0.15, 0.2, 0.25$. (a-d) Many-body spectra versus the magnetic field. The orange line is the first excited state. (e-h) Differential conductance in magnetic fields. (i-p) Evaluation of Majorana components (probability amplitudes) in different sites in magnetic fields. The color denotes $|\langle E|\gamma_{x,s,\uparrow}|G\rangle|^2 + |\langle E|\gamma_{x,s,\downarrow}|G\rangle|^2$ in (i-l) and $|\langle E|\gamma_{y,s,\uparrow}|G\rangle|^2 + |\langle E|\gamma_{y,s,\downarrow}|G\rangle|^2$ in (m-p), where $s = 1, 2, 3$ is the site, $|G\rangle$ is the ground state, $|E\rangle$ is the first excited state. In Fig. 4.13, different induced superconducting gap strengths in dot2 are studied. Δ_2 has little effect on the distribution of Majorana wavefunctions. When $\Delta_2 = 0.1, 0.15, 0.2, 0.25$ and $\Delta_1 = \Delta_3 = 0.2$, separated Majorana modes are

still present.

Simulation data and code are available on Zenodo [94].

4.4 Conclusions

We build a tight-binding model of a quantum dot chain containing three sites. We study the model with all tunable parameters. We simulate the energy spectrum and transport of the triple-dot chain. Well-separated Majorana zero modes are not expected for the 3-site chain outside of fine-tuned regimes, i.e., when Andreev states from all three dots reach zero bias at the same magnetic field and a zero-bias peak extends in magnetic fields would appear.

For a short chain (3-site), within a narrow parameter window (fine-tuned regimes), the probability distribution of Majorana wavefunctions indicates a partial separation of two Majorana zero modes localized at two end sites. Shown in Figs. 4.9, 4.11, and 4.12, it is possible to have separated Majorana modes at the ends of the 3-site chain only when parameters of each dot are similar. It implies that in experiments, all three dots need to be uniform, or the device has to be extremely tunable, such that the requirements are satisfied for all parameters to be inside of the narrow window to host topological phases, i.e., the Kitaev regime.

A longer chain should have a larger window in parameter space to achieve the Kitaev regime and be more robust against disorder and nonuniformity in parameters, although the experimental realization will be much more challenging.

After showing the experimental results of the triple-dot device in Chapter 5, we discuss the relevance of our model and our device, together with other theoretical models in Sec. 5.6.

5.0 Triple Andreev dot chains in semiconductor nanowires

5.1 Introduction

In Sec. 4.1, we addressed our concern of the omnipresent Andreev bound states in hybrid superconductor/semiconductor nanowire devices. In this chapter, we take an alternative approach to implement the Kitaev chain other than the continuous Majorana wire model [25, 26]. Rather than trying to eliminate Andreev states, we take advantage of them in our Majorana search. Theory suggests a robust topological superconducting phase in chains of Andreev quantum dots, a discrete version of the Kitaev mode [47, 48].

Intending to emulate the discrete Kitaev chain, we build a device of three quantum dots in a chain in an InSb nanowire. At zero magnetic field, we observe Andreev bound states in each of the three dots. No other unwanted or uncontrollable dots are found in the main wire segment. We study their magnetic field and gate voltage dependence and observe dot-dependent zero-bias conductance peaks in magneto-transport spectroscopy. We interpret zero-bias peaks as Andreev states along the triple-dot chain crossing zero energy at finite magnetic fields. In section 4.3, our simulation indicates that triple-dot states acquire Majorana polarization when Andreev states in all three dots reach zero energy in a narrow range of magnetic field. In our device, transport is dominated by one of the quantum dots in the chain, D_3, which has a zero-bias crossing at lower magnetic fields than the other two dots. Thus the parameters lie outside of the simulated non-trivial topological phase. The device geometry is suitable for studying the correlation of two end states with non-local measurements. Even though the desired regime is not accessible, this device with new geometry has overcome many nanofabrication challenges and is one step further towards an unambiguous identification of Majorana zero modes. Devices with greater uniformity or independent control over superconductor-semiconductor coupling should realize the Kitaev chain with a high yield. Due to its overall tunability and design flexibility, the quantum dot system remains promising for quantum simulation of interesting models and particularly for modular topological quantum devices.

Our study of triple Andreev dot chains is published on [95].

5.2 Device description

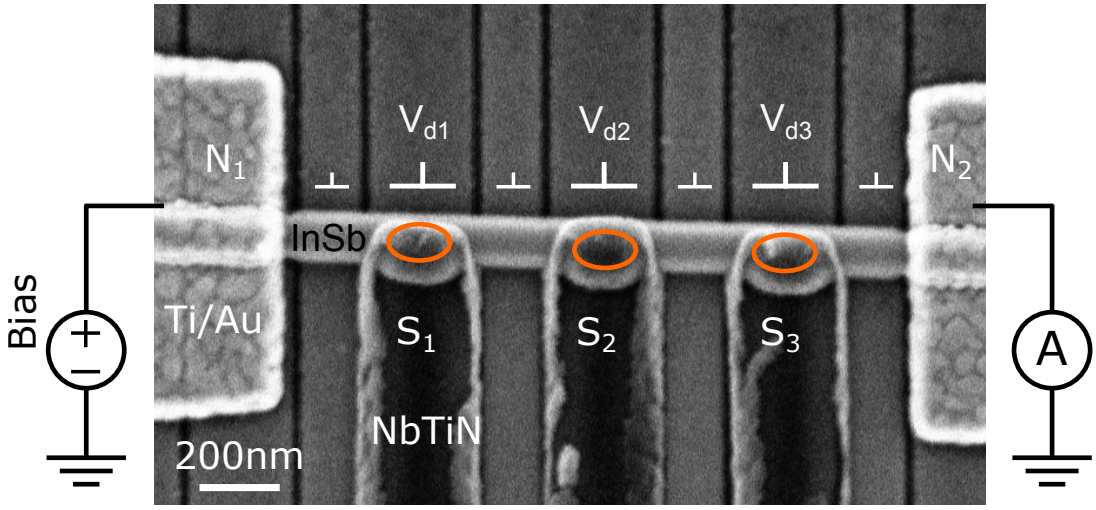

Figure 5.1: Scanning electron micrograph (SEM) of the triple-dot device. Orange circles indicate positions of quantum dots within the InSb semiconductor nanowire underneath three NbTiN superconducting leads (S_1, S_2, S_3), electrostatic gates that separate and tune dots are marked with inverted T's. The circuit shown is the primary measurement configuration where non-superconducting leads N_1 and N_2 are the source and drain.

Fig. 5.1 shows the scanning electron micrograph (SEM) of the triple-dot device. Three separate superconductors (S_1, S_2, S_3, NbTiN) contact an indium antimonide (InSb) semiconductor nanowire to create three Andreev quantum dots (D_1, D_2, D_3) in a chain. The hybrid nanowire device has two non-superconducting leads (N_1, N_2) at wire ends for probing the chain. Three quantum dots are separated along the nanowire by tunnel barriers controlled by narrower unlabeled electrostatic gates located in between contacts. Quantum dots are tuned by wide gates (d1, d2, d3). Magnetic fields parallel to the nanowire axis can be applied. Fig. 5.1 shows the measurement configuration used for most data acquired: we

apply a voltage bias through N_1 and measure current and differential conductance from N_2 while floating S_1, S_2, and S_3. In this configuration, current flows through all three Andreev dots. Thus resonances and their positions are influenced by quantum states in the entire chain. The measurements can be configured differently utilizing other terminals if a specific section of the device is of particular interest (Fig. 5.5).

5.3 Experimental results

In our five-terminal, seven-gate device, we test the routine of setting up quantum dots within the chain. We understand where the dots are located, their individual states, and how to control them and their couplings. Fig. 5.2 shows representative differential conductance spectra of the dot chain while tuning each dot over several occupation values. Current passes through all three dots between N_1 and N_2. Conductance resonances are pinned to finite bias and exhibit varying degrees of wiggling but never cross zero bias at zero magnetic field (Figs. 5.2(a)-(c)).

In a single quantum dot, these resonances are transitions from ground to excited Andreev states: the dot is in the ground state at the start of the charge transfer cycle, and the additional electron passing through the dot enters the excited state [43, 91]. Because the dots are directly underneath the leads, they are expected to be strongly coupled to superconductors, with the ground state always a singlet while the excited state a doublet, at zero magnetic field. In a triple-dot chain where current passes through all three dots, these resonances are a convolution of ground-excited state transitions in all dots. Thus we cannot unambiguously extract energy scales in each dot from these data. However, we can evaluate the effect of each dot's gate on the resonances. In Figs. 5.2(a,b), Andreev bound states appear flatter. We interpret this as D_1 and D_2 being stronger coupled to leads S_1 and S_2. In Fig. 5.2(c), Andreev states appear wavier, suggesting a weaker coupling of D_3 to S_3.

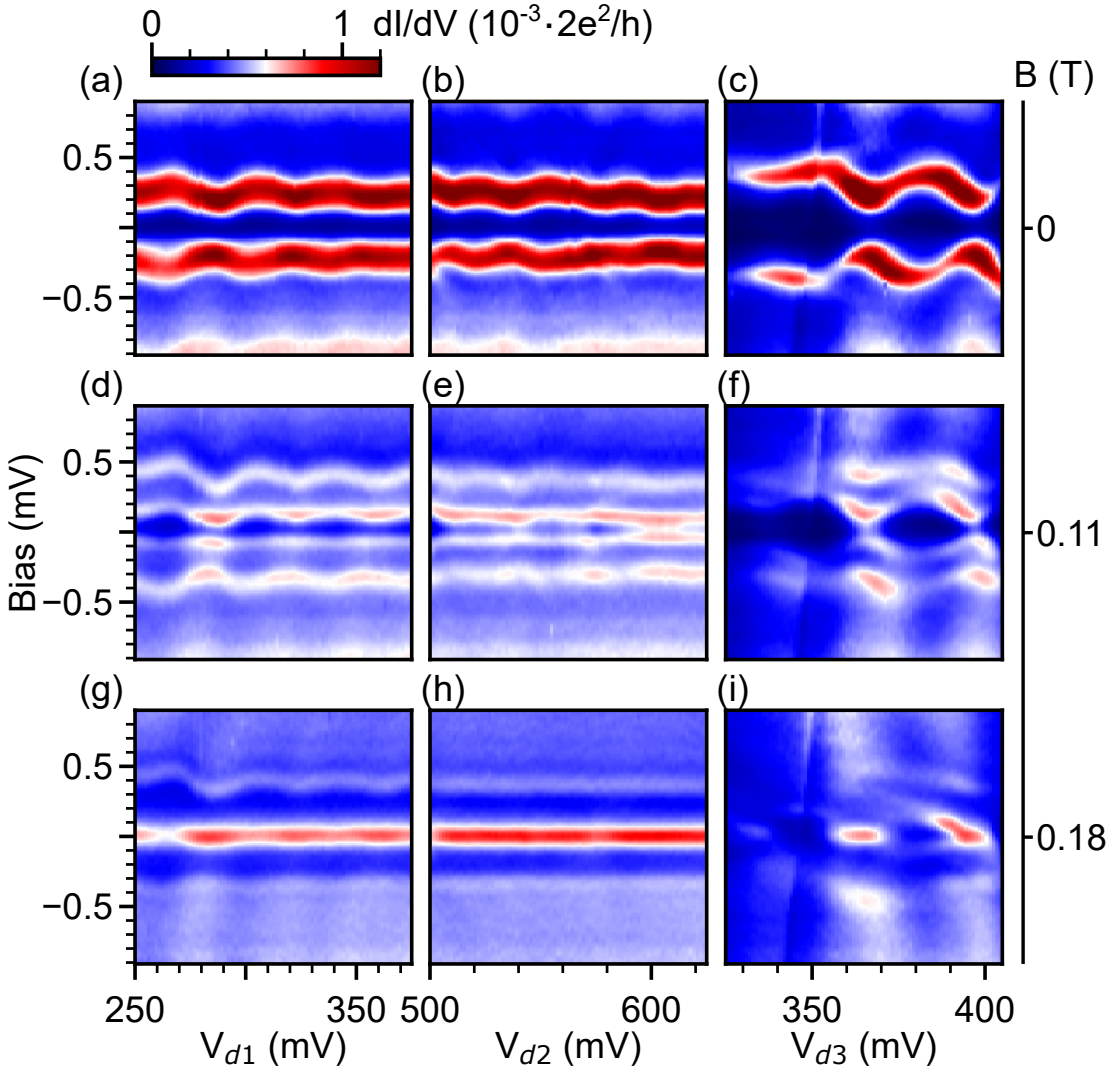

Figure 5.2: Bias spectroscopy of Andreev bound states in each dot at different magnetic fields. (a)-(c): B=0, (d)-(f): B=0.11T, (g)-(i): B=0.18T. Gate settings in (a,d,g): V_{d2}=576.5mV, V_{d3}=395mV. (b,e,h): V_{d1}=322.5mV, V_{d3}=395mV. (c,f,i): V_{d1}=322.5mV, V_{d2}=576.5mV. Measured from N_1 to N_2.

We note that the differential conductance is relatively low, less than a percent of a quantum of conductance. This is because the current has to pass through four tunneling barriers. For measurements in all figures, we set the barrier between S_3 and N_2 to be the least transmitting. This is a compromise tuning strategy: raising more barriers leads to sharper resonances, but the signal decreases further.

We observe doubling the number of resonances when a parallel magnetic field is applied in Figs. 5.2(d)-(f), at B=0.11T. This is because the excited Andreev states (doublets) Zeeman split, while the ground state remains a singlet and does not split with an applied magnetic field. One branch of resonances moves to lower voltage bias. The resonances reach zero voltage bias for the first time at B=0.18T (Figs. 5.2(g)-(i)).

A softened induced gap allows us to observe the resonance in D_3 at zero voltage bias even when states in D_1 and D_2 are not near zero-energy. For quantum dot chain with a hard induced gap, zero-bias peak only occurs when states of all dots cross zero voltage bias simultaneously at a fixed magnetic field. When sweeping the gates of dots D_1 and D_2, we observe zero-bias conductance peaks across the entire gate voltage range of these figures (Figs. 5.2(g,h)). In dot D_3, we observe zero-bias peaks at three narrow intervals of gate voltage V_{d3}. If we set V_{d3}=365mV, we have zero-bias peaks on both ends of the nanowire.

This is not the situation we expect when delocalized Majorana zero modes are present. We can tell this from the fact that these zero-bias peaks are sensitive to V_{d3} and not to the gates (V_{d1}, V_{d2}) controlling the other dots (D_1, D_2). In the Kitaev chain regime, we expect zero-bias peaks to depend on the tuning of all dots. In Figs. 5.2(g,h), V_{d3} is set to 395mV, where one of the zero-energy crossings occurs. The 'long' zero-bias peaks in Figs. 5.2(g,h) indicate dot gate d1 and d2 are not coupled to the state that crosses zero voltage bias at B=0.18T, which is localized at D_3. The states localized at D_1 and D_2 likely cross zero voltage bias at higher magnetic fields since those Andreev states are coupled stronger to leads S_1 and S_2.

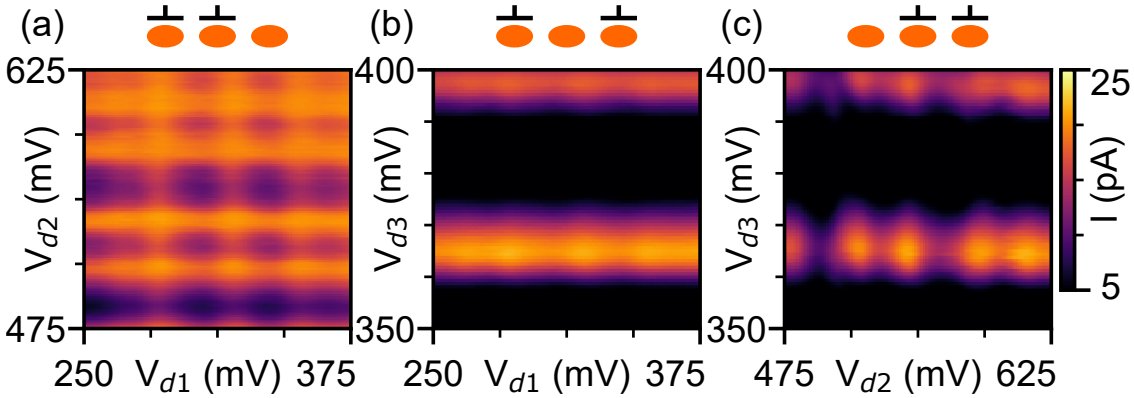

Figure 5.3: Stability diagrams between (a) D_1 and D_2, V_{d3}=366.25mV. (b) D_1 and D_3, V_{d2}=537.5mV. (c) D_2 and D_3, V_{d1}=315mV. Measured from N_1 to N_2. Bias voltage V=0.2mV. B=0.

To characterize the chain of dots, we provide current maps in which pairs of dot gates are tuned, with three possible combinations (D_1-D_2, D_1-D_3, D_2-D_3), in Fig. 5.3. These data are at zero magnetic field and a fixed bias voltage (V=0.2mV). Note that these plots show current rather than conductance, signaled using a different colormap than other figures. High current here is where Andreev resonances dip to lower bias because as Fig. 5.2 shows, resonances never cross zero bias at zero field. Lines of high current regions form rectangular grid patterns, which indicate that capacitive couplings between the dots are weak. This is because the dot gates are screened by leads S_1, S_2, S_3. We only observe current maxima related to the three dots and no extra states within the central nanowire segment. Resonances related to D_3 dominate over resonances from D_1 and D_2, further confirming that D_3 is the bottleneck of transport in this device.

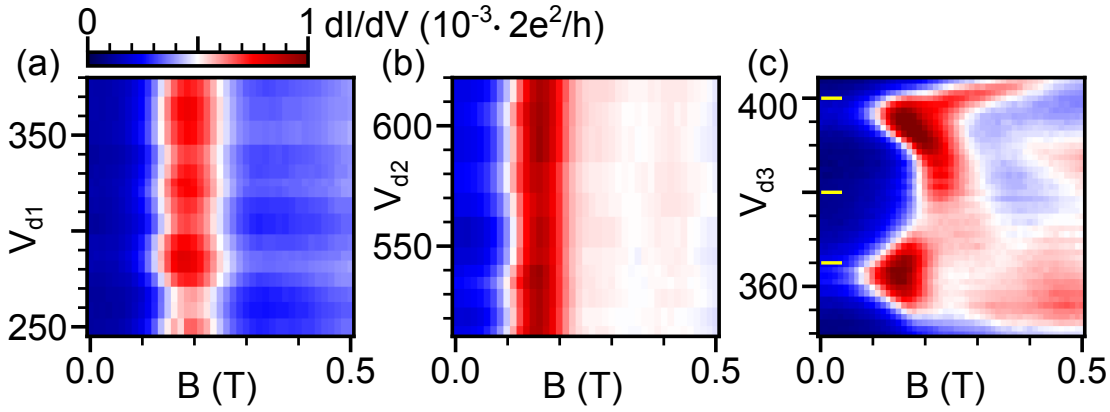

Figure 5.4: Zero-bias tunneling conductance as a function of magnetic fields in (a) D_1, V_{d2}=576.5mV, V_{d3}=392.5mV. (b) D_2, V_{d1}=322.5mV, V_{d3}=360mV. (c) D_3, V_{d1}=185mV, V_{d2}=472.5mV. Measured from N_1 to N_2. Magnetic field evolution of the triple-dot Andreev bound states at different V_{d3} values indicated by yellow short lines in (c) are in supplementary materials.

Fig. 5.4 shows the extracted zero-bias tunneling conductance as a function of dot gate voltages and parallel magnetic fields. Figs. 5.4(a)-(c) are effective phase diagrams of zero-bias peaks for all three dots: red regions correspond to zero-bias peaks, and blue regions correspond to no peak at zero bias. In Figs. 5.4(a,b), the zero-bias peaks are mostly gate independent, which is in agreement with Figs. 5.2(g,h). Fig. 5.4(c) shows the onset point of the first zero-energy crossing in magnetic fields is strongly dependent on V_{d3}. The first zero-energy crossing (peak center) can occur in a range of magnetic fields between 0.16T and 0.35T.

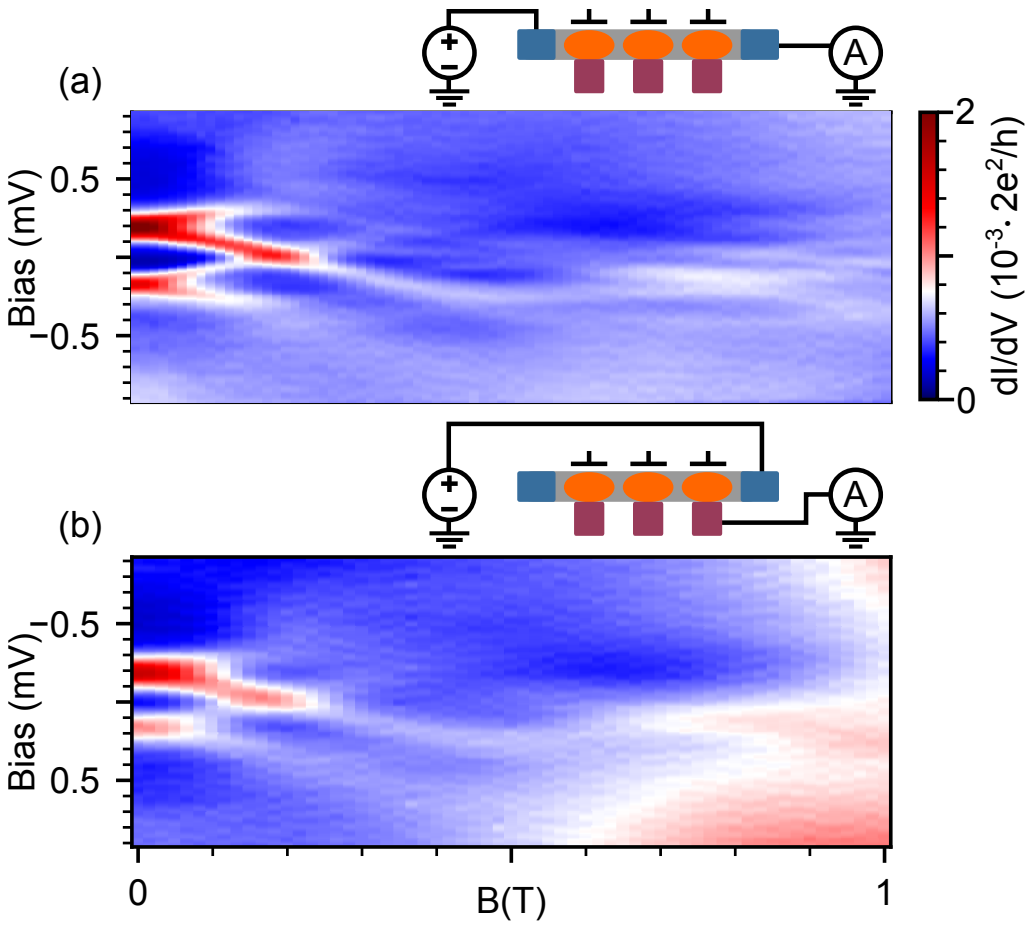

Figure 5.5: Magnetic field evolution of the triple-dot Andreev bound states with different measurement configurations shown in circuit diagrams above panels, (a) N_1-N_2, (b) N_2-S_3. V_{d1}=315mV, V_{d2}=537.5mV, V_{d3}=396mV. Because the source and drain are reversed in (b) compared to (a), we have flipped voltage bias axis in (b).

Fig. 5.5 shows magnetic field evolution of the triple-dot Andreev bound states to higher magnetic fields (up to 1T). Between B=0 and 0.2T the splitting of Andreev resonances and zero energy crossing are clear and in high contrast. However, signals are less prominent in magnetic fields above $\approx$ 0.2T. This is due to the soft superconducting gap of NbTiN in finite magnetic fields. Though it is possible to observe sharp resonances to higher fields in NbTiN devices [27, 82, 62], here we have an additional constraint that our NbTiN electrodes are

relatively narrow ($\approx$ 200 nm) and thin ($\approx$ 60 nm) in order to reduce the stress that may break nanowires for devices with multiple superconducting electrodes. The narrow and thin NbTiN contacts can explain the weakened proximity-induced superconductivity.

At fields above 0.2T, there are several additional resonances at low voltage bias. Spectrum and transport simulations predict up to 3 zero energy crossings in magnetic fields depending on parameters of the triple-dot chain (see supplementary materials). It is plausible that resonances at higher fields originate from D_1 and D_2. However, reduced contrast prevents their unambiguous identification.

Fig. 5.5(b) illustrates how we can use the five-contact geometry of this device to gain additional information on state localization along the chain. We apply voltage bias through N_2 and measure current and differential conductance from S_3 while floating N_1, S_1, and S_2. The overall differential conductances are comparable in Figs. 5.5(a,b), confirming that transport features observed in this paper are dominated by D_3. We are essentially measuring resonances with sharp features of D_3 on a faint background of D_1 and D_2. Some of the resonances beyond 0.2T do not show up in panel (b). This may confirm that they are due to D_1 and D_2, which are not in the path of current in panel (b). However, it may also be due to slightly more broadened features in panel (b) reducing the sensitivity to those resonances.

We also show in Fig. 5.13 that the tunnel barrier located at the left end near N_1 is significantly more open compared to the right tunnel barrier at N_2. The inter-dot barriers are also low. Thus whenever N_2 is excluded from the measurement configuration, the resonances broaden considerably.

Data are available on Zenodo [94].

5.4 Experimental methods

Nanowire growth: InSb nanowires are grown by metal-organic vapor phase epitaxy (MOVPE). A typical nanowire is 3-5 μm in length with 120-150 nm diameter.

Nanowire deposition: InSb nanowires are transferred onto undoped Si substrates with pre-patterned gate electrodes using a micromanipulator under an optical microscope. The

gates are 1.5/6 nm Ti/PdAu covered by 10 nm of HfO_x as the dielectric layer.

Contact deposition: contacts are patterned by standard electron-beam lithography. Sulfur passivation and Ar sputter cleaning are performed to remove the native oxidation layer on nanowires before sputter deposition 5/60 nm of NbTi/NbTiN at an angle of 45 degrees with respect to the substrate. Sulfur passivation removes the oxidation layer before e-beam evaporation of 10/145 nm of Ti/Au.

Measurement: measurements are performed in a dilution refrigerator at a base temperature of 40 mK. Multiple stages of filtering are used to enhance the signal-to-noise ratio. All voltage bias data are two-terminal measurements. Series resistance was taken into account in calculating conductance in all figures.

5.5 Further reading

Background on Majorana zero modes in hybrid superconductor-semiconductor nanowires can be found in [96, 97, 98, 99]. Experiments on multi-terminal nanowire devices can be found in [100, 101, 72, 102]. Proposals of implementing the Kitaev chain with quantum dots and superconductors can be found in [47, 48, 49]. Studies of Andreev bound states in hybrid superconductor-semiconductor nanowire devices are discussed in [43, 90, 91, 85]. Prospects of implementing Majorana-based quantum computation are assessed in [19, 103, 104, 105, 29, 106].

5.6 Discussion on different models

We were motivated by [47] and [48] in the early stages of the project. They propose to use a chain of quantum dots to realize an effective Kitaev model. However, significant details vary between these two proposals, and between the original Majorana proposals [31, 25, 26] and our experimental approach. Thus, our devices do not in fact implement or intend to implement the proposals in [47] and [48].

Model in [47] is for a linear array of quantum dots interspersed with superconducting islands. This model is an effective Kitaev chain when the nearest-neighbor hopping between quantum dots (through a superconducting island) is allowed, and only a single spin-polarized level in each dot participates in transport. Spin-orbit coupling rotates spin polarization as an electron moves inside the dot, allowing proximity-induced superconductivity that pairs electrons from neighboring dots rather than inside one dot (double occupation is forbidden in each dot). The model also requires crossed Andreev reflection, which is a challenging experimental requirement for a chain of dots.

Model in [48] requires spinful quantum dots at single occupations. This model also features a tunable proximity effect between quantum dots and superconductors, which is achieved by applying a phase difference between two superconductors attached to a single dot. The tuning procedures described in [48] which include the tuning of chemical potentials, superconducting phases, and couplings, are done at a fixed Zeeman energy, i.e., at a fixed magnetic field.

Our devices are geometrically and functionally different from those described above. However, they are also suitable for realizing the Kitaev chain, as our model (in Sec. 4.2), tailored to our 3-dot system, demonstrates.

Below we explain in what ways our devices are different from those proposed in [47] and [48]: In our devices, we have exactly three dots. Realizing chains of more dots as suggested in [47] and [48] with their geometry and the current fabrication techniques is challenging. Our device is not an array of alternating quantum dots and superconducting islands [47] or a chain of quantum dots with superconducting loops [48], but a chain of Andreev quantum dots. Each dot is strongly coupled to a superconducting lead in our device and has a singlet ground state (a hybrid of empty and doubly occupied states) at zero magnetic field. At finite magnetic fields, the ground states become spin-up doublet Andreev Bound States. Dots have a quenched charging energy and exhibit no Coulomb blockade.

Devices characteristics captured by our model: Our model included in Chapter. 4 is not a literal representation of our device, but it captures key features of what we measure. Our model of three single-level quantum dots is a generic description of a quantum dot chain with spin-orbit interaction, induced superconductivity, and Zeeman effect. The spin-orbit

length in InSb nanowires has been measured to be in the range of $100 - 200$nm [54, 55]. This is comparable to the distances between dots in our device. Spins undergo full or nearly full rotation while tunneling between the dots over uncovered segments of the nanowire, where spin-orbit is better understood. Our model captures this fact by setting parameters α (spin-orbit coupling) and t (tunneling between dots) to be of similar values. Our model contains superconducting pairing for electrons from the same dot, not adjacent dots, which is consistent with the fact that we only observe Andreev bound states with singlet ground states in each dot at zero magnetic field. In the model, we use small values for U (Coulomb interaction) to capture the lack of charging energy.

Models in [107] and [108] propose to couple several finite-sized segments of topological superconductor through tunnel gates. The chain thus consists of multiple wire sections with individual superconducting islands. In each segment, Andreev bound states can be partially separated into Majorana modes. By coupling the neighboring segments, inner Majorana modes on each segment hybridize and leave the outermost Majorana modes unpaired, similar to a Kitaev chain. Models in [107] and [108] are relevant to our study since the wire segments are of a length similar to our devices. However, these models are too optimistic to assume partially separated Majorana modes already exist in each wire segment, which needs to be first experimentally established.

5.7 Supplementary data

5.7.1 Date from the triple-dot device

Supplementary data are from the triple-dot device shown in Fig. 5.1.

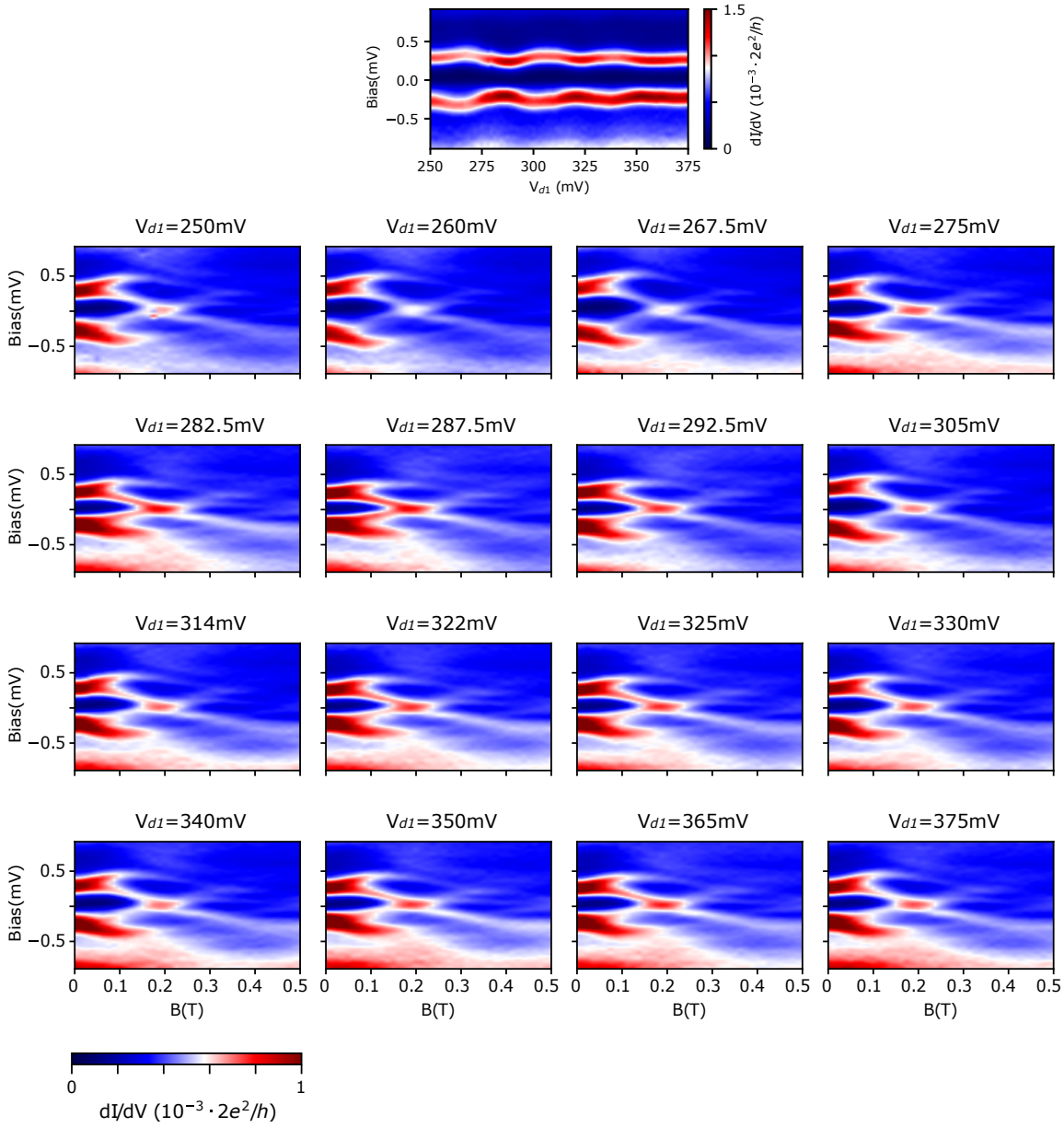

Figure 5.6: Magnetic field evolution of the triple-dot Andreev bound states at different D_1 potentials. Gate voltage V_{d1} is listed above each panel. For all panels, V_{d2}=576.5mV, V_{d3}=392.5mV. Measured from N_1 to N_2.

Fig. 5.6 shows the full data set of D_1 dependence of the magnetic field evolution of the triple-dot Andreev bound states. In the range of 0-0.5T, with various gate voltages V_{d1}, no clear differences in magneto-spectroscopy are observed. It means the triple-dot Andreev

state that generates the zero energy crossing near 0.2T is not D_1 dependent, and the Andreev state does not locate at D_1, the left end of the device.

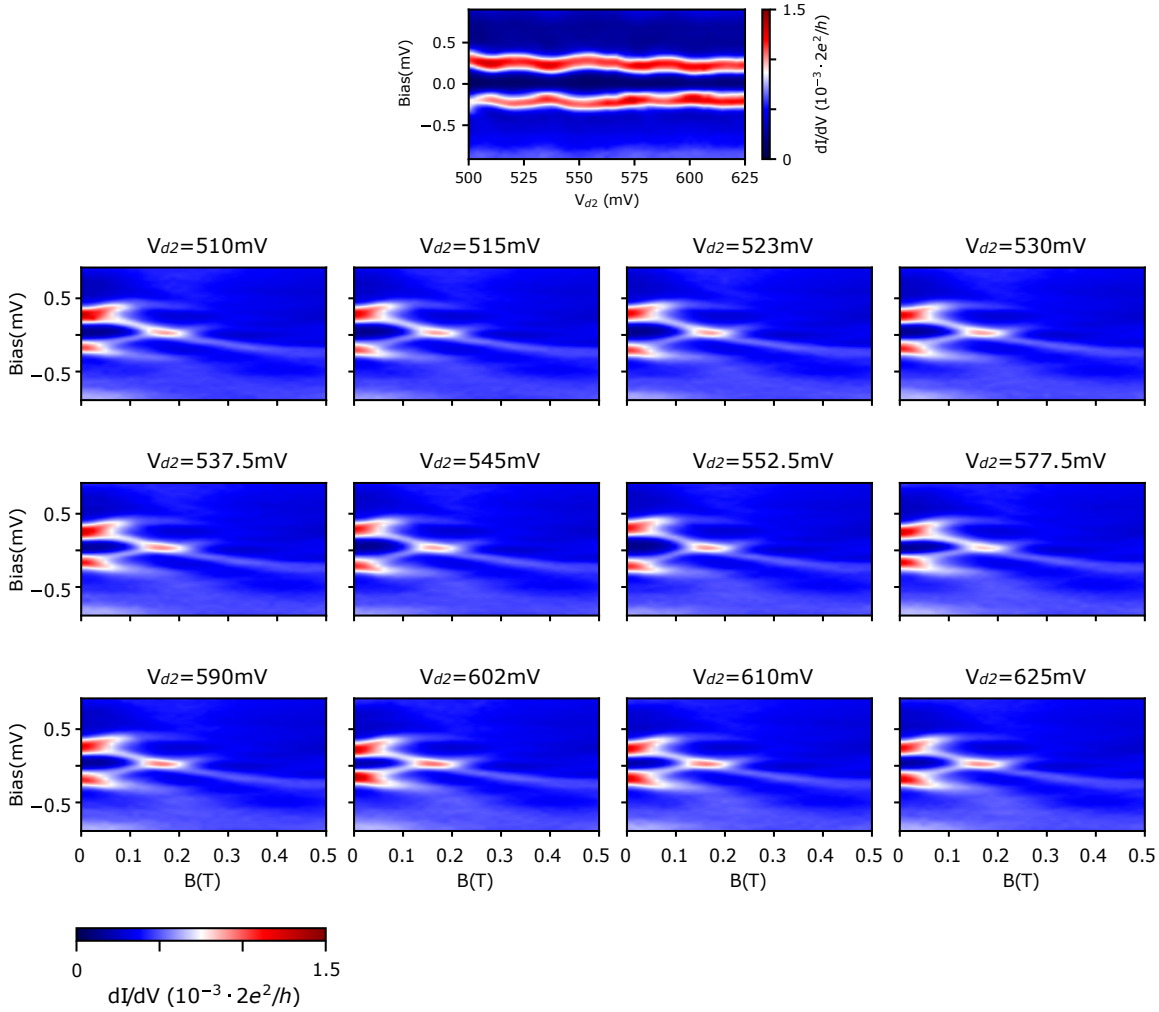

Figure 5.7: Magnetic field evolution of the triple-dot Andreev bound states at different D_2 potentials. Gate voltage V_{d2} is listed above each panel. For all panels, V_{d1}=322.5mV, V_{d3}=395mV. Measured from N_1 to N_2.

Fig. 5.7 shows the full data set of D_2 dependence of the magnetic field evolution of the triple-dot Andreev bound states. In the range of 0-0.5T, with various gate voltages V_{d2}, no clear differences in magneto-spectroscopy are observed. It means the triple-dot Andreev state that generates the zero energy crossing near 0.2T is not D_2 dependent, and the Andreev

state does not locate at D_2, the middle of the device.

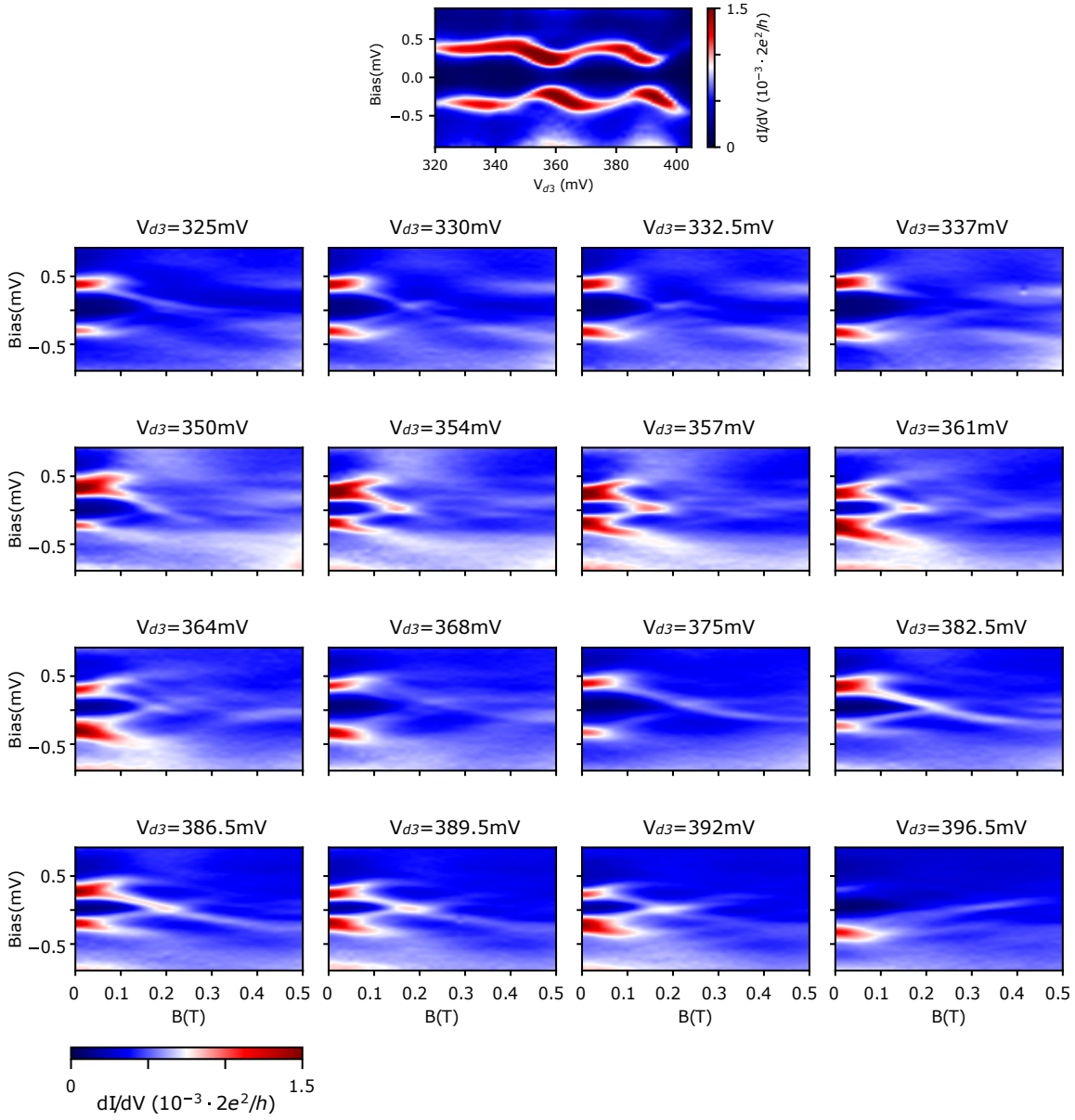

Figure 5.8: Magnetic field evolution of the triple-dot Andreev bound states at different D_3 potentials. Gate voltage V_{d3} is listed above each panel. For all panels, V_{d1}=322.5mV, V_{d2}=576.5mV. Measured from N_1 to N_2.

Fig. 5.8 shows the full data set ofD_3 dependence of the magnetic field evolution of the triple-dot Andreev bound states. In the range of 0-0.5T, with various gate voltages V_{d3}, clear

differences in magneto-spectroscopy are observed. The onset point of the first zero-energy crossing in magnetic fields ranges from 0.16 to 0.35T. It means the triple-dot Andreev state that generates the first zero-energy crossing in magnetic fields is D_3 dependent, and the Andreev state locates at D_3, the right end of the device. At some gate voltages V_{d3}, several additional resonances at low voltage bias are visible.

Data in Figs. 5.6, 5.7, and 5.8 are used to extract the zero-bias tunneling conductance and plot the effective phase diagrams of zero-bias peaks for all three dots in Fig. 5.4. Fig. 5.4 summarizes the dot dependence and magnetic field dependence of the triple-dot chain.

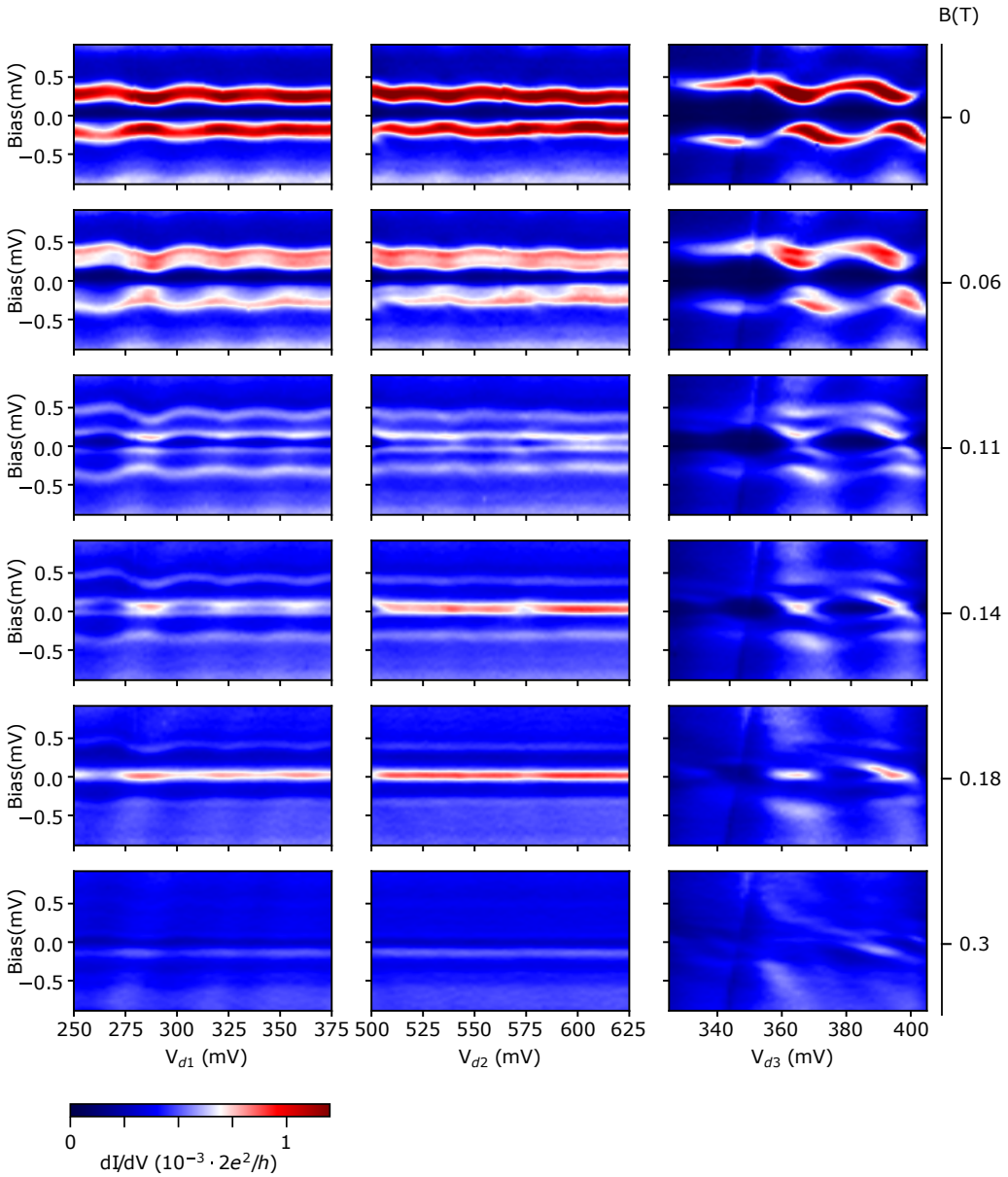

Figure 5.9: Additional data to Fig. 5.2. Bias spectroscopy of Andreev bound states in each dot at different magnetic fields. Emergence of the first zero-energy crossing. When tuning one dot, the other two gate voltages are fixed as: V_{d1}=322.5mV, V_{d2}=576.5mV, V_{d3}=395mV. Measured from N_1 to N_2.

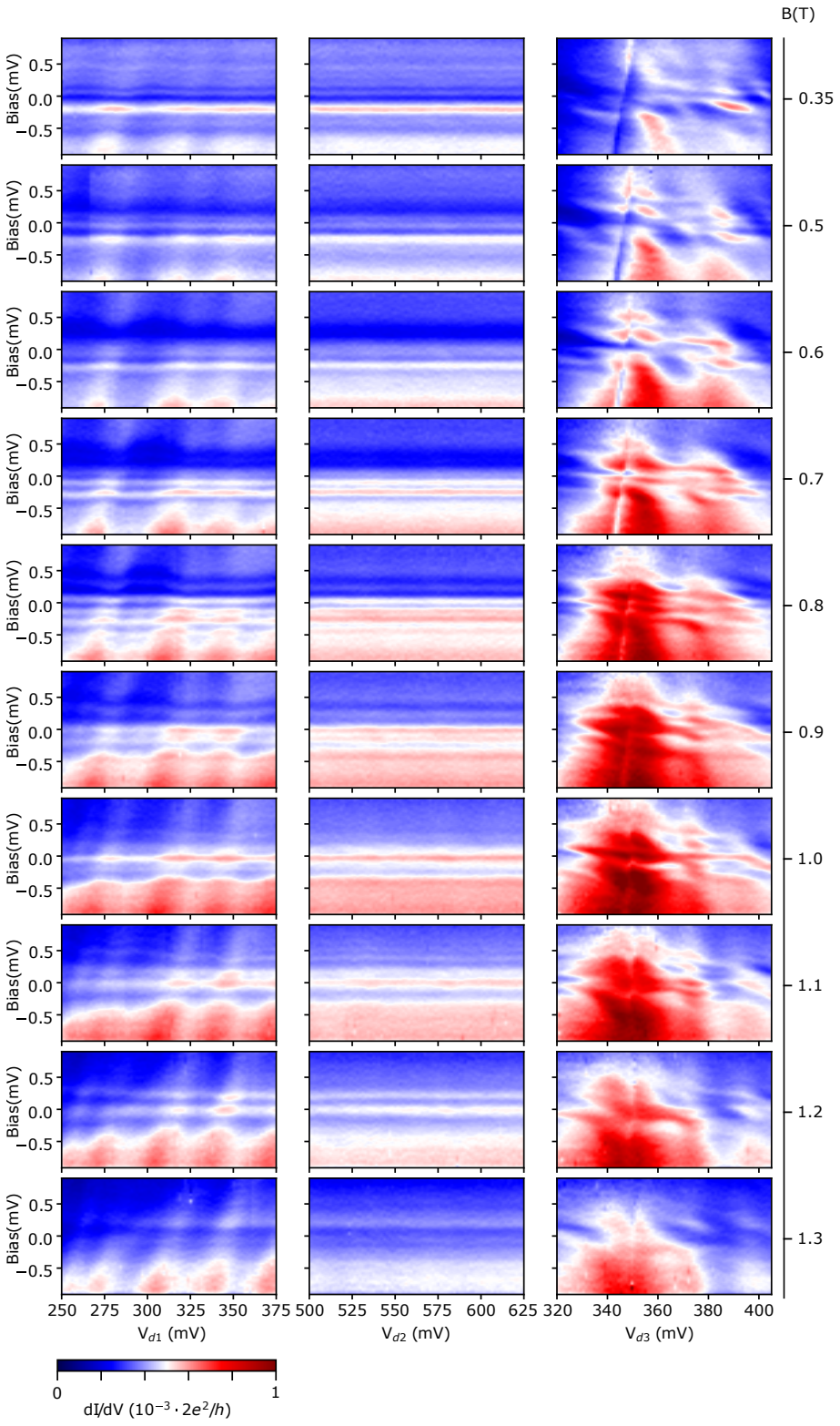

Figure 5.10: Bias spectroscopy of ABS in each dot at higher magnetic fields. When tuning one dot, the other two gate voltages are fixed as: V_{d1}=322.5mV, V_{d2}=576.5mV, V_{d3}=395mV. Measured from N_1 to N_2.

Fig. 5.9 and Fig. 5.10 show bias spectroscopy of Andreev bound states in each dot at different magnetic fields. At B=0, anti-crossing Andreev resonances with Andreev bound states in singlet ground state are observed in all three dots. When a parallel magnetic field is applied, excited Andreev states (doublets) Zeeman split, while the ground state remains a singlet and does not split with the applied magnetic field. We observe the splitting of resonances of Andreev states transition from singlet to doublet ground state. The first zero-energy crossing starts to emerge around B=0.14-0.18T. These zero-bias peaks of the first zero-energy crossing are sensitive to V_{d3} and not to (V_{d1}, V_{d2}). The 'long' zero-bias peaks in V_{d1} dependence and V_{d2} dependence indicate that dot gate d1 and d2 are not coupled to the state that crosses zero voltage bias at B=0.18T, which is localized at D_3. At higher magnetic fields, other resonances at low voltage bias are observed.

The states localized at D_1 and D_2 likely cross zero voltage bias at higher magnetic fields since those Andreev states are coupled stronger to superconducting leads S_1 and S_2. However, D_3 dominates the transport, the zero-bias peaks at B=1-1.2T show some V_{d1} dependence but strong V_{d3} dependence. Moreover, as the superconducting gap softens in higher magnetic fields, background conductance increases, and the resonances become broad and low in contrast. It is implausible to claim the origins of the zero-energy crossings at high magnetic fields.

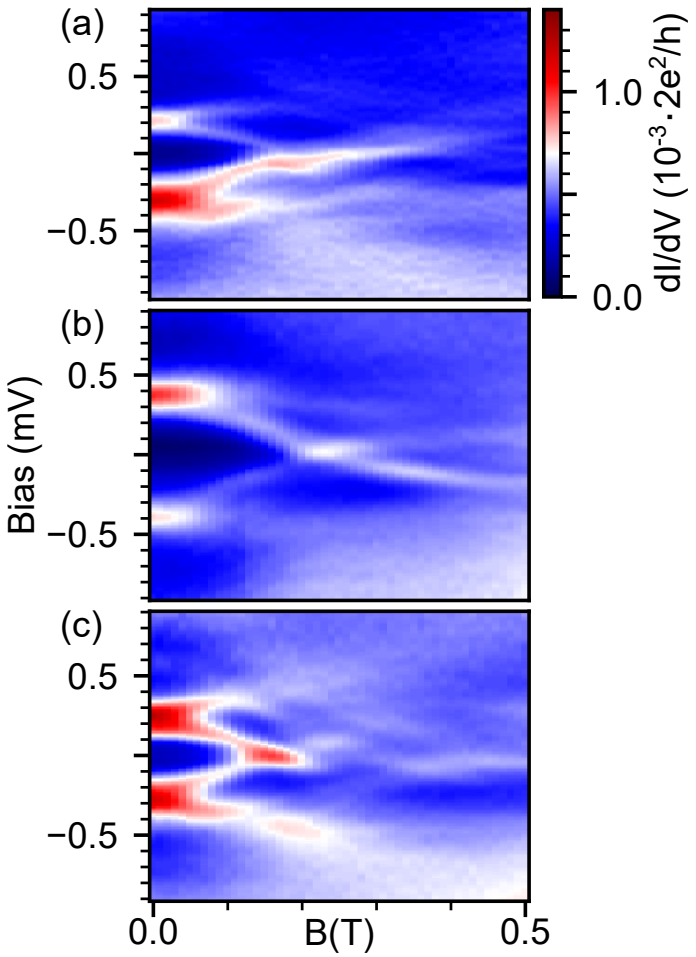

Figure 5.11: Magnetic field evolution of the triple-dot Andreev bound states at different V_{d3} indicated by short yellow lines in Fig. 5.4(c). (a) V_{d3}=400mV, (b) V_{d3}=380mV, (c) V_{d3}=365mV. V_{d1}=185.0mV, V_{d2}=472.5mV. Measured from N_1 to N_2.

Fig. 5.11 shows magnetic field evolution of the triple-dot Andreev bound states at three different V_{d3} values indicated by short yellow lines in Fig. 5.4(c). From Fig. 5.4(c), the onset point of the first zero-energy crossing in magnetic fields is V_{d3} dependent. Fig. 5.11 provides more details on how the Andreev states evolve and how zero-bias peaks develop in magnetic fields. The spectra can be bias-asymmetric (a-b) or bias-symmetric (c). The first zero-energy crossing can appear with different lengths in magnetic fields. Together with phase diagrams in Fig. 5.4, we conclude the origin of the first zero-energy crossing in magnetic fields is Andreev states localized at D_3.

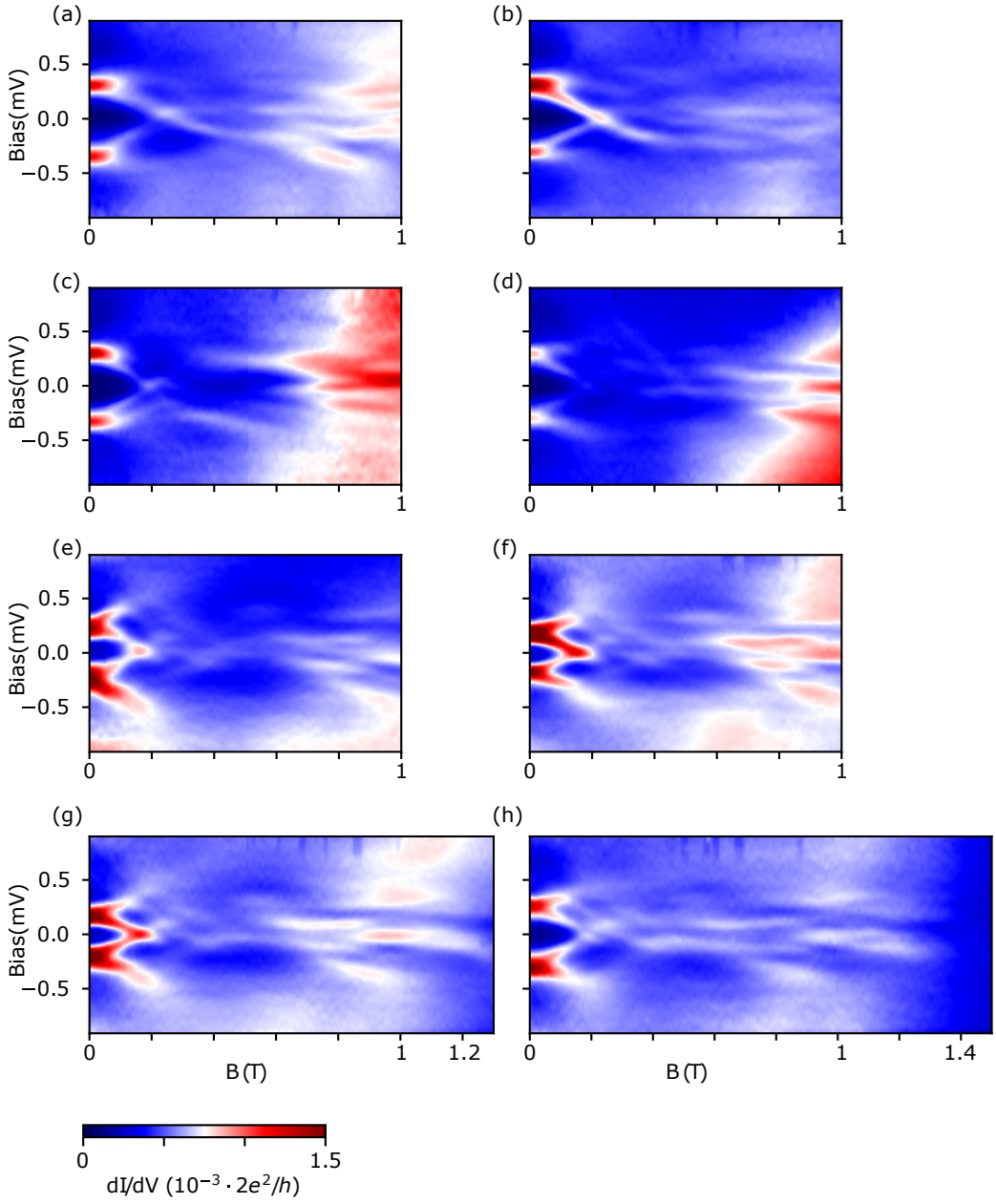

Figure 5.12: Magnetic field evolution of the triple-dot Andreev bound states to higher magnetic fields at different dot potentials, measured from N_1-N_2. (a) V_{d1}=320mV, V_{d2}=537.5mV, V_{d3}=377.5mV. (b) V_{d1}=288mV, V_{d2}=540mV, V_{d3}=390mV. (c) V_{d1}=320mV, V_{d2}=537.5mV, V_{d3}=335mV. (d) V_{d1}=285.5mV, V_{d2}=576.5mV, V_{d3}=370mV. (e) V_{d1}=322.5mV, V_{d2}=576.5mV, V_{d3}=360mV. (f) V_{d1}=320mV, V_{d2}=537.5mV, V_{d3}=362.5mV. (g) V_{d1}=320mV, V_{d2}=537.5mV, V_{d3}=365mV. (h) V_{d1}=288mV, V_{d2}=540mV, V_{d3}=375mV.

Fig. 5.12 shows magnetic field evolution of the triple-dot Andreev bound states at different gates voltages to higher magnetic fields.

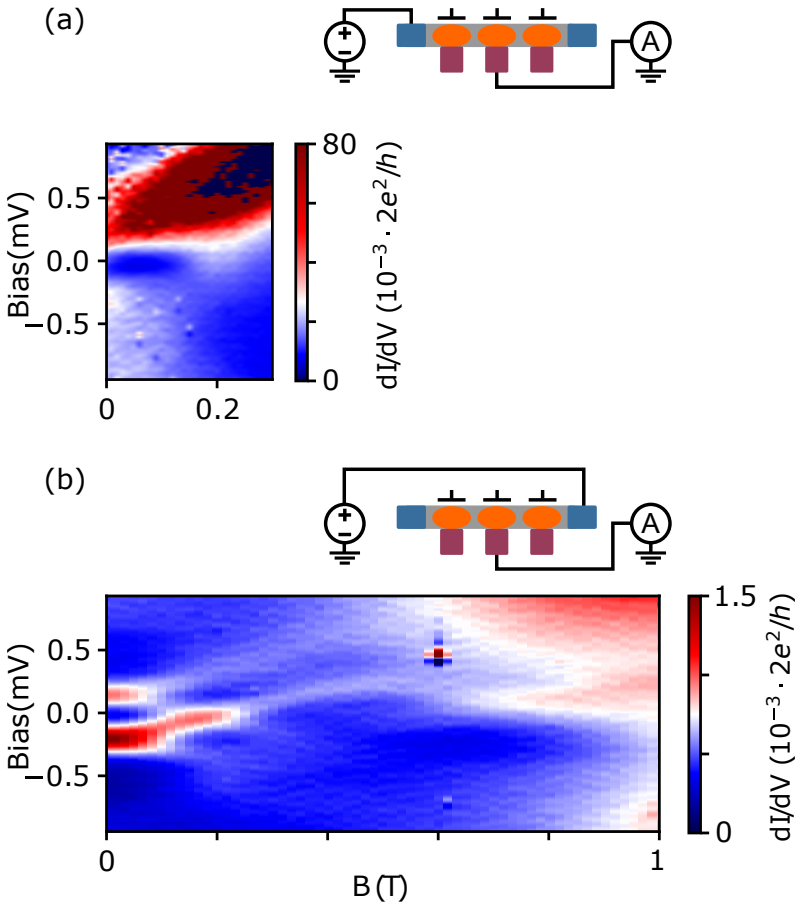

Figure 5.13: Additional data to Fig. 5.5. Magnetic field evolution of the triple-dot Andreev bound states with different measurement configurations shown in circuit diagrams above panels, (a) N_1-S_2, (b) N_2-S_2. V_{d1}=315mV, V_{d2}=537.5mV, V_{d3}=396mV.

Fig. 5.13 shows magnetic field evolution of the triple-dot Andreev bound states with different measurement configurations. Conductances are much higher in (a) than in (b), which indicates that the tunnel barrier located at the left end near N_1 is significantly more open compared to the right tunnel barrier near N_2. (b) is comparable to Figs. 5.5(a-b), suggesting the inter-dot barriers are also low. Thus whenever N_2 is excluded from the

measurement configuration, the resonances broaden considerably.

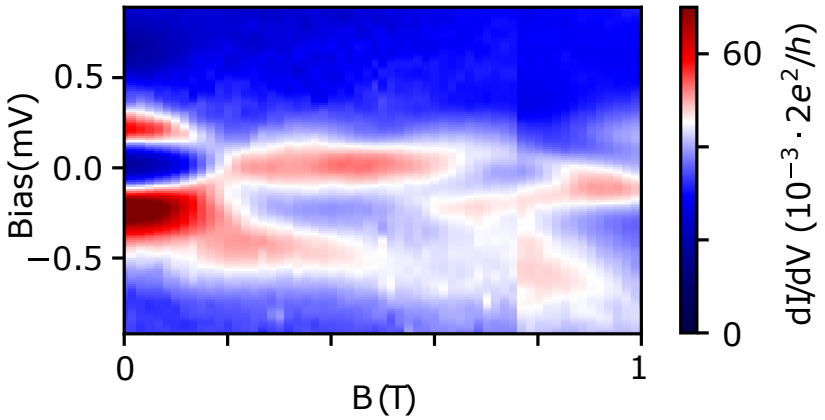

Figure 5.14: Magnetic field evolution of the triple-dot Andreev bound states when inter-dot barriers are lifted, i.e., tune the quantum dot chain towards a continuous wire.

Fig. 5.14 shows magnetic field evolution of the triple-dot Andreev bound states in a more open regime when inter-dot barriers are lifted, i.e., tune the quantum dot chain towards a continuous wire. Due to fewer and weaker tunnel barriers, conductance is much higher than measured with N_1-N_2 configuration, and the resonances are broadened. Instead of clear splitting of Andreev states, zero energy crossing, and resonances at low voltage bias beyond the first crossing shown in Fig. 5.12, a long zero-bias peak extends for near a half Tesla is present. The differences might be related to increased inter-dot couplings as lowering inter-dot barriers. However, a conclusion cannot be drawn based on these broadened resonances.

5.7.2 Data from another device with different geometry

Fig. 5.15 shows SEM of device B with a different triple-dot design. In an InSb nanowire, three quantum dots are defined to the side of superconducting contacts by fine gates (indicated by yellow lines). Quantum dots defined this way have weaker but gate-tunable coupling to superconductors compared to the triple-dot design used in Fig. 5.1. (V_L, V_M,

V_R) are plunger gate voltages tuning potentials in the left, middle, and right dot (D_L, D_M, D_R). All three electrodes are superconducting NbTiN. The middle lead has a small triangular contact to reduce stress. Transport measurements are performed using the two outer leads as the source and drain while floating the center lead. Lack of non-superconducting leads may result in additional resonances in spectra and complicate the interpretation of the triple-dot states [109].

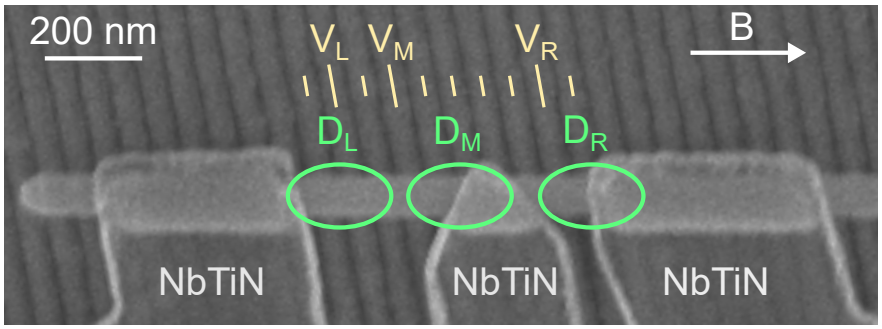

Figure 5.15: SEM of another triple-dot device with a different design in which quantum dots are defined to the side of superconducting leads.

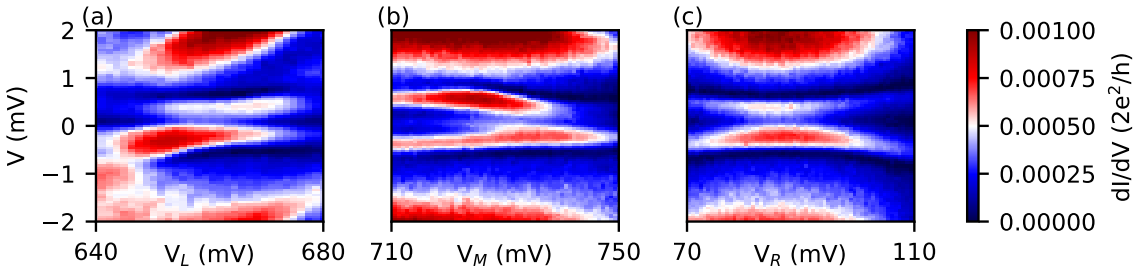

Figure 5.16: Bias spectroscopy of (a) D_L, (b) D_M, (c) D_R, B=0. Anti-crossing resonances indicate Andreev bound states in all three dots have singlet ground state with even parity.

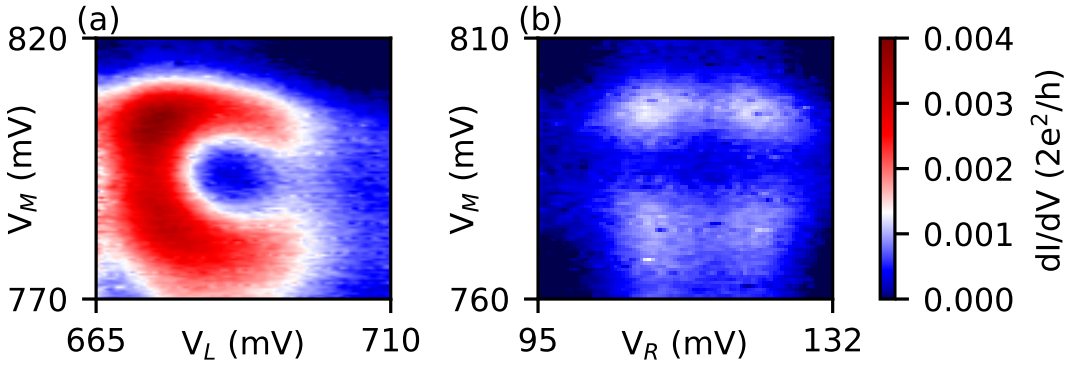

Figure 5.17: Stability diagrams of dot pairs (a) D_L-D_M, at 0.25 mV, and (b) D_M-D_R, at 0.3 mV. B=0.

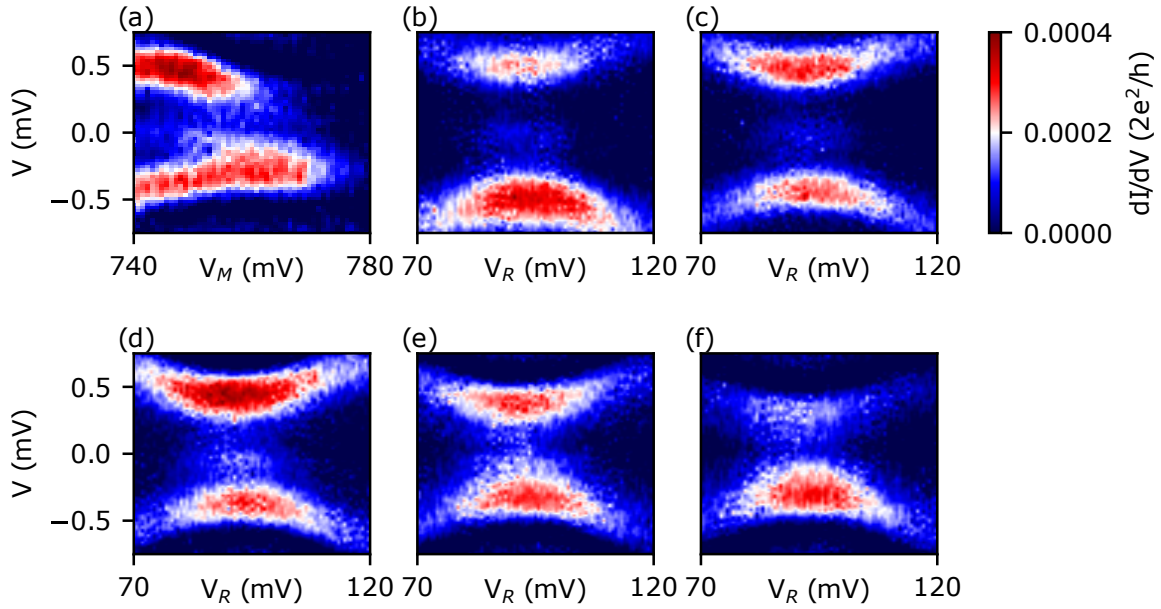

Figure 5.18: Bias spectroscopy of D_R with different V_M, at B=0. (a) dI/dV vs. V_M as a reference for V_M settings in the rest panels. (b-f) $V_M = 730, 740, 750, 755, 760$mV.

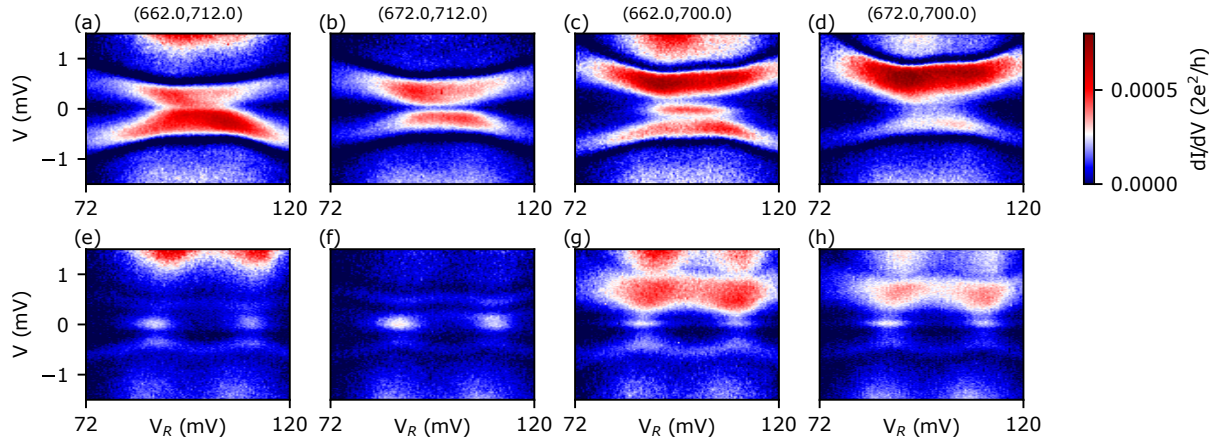

Figure 5.19: Bias spectroscopy of D_R with different (V_L, V_M), at (a-d) B=0 and (e-h) B=0.2T. Gate settings of (V_L, V_M) in mV are listed on top of each column. From B=0 to B=0.2T, ground state transition from singlet to doublet [91].

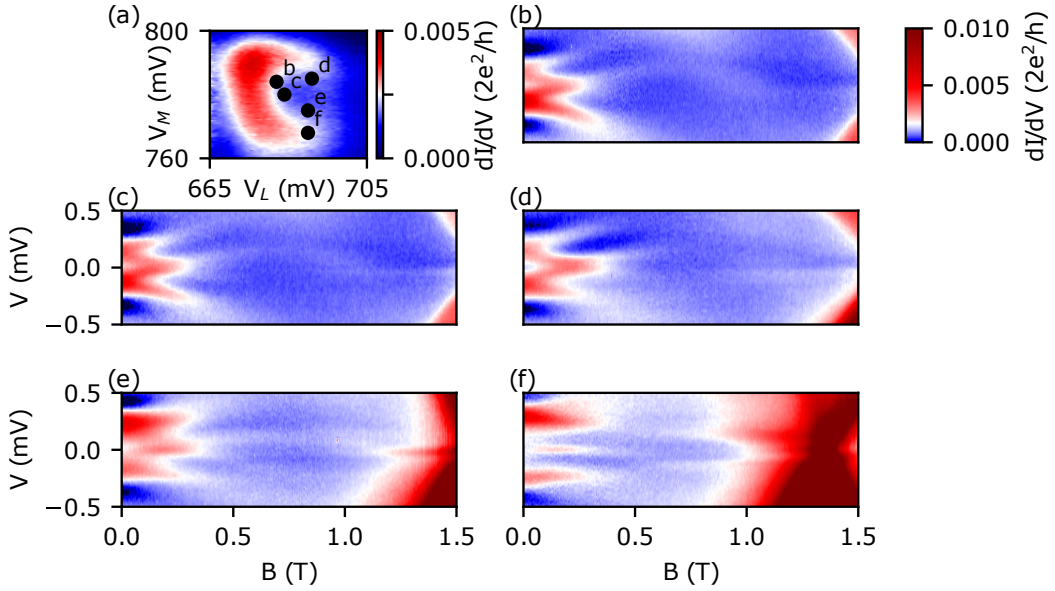

Figure 5.20: Magnetic field evolution of the triple-dot Andreev bound states at different gate configurations. (a) Stability diagram of V_L-V_M, as a map for gate configurations used in the rest panels. V_R is kept the same during the measurement. (b-d) The evolution resembles Zeeman splitting of trivial Andreev bound states. (e-f) A short and extensive zero-bias peak appears.

5.8 Conclusions

Two conclusions can be drawn from our study.

First, our measurement technique can help identify where the states that generate zero-bias peaks are localized along the chain. Therefore, applying this technique in future devices will lead to the successful identification of the Kitaev chain regime.

Second, despite a large degree of control over Andreev states in multiple dots, the devices we made here are still off from the Kitaev chain regime. Superconducting gap surviving to higher magnetic fields and further optimized coupling between the nanowire and the superconductor are desired. The limit to which we could push these measurements toward the Kitaev chain mirrors efforts to realize Majorana modes in continuous 'bulk' nanowires and faces similar challenges.

A more nuanced discussion of limiting aspects follows. Tunnel barrier gates have steep gate traces making it harder to tune the chain in a balanced way, as the current through the chain is sensitive to all barrier gates, and the same for inter-dot couplings. Leaving some barriers open limits the ability to use all five contacts of the device as probes, since some probes do not have high barriers between them. In future devices, reducing the width of barrier gates can help by reducing gate lever arms and increasing the maximum possible inter-dot coupling.

Another limitation of our design is that the coupling between dot and superconductor is fixed. Due to weaker coupling between D_3 and S_3, Andreev states in D_3 behave differently in magnetic fields. An important regime to study in the future is where zero energy crossings of all three dots happen closely in magnetic fields. This requires either identical dots or larger tunability of dot-superconductor coupling. Intuitively, we want maximal coupling of quantum dots to superconductors in order to have the largest induced gap such that the parameter window for hosting the topological phase is maximized. However, it may be beneficial to have a fixed or a tunable tunnel barrier between the semiconductor and the superconductor in practice. In Sec. 5.7.2, we show another device design with triangular NbTiN electrodes where dots are defined to the side of contacts as a way to control dot-superconductor coupling.

Collectively, these limitations make clear that within this design and fabrication method, realizing chains longer than three dots is increasingly challenging. Well-separated Majorana zero modes are not expected for a chain of three dots outside of fine-tuned regimes, i.e., when Andreev states from all three dots reach zero bias at the same magnetic field (see simulation results in Sec. 4.3).

On the other hand, realizing Majorana zero modes with a few quantum dots may be less challenging than a simple chain model suggests. The total length of our triple-dot device is more than 1μm, which would be sufficient to separate Majorana modes in a continuous nanowire with a 'bulk' topological phase [83, 110, 111]. The length of each dot is $\approx$200 nm, comparable to spin-orbit-interaction length of InSb [54, 55]. Each dot can be treated as one short wire section, in which Andreev bound states can be partially separated into Majorana modes [112, 113]. Several models already considered multiple segments of topological superconductor that couple through tunnel gates [107, 108, 105, 114], which hybridizes inner Majorana modes on each dot, leaving the outer ones unpaired, similar to the original Kitaev proposal [31].

Advances in materials synthesis and improvements in processing and nanofabrication may help resolve some issues discussed above. In-situ techniques for superconductor deposition can achieve uniform contacts and cleaner superconductor-semiconductor interfaces [64, 71, 93]. Selective-area grown (SAG) nanowires [76, 77] with carefully designed shadow wall structures present a promising platform for scaling up to longer chains [72, 73, 78]. Superconducting materials with large and hard gap can be used, such as Sn [115] or Pb [116]. With hard superconducting gap persisting in a much larger magnetic field, Andreev resonances can still be prominent and in high contrast.

6.0 Indium antimonide nanowires with tin shells

6.1 Introduction

As we enter the era of intermediate-scale quantum circuits [117, 118], materials considerations come into renewed focus through their impact on quantum gate fidelity. The most successful solid-state approaches rely either on superconductors [2], or on semiconductors [119], with the future topological platform to require a hybrid of both [98]. The search continues for the ultimate material capable of delivering low intrinsic decoherence. In this context, the push for qubits based on Majorana zero modes that are expected to be topologically immune to decoherence [120, 29, 121, 122] has accelerated the discovery of high-quality interfaces between superconducting metals and low-dimensional semiconductors [64, 123, 71, 124]. Only a few superconductors were explored for Majorana qubits, most notably aluminum which is also the material of choice for transmon quantum processors [117]. Among the advantages of aluminum are its' self-limiting native oxide and a hard induced gap in proximate semiconductors [64, 67, 62, 71]. Due to this, aluminum is widely known to exhibit 2e charging in small islands, a fundamental property that makes it a low-decoherence superconductor [125, 126, 127, 128, 129, 68, 130, 73]. Among the disadvantages of aluminum are a relatively small superconducting gap equivalent to 1 K, and a low critical magnetic field. This confines quantum computing to ultra-low temperatures and even further constrains the design of future topological qubits, which will require a precise balance of several energy scales [131].

Our study on Indium Antimonide nanowires with tin shells is published on [115].

6.2 Experimental results

We report induced superconductivity in InSb nanowires [59, 50] with Sn shells. InSb is the highest electron mobility group III-V semiconductor with strong spin-orbit coupling [54]

and large Landé g-factors in the conduction band [56]. These are the primary ingredients of the Majorana recipe [25, 26], making InSb an optimal material for the investigation of induced topological superconductivity [27, 132, 82, 133].

We find that InSb nanowires coupled to tin exhibit a hard induced superconducting gap up to 700 μeV. Superconductivity persists to a significant magnetic field, up to 4T for 15 nm thick Sn shells. Islands of tin do exhibit 2e-periodic charging patterns. This effect is a landmark requirement for topological quantum computing and transmon qubits, as it is a prerequisite for long quasiparticle stability times. Fluctuations of the quasiparticle number on superconducting islands scramble qubit readout, while quasiparticle hopping between islands is a source of decoherence [120, 29, 121, 122, 134]. Results are obtained even though Sn and InSb exhibited no epitaxial relationship, which was previously viewed as essential [67, 71].

We study electron tunneling into Sn through InSb in the normal metal-superconductor (N-S) configuration. For this, we need a nanowire with only one end covered by Sn. We use the uncovered end to define a tunnel barrier and an N-contact. In order to avoid damage to InSb that results from etching away part of the Sn shell, we employ in-situ nanoscale shadowing [71, 73]. An InSb flake stands in front of the nanowire, shadows the bottom of the wire during deposition of Sn in ultra-high vacuum [135] (Fig. 6.1 (A)). We expect that junctions defined by wet etching or lift-off would yield similar results [136, 137].

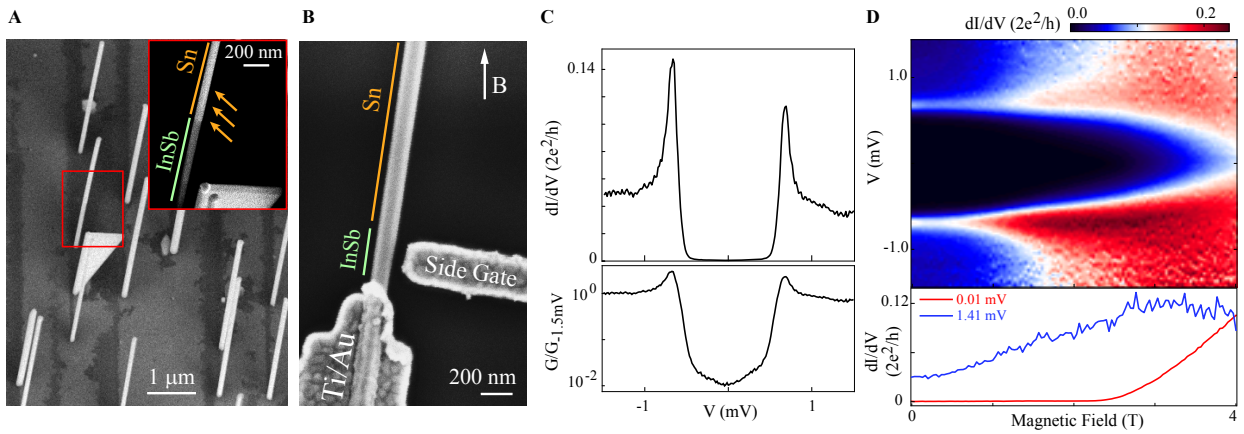

Figure 6.1: (A) Scanning electron micrograph (SEM) showing a triangular InSb flake that stood in the path of a beam of Sn atoms, shadowing the InSb nanowire in behind. Dark streaks on the InSb substrate are also due to shadowing of the Sn beam by nanowires and flakes. The inset shows the direction of Sn beam and indicates the shadowed and exposed segments of the nanowire. (B) SEM of an N-S device (device A) with a flake-shadowed Sn-InSb nanowire and Ti/Au contacts and a side gate. Magnetic field is in the plane of the sample as shown by the arrow. (C) Zero magnetic field tunneling conductance spectrum of device A in linear scale (top) and logarithmic scale (bottom), $V_{BG} = 7.5$ V, $V_{SG} = -0.4$ V. (D) Magnetic field evolution (top) of the zero-field spectrum shown in panel (C). Line cuts at two specific source-drain bias voltages are shown in the bottom.

The nanowire with Sn shell is positioned onto a doped Si/SiO_x substrate which is used as a back gate (BG) shown in Fig. 6.1 (B). A side gate (SG) is used to define and tune the tunnel barrier near the edge of the tin-free segment. In Fig. 6.1 (C), the tunneling spectrum reveals a two-orders-of-magnitude suppression in conductance around zero bias. The hard gap indicates the elimination of decoherence pathways due to disorder and spurious subgap states. A superconducting tunneling peak is at ± 680 μeV, which is comparable to the gap of tin. In magnetic fields, the hard gap is found to persist beyond 2T, with the gap "softening" at higher fields and fully closing around 4T, shown in Fig. 6.1 (D). Magnetic field resilience is an indicator of a thin uniform shell, and this resilience is another advantage of Sn since

topological, spin, and some superconducting qubits operate at high magnetic fields.

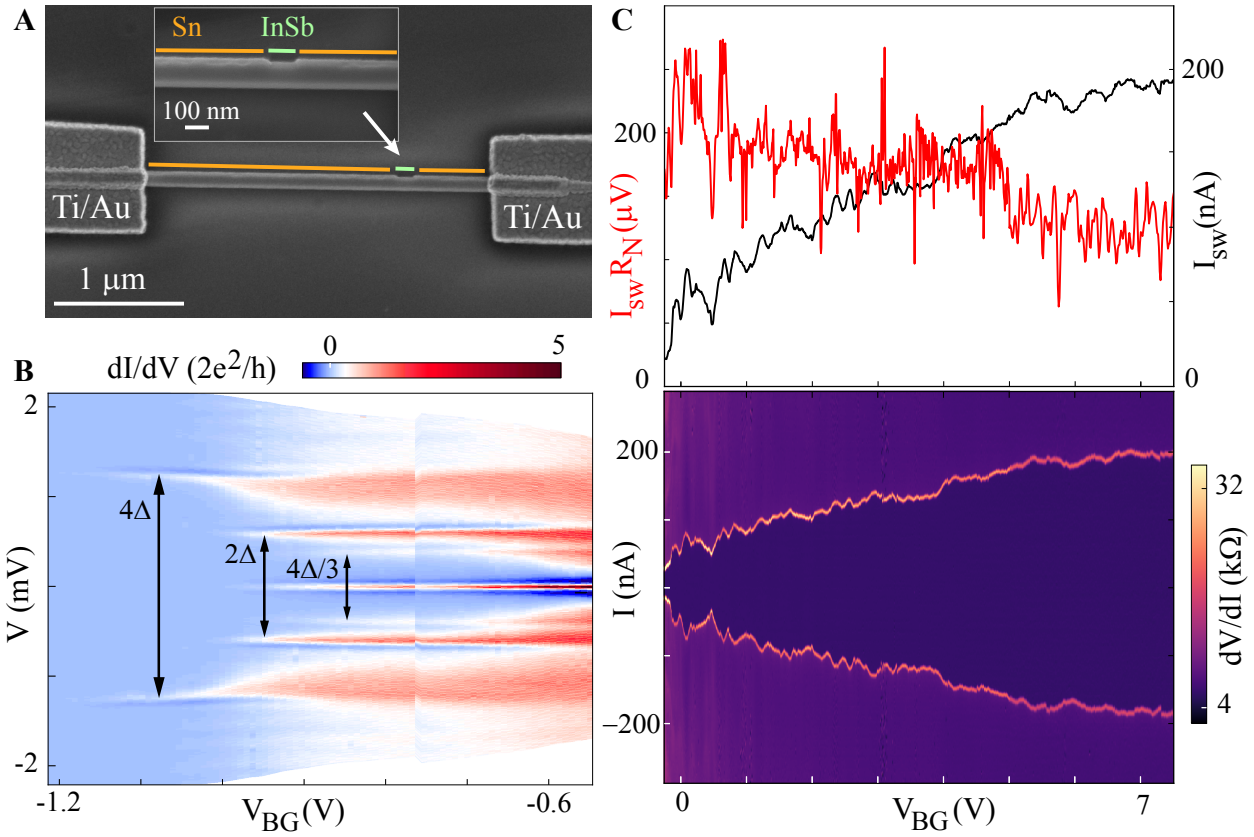

Figure 6.2: (A) SEM of device B (S-S device). Inset zooms in the shadow junction where Sn shell is visible. (B) Differential conductance as a function of source-drain voltage bias V and back gate voltage, V_{BG}. The double arrows mark resonances at 4Δ, $4\Delta/2$ and $4\Delta/3$. (C) Differential resistance as a function of current bias I and V_{BG} (bottom). Top panel shows extracted switching current I_{sw} (black) and $I_{sw}R_N$ (red) as a function of back gate voltage.

Fig. 6.2 (A) shows a superconductor-superconductor (S-S) device with both ends of the nanowire covered by tin and only a narrow break in the shell to define an InSb weak link. For this, we use a previously developed method of shadowing by crisscross nanowires [71]. We study tunneling between two tin islands. In Fig. 6.2 (B), we observe a smooth nanowire pinch off void of accidental quantum dot states. Three finite-bias resonances are observed, marked 4Δ, $4\Delta/2$, and $4\Delta/3$. This sequence is a manifestation of Multiple Andreev Reflection

processes, which are characteristic of transparent S-S junctions. They correspond to 615 μeV $\pm$ 10 μeV, which is somewhat smaller than the gap observed in the N-S device (Fig. 6.1 (C)). At $V_{BG} < -1$ V, only the 4Δ resonance is observed. We interpret this as the superconducting tunneling regime. Because the S-S tunneling resonance is a peak in current, it appears as a peak-dip structure in conductance.

The resonance at zero bias in Fig. 6.2 (B) is the Josephson supercurrent. This effect is best studied in the current-bias configuration (Fig. 6.2 (C)). The switching current (I_{sw}) from superconducting to normal state is a peak in differential resistance. I_{sw} decays smoothly with more negative V_{BG}. The current-voltage characteristics are weakly hysteretic, which is reflected in the asymmetry of I_{sw} in positive and negative current bias. In magnetic fields, the Josephson effect is observed up to 1.5 T and remains significant with sharp switching up to 0.5 T (Fig. 6.8). This significant field range is a positive development for schemes that require coupling and decoupling of topologically superconducting islands at a finite magnetic field for Majorana fusion or braiding [30, 105]. Measurements on continuous-shell nanowires without shadow junctions yielded supercurrents in the range $20 - 30$ μA corresponding to the critical current density of 2×10^6 A/cm^2 (Fig. 6.11). The extracted products $I_{sw}RN$ (R_N is the normal state resistance) are in the range $125 - 225$ μeV, which is significant, and of the same order of magnitude as the gap.

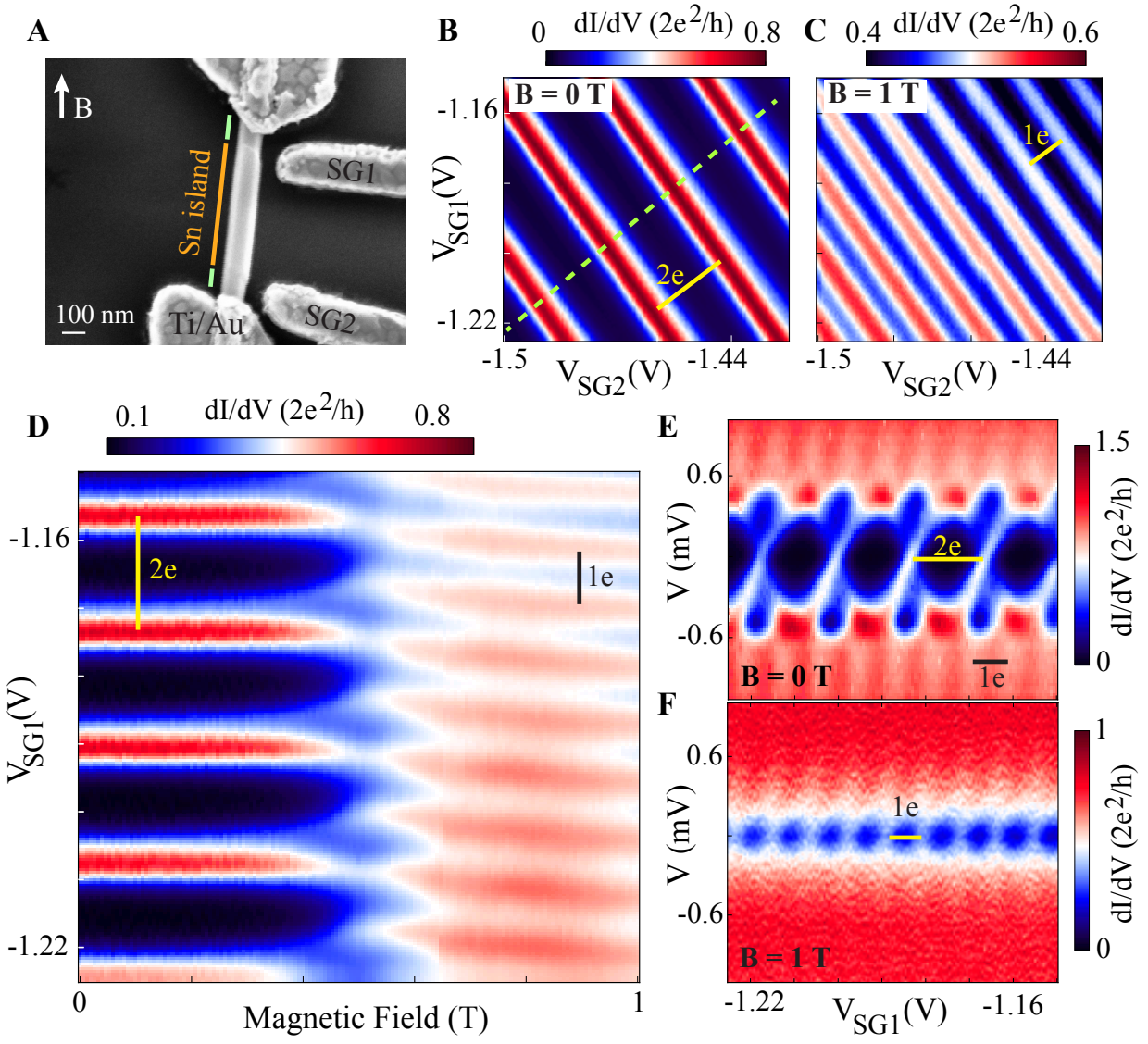

Figure 6.3: (A) SEM of device C showing the Sn island, two shadow junctions with bare InSb, side gates SG1 and SG2, and Ti/Au source-drain contacts which cover the outside Sn segments and suppress superconductivity there. (B-C): 2e and 1e tunneling conductance resonances measured at $V = 0$ at B = 0 T and B = 1 T, respectively. (D) Magnetic field evolution of conductance along the dashed cut in panel (B). (E-F): V vs. gate spectroscopy at B = 0 T and B = 1 T, respectively. The duration of data acquisition for each panel is of order 1 hour, and the parity pattern is reproducible over days.

In Fig. 6.3, we present key findings on 2e charging of a tin island. The island is defined between two nanowire-shadow junctions in the N-S-N geometry (Fig. 6.3 (A)). At zero magnetic field, we observe a single family of Coulomb peak resonances consistent with charging the entire island (Fig. 6.3 (B)). At a finite magnetic field of 1 T, the frequency of Coulomb resonances doubles (Figs. 6.3 (C-D)). We attribute data at zero field to 2e charging, and data at finite field to 1e charging. The transition from 2e to 1e is due to the superconducting gap or the lowest subgap state dropping in energy below the charging energy, which we estimate to be 0.3 meV (Figs. 6.3 (E-F)). At finite magnetic field, it costs less energy to add electrons to the island one by one, while near zero field, due to hard gap superconductivity, it is advantageous to add electrons in pairs.

The two-electron charging effect is central for topological quantum computing because the states of a topological qubit are distinguished by even/odd island charge parity. If only 1e charging periodicity were observed, it would mean that despite a well-defined superconducting gap, electrons can be added to an island one at a time, and the ability to distinguish the states of a topological qubit is scrambled. 1e periodicity is also detrimental for transmon qubits where single-electron tunneling is a decoherence mechanism [134].

Tin is an unusual material that has two different crystal phases with a phase transition at 13°C. The low-temperature α-Sn has a diamond cubic lattice, while the high temperature β-Sn is tetragonal. The electronic properties of both phases are very different. α-Sn is a semimetal that can also be a topological insulator in monolayer form [138, 139, 140], whereas β-Sn is a metal with a superconducting transition temperature of 3.7 K.

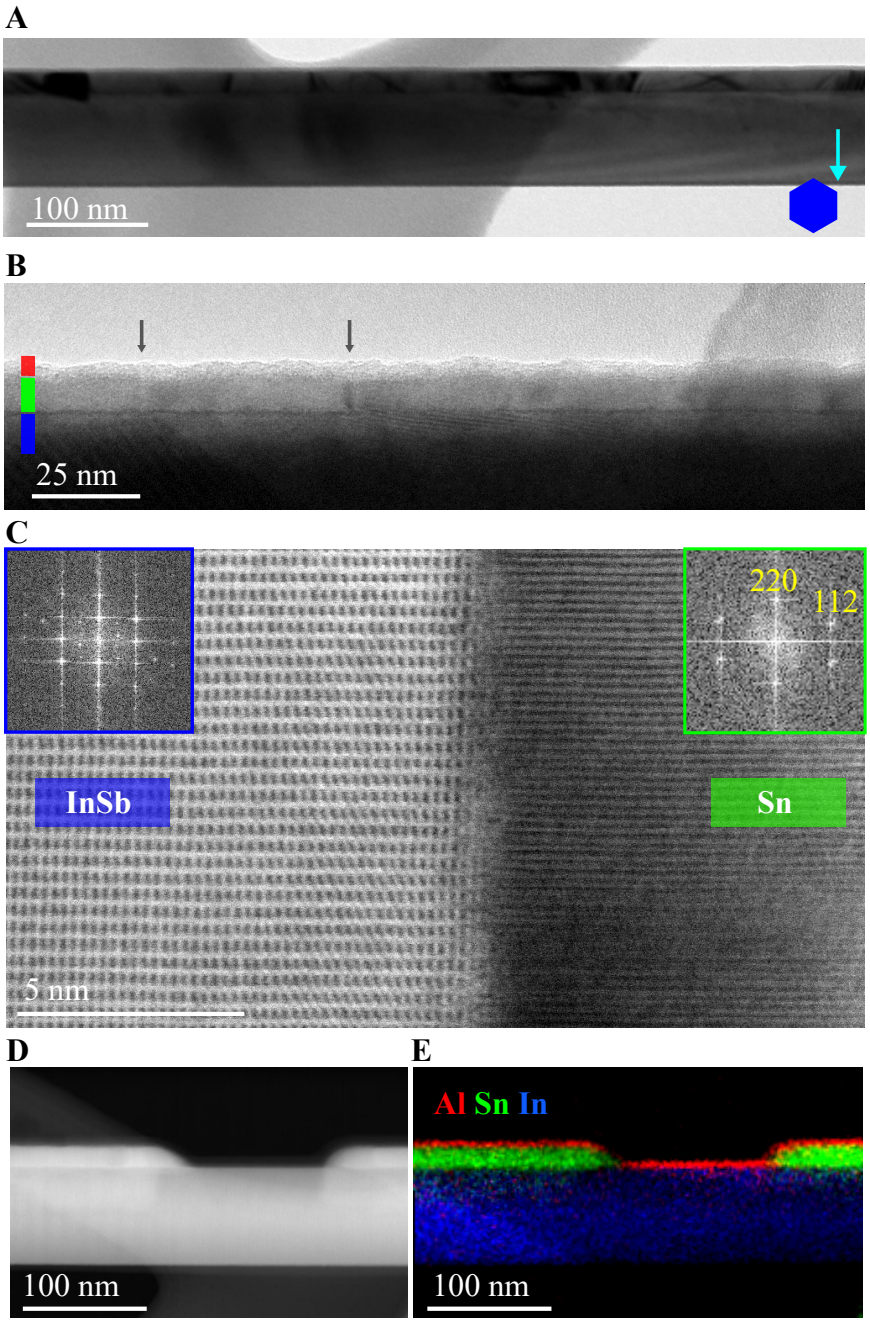

Figure 6.4: (A) Side-view TEM image along the ⟨112⟩ zone axis showing a homogeneously thin shell. (B) Higher magnification TEM of the AlO_x (red) - Sn (green) - InSb (blue) stack. Arrows highlight the Sn grain boundaries. (C) HR-STEM image of the Sn-InSb interface. The insets show Fourier transforms to the left and the right of the interface. (D) High-angle annular dark-field STEM image of a shadow junction. (E) EDX elemental mapping of the shadow junction in (D). The Al-rich layer (red) corresponds to AlO_x, oxygen not shown for clarity.

For tin on InSb nanowires, we assess the structural properties and elemental distribution using transmission electron microscopy (TEM). TEM images reveal a polycrystalline Sn shell of uniform thickness around the InSb nanowire (Fig. 6.4 (A)): the shell features grains of sizes 25 × 25 nm to 50 × 60 nm (Fig. 6.12). The Sn-InSb interface is abrupt, and some Sn grains show epitaxial relationship with InSb. The high-resolution annular bright field-scanning TEM image (Fig. 6.4 (C)) shows a section of the interface where the {111} planes of zincblende InSb are aligned with lattice planes of a Sn grain with a lattice distance of 2.04 Å. This matches the {220} interplanar distance of β-Sn. This grain is one of thirteen analyzed along the same nanowire. Eleven of the grains are identified as β-Sn from the fast Fourier transform analysis of the interplanar distances (Fig. 6.4 (C), inset). Only two of those β-Sn grains show a preferential epitaxial relationship with InSb. In contrast, α-Sn is lattice-matched to InSb and can grow epitaxially [141]. The predominantly β-Sn shell observed at room temperature by TEM agrees with superconductivity observed at low temperatures, suggesting that no phase transformation of Sn occurred upon device cooldown.

In addition to the uniform shell thickness, the nanowire shadow junctions used in S-S and N-S-N devices are sharp, with Sn islands defined abruptly on each side of the junction (Fig. 6.4 (C)). Energy-dispersive x-ray spectroscopy (EDX) confirms that the Sn islands are isolated from each other, and no interdiffusion between Sn and In is detected (Fig. 6.4 (D)). A uniform 3-nm-thick AlO_x passivation layer covers the entire nanowire, this layer maintains integrity and smoothness of the shell on the scale of at least three months. Oxidation at the Sn-InSb interfaces is not detected but cannot be fully excluded (Fig. 6.13).

Data are available at [142].

6.3 Materials and methods

Nanowire growth: InSb nanowires are grown using the vapor-liquid-solid technique in a horizontal metal-organic vapor phase epitaxy reactor. The first nanowires used in this work are stemless InSb nanowires with flakes as shadow objects (Fig. 6.1 (A)) [59, 135]. Both InSb nanowires and flakes are grown on an InSb (111)B substrate with a selective-area mask

and gold as catalyst.

The second type of nanowires, shown in FigS. 6.2 (A) and 6.3 (B) are shadowed by other nanowires [71]. The InP (100) substrates are etched to expose the two {111}B facets, on which gold particles are deposited with an offset on the two opposing facets of a trench. Nanowires grow towards each other, such that the front wire shadows the back wire. InSb wires are grown on InP stems.

Sn shell growth: After transiting in air, nanowire chips as grown are loaded in vacuum for subsequent growth of Sn shells. The chips are gallium bonded to 3.3 mm thick, 90 mm diameter molybdenum blocks. The absence of a native nanowire surface oxide is expected to be essential in aiding in inducing a hard superconducting gap [64, 123, 71]. In order to remove the native InSb oxide, atomic hydrogen cleaning is performed in a UHV chamber with a base pressure $< 1 \times 10^{-10}$ Torr at 380°C (thermocouple temperature) for 30 minutes, at an operating pressure of 5×10^{-6} Torr consisting primarily of hydrogen ambient [71]. Once cleaned, the samples are transferred in-vacuo to an ultra-high vacuum chamber dedicated for metal evaporation (base pressure $< 5 \times 10^{-11}$ Torr). Here, the nanowire samples are cooled to 85 ± 5K (-188 ± 5°C) for 2 hours, prior to tin evaporation. 15-nm-thick tin is then evaporated from an effusion cell at a growth rate of 7.5 nm/hr and an evaporation angle close to 60° from sample normal. This shallow evaporation angle aids the in-situ formation of Sn islands with nanowire or flake shadows. After Sn evaporation, while the sample is still expected to be at cryogenic temperatures (due to the thermal mass of the molybdenum block), it is moved to an interconnected UHV chamber for the electron-beam evaporation of a 3-nm-thick shell of AlO_x, at normal incidence. This is done to prevent coagulation of the evaporated tin layer on InSb nanowires (See Figure S10). The samples are then allowed to warm up to room temperature in vacuum.

Device fabrication and measurements: Device fabrication is similar to previous work on wires with epitaxial Al film [71]. We made global back gate substrates with doped and thermally oxidized Si wafers, then covered them with 15nm HfO_x to get a better dielectric layer. Wires are transferred onto substrates using a micromanipulator under an optical microscope. Contacts and gates are patterned by electron-beam lithography by curing the resist at room temperature in a vacuum chamber (operating pressure $< 1 \times 10^{-4}$ Torr) to avoid nanowire

heating and potential interdiffusion of Sn and In. Ar ion milling is performed to remove the AlO_x layer before evaporating 10/150 nm of Ti/Au. Measurements are performed in a dilution refrigerator with a 30 mK base temperature using a combination of direct current and lock-in techniques. All voltage bias data are two-terminal measurements. A series resistance of ≈ 5 kΩ due to measurement setup was taken into account in calculating conductance in all figures as well as renormalizing V axis in Figs. 6.2 (B), 6.5, 6.6 (A). TEM studies were performed using a probe corrected microscope operated at 200 kV, equipped with a 100 mm^2 EDS detector.

6.4 Supplementary data

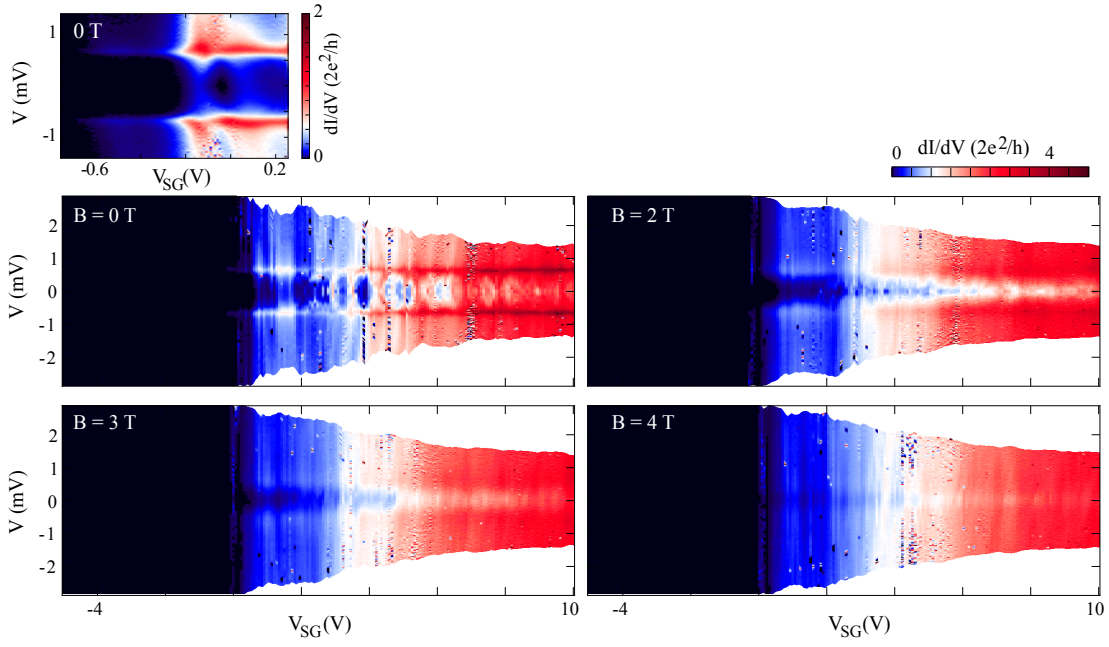

Figure 6.5: Additional gate dependence data for flake-shadowed device A studied in Fig. 6.1. The zero-field hard gap regime displays the presence of a quantum dot in the vicinity of a tunnel barrier. A soft gap is observed for higher magnetic fields up to 4T. $V_{BG} = 7.5$ V.

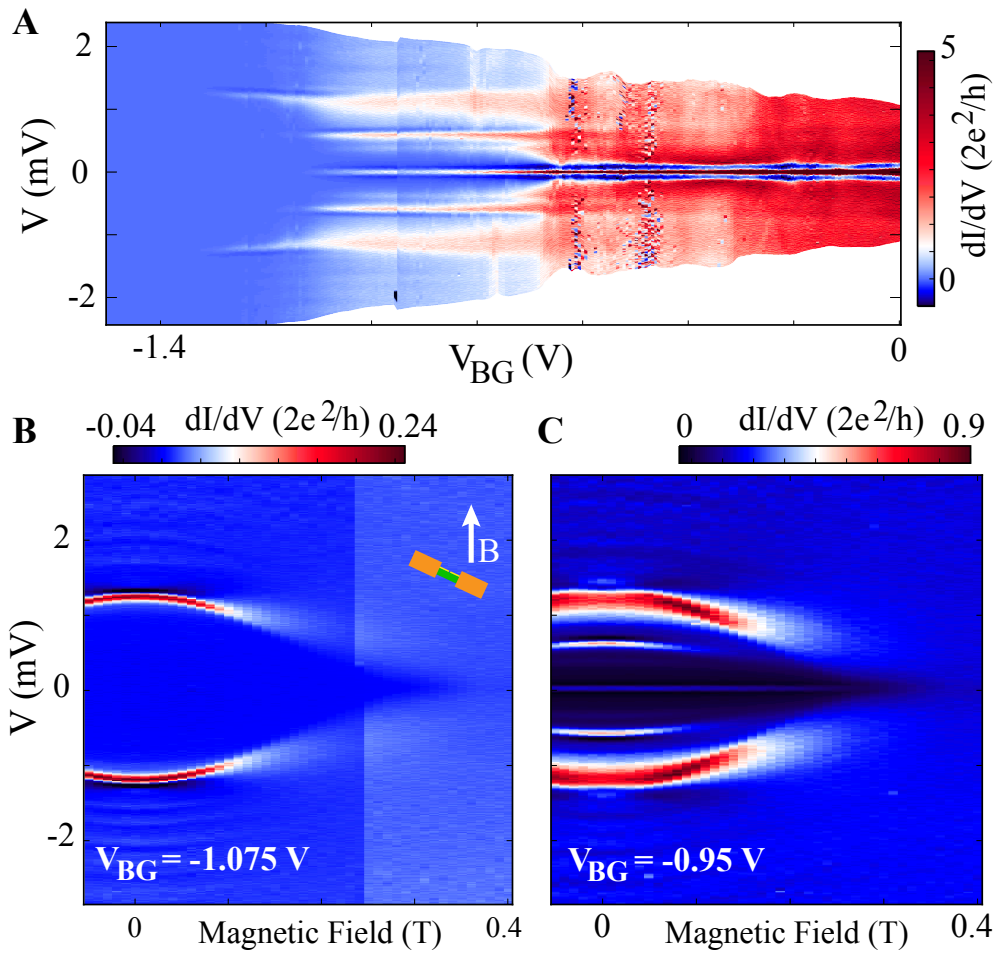

Figure 6.6: Additional data for device B studied in Fig. 6.2. (A) Differential conductance as a function of bias voltage and back gate voltage in the extended gate range compared with Fig. 6.2. (B) and (C) show magnetic field dependence at $V_{BG} = -1.075$ V, and $V_{BG} = -0.95$ V, respectively. This device is at $\approx 60°$ angle with magnetic field, and as a result, the gap closes at B ≈ 0.4 T, a lower field than in devices that were aligned parallel to the field, e.g., Fig. 6.1.

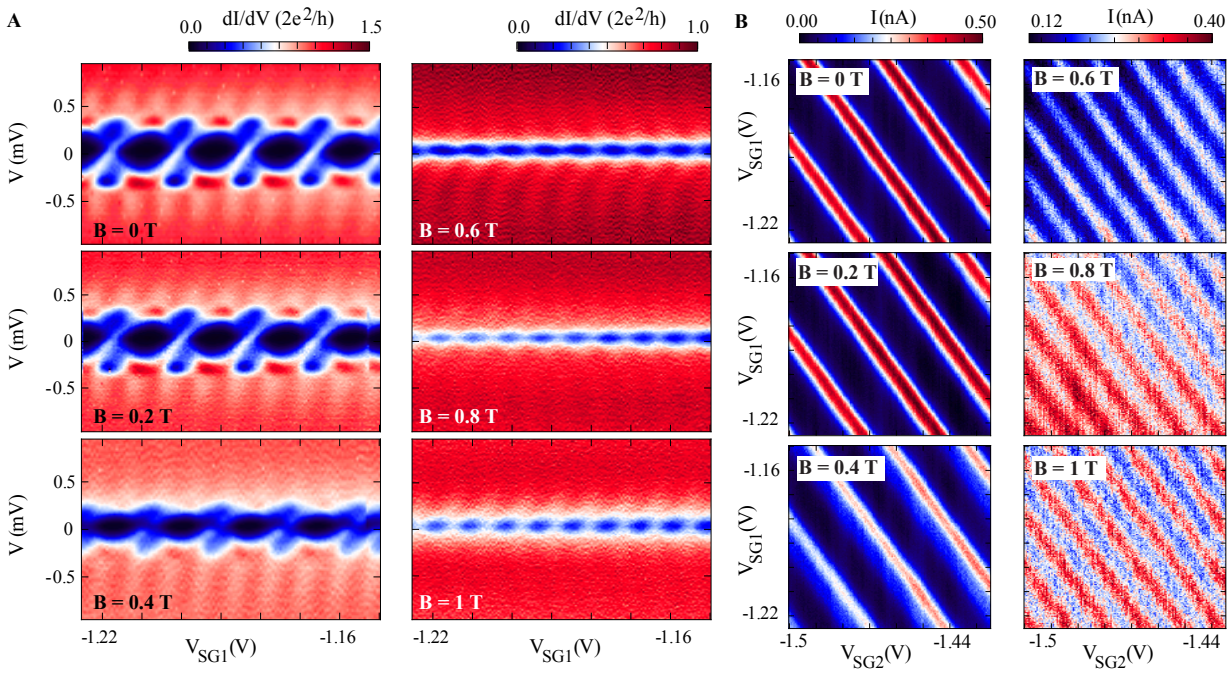

Figure 6.7: Additional data for device C studied in Fig. 6.3. (A) Bias vs a combination of SG1 and SG2 at different magnetic fields, in the same regime as Fig. 6.3 (E). (B) Gate dependent DC current measured at 10 μV bias. The gates are scanned in the same regime as Fig. 6.3 (B).

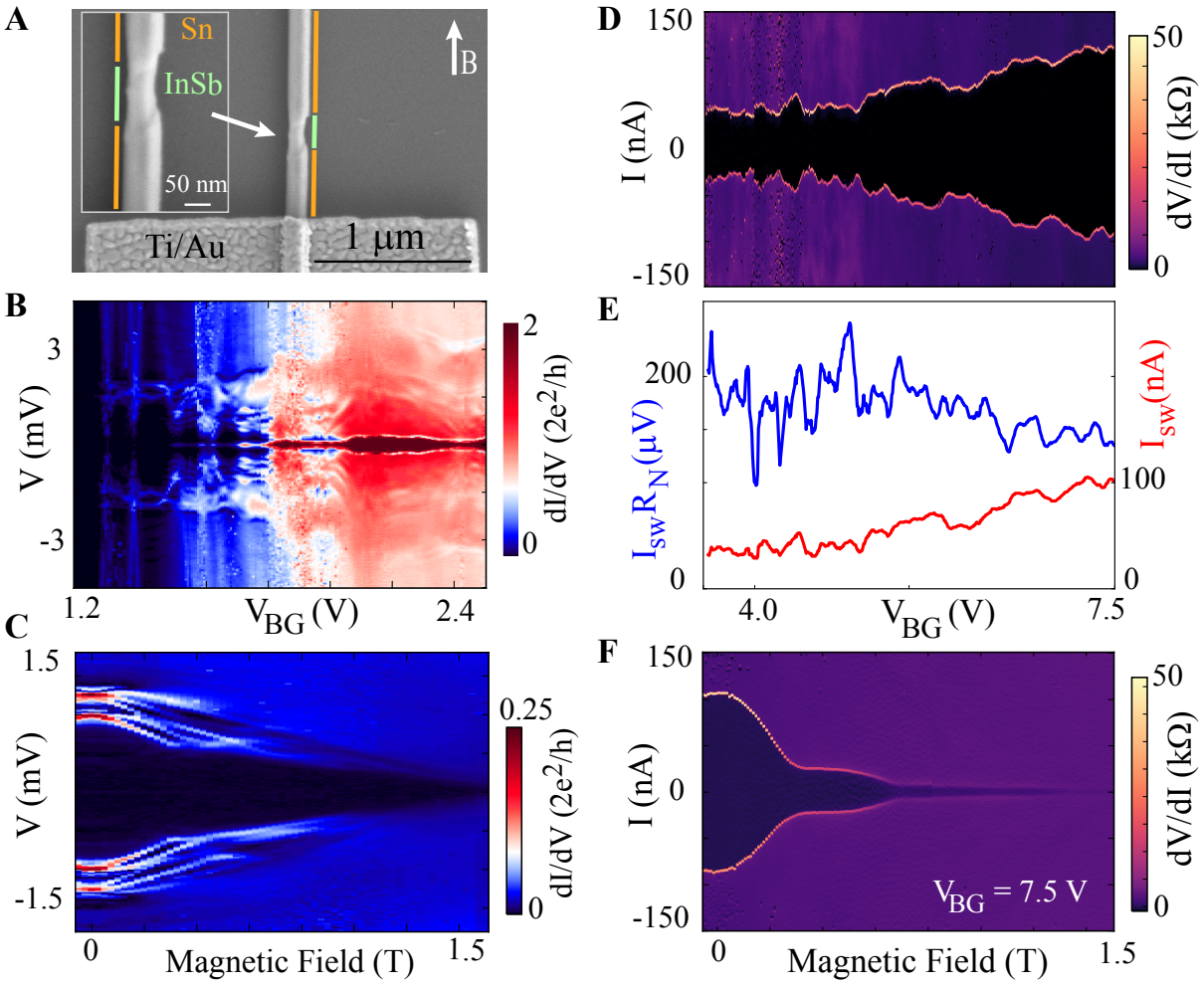

Figure 6.8: (A) SEM image of device D with a nanowire shadow-defined break in the Sn shell. (B) Differential conductance as a function of bias voltage and back gate voltage. (C) Andreev bound states evolution in parallel magnetic fields at $V_{BG} = 1.4$ V. (D) Current bias measurement in the more positive back gate regime. (E) Extracted $I_{sw}R_N$ (blue) and switching current I_{sw} (red) as a function of back gate voltage. (F) Magnetic field dependence of critical current.

Fig. 6.8 shows the characteristic of an S-S device D. The electron beam resist was baked to 175°C in the process of making this device. Magnetic field is applied parallel to this

device. Differential conductance as a function of bias voltage and back gate voltage in Fig. 6.8 (B) shows an evolution from the supercurrent regime at more positive V_{BG} to the quantum dot regime for more negative V_{BG}. V axis is as measured and not renormalized due to series resistance. Fig. 6.8 (C) shows Andreev bound states evolution in parallel magnetic fields at $V_{BG} = 1.4$ V. The resonances never reach zero bias due to the hard gap. However, at $B = 0.3 - 0.4$ T, the finite bias resonances exhibit kinks. These are the points where Andreev bound states cross zero chemical potential and undergo a ground state quantum phase transition. Resonances are shifted by $\pm\Delta(B)$ in $\pm$ bias [109]. In an N-S device, a zero-bias peak would have been observed instead of finite-bias kinks. The superconducting gap remains open to 1.5 T in this device. Fig. 6.8 (D) shows the gate evolution of the supercurrent. Fig. 6.8 (E) shows the extracted $I_{sw}R_N$ (blue) and switching current I_{sw} (red) as a function of back gate voltage. Magnetic field dependence of critical current is shown in Fig. 6.8 (F). Josephson effect persists up to 1.5 T. This is consistent with the magnetic field decay of the induced gap (Fig. 6.8 (C)). Previously, rapid decay of supercurrent in InSb nanowires was reported on the scale of 100 mT [143]. It was explained in the context of interference of supercurrent carried by multiple occupied subbands. Here, supercurrent remains significant up to 0.5 T. This can be due to shorter junctions studied, enhanced magnetic field screening by the Meissner effect in the Sn contacts, or a lower subband occupation.

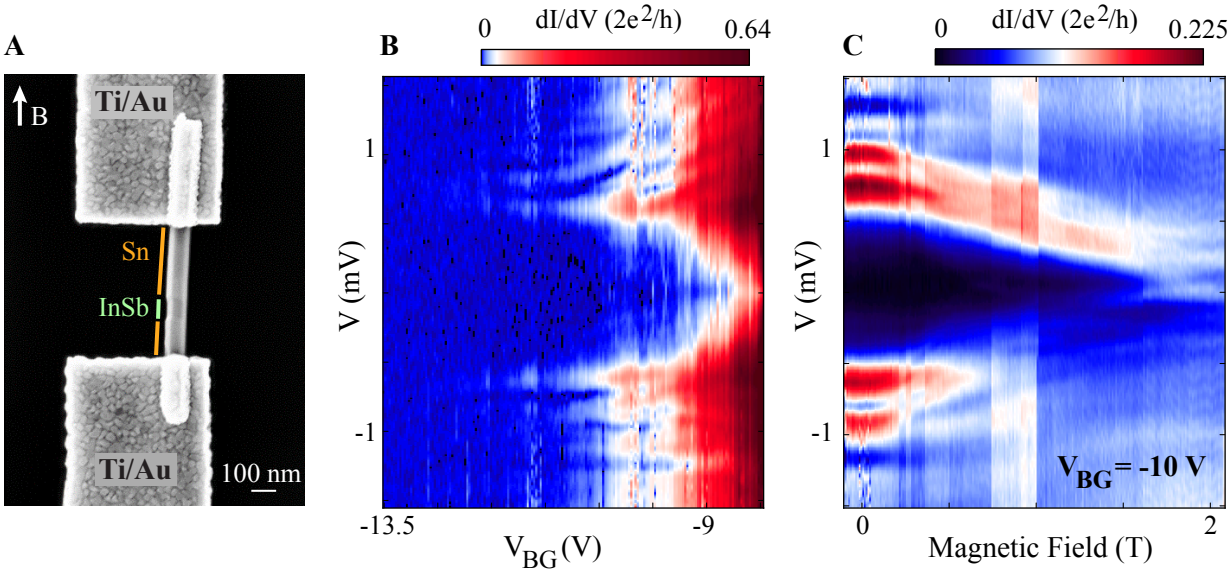

Figure 6.9: (A) SEM image of device E, a single shadow S-S device. The nanowire is aligned parallel with magnetic field. (B) Differential conductance as a function of bias and back gate voltages. V axis is as measured and not renormalized due to series resistance. (C) Magnetic field evolution of conductance at $V_{BG} = -10$ V. Near $B = 1.75$ T a zero-bias conductance peak emerges from the coalescence of two higher bias resonances. At these high magnetic fields, the induced gap is soft, allowing for conductance at low bias, including the zero bias. The zero-bias peak is approximately 0.1 $2e^2/h$. We attribute this peak to a trivial zero-bias crossing by subgap Andreev states.

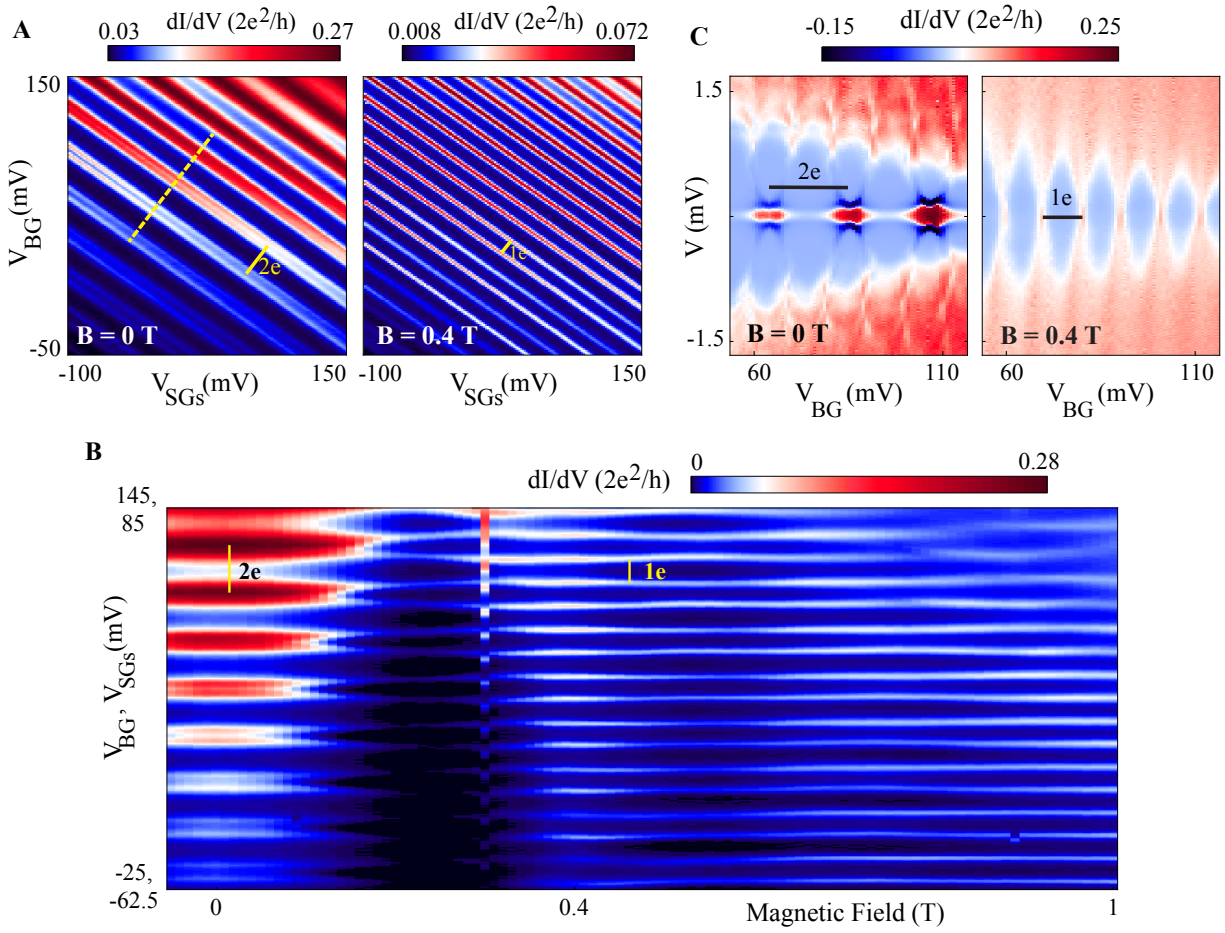

Figure 6.10: (A) Zero-bias conductance showing a 2e-periodic pattern of resonances at zero field and an 1e-periodic pattern at B = 0.4 T. (B) Magnetic field evolution showing a transition from 2e-periodic to 1e-periodic pattern at finite field. (C) Differential conductance as a function of bias voltage and a combination of back gate and side gate voltages along the yellow dashed line in panel A.

Device F is a two-shadow device of similar geometry to device C in Fig. 6.3, however, with a short Sn island of the order 100 nm. For this device, like device D, the electron beam resist was baked at 175°C in the process of making side gates and contacts. Like device C, device F has two side gates aligned with the shadow junctions and a back gate. In contrast to device C, which is in the N-S-N configuration, device F is in the S-S-S configuration,

with the center Sn island having two superconducting leads due to the Sn shell. Nanowire F is at a 30° angle with magnetic field. In Fig. 6.10 (A), zero-bias conductance showing a 2e-periodic pattern of resonances at zero field and a 1e-periodic pattern at B = 0.4 T. Note that some resonances appear split at zero magnetic field. This is due to a subgap state that is lower in energy than the charging energy [130]. In Fig. 6.10 (B), magnetic field evolution shows a transition from 2e-periodic to 1e-periodic pattern at finite field. Fig. 6.10 (C) shows differential conductance as a function of bias voltage and a combination of back gate and side gate voltages along the yellow dashed line in (A). On the left, a zero-field scan reveals that the zero-bias conductance resonances are due to supercurrent through the S-S-S device, which here manifests as zero-bias conductance peaks due to a voltage-bias measurement [144]. At finite field (right) a pattern of Coulomb diamonds is observed, and no supercurrent is observed.

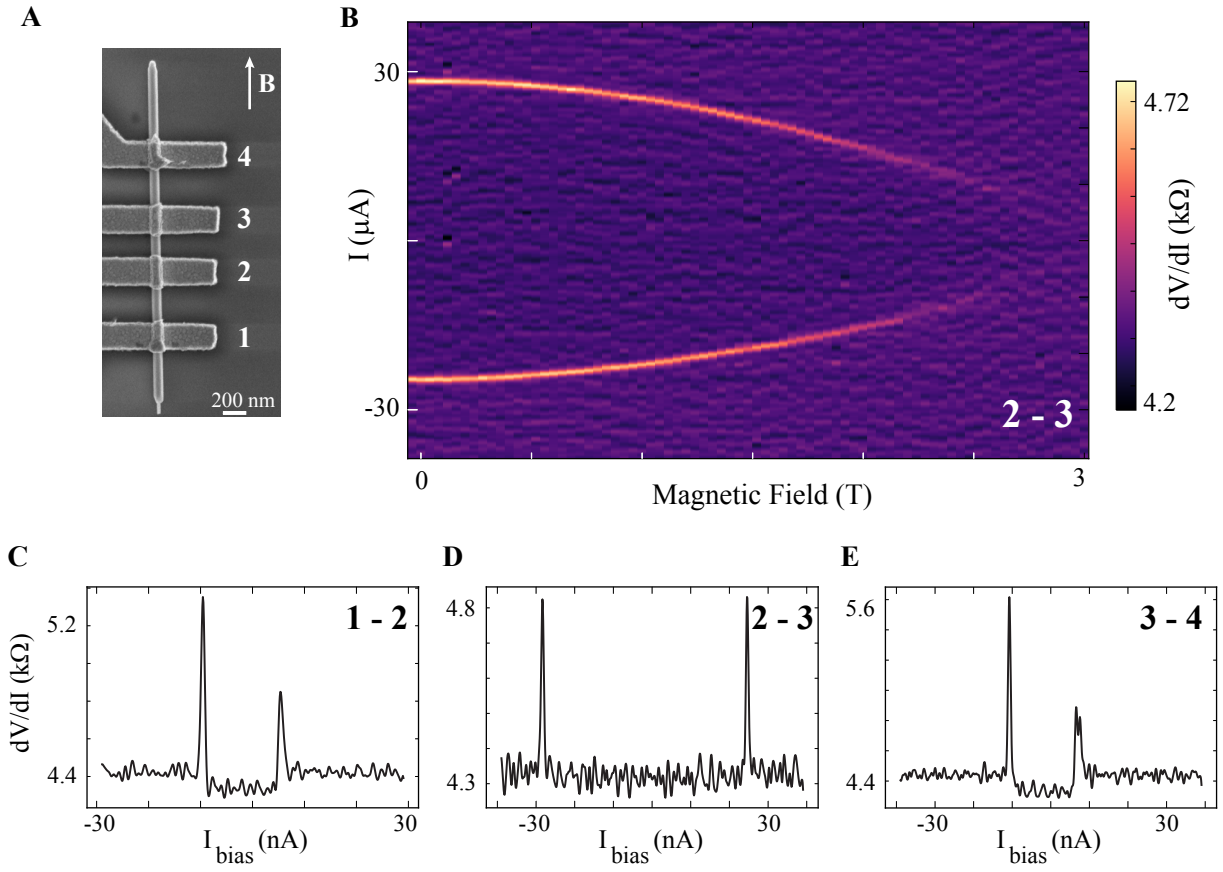

Figure 6.11: Device G has an uninterrupted Sn shell on an InSb nanowire without any shadows. The nanowire is grown on an InP stem. (A) SEM image showing 4 Ti/Au contacts labeled 1 to 4 noting different configurations for 2-terminal current bias measurements. (B) 2-terminal differential resistance as a function of bias current and magnetic field. Supercurrent persists up to 3 T, magnetic field is aligned parallel with the nanowire. (C-E) Differential resistance at zero magnetic field from different 2 terminal configurations. A variation in critical currents is observed along the shell, with the critical current being the highest in the central region of the nanowire. One possible explanation is the presence of grains of α-Sn, which are not superconducting, with a random distribution along the nanowire.

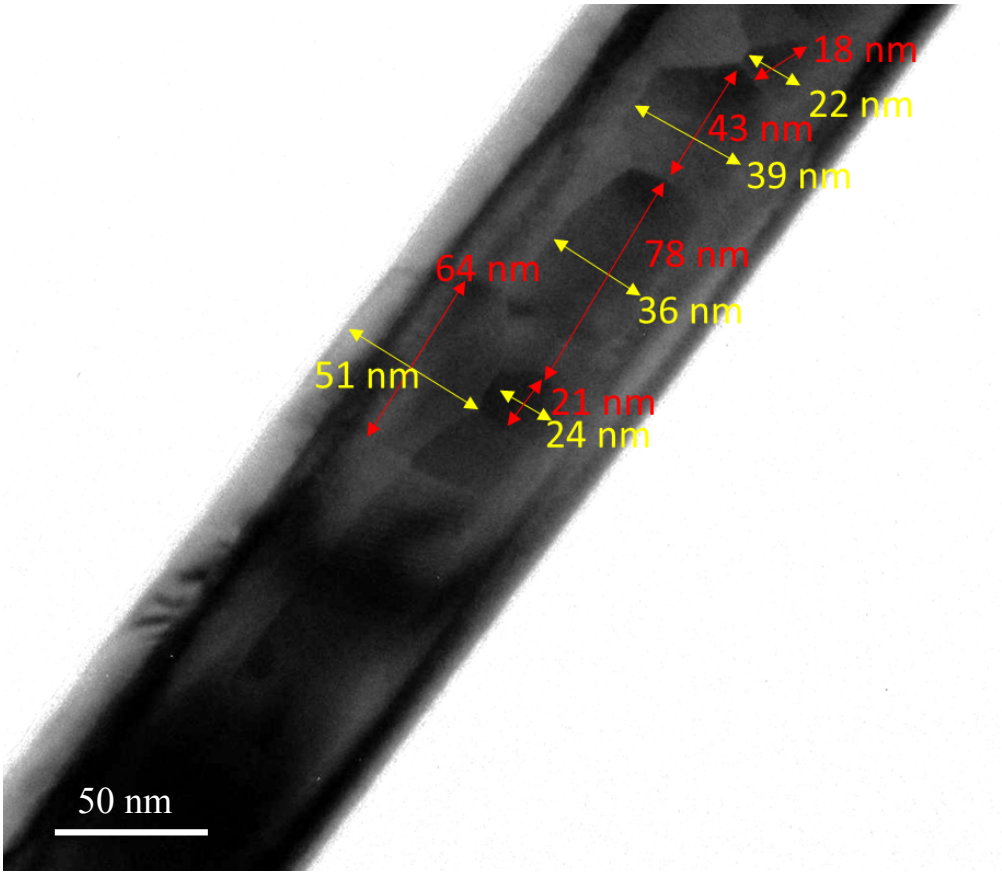

Figure 6.12: Side view bright field TEM image acquired along the ⟨110⟩ zone axis showing multiple Sn grains in the shell. Arrows and numbers are used to indicate the sizes of grains.

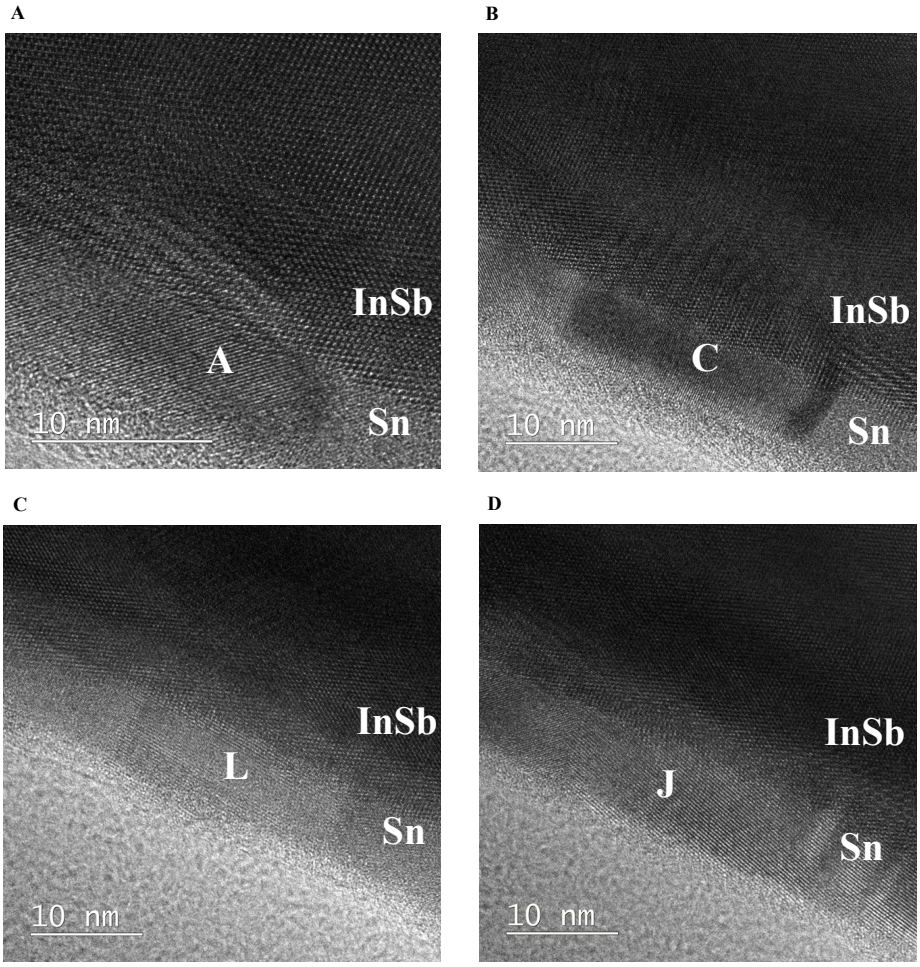

Figure 6.13: Side view TEM images of the core-shell interface, displaying four of the Sn grains listed in Table.1. (A) Grain A, which cannot unambiguously be assigned to either α-Sn or β-Sn. (B) Grain C, β-Sn grain epitaxially related to the InSb lattice. (C) Grain L, α-Sn. (D) Grain J, β-Sn.

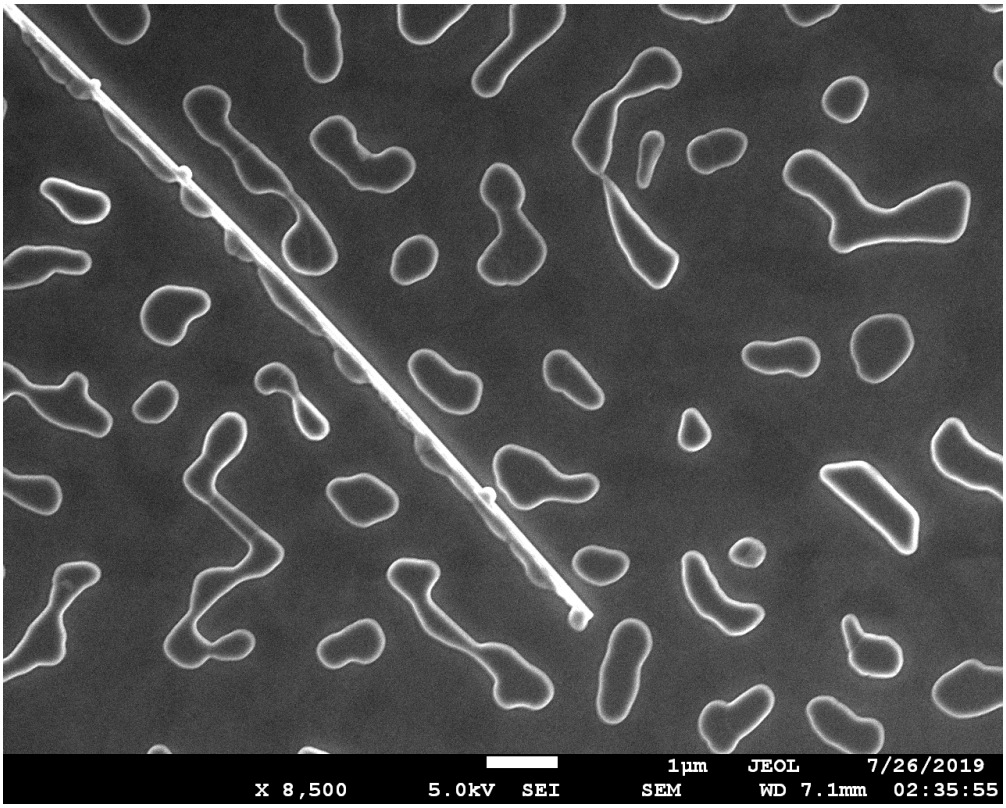

Figure 6.14: SEM image of a 15 nm tin film on an InSb nanowire grown at 85 ± 5 K that was allowed to warm up to 300 K in vacuum, without any immediate cap layer or oxidation. The tin layer coagulates to form disconnected islands or droplets on the nanowire. In a separate sample, such a film was also measured to be insulating across the wafer which confirms that the tin metal droplets are discontinuous. It was also observed that coagulation of the tin layer could be avoided by immediate oxidation of the tin film in a load lock, but such films were found to show rapidly changing superconducting properties over days which was attributed to continued oxidation of the tin layer underneath. No such change was observed in tin films capped with AlO_x which were found to be robust on the scale of 3 months.

Grain	d_{hkl} (exp)	hkl β	d_{hkl} β (lit)	% deviation from lit β	hkl α	d_{hkl} α (lit)	% deviation from lit α	epitaxy
A	0.198	211	0.2010	-1.2%	311	0.1956	+1.5%	
C	0.209	220	0.2065	+1.0%	311	0.1956	+6.7%	YES
D	0.203	220	0.2065	-1.4%	311	0.1956	+4.1%	
		211	0.2010	+1.3%	-	-	-	
E	0.206	220	0.2065	-0.4%	311	0.1956	+5.1%	
F	0.205	220	0.2065	-0.5%	311	0.1956	+5.0%	
G	0.274	101	0.2772	-1.3%	211	0.264	+3.7%	
I	0.282	101	0.2772	+1.7%	211	0.264	+6.7%	
J	0.277	101	0.2772	-0.0%	211	0.264	+5.0%	
K	0.203	220	0.2065	-1.8%	311	0.1956	+3.7%	
L	0.267	101	0.2772	-3.7%	211	0.264	+1.1%	
M	0.280	101	0.2772	+1.2%	211	0.264	+6.2%	
N	0.287	200	0.2920	-0.8%	-	-	-	
R	0.204	220	0.2065	-1.2%	-	-	-	
	0.149	112	0.1472	+1.3%	-	-	-	

Table 6.1: Phase identification based on lattice spacings dhkl of 13 Sn grains imaged using high-resolution TEM. All dhkl values are determined from Fast Fourier Transform patterns constructed from the HRTEM images. All patterns were calibrated by InSb lattice spacings present in the same images. The 211α spacing is not allowed based on crystal symmetry but can appear in HRTEM images. The experimental inaccuracy in the dhkl values is estimated to be 2.0 percent considering the limited number of pixels in the FFT patterns. Based on this criterion, all grains can be assigned to the β-Sn phase apart from grains A and L. Grain R is presented in Fig. 6.4 (C).

6.5 Conclusions

We study bottom-up grown semiconductor indium antimonide nanowires that are coated with shells of tin. The shells are uniform in thickness. No inter-diffusion is observed at the interface between Sn and InSb. Tunnel junctions are prepared by in-situ shadowing using nearby nanowires as well as flakes. A 15 nm thick tin shell is found to induce a hard superconducting gap in the range 600-700 μeV. Superconductivity persists up to 4 T in magnetic field. A small island of Sn-InSb exhibits the coveted two-electron charging effect, a hallmark of charge parity stability. The findings open avenues for superconducting and topological quantum circuits based on new superconductor-semiconductor combinations.

Furthermore, our results illustrate that neither defect-free epitaxial wire-shell interfaces nor single vacuum cycle growth of nanowire and shell are crucial requirements for demonstrating a hard gap, field-resilient superconductivity, and 2e charging. We conclude that the key components in attaining robust induced superconductivity are (i) removal of InSb native oxide using atomic hydrogen prior to Sn growth, followed by (ii) liquid nitrogen cooling of the nanowires during metal evaporation to produce a homogeneous ultrathin shell and (iii) immediate passivation of the wire-shell hybrid with a stable dielectric. Fig. 6.14 illustrates that when the sample is allowed to warm up without AlO_x passivation immediately after the cryogenic Sn shell growth, tin coagulates into discontinuous grains.

Without the need for epitaxial matching, many more superconductor-semiconductor combinations can be tried in search for decoherence-free qubit materials [73, 145, 146, 116, 137]. An immediate follow-up of our work are experiments on Sn-InSb devices in the Majorana geometry in search for clear signatures of topological superconductivity, as well as characterization of coherence times of Sn-based transmon qubits.

7.0 Andreev blockade in a double quantum dot coupled to a superconductor

7.1 Introduction

Hybrid superconductor-semiconductor nanostructures are of interest in the context of quantum computing. Most prominently, they are a platform investigated as a host of Majorana zero modes that can be used to build topological qubits [27, 28, 147, 17, 25, 148, 30, 29]. While these qubits have not been realized, other types of qubits, namely Andreev, fluxonium, and transmon have all been demonstrated with hybrid superconductor-semiconductor heterostructures [149, 150, 151]. Spin qubits can also be realized by quantum dots defined in semiconductor nanowires [152, 153, 154, 155]. Quantum dots exhibit iconic transport blockade phenomena: Coulomb blockade, which is used in metrology to set quantum current standard [156], and Pauli spin blockade, which is used for readout and initialization of spin qubits [157, 152]. In quantum dots coupled to superconductors, Andreev bound states form as quantum dot energy levels hybridize with many-body particle-hole quasiparticles [158, 90].

The overwhelming majority of superconductors are known to host spin-singlet Cooper pairs. The possibility of generating triplet Cooper pairs has been considered in proximity induced superconductivity both theoretically and experimentally [24, 26, 25, 27, 28]. Real-space oscillations of the superconducting order parameter, akin to the classic Fulde-Ferrell-Larkin-Ovchinnikov phase but in the proximity region, were observed and referred to as 'finite momentum Cooper pairing' [159]. In quantum dots coupled to superconductors, supercurrent flow through a single spin state has been demonstrated [160]. The interplay of spin polarization and supercurrent results in the π-Josephson effect characterized by a negative critical supercurrent. When spin-orbit interaction is added, this can lead to ϕ_0-Josephson junctions and the topologically superconducting state carrying Majorana modes [161, 162]. Cooper pair splitting via crossed Andreev reflection was studied as means of generating entangled charge pairs [163, 164].

Several versions of a triplet blockade in quantum dots closely related to Andreev blockade have been considered theoretically [163, 164, 165, 166, 167], with several works focusing on a

parallel combination of quantum dots, which is relevant for crossed Andreev reflection [168, 169, 170]. Other types of blockade related to Andreev reflection, such as chiral blockade, have been proposed [171]. A concurrent experiment to this one in a similar double dot setup with two rather than one superconducting lead has studied a triplet blockade that develops at a large magnetic field, where spin-triplet is the unique ground state of the double dot [172]. In contrast, Andreev blockade demonstrated in this work at zero magnetic field, due to the stochastic filling of a quantum dot by random spins.

Our study of Andreev blockade in a double quantum dot is published on [173].

7.2 Theory of Andreev blockade

The theory of Andreev blockade and the details of the numerical modeling are covered in a separate paper [174]. Here we summarize key concepts that are relevant for our interpretation of the experimental data.

Andreev blockade is a consequence of a dynamical formation of a stable sub-gap spin-triplet state. The series double dot setup allows for this to happen: a triplet state with one spin on each dot can have a low chemical potential due to small exchange interaction between spins.

Andreev blockade is the phenomenon that suppresses Andreev reflection due to spin parity mismatch between the double quantum dot and the superconductor. Andreev blockade is most apparent when the superconductor induces a hard gap in the nanowire. The hard gap ensures the suppression of single-particle tunneling and enforces Andreev reflection as the dominant means of transport.

Andreev reflection transfers a charge of 2e into the superconductor, where 'e' is the electron charge (Sec. 2.3.2). In order to move the two electrons between the normal and the superconducting lead, the double dot transitions through four charge configurations per Andreev cycle. Therefore transport is only allowed at quadruple charge degeneracy points where four charge configurations have similar chemical potentials all within a source-drain bias window that does not exceed the superconducting gap. As a point of comparison, in

non-superconducting double dots, transport involves moving just one electron between the leads and takes place at triple, rather than quadruple, degeneracy points, which results in the formations of the well-known honeycomb charge stability diagram [33].

Andreev blockade is controlled by the occupation of the normal dot QD_N, but it is not sensitive to the occupation of the superconducting dot QD_S. QD_S is strongly coupled to the superconductor, and thE coupling hybridizes all states of the same parity. For example, states with 0 and 2 charges are hybridized, and so are the states with 1 and 3 charges. Coupling to the superconductor imposes an approximate particle-hole symmetry which mandates that transport at odd-to-even and even-to-odd degeneracy points is the same. This translates into the insensitivity of Andreev blockade to the occupation of QD_S.

A complementary way to see why transport is insensitive to the charging state of QD_S is as follows. Throughout a transport cycle, two electrons must be added to QD_S, driving the dot from an even parity state to an odd parity state and back to an even parity state. If the normal dot QD_N has two charges on it, they must be of opposite spins, and one can always escape into QD_S. Specifically, if QD_S is in the even parity state, either spins on QD_N can move to QD_S, thus putting QD_S into an odd parity state. If QD_S is in an odd parity state, one of the electrons on QD_N has the opposite spin and can move to QD_S resulting in a transition to an even parity state. On the other hand, if QD_N only has one spin, then that spin cannot escape to QD_S if QD_S is an odd parity state of the same spin. Hence, the charging state of QD_N determines if an Andreev blockade can be established.

Reversing the direction of bias leads to a similar analysis, except the transport becomes blockaded by the inter-dot triplet when QD_N is doubly occupied. Specifically, if QD_S is in the even parity state, it can give up an electron of either spin to QD_N and transition to the odd parity state. However, if QD_S is in the odd parity state, then the electron it can give up to the QD_N has a definite spin, and transport becomes blocked if QD_N already has an electron of the same spin on it.

7.3 Device description

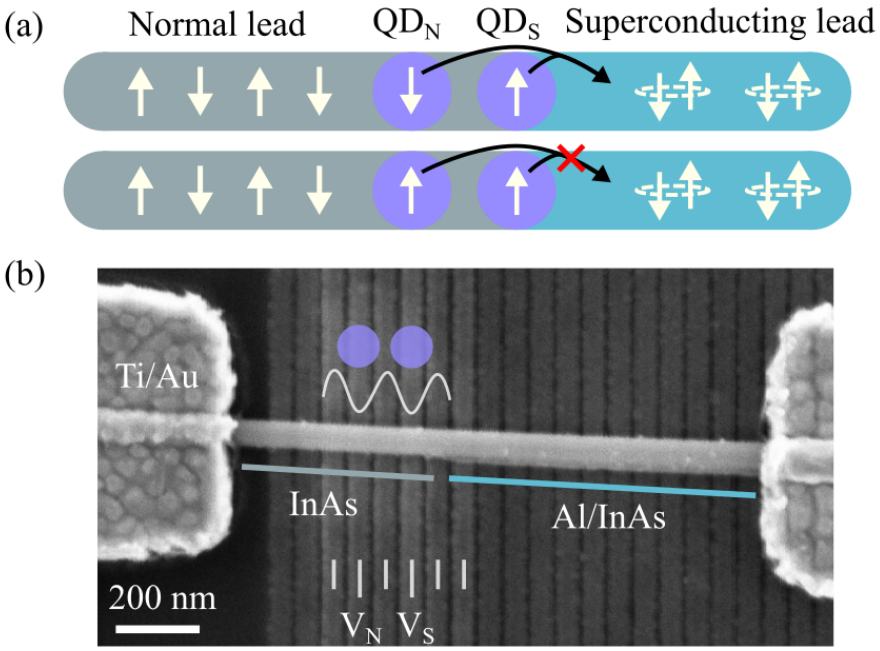

Figure 7.1: (a) Schematic of Andreev blockade. The blockaded configuration is indicated with a red cross showing how a spin-triplet in DQD is prevented from forming a spin-singlet Cooper pair. (b) Scanning electron microscope (SEM) image of a device similar to the one studied in the main text. Section marked 'Al/InAs' is an InAs nanowire covered by an Al shell. A section where the shell is etched and exposed bare InAs nanowire is marked 'InAs'. Vertical white lines mark gate electrodes used in creating the DQD.

We reproduce the experimental conditions required for the observation of Andreev blockade following a theoretical proposal [174]. We use a double quantum dot (DQD) to trap a spin-triplet state in a semiconductor nanowire (Fig. 7.1 (a)). One side of the double dot is connected to a superconductor so that transport out of the dot is via Andreev reflection. The other side of the double dot is connected to a non-superconductor lead so that transport into the dot is via single-electron tunneling. Charge carriers entering the double dot via single-electron tunneling have a random spin orientation. While a spin-singlet configuration makes Andreev reflection possible, a triplet configuration suppresses Andreev reflection and

blocks the current.

QD_N is a normal dot in the multi-electron regime, while QD_S is a superconducting dot. The levels of QD_S hybridize with the superconductor, resulting in Andreev bound states [158], and therefore the particle number is no longer a good quantum number in QD_S. We describe the charge states in both dots by their parity, either even or odd. The parity of states in QD_N can be inferred by studying how the degeneracy points shift in magnetic fields, with odd regions expanding and even regions shrinking at higher fields (see Fig. 7.12). The parity of states in QD_S can be inferred from Andreev spectra, with a region inside loop-like resonance being odd (Figs. 7.2 (a-b)).

Fig. 7.1 (b) shows a scanning electron microscope (SEM) image of the nanowire device. An InAs nanowire covered with $\sim$ 15 nm epitaxial Al is placed on top of 60 nm pitch gate electrodes. The DQD is defined by electrostatic gate electrodes indicated in the image. V_N and V_S are the gate voltages primarily used for tuning the dot states. Al on the left section of the wire is selectively etched to make the normal contact.

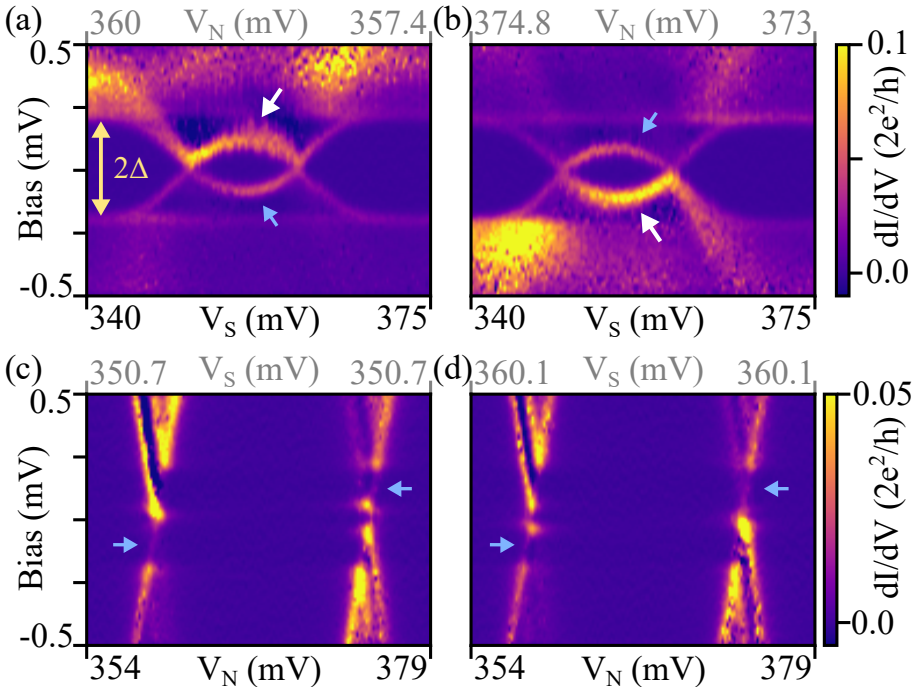

Figure 7.2: Differential conductance spectra for (a-b) QD_S and (c-d) QD_N. Spectra are taken by fixing one dot at a degenerate state while tuning the other dot with the (V_S, V_N) combination. The voltage combinations are indicated in Fig. 7.3(a). The large white arrows and small blue arrows indicate resonance peaks with different amplitudes.

Fig. 7.2 shows differential conductance spectra of a device similar to the one shown in Fig. 7.1 (b). The device is first set to a double-dot regime by tuning all gates adjacent to the superconducting lead. Spectra are then taken by fixing one dot at a degeneracy point while tuning the other dot. Spectra of QD_S show induced superconducting hard gap $\Delta = 0.2$ mV, which is consistent with other works [64, 67, 71, 137]. Inside the gap, loop-like resonances due to gate-tuned Andreev bound states are observed. Spectra of QD_N show Coulomb diamonds and no clear induced gap. Together, these spectra demonstrate that we have the right ingredients for Andreev blockade, i.e., a normal dot, an Andreev dot, and a hard gap superconducting lead. To better understand the four panels of Fig. 7.2, it is helpful to look at Fig. 7.3 (a), which shows a charge stability diagram and cuts in V_N-V_S space that

correspond to Fig. 7.2.

Below we discuss other more subtle conditions that the system must meet for Andreev blockade to be observable.

The induced superconducting gap should be hard [67] in order to suppress single-particle transport below the gap. Any single-particle transport is a lifting mechanism of Andreev blockade. Thus the softer the induced gap, the weaker are the Andreev blockade signatures. The barrier to the superconducting lead should be low in order to induce Andreev bound states. This is in contrast with Pauli blockade setups which typically require few-electron regimes and hence high barriers. The inter-dot charging energy should be smaller than the induced gap because the size of Andreev transport triangles shrinks rapidly with increasing inter-dot charging energy. This parameter is largely controlled by the device's geometry and is difficult to extract from the data. In our numerical simulations, we set it to 10 μeV.

Following theoretical proposal [174], we are looking for the following experimental signatures of Andreev transport and blockade in a N-QD$_N$-QD$_S$-S system.

1. At subgap voltage biases, current is confined to triangular regions of the charge stability diagram. The triangles do not appear in closely spaced pairs as in non-superconducting double dots where they form around triple points. Instead, each quadruple Andreev degeneracy point is associates with a single transport triangle, the quadruple Andreev degeneracy points themselves form a parallelogram grid in V_S vs. V_N space.
2. An alternating pattern of 'blockade/no blockade' is observed when V_N tunes the quadruple points. V_S does not affect whether blockade is present or not. An ideal blockade corresponds to total suppression of current below the gap. Various blockade lifting mechanisms discussed below result in partial lifting of Andreev blockade, in which case current is observed at all quadruple points but is smaller at the blockaded ones.
3. The sign of source-drain bias voltage flips Andreev blockade. A quadruple point that is blockaded in positive bias is lifted in negative bias, and vice versa. Signatures (2) and (3) can be formulated together as follows.

   Andreev blockade is expected for (odd,odd)→(even,even) charge parity transitions and for (odd,even)→(even,odd) transitions, where the arrows indicate the direction of charge transfer so that the conditions are valid for both signs of the applied bias.

4. Andreev blockade is not present when superconductivity is suppressed by magnetic field or temperature. An alternating pattern of current at degeneracy points or asymmetry in source-drain bias should vanish under these conditions. Charge degeneracy points should revert from single-triangle quadruple points to double-triangle triple points, signifying a transition from Andreev 2e transport to normal 1e transport.
5. Andreev blockade can also be suppressed by the presence of sub-gap quasi-particles and thermally excited quasi-particles, which result in leakage current through the double quantum dot in the notionally blockaded regions of the charge stability diagram.

In principle, there should be no fine-tuning required to observe Andreev blockade. All that is needed is one normal dot, one superconducting dot, and a hard gap superconductor lead. Thus we are looking for a region of V_S vs. V_N that includes many charge degeneracy points that exhibit blockade signatures. In practice, mesoscopic factors such as additional quantum dots in the nanowire segments covered by the leads can introduce their own current modulations. Thus some gate tuning may still be required to observe the Andreev blockade.

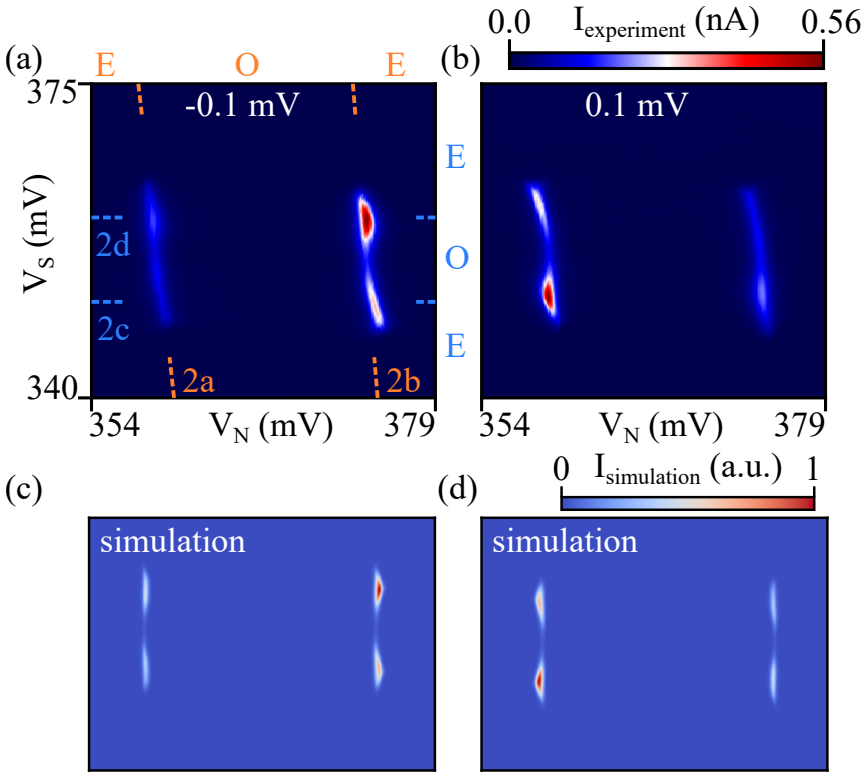

Figure 7.3: (a-b) Experimental and (c-d) simulation results of a 'unit' stability diagram with 2×2 quadruple degeneracy points. Parities in QD_N and QD_S are labeled on top and right axes in panel (a), respectively. Dashed lines are traces along which spectra in Fig. 7.2 are taken. The source-drain bias voltage is indicated in white. Parameters for simulation (in meV): source-drain bias $\mu_S - \mu_N$ = -0.1 in (c), 0.1 in (d), charging energy $U_N = 4$, $U_S = 0.7$, inter-dot charging energy $U_{NS} = 0.01$, induced gap $\Delta_S = 0.2$, temperature $T = 0.02$.

Sig. 1, which is current confined to single, not double, triangles in the charge stability diagram is illustrated in Figs. 7.3 (a,b). Stability diagrams are taken at two opposite bias voltages. We observe elongated triangles for both bias directions, rounded due to relatively low bias voltages required to stay below the aluminum induced gap. Numerical model results in Figs. 7.3 (c,d) closely reproduce the experiment. The model uses realistic assumptions of finite temperature discussed below in the Methods section. Larger gate range shown in Fig. 7.4 confirms the single-triangle character of charge degeneracy points.

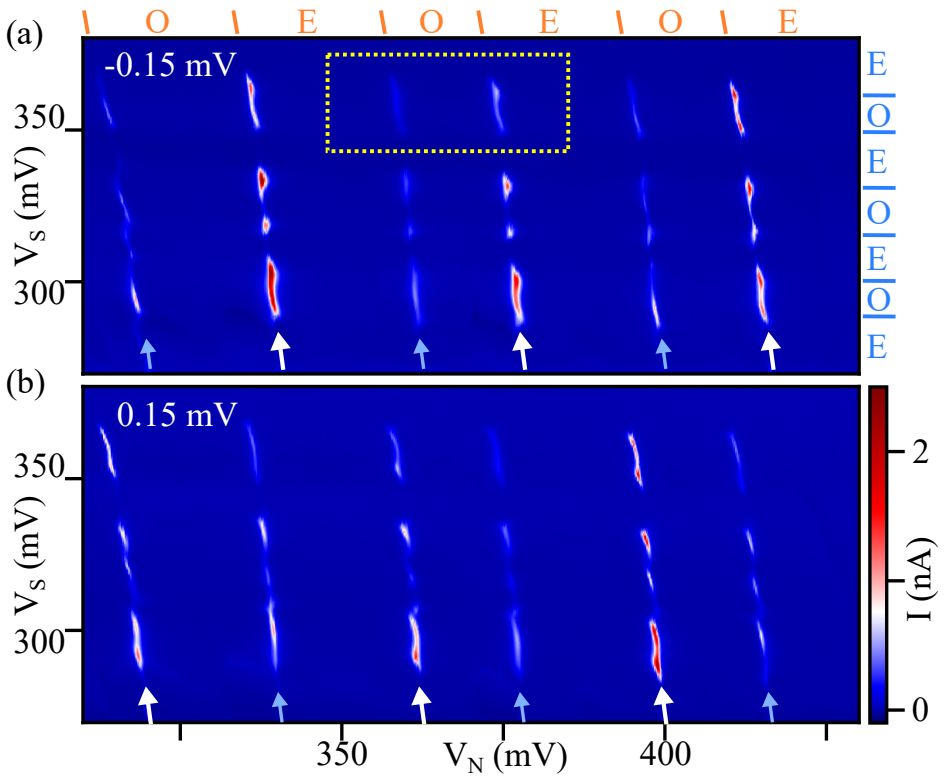

Figure 7.4: Stability diagrams in a larger (V_S, V_N) parameter space. The yellow dashed rectangle in panel (a) encloses the 'unit cell' discussed in other figures. There are 6×6 quadruple degeneracy points. Parities in QD_N and QD_S are labeled on top and right axes, respectively. Blue (white) arrows indicate columns of conductance triangles with low (high) current. The source-drain bias voltage is indicated in white. The blockade is column-wise and bias-wise, consistent with the Andreev blockade prediction.

Sig. 2, an alternating pattern of high current/low current when the occupation of QD_N is changed, is illustrated in Figs. 7.3 and 7.4. We see dim degeneracy points followed by bright ones. In Fig. 7.4 the dim columns are marked by dim arrows, while bright arrows mark the bright columns. The region of (V_S, V_N) parameter space depicted contains 6×6 degenerate points. This behavior is also captured in the simulation Figs. 7.3 (c,d). All degeneracy points are detectable, which means the blockade is partially lifted in the context of Andreev blockade. In the simulation, we had to assume finite temperature to reproduce this behavior. Finite temperature enables single-particle tunneling into a hard-gap superconducting lead

via thermally excited quasi-particles.

Sig. 3 is the reversal of the alternating pattern of current carrying and blockaded triangles in opposite bias. In Fig. 7.3 (a), at -0.1 mV, current is smaller for the degeneracy points on the left. In Fig. 7.3 (b), at $+0.1$ mV, the current is smaller for the degeneracy points on the right. Simulated Andreev blockade regime shows good agreement with this observation (see Figs. 7.3 (a,b)). The same behavior largely holds in Figs. 7.4(a,b) over an expanded range of gate voltages covering 6×6 degeneracy points.

Bias asymmetry can also be seen in Fig. 7.2. In the upper panels, Andreev loops have non-symmetric amplitudes between positive and negative bias voltages marked by large and small arrows so that either the upper or the lower half of the loop is brighter than the other half. In Coulomb diamonds shown in the lower panels, the intensity pattern is anti-symmetric with respect to the center of the figure. For example, in Fig. 7.2 (c), the left region is bright at positive bias, while the right region is bright at negative bias. These patterns are consistent with Andreev blockade: when the occupation of QD_S is changed AB is not affected, and when the occupation of QD_N is changed AB appears at the opposite bias. The full picture is more complicated as bias asymmetries are also observed at currents above the induced gap. However, Figs. 7.8 and 7.9 illustrate that in general, bias asymmetry at high bias does not follow the same pattern as low-bias asymmetry.

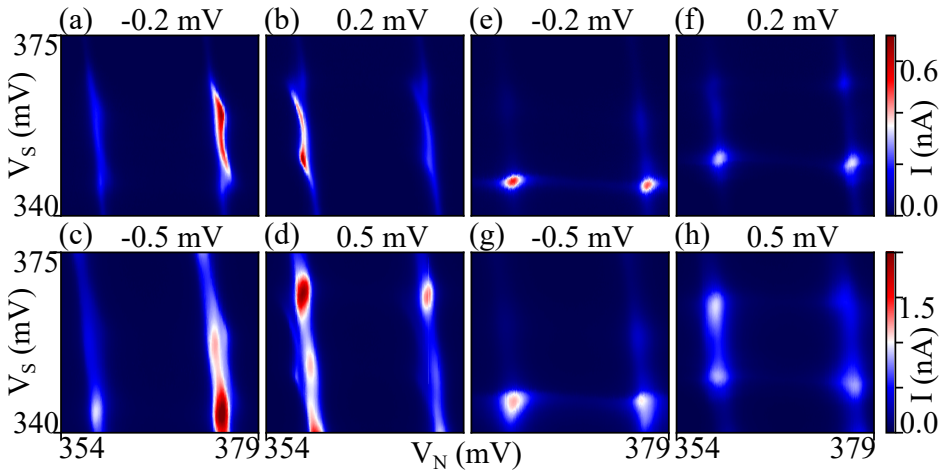

Figure 7.5: Stability diagrams at different bias voltages and magnetic fields. (a-d) $B = 0$ and (e-h) $B = 0.6$ T. The bias voltage is indicated in each panel. The magnetic field is in the sample plane at ≈24 degrees angle with the nanowire.

Finally, Sig. 4 which is the disappearance of other signatures when superconductivity is suppressed, is presented in Fig. 7.5 and supplementary Figs. 7.7, 7.11, 7.14, 7.15. Figs. 7.5(a-d) reproduce the same regime as in Fig. 7.3 for different bias voltages. When a magnetic field of 0.6 T is applied, in Figs. 7.5(e-h), we observe that the alternating patterns of bright/dim degeneracy points are no longer present, and neither is the bias voltage asymmetry. The same holds true at elevated temperature as illustrated in Fig. 7.7.

Single elongated degeneracy points are replaced by less elongated points at higher fields where superconductivity of the aluminum shell is suppressed (Figs. 7.5(e-h)) - in this regime the charge degeneracy points appear more similar to those of a normal double dot with pairs of triangular triple points, but with significant rounding and blurring and a weak inter-dot capacitive coupling. This double dot is different from how normal dots are tuned in many experiments because QD_S is strongly coupled to the superconducting lead introducing tunnel broadening at high bias above the gap. This is confirmed by higher co-tunneling current in the vertical direction of almost all charge stability diagrams. In future experiments using a larger gap superconductor such as Sn or Pb [115, 116, 137] as a shell can provide a larger bias voltage range for the observation of Andreev blockade and make this observation more

clear by reducing the role of tunnel broadening.

Data and code are available at [175].

7.5 Experimental methods

The growth of InAs nanowires with Al shells is performed using molecular beam epitaxy (MBE). First, InAs nanowires are grown from pre-defined Au catalysts via vapor-liquid-solid mechanism. After the nanowire growth, the growth chamber is cooled down, and in-situ Al growth is carried out, ensuring the high-quality interface of the hybrid superconductor-semiconductor heterostructures. Further discussion about the growth can be found in [137].

Electrostatic 60 nm pitch gates are patterned by 100 kV e-beam lithography (EBL) with PMMA 950 A1 as the resist. The development for gate patterns is performed in 1:3 MIBK/IPA for 1 minute at a low temperature of -15 °C to enhance the resolution [176]. Then a bilayer of 1.5/6 nm Ti/PdAu is evaporated by electron-beam evaporation. The gates are covered by 10 nm of HfO_x as the dielectric layer, patterned by EBL and grown by atomic layer deposition (100 cycles).

Nanowires are transferred onto the gate chip using a micro-manipulator under an optical microscope. Windows for Al-etching are defined by 10 kV EBL. The PMMA resist is dried in a vacuum chamber at room temperature to avoid heating the Al layer [71]. AlO_x/Al on the InAs wire is selectively etched using MF CD-26 developer/DI water solution for 2 minutes, at a volume ratio of 1:20 at room temperature. Leads are made with EBL, Ar cleaning, followed by e-beam evaporation of 10/130 nm of Ti/Au.

Measurements are performed in a dilution refrigerator with a 40 mK base temperature.

7.6 Further reading

Background information on single and double quantum dots can be found in [33].

An introduction to Andreev bound states can be found in [158].

Majorana zero modes in 1D wires are discussed in [31, 25, 26].

Epitaxial growth of Al on nanowires and the hard gap can be found in Ref. [64, 67].

Transport properties in hybrid structures such as S-DQD-S [163, 165, 166, 172], QD-S-QD [168, 169, 170], and N-DQD-S [167, 174, 177] have been studied extensively. Very few studies are directly related to blockade phenomena. A recent experimental paper shows that the Josephson current in an S-DQD-S device can be blocked due to spin-triplet pairs in a magnetic field [172].

7.7 Discussion

A quantum transport blockade phenomenon is demonstrated, where a spin-triplet state is stabilized at a boundary of a superconductor. The triplet prevents further charge transfer into the spin-singlet superconductor. This blockade phenomenon could be used to study the spin structure of superconductivity itself by analyzing the residual current that avoids blockade. Moreover, it can play a role in quantum devices that combine spin polarization and superconductivity, for example, in topological qubits.

We have considered the possibility that signatures (Sigs. 1, 2, 3, 4) arise due to fine-tuning obtained by a deliberate search for predicted patterns in the experimental data. In this scenario, signatures such as alternating bright/dim degeneracy points and bias asymmetries are not due to Andreev blockade, but instead they arise accidentally due to additional states co-existing with the QD_N-QD_S system in the same nanowire. For example, spurious Andreev and normal quantum dots in the nanowire lead segments. Those other states are fine-tuned to modulate transport in the double dot in just the right way to be consistent with Andreev blockade.

We have observed that the Al etching process, which we use to remove the shell where we define the double dot and the normal lead may leave behind Al islands which superconduct, it can also damage the nanowire surface, leading to the formation of extra quantum dots, or intermediate regimes with Al partially etched. While the device presented in the main text results from optimized fabrication that addressed these issues, we cannot exclude the

possibility of their presence. We see from e.g., Fig. 7.4 that while the stability points form a dominating double-dot pattern, their intensities vary across a large V_S-V_N range suggesting non-monotonic coupling to states outside the dots or non-monotonic inter-dot barriers.

Our argument for not favoring the above explanation is that a pattern consistent with AB Sigs. 1, 2, 3 are observed over a regime covering 6×6 degeneracy points, in several alternative double dot configurations, and, in a more limited range in another device. Furthermore, the fact that bias asymmetry and alternating current patterns disappear when superconductivity is suppressed (Sig. 4) convinces us that these phenomena have to do with sub-gap superconducting transport, which is the regime of Andreev reflection.

Both Pauli blockade and Andreev blockade occur in double quantum dots with two charges in a spin-triplet state. However, they have different origins. Pauli blockade is due to Pauli principle, which prevents two electrons of the same spin from occupying the same orbital. Andreev blockade is due to the inability of forming Cooper pairs out of spin-triplet pairs. The characteristic energy scale of Andreev blockade is the induced superconducting gap. The characteristic energy scale of Pauli blockade is the singlet-triplet energy level spacing in the (0,2) charge configuration.

Andreev and Pauli blockades appear in different yet overlapping parameter spaces and can be observed in the same device. In soft gap Andreev double quantum dots, Pauli blockade has been previously observed in [90]. Though we did not observe Pauli blockade in the device studied here. This is consistent with what is known of Pauli blockade - it is a relatively rare phenomenon observed more frequently in few-electron double dots due to larger singlet-triplet energies. Whereas, in multi-electron dots, such as those studied here, Pauli blockade appears in one out of every 10 or 100 degeneracy points [178]. In contrast, Andreev blockade is not expected to be as sensitive to quantum dot energy scales and is, in principle, guaranteed by the superconducting gap. Even if singlet-triplet energies were significant for all orbitals, Pauli blockade would be expected in 1 out of 4 degeneracy points, while Andreev blockade is expected in 2 out of 4.

7.8 Supplementary data

7.8.1 Supplementary data for the device presented in Sec. 7.4

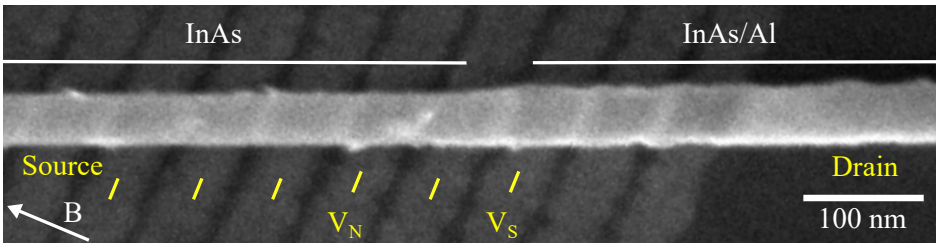

Figure 7.6: SEM image of device A that corresponds to data in Sec. 7.4. The image is taken after Al is etched but before Ti/Au contacts deposition. The DQD is created electrostatically using six gate electrodes (yellow lines) and the underlying doped Si substrate (as a global gate).

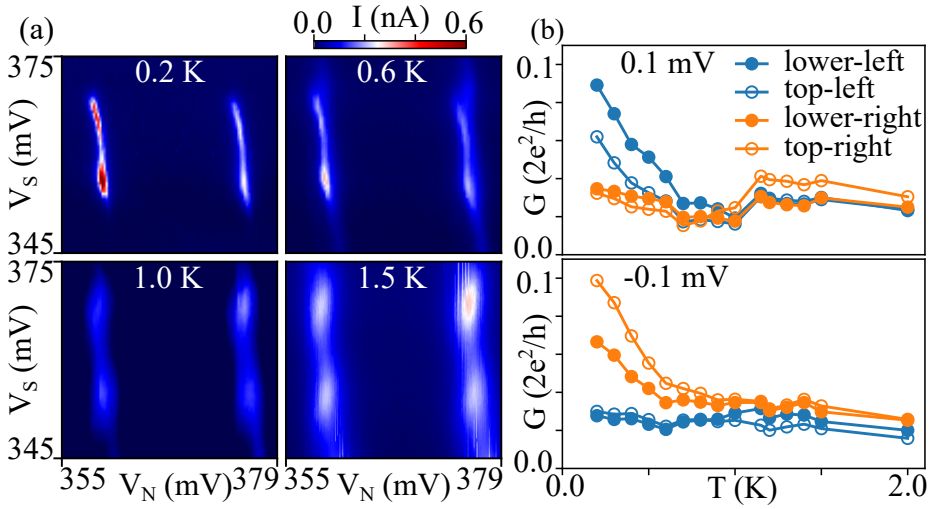

Figure 7.7: Temperature dependence of the transport region in Fig. 7.3. (a) Stability diagrams at different temperatures. The temperature is labeled in each sub-panel. The source-drain bias voltage is 0.1 mV. (b) Local maximum conductance extracted near four degeneracy points versus the temperature. The asymmetry between the left and right maxima disappears above the critical temperature of bulk aluminum (1.2 K). B=0.

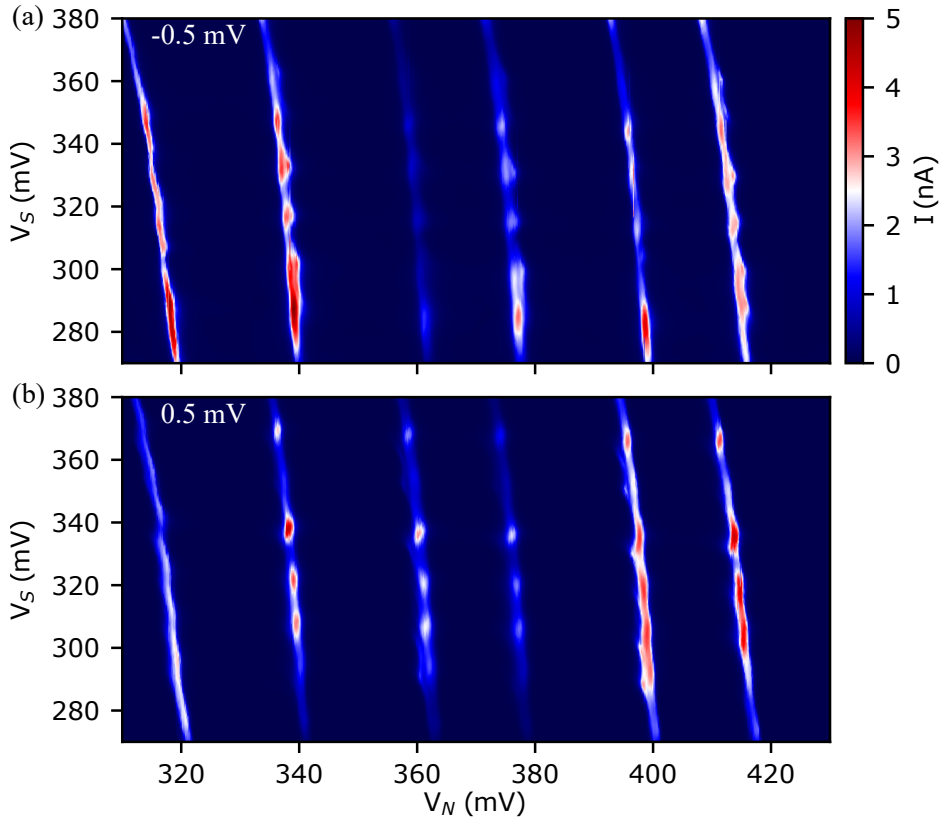

Figure 7.8: Additional data to Fig. 7.4, at bias voltages above the gap. The source-drain bias voltage is indicated in white. B=0.

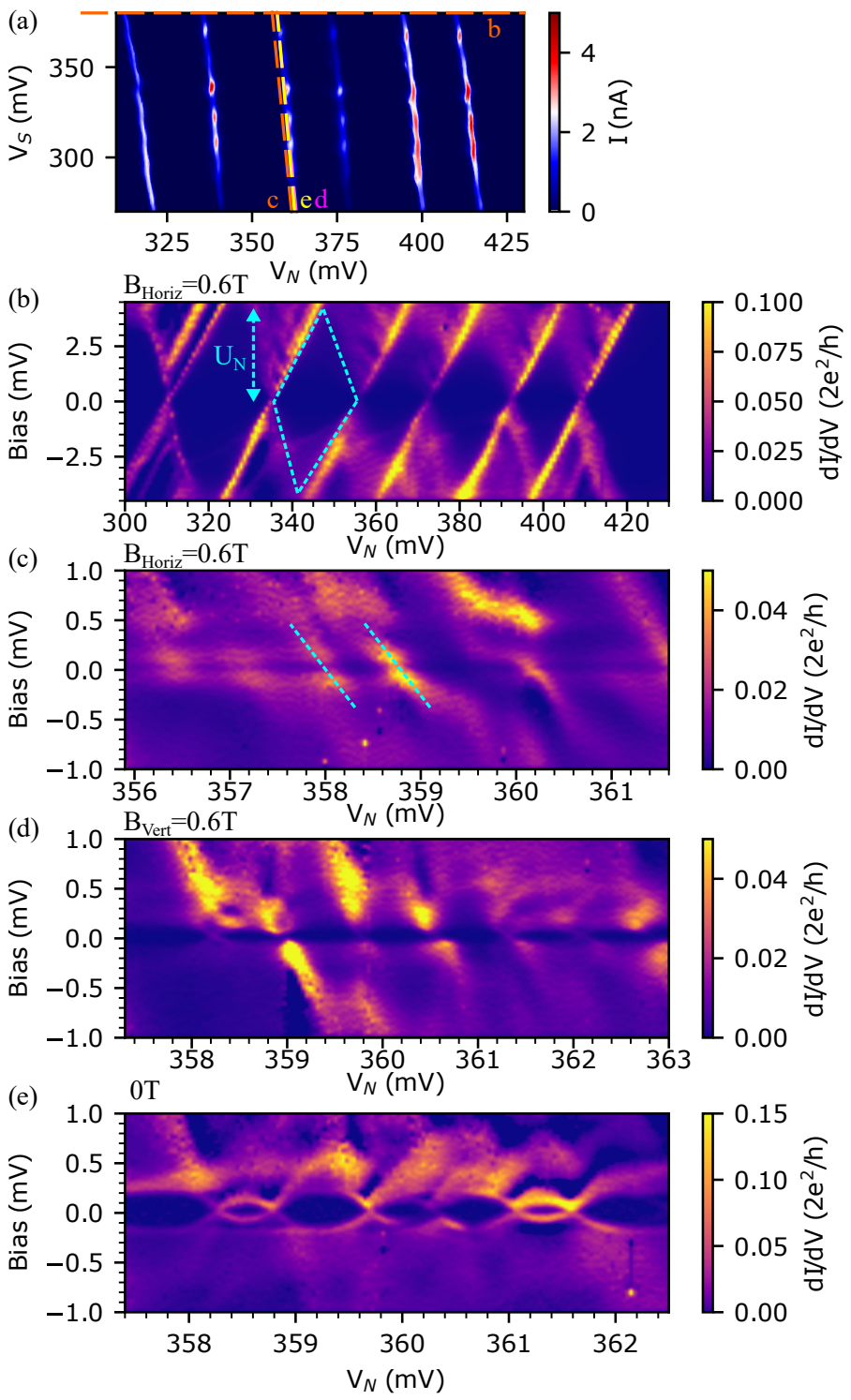

Figure 7.9: (a) Stability diagram. (b-e) Bias spectroscopy as a function of gate voltages along traces in (a).

Fig. 7.9 (a) Stability diagram is the same as in Fig. 7.8 (b). The dashed lines are traces along which bias-gate spectra in panels (b-e) are taken. The magnetic fields are noted for each bias-gate panel. B_{Vert} is the magnetic field used in Sec. 7.4. B_{Horiz} is used only in this figure. B_{Horiz} is not aligned to perpendicular to the chip but is perpendicular to B_{Vert}. The Coulomb diamond (blue dashed diamond) in panel (b) yields charging energy of roughly 4 mV in QD_N. Determining the charging energy in QD_S is difficult. The blue dashed lines in panel (c) show edges of Column diamonds with negative slopes. The positive slope edges are hard to distinguish except near $V_N = 360$ mV. This is because in our device, the QD_S has a shallow barrier to the superconducting lead causing strong asymmetry. We assume the charging energy in QD_S to be below 1 meV.

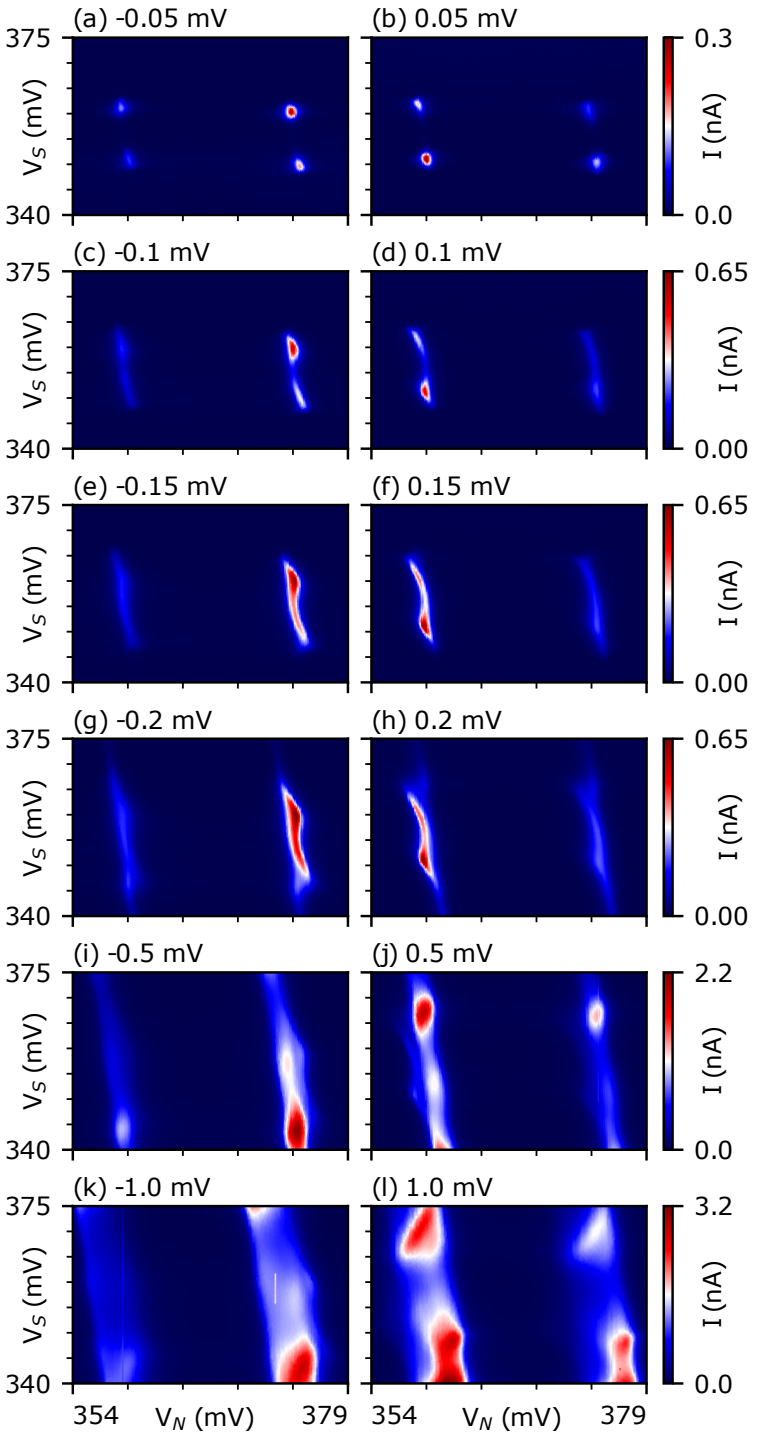

Figure 7.10: Additional data to Fig. 7.5, at zero magnetic field. Bias voltages are noted on each panel.

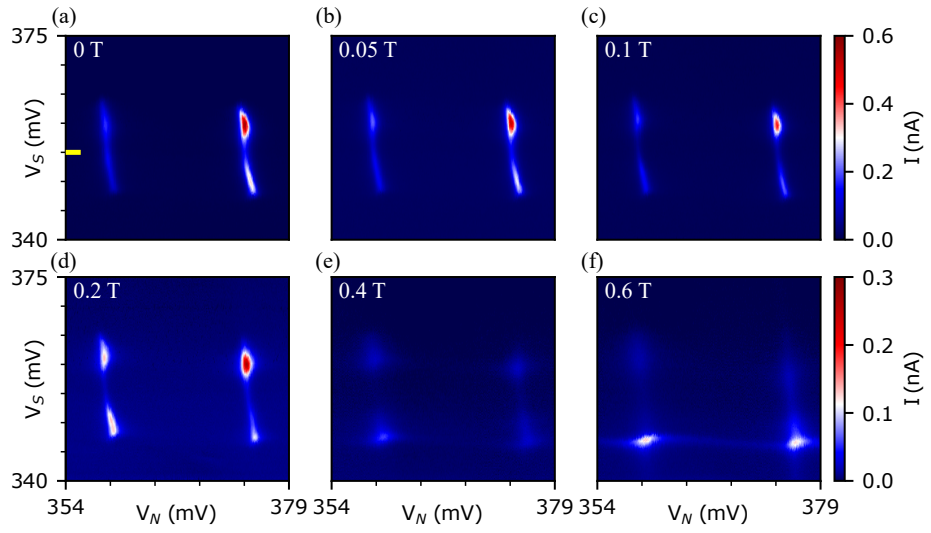

Figure 7.11: Additional data to Fig. 5, at -0.1 mV bias and different fields. The yellow short line in panel (a) indicates where $V_S = 355$ mV (see Fig. 7.12).

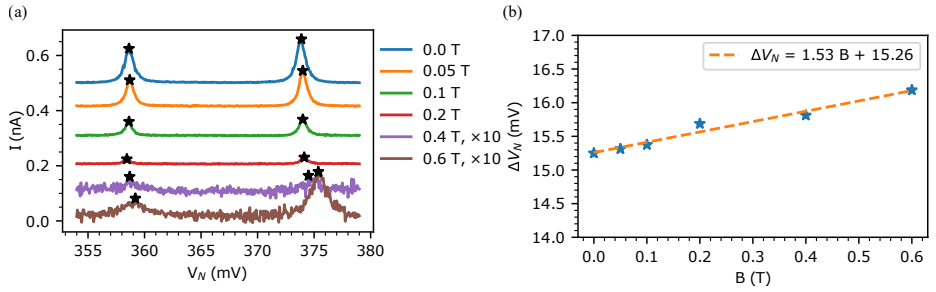

Figure 7.12: (a) Current vs. V_N extracted from data in Fig. 7.11, at $V_S = 355$ mV. Curves are shifted vertically for clarity, with a step of 0.1 nA. Black asterisks marks resonance peaks due to levels in QD_N. Data at 0.4 T and 0.6 T are multiplied by 10 to highlight the peaks. (b) Peak-to-peak distance vs. magnetic field shows Zeeman splitting of QD_N levels. The dashed line is a linear fit to the points. The charging energy E_C of the QD_N is about 4 mV (Fig. 7.9). An effective g-factor of 6.9 can be estimated with equation $\Delta V_N = \alpha(g\mu_B B + E_C)$, where α is a coefficient be determined, μ_B is the Bohr magneton, $g\mu_B B$ is the Zeeman energy. These data can be used to assign even and odd occupations in QD_N.

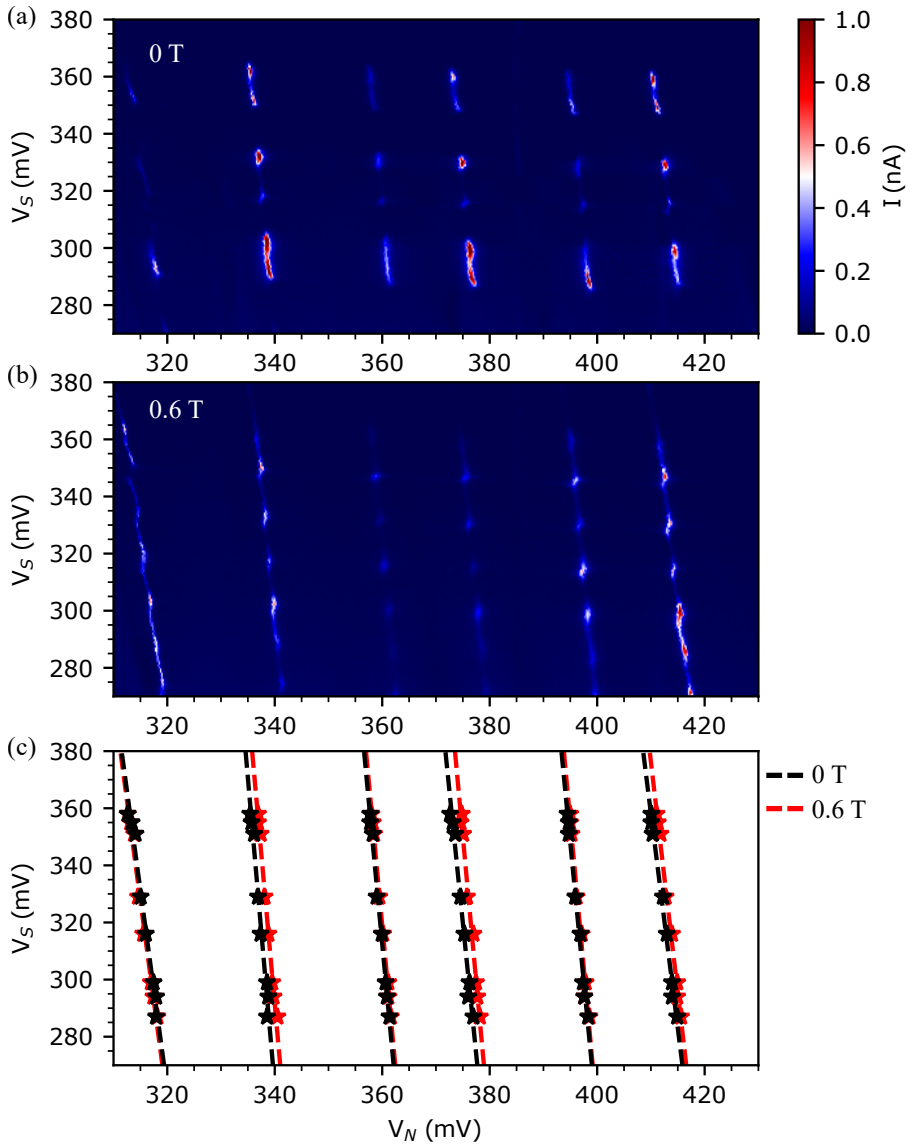

Figure 7.13: Zeeman splitting of QD_N in the large regime discussed in Sec. 7.4. (a-b) Stability diagrams at -0.1 mV. The magnetic field is noted in each panel. (c) Asterisks show peak positions extracted from a series of horizontal linecuts. Dashed lines are linear fitting lines. These data can be used to assign even and odd occupations in QD_N.

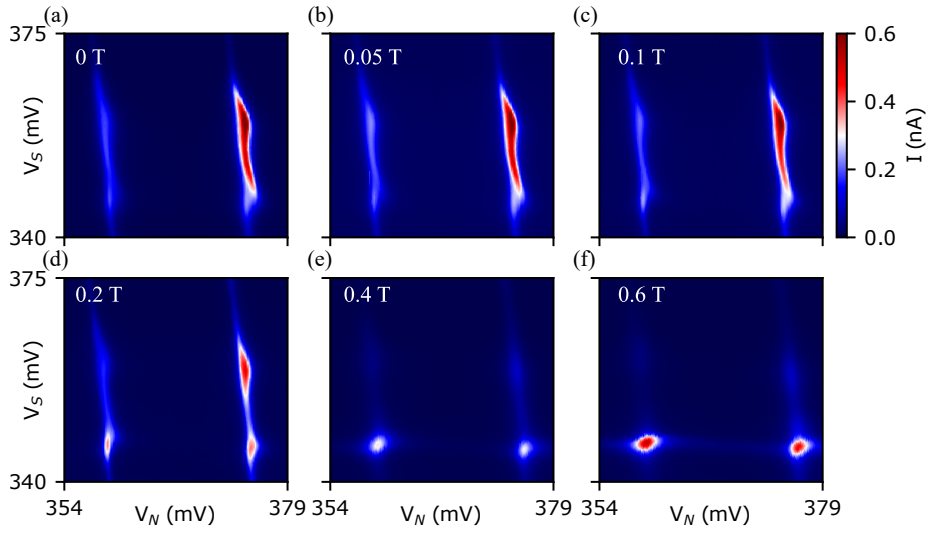

Figure 7.14: Additional data for Fig. 7.5, at -0.2 mV bias and at different magnetic fields.

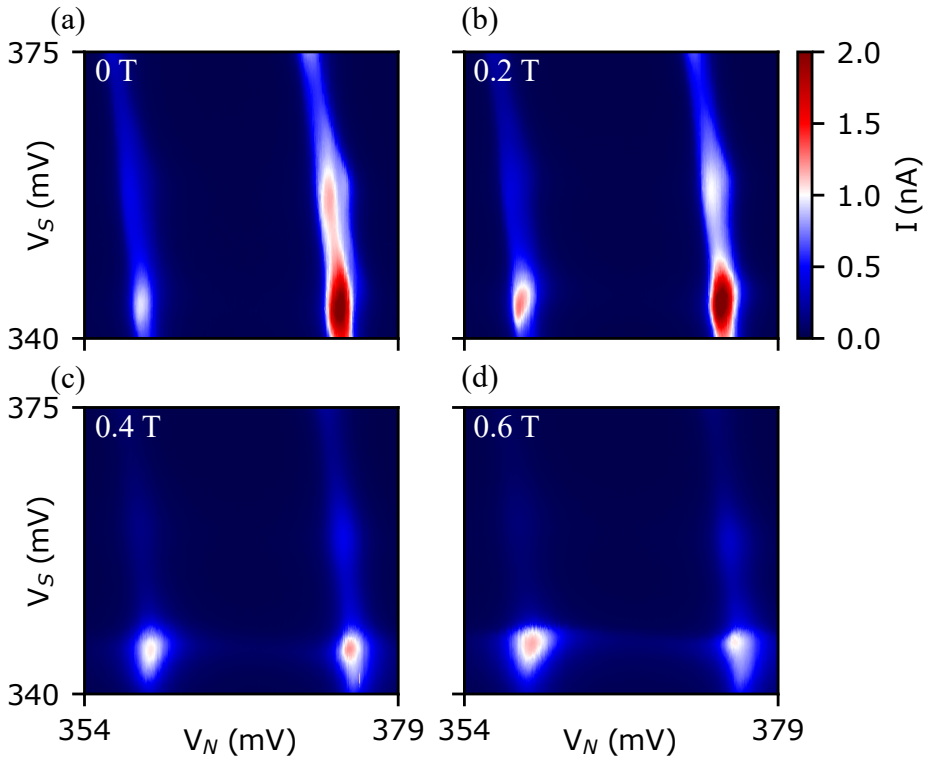

Figure 7.15: Additional data for Fig. 7.5, at -0.5 mV and different applied magnetic fields.

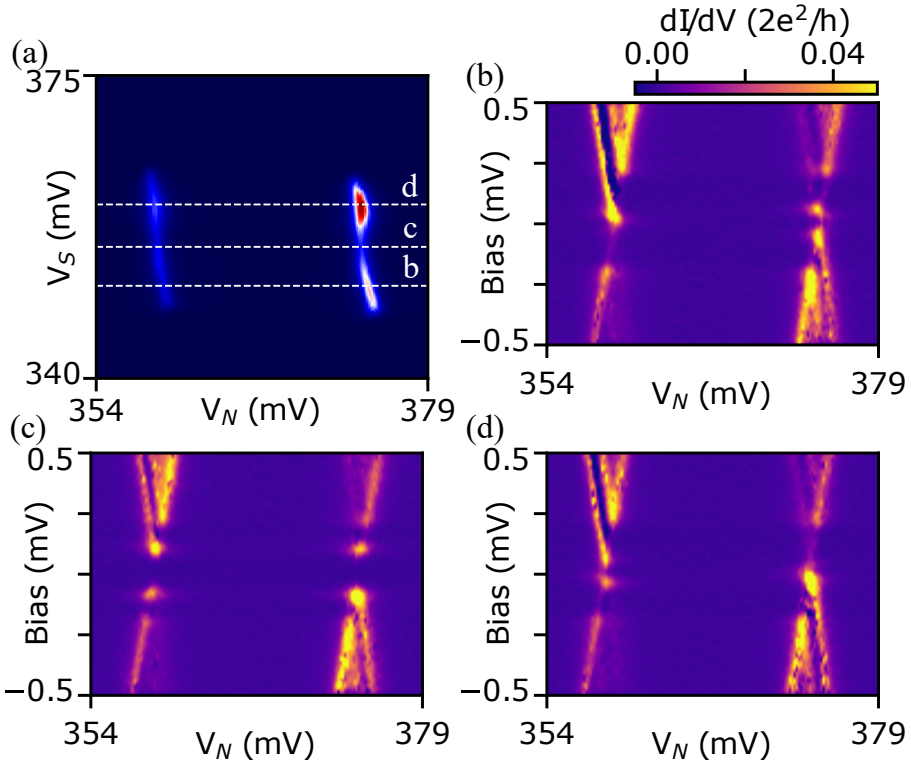

Figure 7.16: (a) This is a repeat from Fig. 7.3 (a). The white dashed lines are traces along which spectra (b-d) are taken. (b-d) Spectra at different V_S values. (b,d) are the same as Fig. 2(c,d). While panel (c) is a new dataset in between (d) and (b).

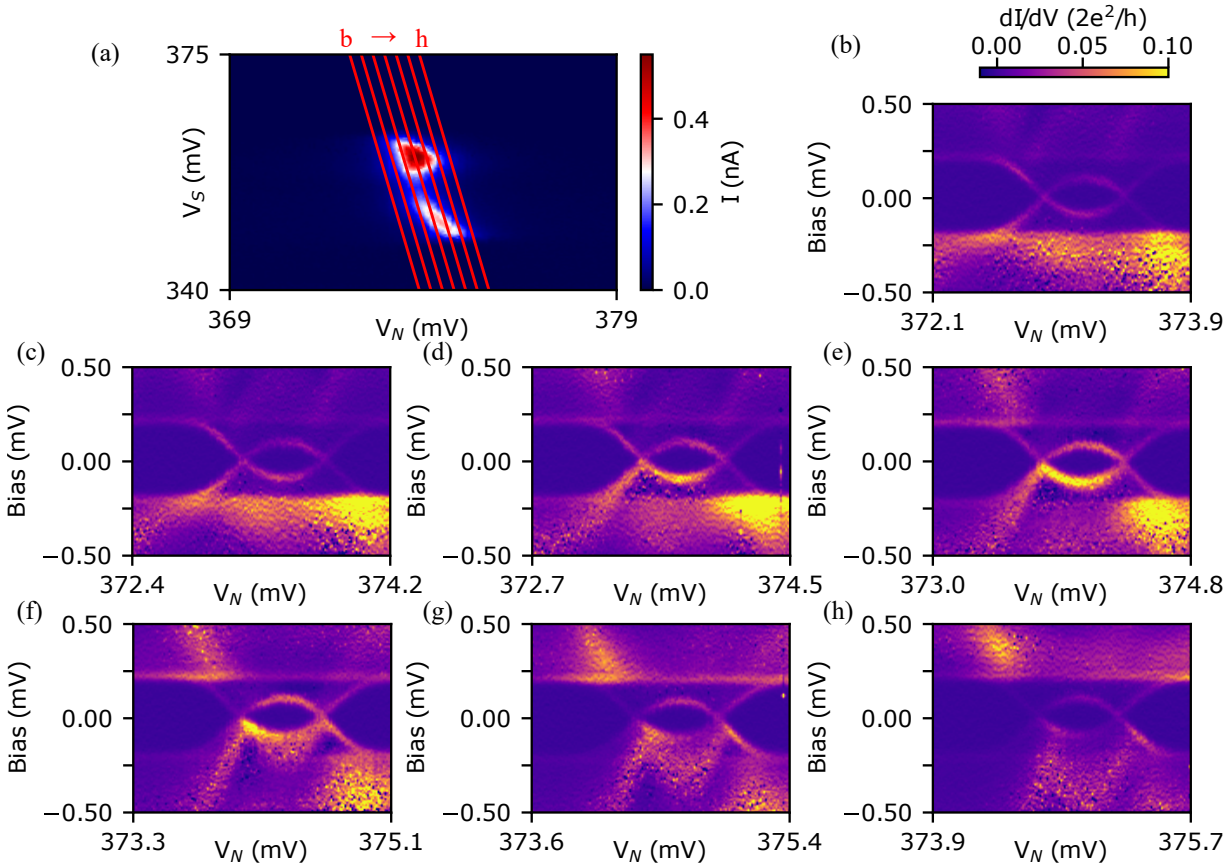

Figure 7.17: Differential conductance spectra for a series of slightly shifting traces in V_S-V_N. (a) is the same as Fig. 7.11(a). Red lines are traces along which spectra (b-h) are taken. The asymmetry between positive-bias and negative-bias Andreev resonance half-loops shows up for cuts taken through the middle of the bias triangles (d-f) but is not apparent for cuts away from that regime.

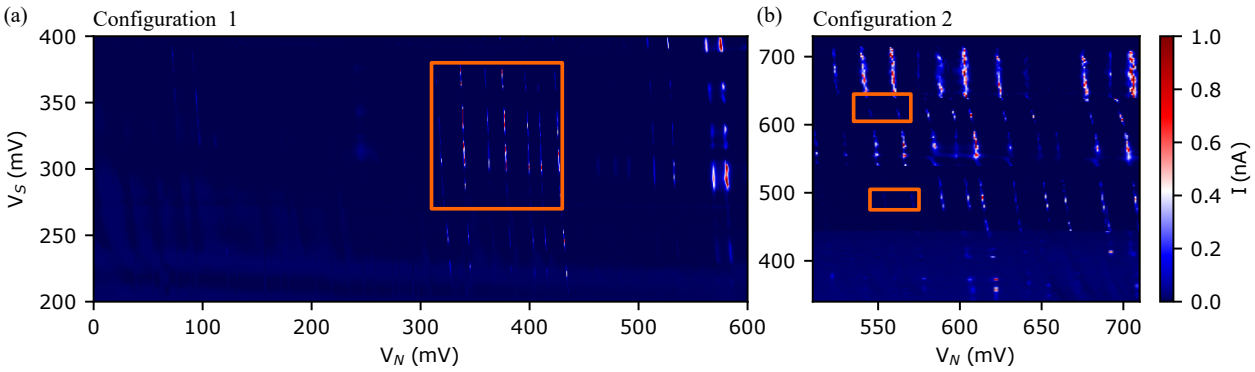

Figure 7.18: (a) The rectangle shows the regime in Fig. 7.4. There is a charge jump near $V_N = 407$ mV due to the instability caused by the large scan range. (b) The same device in another gate voltage configuration was obtained by re-tuning all six gates. This panel contains data from seven small-range scans. The rectangles indicate regimes where data in Fig. 7.19 and Fig. 7.20 are taken.

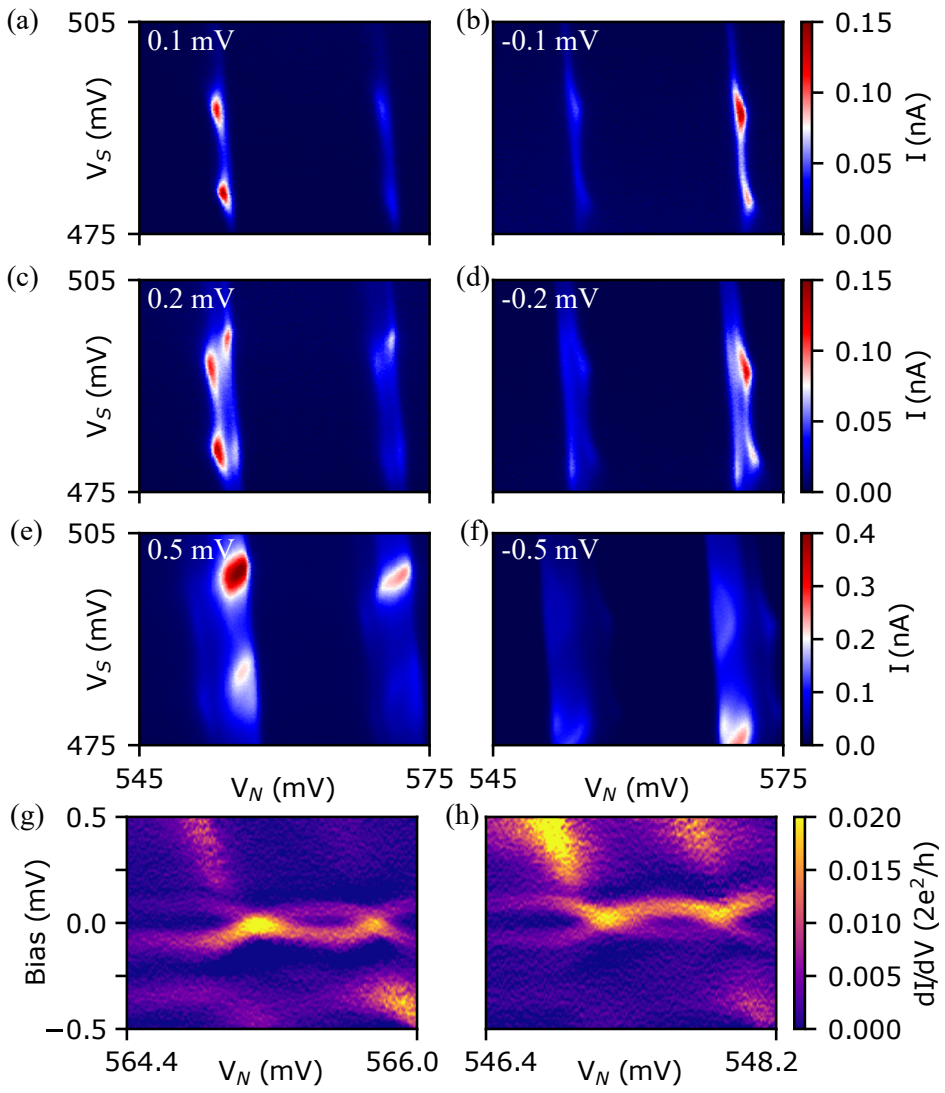

Figure 7.19: A different regime with a different gate voltage configuration (see Fig. 7.18). The stability diagrams show bias asymmetry that is similarly consistent with Andreev blockade. However, in this regime, the pattern does not clearly repeat over multiple periods as it does in Fig. 7.4. (a-f) The bias is noted in each panel. Spectra of QD_S are taken when QD_N is at (g) right and (h) left degeneracy point.

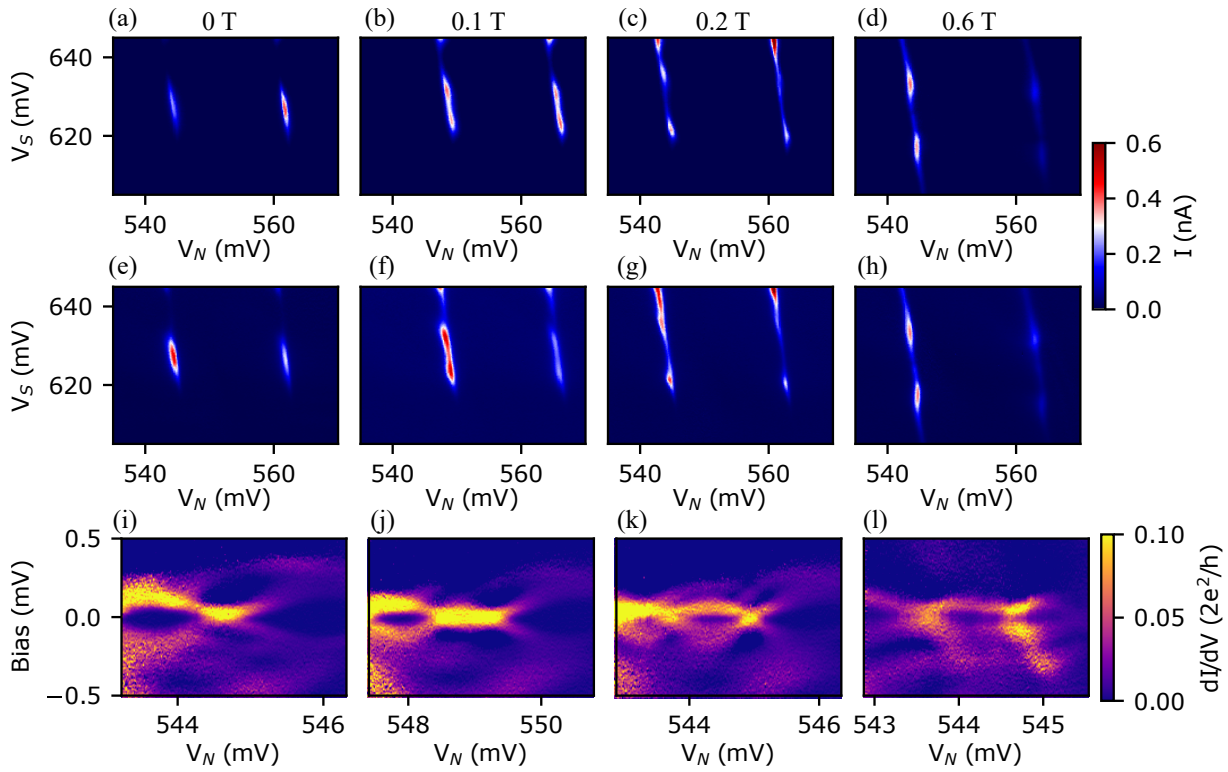

Figure 7.20: A different regime with a different gate-voltage configuration (see Fig. 7.18). The stability diagrams show bias asymmetry consistent with Andreev blockade. The asymmetry does not obviously repeat in adjacent degeneracy points. The dot QD_S is stronger coupled to the superconducting lead such that the Andreev loop containing the odd-parity region is reduced to a point, and we observe a single degeneracy point on the left and a single on the right at zero magnetic field. At finite field, the pattern of four degeneracy points is restored at QD_S undergoes a quantum phase transition, and the odd-parity region develops. (a-d) -0.05 mV. (e-h) 0.05 mV. Spectra of QD_S are taken along traces near QD_N's 0-1 transition.

7.8.2 Data from other devices

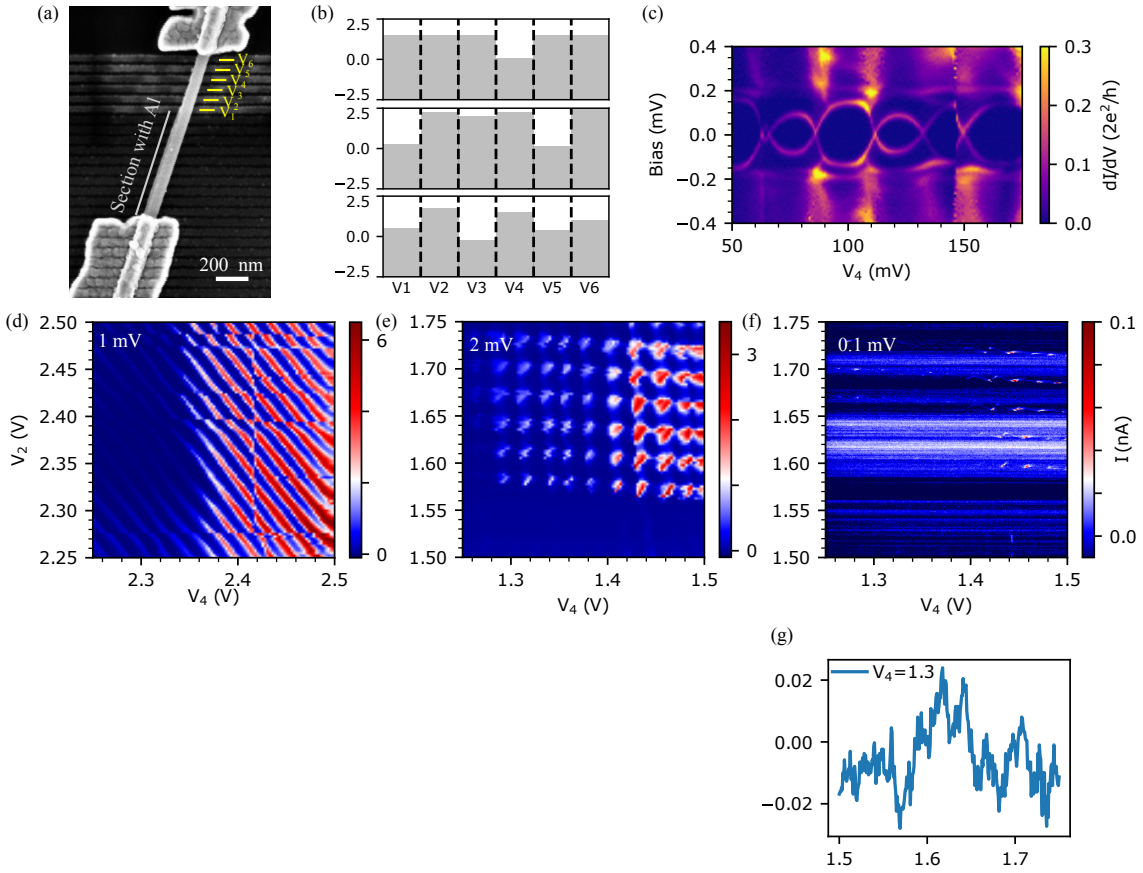

Figure 7.21: Characterization of Device B. (a) The SEM image. (b) Gate voltage configurations for data in panel c (top), d (middle), and e-f (bottom). The device can be tuned from a single dot regime (panel c, spectrum, and panel d, stability diagram) to a double dot regime (panel e-f). The bias voltage is indicated in white in each stability diagram. (g) linecut for (f) at $V_4 = 1.3$V.

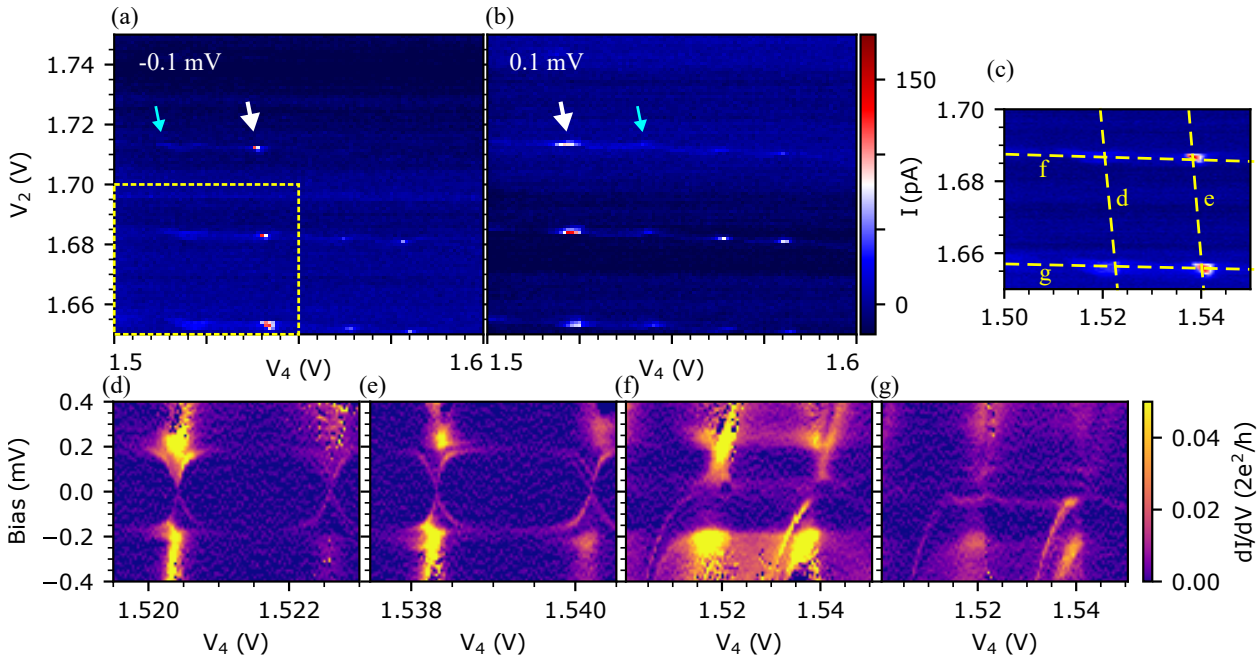

Figure 7.22: (a-b) Device B in a regime that shows bias asymmetry. The large white and small blue arrows indicate columns that have high and low currents. The pattern does not obviously repeat itself along the V_4 direction. We can not conclude whether the bias asymmetry is due to a coincidence or due to Andreev blockade. (c) The rectangle-enclosed regime in panel a. Dashed lines are traces along which spectrum (d-g) are taken. Andreev bound states in QD_S have weak and squared-shape loops (d-e) due to relatively large charging energy.

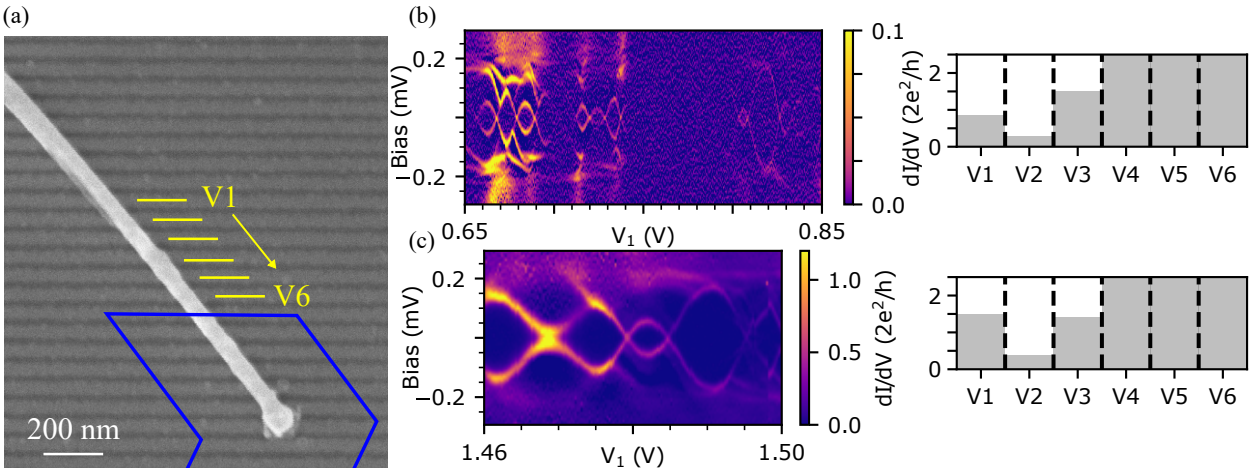

Figure 7.23: Characterization of Device C. (a) The SEM picture after etching. The blue polygon is the design pattern for the normal lead. (b-c) Spectra taken by tuning V_1 Andreev bound states. The gate voltage configurations are shown on the rightmost column.

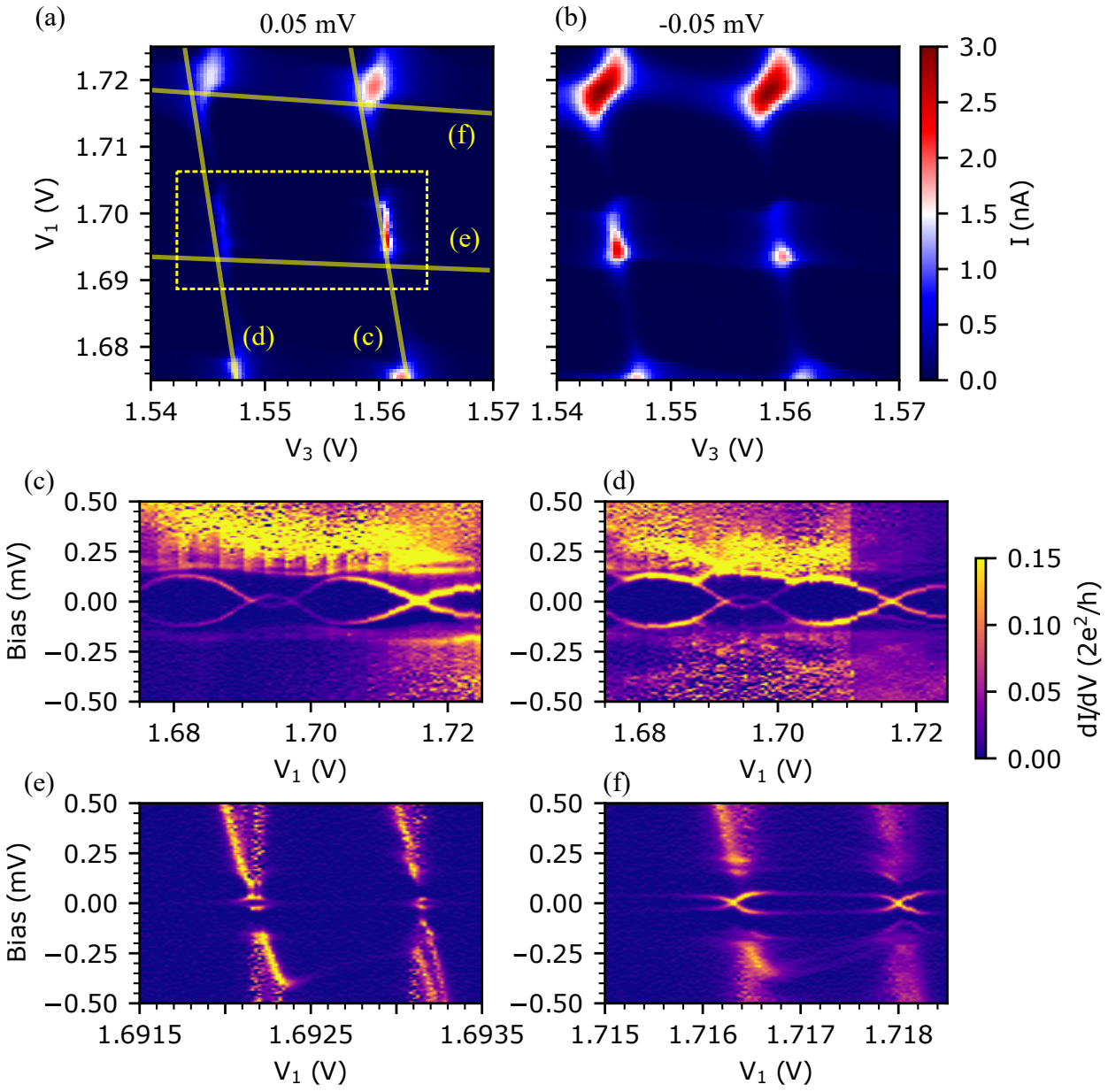

Figure 7.24: (a-b) Stability diagrams of device C. Yellow lines are traces along which the spectra in panels (c-f) are taken. The dashed rectangle highlights a regime where there is bias asymmetry.

7.9 Conclusions

We design and investigate an experimental system capable of entering an electron transport blockade regime in which a spin-triplet localized in the path of current is forbidden from entering a spin-singlet superconductor. A double quantum dot is created electrostatically near a superconducting lead in an InAs nanowire. The superconducting lead is a molecular beam epitaxy grown Al shell. The shell is etched away over a wire segment to make room for the double dot and the normal metal gold lead. The quantum dot closest to the normal lead exhibits Coulomb diamonds (Fig. 7.2 (c-d)), the dot closest to the superconducting lead exhibits Andreev bound states and an induced gap (Figs. 7.2 (a-b)). At low voltage bias across the double dot, below the induced gap, transport exhibits patterns that our theory predicted for a four-step Andreev charge transport cycle which arises when two electrons are transported through the double dot. As evidence of Andreev blockade, we find asymmetry between quadruple charge degeneracy points at even-to-odd and odd-to-even transitions in the normal dot. The observed asymmetry has the properties predicted by theory [174]: it is flipped at opposite bias, and it disappears at higher temperature and at higher magnetic field. Experimentally, we find that current is not completely blocked in the regimes we label as Andreev blockade. Our numerical model, based on [174], accounts for this by introducing finite temperature, a soft induced gap, and disorder. We observe the predicted quadruple level degeneracy points of high current and a periodic conductance pattern controlled by the occupation of the normal dot. Even-odd transport asymmetry is lifted with increased temperature and magnetic field. This blockade phenomenon can be used to study spin textures and dynamics in the vicinity of superconductors. It may also find utility in quantum computing devices that utilize Andreev or Majorana states.

Recently larger hard gaps have been induced in semiconductor nanowires in experiments with tin (gap of 0.6 mV) and lead (gap of 1.2 mV) shells [115, 116]. It would be interesting to repeat Andreev blockade experiments using these superconductors. First, a higher ratio of gap to measurement temperature may result in stronger blockade. Second, the ability to work at higher bias and larger charging energies would make the observation of various blockade features such as bias triangles more conclusive and reduce the role that rounding

plays at low biases. Finally, blockade can be studied to higher magnetic fields, allowing for a detailed investigation of spin textures in the parent superconductor.

Several improvements can be made in immediate follow-on work related to materials processing and device fabrication. This would impact Andreev blockade experiments and many works aimed at searching for Majorana modes and building superconductor-semiconductor qubits. For instance, the wet etch degrades the quality of nanowires by introducing defects. The supplementary information in [73, 137] shows that even using the 'standard' etchant for InAs-Al wires may result in InAs damage or Al islands. The use of shadow walls or dry etching is a promising avenue to explore for alleviating these issues.

At the most basic level, Andreev blockade offers a means of studying spin-resolved transport in hybrid devices at zero magnetic field. We foresee the application of Andreev blockade in experiments that probe spin pairing in superconductors. Much like Pauli blockade was used to investigate spin mixing mechanisms in semiconductors due to hyperfine, spin-orbit, or electron-phonon coupling, Andreev blockade can be used to detect triplet pairing or admixtures thereof in the superconducting lead. A two-arm Andreev blockade device with two double dots in parallel can be used as a spin-sensitive probe for crossed Andreev reflection. Quantum dots with superconducting leads are building blocks of Andreev qubits, Kitaev emulators, and topological qubits [149, 47, 29]. These devices may manifest Andreev blockade or utilize it to detect the state of a qubit or an emulator by providing a spin-dependent transport or transition rate element.

8.0 Conclusions and outlook

8.1 Conclusions

Kitaev chain is a theoretical model of a one-dimensional topological superconductor with Majorana zero modes at the two ends of the chain. Intending to emulate this model, in Ch. 4, we study a tight-binding model of a 3-site quantum dot chain. Simulations of the energy spectrum and transport suggest partially-separated Majorana zero modes localize at two end sites within a narrow parameter window. Theory indicates that the triple-dot states acquire Majorana polarization in the fine-tuned regime (Kitaev regime) when Andreev states in all three dots reach zero-energy in a narrow range of magnetic field. A zero-bias peak that extends in magnetic fields would appear. In Ch. 5, we build a chain of three Andreev quantum dots in a semiconductor InSb nanowire. We observe Andreev bound states in each of the three dots and study their magnetic field and gate dependence. However, in our device, Andreev states in one of the dots reach zero-energy at a lower field than in the other two, placing the Kitaev regime with Majorana end modes out of reach. Our Andreev quantum dot chain experiment has two major limitations. (i) Despite a large degree of control over Andreev states in multiple dots, our devices are still off from the Kitaev chain regime. Devices with greater uniformity and tunability should realize the Kitaev chain with a high yield. This remains challenging for device fabrication with ex-situ oxide removal and contact deposition, in which disorder is easily introduced. (ii) A hard induced superconducting gap surviving to higher magnetic fields and further optimized coupling between the nanowire and the superconductor are desired.

To solve the limitations, in Ch. 6, we present a study of hybrid InSb/Sn nanowire devices fabricated with in-situ shadow technique. A hard induced superconducting gap that persists up to 4 T in magnetic field is observed. A small island of Sn-InSb exhibits the two-electron charging effect, a hallmark of charge parity stability. In Ch. 7, we study Andreev blockade phenomenon, in which a hard superconducting gap is required. We build a double quantum dot in a hybrid InAs/Al nanowire. One normal dot exhibits Coulomb diamonds, and the

other superconducting dot exhibits Andreev bound states and an induced gap. At voltage bias below the induced gap, the double dot could enter Andreev blockade regime, in which an electron of the spin-triplet state is forbidden from entering a spin-singlet superconductor. We observe asymmetry between quadruple charge degeneracy points at even-to-odd and odd-to-even transitions in the normal dot with predicted signatures of Andreev blockade. Even-odd transport asymmetry is lifted with increased temperature and magnetic field.

8.2 Outlook

As an alternative approach to realizing Majorana zero modes other than a continuous wire, a chain of quantum dots can help overcome the disorder and allows spatially resolved transport measurements. The device geometry (multiple contacts and local gates) enables identifying where the states that generate zero-bias peaks are localized along the chain. For both continuous wires and quantum dot chains, multi-terminal is suitable for studying the correlation of two end states with non-local measurements and distinguish delocalized Majorana bound states from localized Andreev bound states. Therefore, applying this technique in future devices will lead to the successful identification of the Kitaev chain regime and definitive proof of well-separated Majorana zero modes.

Our Andreev quantum dot chain experiment is limited by a soft induced gap of thin and narrow NbTiN contacts nonuniformly deposit ex-situ. Superconducting materials with large and hard gap can be used, such as Sn [115] or Pb [116]. With a hard superconducting gap persisting in a much larger magnetic field, Andreev resonances can still be prominent and in high contrast. To avoid ex-situ etching, various in-situ shadow lithography techniques have been used for superconductor deposition [71, 72, 73].

However, the in-situ shadow lithography techniques for hard-gap superconductor deposition, such as Sn and Pb, are only available to the semiconductor nanowire/superconductor shell geometry. Because as discussed in Sec. 6.5, a thin and uniform superconducting shell is the key to hard-gap and field-resilient superconductivity. It means the advanced nanowires with hard-gap superconductors (such as those used for experiments in Chs. 6 and 7) have to

be in a core/shell geometry. Therefore, they are inapplicable for a three-terminal geometry, as contacting the shell through ex-situ deposition of a superconducting lead (as thick as the nanowire diameter) would damage the thin and uniform shell, which is required for a hard gap.

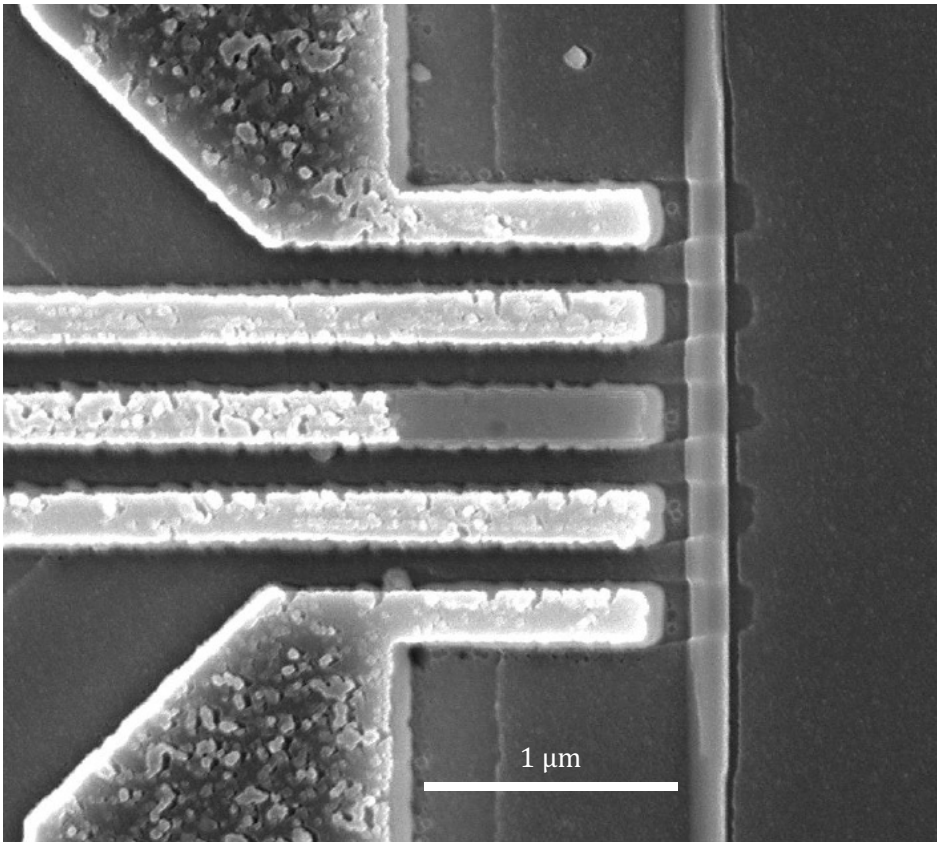

Figure 8.1: Hybrid InAs SAG nanowire/Al with shadow wall structures for quantum dot chain.

Selective-area grown (SAG) nanowires [75, 76, 77] with carefully designed shadow wall structures present a promising platform for multi-terminal experiments on hybrid semiconductor SAG nanowire/superconductor structures through in-situ superconductor deposition [72, 73, 78].

SAG semiconductor nanowires often suffer from a high density of defects due to lattice and symmetry mismatch between the nanowire material and the substrate. This results in poor electrical characteristics, including low electron mobility and low coherence lengths.

Low electron mobility and low coherence lengths suggest that it is not suitable for realizing Majorana zero modes in a continuous SAG nanowire. Further development of SAG growth may eventually solve this problem. For example, lateral heterostructures growth can potentially help with this issue by incorporating buffer layers to reduce lattice mismatch and using capping layers to reduce surface scattering.

However, the low electron mobility of SAG nanowire is not a problem for realizing Majorana zero modes in a quantum dot chain. Fig. 8.1 shows a SAG InAs nanowire with selective grown Al superconducting contacts achieved by a shadow wall structure and angle superconductor deposition discussed in Sec. 3.3.2. The SAG InAs nanowire is covered by smooth Al superconducting contacts separated by abrupt shadowed regions free of Al. Without the screening effect of the superconductor, tunnel barriers can be created in the InAs nanowire segments of the shadowed regions through side gates (to be fabricated). These gate-controlled tunnel barriers can define quantum dots in the nanowire. As shown in Fig. 3.12 (e), depending on the crystallographic directions, SAG nanowires can have different cross-sectional shapes. With angled deposition, a thin superconducting contact can fully cover nanowire facets and extend. It allows using the extended superconducting contacts as probe electrodes rather than superconducting islands, enabling the multi-terminal measurements.

Appendix A Fabrication recipes

A.1 Substrate preparation

1. Ultrasonicate chip in Acetone for 5 min.
2. Ultrasonicate chip in IPA for 5 min.
3. Rinse chip in IPA.
4. Blow dry by N2.
5. Bake at 120C for 2 min.
6. Oxygen plasma cleaning with 200 W at 500 mTorr for 2 min.

A.2 Standard EBL process

1. Spincoat PMMA 950 A4 at 4000rpm for 1 min, bake at 175C for 15 min.
2. EBL at 10kV with 10/30/60 μm aperture and $\approx 135 \mu C/cm^2$ dosage.
3. Develop in MIBK/IPA(1:3) for 1 min and in IPA for 1 min.
4. Resist residual removal by oxygen plasma cleaning with 200 W at 500 mTorr for 15 s.

A.3 Markers

1. Standard EBL process to define markers.
2. Evaporation of 5 nm Ti and 50 nm Au.
3. Lift off in Acetone for at least 2 hours.

A.4 Deposition of HfO_x

1. Standard EBL process to define windows for dielectric layer on local gates.
2. Set temperature of all stages to 120C.
3. Set temperature of precursor tetrakis dimethylamino hafnium (TDMAHf) to 75C.
4. ALD thermal deposition of $\approx 10nm$ HfO_x for 100 cycles.
5. Lift off in Acetone for at least 2 hours.

A.5 Deposition of superconducting contacts

1. SEM imaging of nanowires and design contact patterns.
2. Standard EBL process to define contacts.
3. Oxide removal by sulfur passivation with 1:200 concentration at 60 C for 30 min.
4. Rinse chip in DI water and blow dry.
5. Mount chip on sample holder with a 30 degree wedge (for deposition with an angle of 60 degree).
6. Load sample in load-lock, turn on turbo pump and wait for pressure to drop below 5×10^{-b} Torr. Then transfer sample into AJA main vacuum chamber and wait for pressure to reach UHV. A typical pressure of 1.5×10^{-8} Torr can be achieved by a cryogenic pump in less than 2 hours. For a better vacuum below 1×10^{-8} Torr, a short thermal evaporation of Ti can be applied.
7. Nanowire surface cleaning by gentle in-situ sputter cleaning with 20 W at 10 mTorr for 10 s.
8. Sputter deposition of 5 nm NbTi and 60 nm NbTiN at 3 mTorr.
9. Lift off in Acetone for at least 2 hours.

A.6 Deposition of normal contacts

1. SEM imaging of nanowires and design gate and contact patterns.
2. Standard EBL process to define contacts.
3. Oxide removal by sulfur passivation with 1:200 concentration at 60 C for 30 min.
4. Rinse chip in DI water and blow dry.
5. Load sample in Plassys MEB 500 vacuum chamber wait for pressure to reach UHV. A typical pressure is 2×10^{-8} mbar.
6. Evaporation of 10 nm Ti and 145 nm Au.
7. Lift off in Acetone for at least 2 hours.

A.7 Sulfur passivation

1. Mix 0.29 g elemental sulfur with 3 mL ammonium sulfide to get ammonium polysulfide $(NH_4)_2S_x$ solution.
2. Dilute ammonium polysulfide solution with DI water at a ratio of 1:200.
3. Put device chip into a beaker with 5 mL diluted ammonium polysulfide solution and heat in a water bath at 60 C for 30 min. Wrap the beaker in aluminum foil to avoid light exposure.
4. Rinse chip in DI water and blow dry.

A.8 Fabrication with hybrid InSb/Sn nanowires

1. SEM imaging of nanowires and design gate and contact patterns.
2. Spincoat PMMA 950 A4 at 4000rpm for 1 min. To prevent heating the superconducting shell from baking the resist, leave the chip in vacuum at room temperature for the resist to dry.
3. Standard EBL process to define contacts.

4. Oxide removal by Ar ion milling at 250 V with 15 mA for 1 min.
5. Evaporation of 10 nm Ti and 140 nm Au.
6. Lift off in Acetone for at least 2 hours.

A.9 Fabrication with hybrid InAs/Al nanowires

1. SEM imaging of nanowires and design gate and contact patterns.
2. Spincoat PMMA 950 A4 at 4000rpm for 1 min, dry in vacuum.
3. Standard EBL process to define windows for Al etching.
4. Selective Al etching by MF CD-26 developer/DI water a volume ratio of 1:20 for 2 min.
5. Spincoat PMMA 950 A4 at 4000rpm for 1 min, dry in vacuum.
6. Standard EBL process to define contacts.
7. Oxide removal by Ar ion milling at 250 V with 15 mA for 1 min.
8. Evaporation of 10 nm Ti and 130 nm Au.
9. Lift off in Acetone for at least 2 hours.

A.10 Fabrication with SAG InAs nanowires with Al or Sn shells

1. SEM imaging of nanowires and design gate and contact patterns.
2. Spincoat PMMA 950 A4 at 4000rpm for 1 min, dry in vacuum.
3. Evaporation of 10 nm Al as an anti-charging layer for EBL.
4. EBL at 10kV with 10/30/60 μm aperture and $\approx 135 \mu C/cm^2$ dosage.
5. Removal of the anti-charging layer by MF CD-26 developer for 2 min.
6. Develop in MIBK/IPA(1:3) for 1 min and in IPA for 1 min.
7. Resist residual removal by oxygen plasma cleaning with 200 W at 500 mTorr for 15 s.
8. Selective removal of superconductors.
    - Selective removal of Al by etching with MF CD-26 developer/DI water a volume ratio of 1:20 for 2 min.

- Selective removal of Sn by Ar ion milling at 500 V with 25 mA for 3 min.

9. Lift off in remover PG.
10. Spincoat PMMA 950 A4 at 4000rpm for 1 min, dry in vacuum.
11. Standard EBL process to define contacts.
12. Oxide removal by Ar ion milling at 250 V with 15 mA for 1 min.
13. Evaporation of 5 nm Ti and 100 nm Au.
14. Lift off in remover PG.
15. ALD thermal deposition of 10 nm HfO_x at 90 C.
16. Spincoat PMMA 950 A4 at 4000rpm for 1 min, dry in vacuum.
17. Standard EBL process to define top gates.
18. Evaporation of 5 nm Ti and 120 nm Au.
19. Lift off in Acetone.

Appendix B List of publications

Hao Wu, Po Zhang, John P. T. Stenger, Zhaoen Su, Jun Chen, Ghada Badawy, Sasa Gazibegovic, Erik P. A. M. Bakkers, and Sergey M. Frolov, Triple andreev dot chains in semiconductor nanowires (2021), arXiv:2105.08636.

Po Zhang, **Hao Wu**, Jun Chen, Sabbir A. Khan, Peter Krogstrup, David Pekker, and Sergey M. Frolov, Evidence of andreev blockade in a double quantum dot coupled to a superconductor (2021), arXiv:2102.03283.

M. Pendharkar, B. Zhang, **H. Wu (co-first author)**, A. Zarassi, P. Zhang, C. P. Dempsey, J. S. Lee, S. D. Harrington, G. Badawy, S. Gazibegovic, R. L. M. Op het Veld, M. Rossi, J. Jung, A.H. Chen, M. A. Verheijen, M. Hocevar, E. P. A. M. Bakkers, C. J. Palmstrom, and S. M. Frolov, Parity-preserving and magnetic field-resilient superconductivity in InSb nanowires with Sn shells, Science **372**, 508-511 (2021).

Z. Su, R. Zitko, P. Zhang, **H. Wu**, D. Car, S. R. Plissard, S. Gazibegovic, G. Badawy, M. Hocevar, J. Chen, E. P. A. M. Bakkers, and S. M. Frolov, Erasing odd-parity states in semiconductor quantum dots coupled to superconductors, Phys. Rev. B **101**, 235315 (2020).

Bibliography

[1] Anasua Chatterjee, Paul Stevenson, Silvano De Franceschi, Andrea Morello, Nathalie P. de Leon, and Ferdinand Kuemmeth. Semiconductor qubits in practice. *Nature Reviews Physics*, 3(3):157–177, Feb 2021.

[2] P. Krantz, M. Kjaergaard, F. Yan, T. P. Orlando, S. Gustavsson, and W. D. Oliver. A quantum engineer's guide to superconducting qubits. *Applied Physics Reviews*, 6(2):021318, 2019.

[3] M. D. Shulman, O. E. Dial, S. P. Harvey, H. Bluhm, V. Umansky, and A. Yacoby. Demonstration of entanglement of electrostatically coupled singlet-triplet qubits. *Science*, 336(6078):202–205, 2012.

[4] Dohun Kim, Zhan Shi, C. B. Simmons, D. R. Ward, J. R. Prance, Teck Seng Koh, John King Gamble, D. E. Savage, M. G. Lagally, Mark Friesen, S. N. Coppersmith, and Mark A. Eriksson. Quantum control and process tomography of a semiconductor quantum dot hybrid qubit. *Nature*, 511(7507):70–74, Jul 2014.

[5] M. Veldhorst, C. H. Yang, J. C. C. Hwang, W. Huang, J. P. Dehollain, J. T. Muhonen, S. Simmons, A. Laucht, F. E. Hudson, K. M. Itoh, A. Morello, and A. S. Dzurak. A two-qubit logic gate in silicon. *Nature*, 526(7573):410–414, October 2015.

[6] J. Medford, J. Beil, J. M. Taylor, S. D. Bartlett, A. C. Doherty, E. I. Rashba, D. P. DiVincenzo, H. Lu, A. C. Gossard, and C. M. Marcus. Self-consistent measurement and state tomography of an exchange-only spin qubit. *Nature Nanotechnology*, 8(9):654–659, Sep 2013.

[7] T. A. Baart, M. Shafiei, T. Fujita, C. Reichl, W. Wegscheider, and L. M. K. Vandersypen. Single-spin ccd. *Nature Nanotechnology*, 11(4):330–334, Apr 2016.

[8] Charles Tahan. Democratizing spin qubits. *arXiv preprint arXiv:2001.08251*, 2020.

[9] T. F. Watson, S. G. J. Philips, E. Kawakami, D. R. Ward, P. Scarlino, M. Veldhorst, D. E. Savage, M. G. Lagally, Mark Friesen, S. N. Coppersmith, M. A. Eriksson, and L. M. K. Vandersypen. A programmable two-qubit quantum processor in silicon. *Nature*, 555(7698):633–637, Mar 2018.

[10] W. Huang, C. H. Yang, K. W. Chan, T. Tanttu, B. Hensen, R. C. C. Leon, M. A. Fogarty, J. C. C. Hwang, F. E. Hudson, K. M. Itoh, A. Morello, A. Laucht, and A. S. Dzurak. Fidelity benchmarks for two-qubit gates in silicon. *Nature*, 569(7757):532–536, May 2019.

[11] T. Hensgens, T. Fujita, L. Janssen, Xiao Li, C. J. Van Diepen, C. Reichl, W. Wegscheider, S. Das Sarma, and L. M. K. Vandersypen. Quantum simulation of a fermi–hubbard model using a semiconductor quantum dot array. *Nature*, 548(7665):70–73, Aug 2017.

[12] J. P. Dehollain, U. Mukhopadhyay, V. P. Michal, Y. Wang, B. Wunsch, C. Reichl, W. Wegscheider, M. S. Rudner, E. Demler, and L. M. K. Vandersypen. Nagaoka ferromagnetism observed in a quantum dot plaquette. *Nature*, 579(7800):528–533, Mar 2020.

[13] C. J. van Diepen, T. K. Hsiao, U. Mukhopadhyay, C. Reichl, W. Wegscheider, and L. M. K. Vandersypen. Quantum simulation of antiferromagnetic heisenberg chain with gate-defined quantum dots, 2021.

[14] M Hays, V Fatemi, K Serniak, D Bouman, S Diamond, G de Lange, P Krogstrup, J Nygård, A Geresdi, and MH Devoret. Continuous monitoring of a trapped superconducting spin. *Nature Physics*, 16(11):1103–1107, 2020.

[15] Austin G. Fowler, Matteo Mariantoni, John M. Martinis, and Andrew N. Cleland. Surface codes: Towards practical large-scale quantum computation. *Phys. Rev. A*, 86:032324, Sep 2012.

[16] R. Barends, J. Kelly, A. Megrant, A. Veitia, D. Sank, E. Jeffrey, T. C. White, J. Mutus, A. G. Fowler, B. Campbell, Y. Chen, Z. Chen, B. Chiaro, A. Dunsworth, C. Neill, P. O'Malley, P. Roushan, A. Vainsencher, J. Wenner, A. N. Korotkov, A. N. Cleland, and John M. Martinis. Superconducting quantum circuits at the surface code threshold for fault tolerance. *Nature*, 508(7497):500–503, Apr 2014.

[17] C. Nayak, S. H. Simon, A. Stern, M. Freedman, and Sankar S. Das Sarma. Non-abelian anyons and topological quantum computation. *Rev. Mod. Phys.*, 80:1083, Sep 2008.

[18] Meng Cheng, Roman M. Lutchyn, and S. Das Sarma. Topological protection of majorana qubits. *Phys. Rev. B*, 85:165124, Apr 2012.

[19] Sankar Das Sarma, Michael Freedman, and Chetan Nayak. Majorana zero modes and topological quantum computation. *npj Quantum Information*, 1(1):15001, Oct 2015.

[20] David J Clarke, Jason Alicea, and Kirill Shtengel. Exotic non-abelian anyons from conventional fractional quantum hall states. *Nature communications*, 4:1348, 2013.

[21] C. W. J. Beenakker. Search for non-Abelian Majorana braiding statistics in superconductors. *SciPost Phys. Lect. Notes*, page 15, 2020.

[22] Gregory Moore and Nicholas Read. Nonabelions in the fractional quantum hall effect. *Nuclear Physics B*, 360(2-3):362–396, 1991.

[23] D. A. Ivanov. Non-abelian statistics of half-quantum vortices in p-wave superconductors. *Phys. Rev. Lett.*, 86:268–271, Jan 2001.

[24] Liang Fu and C. L. Kane. Superconducting proximity effect and majorana fermions at the surface of a topological insulator. *Phys. Rev. Lett.*, 100:096407, Mar 2008.

[25] Roman M. Lutchyn, Jay D. Sau, and S. Das Sarma. Majorana fermions and a topological phase transition in semiconductor-superconductor heterostructures. *Phys. Rev. Lett.*, 105:077001, Aug 2010.

[26] Yuval Oreg, Gil Refael, and Felix von Oppen. Helical liquids and majorana bound states in quantum wires. *Phys. Rev. Lett.*, 105:177002, Oct 2010.

[27] V. Mourik, K. Zuo, S. M. Frolov, S. R. Plissard, E. P. A. M. Bakkers, and L. P. Kouwenhoven. Signatures of majorana fermions in hybrid superconductor-semiconductor nanowire devices. *Science*, 336(6084):1003–1007, 2012.

[28] M. T. Deng, S. Vaitiekenas, E. B. Hansen, J. Danon, M. Leijnse, K. Flensberg, J. Nygård, P. Krogstrup, and C. M. Marcus. Majorana bound state in a coupled quantum-dot hybrid-nanowire system. *Science*, 354(6319):1557–1562, 2016.

[29] Torsten Karzig, Christina Knapp, Roman M. Lutchyn, Parsa Bonderson, Matthew B. Hastings, Chetan Nayak, Jason Alicea, Karsten Flensberg, Stephan Plugge, Yuval Oreg, Charles M. Marcus, and Michael H. Freedman. Scalable designs for quasiparticle-poisoning-protected topological quantum computation with majorana zero modes. *Phys. Rev. B*, 95:235305, Jun 2017.

[30] B van Heck, A R Akhmerov, F Hassler, M Burrello, and C W J Beenakker. Coulomb-assisted braiding of majorana fermions in a josephson junction array. *New Journal of Physics*, 14(3):035019, mar 2012.

[31] A Yu Kitaev. Unpaired majorana fermions in quantum wires. *Physics-Uspekhi*, 44(10S):131–136, oct 2001.

[32] Topology in condensed matter: tying quantum knots. https://topocondmat.org/.

[33] R. Hanson, L. P. Kouwenhoven, J. R. Petta, S. Tarucha, and L. M. K. Vandersypen. Spins in few-electron quantum dots. *Rev. Mod. Phys.*, 79:1217–1265, Oct 2007.

[34] Tobias Meng, Serge Florens, and Pascal Simon. Self-consistent description of andreev bound states in josephson quantum dot devices. *Phys. Rev. B*, 79:224521, Jun 2009.

[35] Luh Yu. Bound state in superconductors with paramagnetic impurities. *Acta Phys. Sin*, 21(1):75–91, 1965.

[36] Hiroyuki Shiba. Classical spins in superconductors. *Progress of theoretical Physics*, 40(3):435–451, 1968.

[37] A I Rusinov. Theory of gapless superconductivity in alloys with paramagnetic impurities. *Zh. Eksp. Theor. Fiz., 56: 2047-56(June 1969).*, 1 1969.

[38] E. Vecino, A. Martín-Rodero, and A. Levy Yeyati. Josephson current through a correlated quantum level: Andreev states and π junction behavior. *Phys. Rev. B*, 68:035105, Jul 2003.

[39] T. Domański and A. Donabidowicz. Interplay between particle-hole splitting and the kondo effect in quantum dots. *Phys. Rev. B*, 78:073105, Aug 2008.

[40] T. Sand-Jespersen, J. Paaske, B. M. Andersen, K. Grove-Rasmussen, H. I. Jørgensen, M. Aagesen, C. B. Sørensen, P. E. Lindelof, K. Flensberg, and J. Nygård. Kondo-enhanced andreev tunneling in inas nanowire quantum dots. *Phys. Rev. Lett.*, 99:126603, Sep 2007.

[41] Silvano De Franceschi, Leo Kouwenhoven, Christian Schönenberger, and Wolfgang Wernsdorfer. Hybrid superconductor–quantum dot devices. *Nature Nanotechnology*, 5(10):703–711, Oct 2010.

[42] A. Martín-Rodero and A. Levy Yeyati. Josephson and andreev transport through quantum dots. *Advances in Physics*, 60(6):899–958, 2011.

[43] E. J. H. Lee, Xiaocheng Jiang, Manuel Houzet, Ramón Aguado, Charles M. Lieber, and Silvano De Franceschi. Spin-resolved andreev levels and parity crossings in hybrid superconductor–semiconductor nanostructures. *Nature Nanotechnology*, 9:79, 2014.

[44] J. Chen, B. D. Woods, P. Yu, M. Hocevar, D. Car, S. R. Plissard, E. P. A. M. Bakkers, T. D. Stanescu, and S. M. Frolov. Ubiquitous non-majorana zero-bias conductance peaks in nanowire devices. *Phys. Rev. Lett.*, 123:107703, Sep 2019.

[45] Benjamin D. Woods, Sankar Das Sarma, and Tudor D. Stanescu. Charge impurity effects in hybrid majorana nanowires, 2021.

[46] Sankar Das Sarma and Haining Pan. Disorder-induced zero-bias peaks in majorana nanowires. *Phys. Rev. B*, 103:195158, May 2021.

[47] Jay D. Sau and S. Das Sarma. Realizing a robust practical majorana chain in a quantum-dot-superconductor linear array. *Nature Communications*, 3(1):964, 2012.

[48] Ion C Fulga, Arbel Haim, Anton R Akhmerov, and Yuval Oreg. Adaptive tuning of majorana fermions in a quantum dot chain. *New Journal of Physics*, 15(4):045020, apr 2013.

[49] P Zhang and Franco Nori. Majorana bound states in a disordered quantum dot chain. *New Journal of Physics*, 18(4):043033, 2016.

[50] Sébastien R. Plissard, Dorris R. Slapak, Marcel A. Verheijen, Moïra Hocevar, George W. G. Immink, Ilse van Weperen, Stevan Nadj-Perge, Sergey M. Frolov, Leo P. Kouwenhoven, and Erik P. A. M. Bakkers. From insb nanowires to nanocubes: Looking for the sweet spot. *Nano Letters*, 12(4):1794–1798, Apr 2012.

[51] Philippe Caroff, Jakob B. Wagner, Kimberly A. Dick, Henrik A. Nilsson, Mattias Jeppsson, Knut Deppert, Lars Samuelson, L. Reine Wallenberg, and Lars-Erik Wernersson. High-quality inas/insb nanowire heterostructures grown by metal–organic vapor-phase epitaxy. *Small*, 4(7):878–882, 2008.

[52] Önder Gül, David J van Woerkom, Ilse van Weperen, Diana Car, Sébastien R Plissard, Erik P A M Bakkers, and Leo P Kouwenhoven. Towards high mobility InSb nanowire devices. *Nanotechnology*, 26(21):215202, may 2015.

[53] Jakob Kammhuber, Maja C. Cassidy, Hao Zhang, Önder Gül, Fei Pei, Michiel W. A. de Moor, Bas Nijholt, Kenji Watanabe, Takashi Taniguchi, Diana Car, Sébastien R. Plissard, Erik P. A. M. Bakkers, and Leo P. Kouwenhoven. Conductance quantization at zero magnetic field in insb nanowires. *Nano Letters*, 16(6):3482–3486, 2016. PMID: 27121534.

[54] S. Nadj-Perge, V. S. Pribiag, J. W. G. van den Berg, K. Zuo, S. R. Plissard, E. P. A. M. Bakkers, S. M. Frolov, and L. P. Kouwenhoven. Spectroscopy of spin-orbit quantum bits in indium antimonide nanowires. *Phys. Rev. Lett.*, 108:166801, Apr 2012.

[55] I. van Weperen, B. Tarasinski, D. Eeltink, V. S. Pribiag, S. R. Plissard, E. P. A. M. Bakkers, L. P. Kouwenhoven, and M. Wimmer. Spin-orbit interaction in insb nanowires. *Phys. Rev. B*, 91:201413, May 2015.

[56] Henrik A. Nilsson, Philippe Caroff, Claes Thelander, Marcus Larsson, Jakob B. Wagner, Lars-Erik Wernersson, Lars Samuelson, and H. Q. Xu. Giant, level-dependent g factors in insb nanowire quantum dots. *Nano Lett.*, 9(9):3151–3156, September 2009.

[57] Michiel W A de Moor, Jouri D S Bommer, Di Xu, Georg W Winkler, Andrey E Antipov, Arno Bargerbos, Guanzhong Wang, Nick van Loo, Roy L M Op het Veld, Sasa Gazibegovic, Diana Car, John A Logan, Mihir Pendharkar, Joon Sue Lee, Erik P A M Bakkers, Chris J Palmstrøm, Roman M Lutchyn, Leo P Kouwenhoven, and Hao Zhang. Electric field tunable superconductor-semiconductor coupling in majorana nanowires. *New Journal of Physics*, 20(10):103049, oct 2018.

[58] Jingwei Mu, Shaoyun Huang, Ji-Yin Wang, Guang-Yao Huang, Xuming Wang, and H Q Xu. Measurements of anisotropic g-factors for electrons in InSb nanowire quantum dots. *Nanotechnology*, 32(2):020002, oct 2020.

[59] Ghada Badawy, Sasa Gazibegovic, Francesco Borsoi, Sebastian Heedt, Chien-An Wang, Sebastian Koelling, Marcel A. Verheijen, Leo P. Kouwenhoven, and E. P. A. M. Bakkers. High mobility stemless insb nanowires. *Nano Letters*, 19(6):3575–3582, Jun 2019.

[60] Philippe Caroff, Maria E Messing, B Mattias Borg, Kimberly A Dick, Knut Deppert, and Lars-Erik Wernersson. InSb heterostructure nanowires: MOVPE growth under extreme lattice mismatch. *Nanotechnology*, 20(49):495606, nov 2009.

[61] Kilian Flöhr, Marcus Liebmann, Kamil Sladek, H. Yusuf Günel, Robert Frielinghaus, Fabian Haas, Carola Meyer, Hilde Hardtdegen, Thomas Schäpers, Detlev

Grützmacher, and Markus Morgenstern. Manipulating inas nanowires with submicrometer precision. *Review of Scientific Instruments*, 82(11):113705, 2011.

[62] Önder Gül, Hao Zhang, Folkert K. de Vries, Jasper van Veen, Kun Zuo, Vincent Mourik, Sonia Conesa-Boj, Michał P. Nowak, David J. van Woerkom, Marina Quintero-Pérez, et al. Hard superconducting gap in insb nanowires. *Nano Letters*, 17(4):2690, 2017.

[63] D B Suyatin, C Thelander, M T Björk, I Maximov, and L Samuelson. Sulfur passivation for ohmic contact formation to InAs nanowires. *Nanotechnology*, 18(10):105307, feb 2007.

[64] P. Krogstrup, N. L. B. Ziino, W. Chang, S. M. Albrecht, M. H. Madsen, E. Johnson, J. Nygård, C. M. Marcus, and T. S. Jespersen. Epitaxy of semiconductor–superconductor nanowires. *Nature Materials*, 14:400, 2015.

[65] Tudor D. Stanescu and S. Das Sarma. Superconducting proximity effect in semiconductor nanowires. *Phys. Rev. B*, 87:180504, May 2013.

[66] So Takei, Benjamin M. Fregoso, Hoi-Yin Hui, Alejandro M. Lobos, and S. Das Sarma. Soft superconducting gap in semiconductor majorana nanowires. *Phys. Rev. Lett.*, 110:186803, Apr 2013.

[67] W Chang, S. M. Albrecht, T. S. Jespersen, F. Kuemmeth, P. Krogstrup, J. Nygård, and C. M. Marcus. Hard gap in epitaxial semiconductor–superconductor nanowires. *Nat Nano*, 10:232, 2015.

[68] S. M. Albrecht, A. P. Higginbotham, M. Madsen, F. Kuemmeth, T. S. Jespersen, J. Nygård, P. Krogstrup, and C. M. Marcus. Exponential protection of zero modes in majorana islands. *Nature*, 531:206, 2016.

[69] S. Vaitiekenas, G. W. Winkler, B. van Heck, T. Karzig, M.-T. Deng, K. Flensberg, L. I. Glazman, C. Nayak, P. Krogstrup, R. M. Lutchyn, and C. M. Marcus. Flux-induced topological superconductivity in full-shell nanowires. *Science*, 367(6485), 2020.

[70] S. Vaitiekėnas, M.-T. Deng, J. Nygård, P. Krogstrup, and C. M. Marcus. Effective g factor of subgap states in hybrid nanowires. *Phys. Rev. Lett.*, 121:037703, Jul 2018.

[71] Sasa Gazibegovic, Diana Car, Hao Zhang, Stijn C. Balk, John A. Logan, Michiel W. A. de Moor, Maja C. Cassidy, Rudi Schmits, Di Xu, Guanzhong Wang, Peter Krogstrup,

Roy L. M. Op het Veld, Kun Zuo, Yoram Vos, Jie Shen, Daniël Bouman, Borzoyeh Shojaei, Daniel Pennachio, Joon Sue Lee, Petrus J. van Veldhoven, Sebastian Koelling, Marcel A. Verheijen, Leo P. Kouwenhoven, Chris J. Palmstrøm, and Erik P. A. M. Bakkers. Epitaxy of advanced nanowire quantum devices. *Nature*, 548(7668):434–438, 2017.

[72] Sebastian Heedt, Marina Quintero-Pérez, Francesco Borsoi, Alexandra Fursina, Nick van Loo, Grzegorz P. Mazur, Michał P. Nowak, Mark Ammerlaan, Kongyi Li, Svetlana Korneychuk, Jie Shen, May An Y. van de Poll, Ghada Badawy, Sasa Gazibegovic, Nick de Jong, Pavel Aseev, Kevin van Hoogdalem, Erik P. A. M. Bakkers, and Leo P. Kouwenhoven. Shadow-wall lithography of ballistic superconductor–semiconductor quantum devices. *Nature Communications*, 12(1):4914, Aug 2021.

[73] Damon J. Carrad, Martin Bjergfelt, Thomas Kanne, Martin Aagesen, Filip Krizek, Elisabetta M. Fiordaliso, Erik Johnson, Jesper Nygård, and Thomas Sand Jespersen. Shadow epitaxy for in situ growth of generic semiconductor/superconductor hybrids. *Advanced Materials*, 32(23):1908411, 2020.

[74] James L. Webb, Johan Knutsson, Martin Hjort, Sepideh Gorji Ghalamestani, Kimberly A. Dick, Rainer Timm, and Anders Mikkelsen. Electrical and surface properties of inas/insb nanowires cleaned by atomic hydrogen. *Nano Letters*, 15(8):4865–4875, Aug 2015.

[75] S. Vaitiekėnas, A. M. Whiticar, M.-T. Deng, F. Krizek, J. E. Sestoft, C. J. Palmstrøm, S. Marti-Sanchez, J. Arbiol, P. Krogstrup, L. Casparis, and C. M. Marcus. Selective-area-grown semiconductor-superconductor hybrids: A basis for topological networks. *Phys. Rev. Lett.*, 121:147701, Oct 2018.

[76] Joon Sue Lee, Sukgeun Choi, Mihir Pendharkar, Daniel J. Pennachio, Brian Markman, Michael Seas, Sebastian Koelling, Marcel A. Verheijen, Lucas Casparis, Karl D. Petersson, Ivana Petkovic, Vanessa Schaller, Mark J. W. Rodwell, Charles M. Marcus, Peter Krogstrup, Leo P. Kouwenhoven, Erik P. A. M. Bakkers, and Chris J. Palmstrøm. Selective-area chemical beam epitaxy of in-plane inas one-dimensional channels grown on inp(001), inp(111)b, and inp(011) surfaces. *Phys. Rev. Materials*, 3:084606, Aug 2019.

[77] Roy L. M. Op het Veld, Di Xu, Vanessa Schaller, Marcel A. Verheijen, Stan M. E. Peters, Jason Jung, Chuyao Tong, Qingzhen Wang, Michiel W. A. de Moor, Bart Hesselmann, Kiefer Vermeulen, Jouri D. S. Bommer, Joon Sue Lee, Andrey Sarikov, Mihir Pendharkar, Anna Marzegalli, Sebastian Koelling, Leo P. Kouwenhoven, Leo Miglio, Chris J. Palmstrøm, Hao Zhang, and Erik P. A. M. Bakkers. In-plane selective

area insb–al nanowire quantum networks. *Communications Physics*, 3(1):59, Mar 2020.

[78] Jason Jung, Roy L. M. Op het Veld, Rik Benoist, Orson A. H. van der Molen, Carlo Manders, Marcel A. Verheijen, and Erik P. A. M. Bakkers. Universal platform for scalable semiconductor-superconductor nanowire networks, 2021.

[79] Frank Pobell. *Matter and methods at low temperatures*, volume 2. Springer, 2007.

[80] QT designed instrumentation. http://qtwork.tudelft.nl/ schouten/ivvi/index-ivvi.htm.

[81] QTLab measurement environment. http://qtlab.sourceforge.net/.

[82] Jun Chen, Peng Yu, John Stenger, Moïra Hocevar, Diana Car, Sébastien R. Plissard, Erik P. A. M. Bakkers, Tudor D. Stanescu, and Sergey M. Frolov. Experimental phase diagram of zero-bias conductance peaks in superconductor/semiconductor nanowire devices. *Science Advances*, 3(9), 2017.

[83] Chun-Xiao Liu, Jay D. Sau, Tudor D. Stanescu, and S. Das Sarma. Andreev bound states versus majorana bound states in quantum dot-nanowire-superconductor hybrid structures: Trivial versus topological zero-bias conductance peaks. *Phys. Rev. B*, 96:075161, Aug 2017.

[84] Yi-Hua Lai, Jay D. Sau, and Sankar Das Sarma. Presence versus absence of end-to-end nonlocal conductance correlations in majorana nanowires: Majorana bound states versus andreev bound states. *Phys. Rev. B*, 100:045302, Jul 2019.

[85] Elsa Prada, Pablo San-Jose, Michiel W. A. de Moor, Attila Geresdi, Eduardo J. H. Lee, Jelena Klinovaja, Daniel Loss, Jesper Nygård, Ramón Aguado, and Leo P. Kouwenhoven. From andreev to majorana bound states in hybrid superconductor–semiconductor nanowires. *Nature Reviews Physics*, 2(10):575–594, Oct 2020.

[86] Fernando Domínguez, Jorge Cayao, Pablo San-Jose, Ramón Aguado, Alfredo Levy Yeyati, and Elsa Prada. Zero-energy pinning from interactions in majorana nanowires. *npj Quantum Materials*, 2(1):13, Mar 2017.

[87] Benjamin D. Woods, Jun Chen, Sergey M. Frolov, and Tudor D. Stanescu. Zero-energy pinning of topologically trivial bound states in multiband semiconductor-superconductor nanowires. *Phys. Rev. B*, 100:125407, Sep 2019.

[88] Anders Jellinggaard, Kasper Grove-Rasmussen, Morten Hannibal Madsen, and Jesper Nygård. Tuning yu-shiba-rusinov states in a quantum dot. *Phys. Rev. B*, 94:064520, Aug 2016.

[89] K. Grove-Rasmussen, G. Steffensen, A. Jellinggaard, M. H. Madsen, R. Žitko, J. Paaske, and J. Nygård. Yu–shiba–rusinov screening of spins in double quantum dots. *Nature Communications*, 9(1):2376, Jun 2018.

[90] Zhaoen Su, Alexandre B. Tacla, Moïra Hocevar, Diana Car, Sébastien R. Plissard, Erik P. A. M. Bakkers, Andrew J. Daley, David Pekker, and Sergey M. Frolov. Andreev molecules in semiconductor nanowire double quantum dots. *Nature Communications*, 8(1):585, 2017.

[91] Z. Su, R. Žitko, P. Zhang, H. Wu, D. Car, S. R. Plissard, S. Gazibegovic, G. Badawy, M. Hocevar, J. Chen, E. P. A. M. Bakkers, and S. M. Frolov. Erasing odd-parity states in semiconductor quantum dots coupled to superconductors. *Phys. Rev. B*, 101:235315, Jun 2020.

[92] J. C. Estrada Saldaña, A. Vekris, R. Žitko, G. Steffensen, P. Krogstrup, J. Paaske, K. Grove-Rasmussen, and J. Nygård. Two-impurity yu-shiba-rusinov states in coupled quantum dots. *Phys. Rev. B*, 102:195143, Nov 2020.

[93] Dong Pan, Huading Song, Shan Zhang, Lei Liu, Lianjun Wen, Dunyuan Liao, Ran Zhuo, Zhichuan Wang, Zitong Zhang, Shuai Yang, Jianghua Ying, Wentao Miao, Yongqing Li, Runan Shang, Hao Zhang, and Jianhua Zhao. In situ epitaxy of pure phase ultra-thin inas-al nanowires for quantum devices, 2020.

[94] Data and code for 'Triple Andreev dot chains in semiconductor nanowires'. Doi: 10.5281/zenodo.4751642.

[95] Hao Wu, Po Zhang, John P. T. Stenger, Zhaoen Su, Jun Chen, Ghada Badawy, Sasa Gazibegovic, Erik P. A. M. Bakkers, and S. M. Frolov. Triple andreev dot chains in semiconductor nanowires, 2021.

[96] C.W.J. Beenakker. Search for majorana fermions in superconductors. *Annual Review of Condensed Matter Physics*, 4(1):113–136, 2013.

[97] Carlo Beenakker and Leo Kouwenhoven. A road to reality with topological superconductors. *Nature Physics*, 12(7):618–621, Jul 2016.

[98] R. M. Lutchyn, E. P. A. M. Bakkers, L. P. Kouwenhoven, P. Krogstrup, C. M. Marcus, and Y. Oreg. Majorana zero modes in superconductor–semiconductor heterostructures. *Nature Reviews Materials*, 3(5):52–68, May 2018.

[99] S. M. Frolov, M. J. Manfra, and J. D. Sau. Topological superconductivity in hybrid devices. *Nature Physics*, 16(7):718–724, Jul 2020.

[100] P Yu, J Chen, M Gomanko, G Badawy, EPAM Bakkers, K Zuo, V Mourik, and SM Frolov. Non-majorana states yield nearly quantized conductance in proximatized nanowires. *Nature Physics*, pages 1–7, 2021.

[101] G. L. R. Anselmetti, E. A. Martinez, G. C. Ménard, D. Puglia, F. K. Malinowski, J. S. Lee, S. Choi, M. Pendharkar, C. J. Palmstrøm, C. M. Marcus, L. Casparis, and A. P. Higginbotham. End-to-end correlated subgap states in hybrid nanowires. *Phys. Rev. B*, 100:205412, Nov 2019.

[102] Anna Grivnin, Ella Bor, Moty Heiblum, Yuval Oreg, and Hadas Shtrikman. Concomitant opening of a bulk-gap with an emerging possible majorana zero mode. *Nature communications*, 10(1):1–7, 2019.

[103] Sagar Vijay, Timothy H. Hsieh, and Liang Fu. Majorana fermion surface code for universal quantum computation. *Phys. Rev. X*, 5:041038, Dec 2015.

[104] S. Plugge, L. A. Landau, E. Sela, A. Altland, K. Flensberg, and R. Egger. Roadmap to majorana surface codes. *Phys. Rev. B*, 94:174514, Nov 2016.

[105] David Aasen, Michael Hell, Ryan V. Mishmash, Andrew Higginbotham, Jeroen Danon, Martin Leijnse, Thomas S. Jespersen, Joshua A. Folk, Charles M. Marcus, Karsten Flensberg, and Jason Alicea. Milestones toward majorana-based quantum computing. *Phys. Rev. X*, 6:031016, Aug 2016.

[106] T. E. O'Brien, P. Rożek, and A. R. Akhmerov. Majorana-based fermionic quantum computation. *Phys. Rev. Lett.*, 120:220504, Jun 2018.

[107] Ryan V. Mishmash, David Aasen, Andrew P. Higginbotham, and Jason Alicea. Approaching a topological phase transition in majorana nanowires. *Phys. Rev. B*, 93:245404, Jun 2016.

[108] John P. T. Stenger, Benjamin D. Woods, Sergey M. Frolov, and Tudor D. Stanescu. Control and detection of majorana bound states in quantum dot arrays. *Phys. Rev. B*, 98:085407, Aug 2018.

[109] Z. Su, A. Zarassi, J.-F. Hsu, P. San-Jose, E. Prada, R. Aguado, E. J. H. Lee, S. Gazibegovic, R. L. M. Op het Veld, D. Car, S. R. Plissard, M. Hocevar, M. Pendharkar, J. S. Lee, J. A. Logan, C. J. Palmstrøm, E. P. A. M. Bakkers, and S. M. Frolov. Mirage andreev spectra generated by mesoscopic leads in nanowire quantum dots. *Phys. Rev. Lett.*, 121:127705, Sep 2018.

[110] Yingyi Huang, Haining Pan, Chun-Xiao Liu, Jay D. Sau, Tudor D. Stanescu, and S. Das Sarma. Metamorphosis of andreev bound states into majorana bound states in pristine nanowires. *Phys. Rev. B*, 98:144511, Oct 2018.

[111] G. C. Menard, G. L. R. Anselmetti, E. A. Martinez, D. Puglia, F. K. Malinowski, J. S. Lee, S. Choi, M. Pendharkar, C. J. Palmstrøm, K. Flensberg, C. M. Marcus, L. Casparis, and A. P. Higginbotham. Conductance-matrix symmetries of a three-terminal hybrid device. *Phys. Rev. Lett.*, 124:036802, Jan 2020.

[112] Christopher Moore, Tudor D. Stanescu, and Sumanta Tewari. Two-terminal charge tunneling: Disentangling majorana zero modes from partially separated andreev bound states in semiconductor-superconductor heterostructures. *Phys. Rev. B*, 97:165302, Apr 2018.

[113] Tudor D. Stanescu and Sumanta Tewari. Robust low-energy andreev bound states in semiconductor-superconductor structures: Importance of partial separation of component majorana bound states. *Phys. Rev. B*, 100:155429, Oct 2019.

[114] Bela Bauer, Torsten Karzig, Ryan V. Mishmash, Andrey E. Antipov, and Jason Alicea. Dynamics of Majorana-based qubits operated with an array of tunable gates. *SciPost Phys.*, 5:4, 2018.

[115] M. Pendharkar, B. Zhang, H. Wu, A. Zarassi, P. Zhang, C. P. Dempsey, J. S. Lee, S. D. Harrington, G. Badawy, S. Gazibegovic, R. L. M. Op het Veld, M. Rossi, J. Jung, A.-H. Chen, M. A. Verheijen, M. Hocevar, E. P. A. M. Bakkers, C. J. Palmstrøm, and S. M. Frolov. Parity-preserving and magnetic field–resilient superconductivity in insb nanowires with sn shells. *Science*, 372(6541):508–511, 2021.

[116] Thomas Kanne, Mikelis Marnauza, Dags Olsteins, Damon J. Carrad, Joachim E. Sestoft, Joeri de Bruijckere, Lunjie Zeng, Erik Johnson, Eva Olsson, Kasper Grove-

Rasmussen, and Jesper Nygård. Epitaxial pb on inas nanowires for quantum devices. *Nature Nanotechnology*, May 2021.

[117] Frank Arute, Kunal Arya, Ryan Babbush, Dave Bacon, Joseph C. Bardin, Rami Barends, Rupak Biswas, Sergio Boixo, Fernando G. S. L. Brandao, David A. Buell, et al. Quantum supremacy using a programmable superconducting processor. *Nature*, 574(7779):505–510, October 2019.

[118] C. Figgatt, A. Ostrander, N. M. Linke, K. A. Landsman, D. Zhu, D. Maslov, and C. Monroe. Parallel entangling operations on a universal ion-trap quantum computer. *Nature*, 572(7769):368–372, August 2019.

[119] Christoph Kloeffel and Daniel Loss. Prospects for spin-based quantum computing in quantum dots. *Annu. Rev. Condens. Matter Phys.*, 4(1):51–81, 2013.

[120] T. Hyart, B. van Heck, I. C. Fulga, M. Burrello, A. R. Akhmerov, and C. W. J. Beenakker. Flux-controlled quantum computation with majorana fermions. *Phys. Rev. B*, 88:035121, Jul 2013.

[121] Stephan Plugge, Asbjørn Rasmussen, Reinhold Egger, and Karsten Flensberg. Majorana box qubits. *New Journal of Physics*, 19(1):012001, jan 2017.

[122] John PT Stenger, Michael Hatridge, Sergey M Frolov, and David Pekker. Braiding quantum circuit based on the 4 π josephson effect. *Physical Review B*, 99(3):035307, 2019.

[123] J. Shabani, M. Kjaergaard, H. J. Suominen, Younghyun Kim, F. Nichele, K. Pakrouski, T. Stankevic, R. M. Lutchyn, P. Krogstrup, R. Feidenhans'l, et al. Two-dimensional epitaxial superconductor-semiconductor heterostructures: A platform for topological superconducting networks. *Phys. Rev. B*, 93:155402, Apr 2016.

[124] Antonio Fornieri, Alexander M Whiticar, F Setiawan, Elías Portolés, Asbjørn CC Drachmann, Anna Keselman, Sergei Gronin, Candice Thomas, Tian Wang, Ray Kallaher, et al. Evidence of topological superconductivity in planar josephson junctions. *Nature*, 569(7754):89, 2019.

[125] L. J. Geerligs, V. F. Anderegg, J. Romijn, and J. E. Mooij. Single cooper-pair tunneling in small-capacitance junctions. *Phys. Rev. Lett.*, 65:377–380, Jul 1990.

[126] M. T. Tuominen, J. M. Hergenrother, T. S. Tighe, and M. Tinkham. Experimental evidence for parity-based 2e periodicity in a superconducting single-electron tunneling transistor. *Phys. Rev. Lett.*, 69:1997–2000, Sep 1992.

[127] P. Lafarge, P. Joyez, D. Esteve, C. Urbina, and M. H. Devoret. Measurement of the even-odd free-energy difference of an isolated superconductor. *Phys. Rev. Lett.*, 70:994–997, Feb 1993.

[128] T. M. Eiles, John M. Martinis, and Michel H. Devoret. Even-odd asymmetry of a superconductor revealed by the coulomb blockade of andreev reflection. *Phys. Rev. Lett.*, 70:1862–1865, Mar 1993.

[129] P. Joyez, P. Lafarge, A. Filipe, D. Esteve, and M. H. Devoret. Observation of parity-induced suppression of josephson tunneling in the superconducting single electron transistor. *Phys. Rev. Lett.*, 72:2458–2461, Apr 1994.

[130] Jie Shen, Sebastian Heedt, Francesco Borsoi, Bernard van Heck, Sasa Gazibegovic, Roy L. M. Op het Veld, Diana Car, John A. Logan, Mihir Pendharkar, Senja J. J. Ramakers, et al. Parity transitions in the superconducting ground state of hybrid insb-al coulomb islands. *Nature Communications*, 9(1):4801, November 2018.

[131] Haining Pan and S. Das Sarma. Physical mechanisms for zero-bias conductance peaks in majorana nanowires. *Phys. Rev. Research*, 2:013377, Mar 2020.

[132] M. T. Deng, C. L. Yu, G. Y. Huang, M. Larsson, P. Caroff, and H. Q. Xu. Anomalous Zero-Bias Conductance Peak in a Nb–InSb Nanowire–Nb Hybrid Device. *Nano Letters*, 12:6414, 2012.

[133] Önder Gül, Hao Zhang, Jouri DS Bommer, Michiel WA de Moor, Diana Car, Sébastien R Plissard, Erik PAM Bakkers, Attila Geresdi, Kenji Watanabe, Takashi Taniguchi, et al. Ballistic majorana nanowire devices. *Nature nanotechnology*, 13:192, 2018.

[134] K. Serniak, M. Hays, G. de Lange, S. Diamond, S. Shankar, L. D. Burkhart, L. Frunzio, M. Houzet, and M. H. Devoret. Hot nonequilibrium quasiparticles in transmon qubits. *Phys. Rev. Lett.*, 121:157701, Oct 2018.

[135] Sasa Gazibegovic, Ghada Badawy, Thijs LJ Buckers, Philipp Leubner, Jie Shen, Folkert K de Vries, Sebastian Koelling, Leo P Kouwenhoven, Marcel A Verheijen, and

Erik PAM Bakkers. Bottom-up grown 2d insb nanostructures. *Advanced Materials*, 31(14):1808181, 2019.

[136] Stephen T. Gill, Jeff Damasco, Blanka. E. Janicek, Malcolm S. Durkin, Vincent Humbert, Sasa Gazibegovic, Diana Car, Erik P. A. M. Bakkers, Pinshane Y. Huang, and Nadya Mason. Selective-area superconductor epitaxy to ballistic semiconductor nanowires. *Nano Letters*, 18(10):6121–6128, 2018.

[137] Sabbir A. Khan, Charalampos Lampadaris, Ajuan Cui, Lukas Stampfer, Yu Liu, Sebastian J. Pauka, Martin E. Cachaza, Elisabetta M. Fiordaliso, Jung-Hyun Kang, Svetlana Korneychuk, Timo Mutas, Joachim E. Sestoft, Filip Krizek, Rawa Tanta, Maja C. Cassidy, Thomas S. Jespersen, and Peter Krogstrup. Highly transparent gatable superconducting shadow junctions. *ACS Nano*, 14(11):14605–14615, Nov 2020.

[138] Yong Xu, Binghai Yan, Hai-Jun Zhang, Jing Wang, Gang Xu, Peizhe Tang, Wenhui Duan, and Shou-Cheng Zhang. Large-gap quantum spin hall insulators in tin films. *Phys. Rev. Lett.*, 111:136804, Sep 2013.

[139] Cai-Zhi Xu, Yang-Hao Chan, Yige Chen, Peng Chen, Xiaoxiong Wang, Catherine Dejoie, Man-Hong Wong, Joseph Andrew Hlevyack, Hyejin Ryu, Hae-Young Kee, et al. Elemental topological dirac semimetal: α-sn on insb(111). *Phys. Rev. Lett.*, 118:146402, Apr 2017.

[140] Xiaohu Zheng, Jian-Feng Zhang, Bingbing Tong, and Rui-Rui Du. Epitaxial growth and electronic properties of few-layer stanene on InSb (1 1 1). *2D Materials*, 7(1):011001, oct 2019.

[141] RFC Farrow, DS Robertson, GM Williams, AG Cullis, GR Jones, IM Young, and PNJ Dennis. The growth of metastable, heteroepitaxial films of α-sn by metal beam epitaxy. *Journal of Crystal Growth*, 54(3):507–518, 1981.

[142] Data for 'Parity-preserving and magnetic field-resilient superconductivity in InSb nanowires with Sn shells'. Doi: 10.5281/zenodo.4466265.

[143] Kun Zuo, Vincent Mourik, Daniel B. Szombati, Bas Nijholt, David J. van Woerkom, Attila Geresdi, Jun Chen, Viacheslav P. Ostroukh, Anton R. Akhmerov, Sebastién R. Plissard, et al. Supercurrent interference in few-mode nanowire josephson junctions. *Phys. Rev. Lett.*, 119:187704, Nov 2017.

[144] Jasper van Veen, Alex Proutski, Torsten Karzig, Dmitry I. Pikulin, Roman M. Lutchyn, Jesper Nygård, Peter Krogstrup, Attila Geresdi, Leo P. Kouwenhoven, and John D. Watson. Magnetic-field-dependent quasiparticle dynamics of nanowire single-cooper-pair transistors. *Phys. Rev. B*, 98:174502, Nov 2018.

[145] Martin Bjergfelt, Damon J Carrad, Thomas Kanne, Martin Aagesen, Elisabetta M Fiordaliso, Erik Johnson, Borzoyeh Shojaei, Chris J Palmstrøm, Peter Krogstrup, Thomas Sand Jespersen, et al. Superconducting vanadium/indium-arsenide hybrid nanowires. *Nanotechnology*, 30(29):294005, 2019.

[146] Nicholas A Güsken, Torsten Rieger, Patrick Zellekens, Benjamin Bennemann, Elmar Neumann, Mihail I Lepsa, Thomas Schäpers, and Detlev Grützmacher. Mbe growth of al/inas and nb/inas superconducting hybrid nanowire structures. *Nanoscale*, 9(43):16735–16741, 2017.

[147] A. Y. Kitaev. Fault-tolerant quantum computation by anyons. *Annals of Physic*, 303:2, 2003.

[148] J. Alicea, Y. Oreg, G. Refael, F. von Oppen, and M. P. A. Fisher. Non-abelian statistics and topological quantum information processing in 1d wire networks. *Nat. Phys.*, 7:412, 2011.

[149] M. Hays, G. de Lange, K. Serniak, D. J. van Woerkom, D. Bouman, P. Krogstrup, J. Nygård, A. Geresdi, and M. H. Devoret. Direct microwave measurement of andreev-bound-state dynamics in a semiconductor-nanowire josephson junction. *Phys. Rev. Lett.*, 121:047001, Jul 2018.

[150] F. Luthi, T. Stavenga, O. W. Enzing, A. Bruno, C. Dickel, N. K. Langford, M. A. Rol, T. S. Jespersen, J. Nygård, P. Krogstrup, and L. DiCarlo. Evolution of nanowire transmon qubits and their coherence in a magnetic field. *Phys. Rev. Lett.*, 120:100502, Mar 2018.

[151] Marta Pita-Vidal, Arno Bargerbos, Chung-Kai Yang, David J. van Woerkom, Wolfgang Pfaff, Nadia Haider, Peter Krogstrup, Leo P. Kouwenhoven, Gijs de Lange, and Angela Kou. A gate-tunable, field-compatible fluxonium. 2019.

[152] S. Nadj-Perge, S. M. Frolov, E. P. A. M. Bakkers, and L. P. Kouwenhoven. Spin-orbit qubit in a semiconductor nanowire. *Nature*, 468(7327):1084–1087, December 2010.

[153] J. W. G. van den Berg, S. Nadj-Perge, V. S. Pribiag, S. R. Plissard, E. P. A. M. Bakkers, S. M. Frolov, and L. P. Kouwenhoven. Fast spin-orbit qubit in an indium antimonide nanowire. *Phys. Rev. Lett.*, 110:066806, Feb 2013.

[154] VS Pribiag, S Nadj-Perge, SM Frolov, JWG Van Den Berg, I Van Weperen, SR Plissard, EPAM Bakkers, and LP Kouwenhoven. Electrical control of single hole spins in nanowire quantum dots. *Nature nanotechnology*, 8(3):170–174, 2013.

[155] Karl D Petersson, Louis W McFaul, Michael D Schroer, Minkyung Jung, Jacob M Taylor, Andrew A Houck, and Jason R Petta. Circuit quantum electrodynamics with a spin qubit. *Nature*, 490(7420):380–383, 2012.

[156] Mark W Keller. Current status of the quantum metrology triangle. *Metrologia*, 45(1):102–109, jan 2008.

[157] J. R. Petta, A. C. Johnson, J. M. Taylor, E. A. Laird, A. Yacoby, M. D. Lukin, C. M. Marcus, M. P. Hanson, and A. C. Gossard. Coherent manipulation of coupled electron spins in semiconductor quantum dots. *Science*, 309(5744):2180–2184, 2005.

[158] J. A. Sauls. Andreev bound states and their signatures. *Philosophical Transactions of the Royal Society A: Mathematical, Physical and Engineering Sciences*, 376(2125):20180140, 2018.

[159] Angela Q Chen, Moon Jip Park, Stephen T Gill, Yiran Xiao, Dalmau Reig-i Plessis, Gregory J MacDougall, Matthew J Gilbert, and Nadya Mason. Finite momentum cooper pairing in three-dimensional topological insulator josephson junctions. *Nature communications*, 9(1):1–9, 2018.

[160] Jorden A. van Dam, Yuli V. Nazarov, Erik P. A. M. Bakkers, Silvano De Franceschi, and Leo P. Kouwenhoven. Supercurrent reversal in quantum dots. *Nature*, 442(7103):667–670, 2006.

[161] D. B. Szombati, S. Nadj-Perge, D. Car, S. R. Plissard, E. P. A. M. Bakkers, and L. P. Kouwenhoven. Josephson ϕ_0 junction in nanowire quantum dots. *Nature Physics*, 12(6):568–572, 2016.

[162] Fabrizio Dolcini, Manuel Houzet, and Julia S. Meyer. Topological josephson ϕ_0 junctions. *Phys. Rev. B*, 92:035428, Jul 2015.

[163] Mahn-Soo Choi, C. Bruder, and Daniel Loss. Spin-dependent josephson current through double quantum dots and measurement of entangled electron states. *Phys. Rev. B*, 62:13569–13572, Nov 2000.

[164] Patrik Recher, Eugene V Sukhorukov, and Daniel Loss. Andreev tunneling, coulomb blockade, and resonant transport of nonlocal spin-entangled electrons. *Physical Review B*, 63(16):165314, 2001.

[165] C. Padurariu and Yu. V. Nazarov. Spin blockade qubit in a superconducting junction. *EPL (Europhysics Letters)*, 100(5):57006, dec 2012.

[166] Stephanie Droste, Sabine Andergassen, and Janine Splettstoesser. Josephson current through interacting double quantum dots with spin–orbit coupling. *Journal of Physics: Condensed Matter*, 24(41):415301, sep 2012.

[167] Yoichi Tanaka, Norio Kawakami, and Akira Oguri. Correlated electron transport through double quantum dots coupled to normal and superconducting leads. *Phys. Rev. B*, 81:075404, Feb 2010.

[168] James Eldridge, Marco G. Pala, Michele Governale, and Jürgen König. Superconducting proximity effect in interacting double-dot systems. *Phys. Rev. B*, 82:184507, Nov 2010.

[169] Martin Leijnse and Karsten Flensberg. Coupling spin qubits via superconductors. *Phys. Rev. Lett.*, 111:060501, Aug 2013.

[170] Zoltán Scherübl, András Pályi, and Szabolcs Csonka. Transport signatures of an andreev molecule in a quantum dot – superconductor – quantum dot setup. *Beilstein J. Nanotechnol.*, 10:363–378, 2019.

[171] N. Bovenzi, M. Breitkreiz, P. Baireuther, T. E. O'Brien, J. Tworzydło, İ. Adagideli, and C. W. J. Beenakker. Chirality blockade of andreev reflection in a magnetic weyl semimetal. *Phys. Rev. B*, 96:035437, Jul 2017.

[172] Daniël Bouman, Ruben J. J. van Gulik, Gorm Steffensen, Dávid Pataki, Péter Boross, Peter Krogstrup, Jesper Nygård, Jens Paaske, András Pályi, and Attila Geresdi. Triplet-blockaded josephson supercurrent in double quantum dots. *Phys. Rev. B*, 102:220505, Dec 2020.

[173] Po Zhang, Hao Wu, Jun Chen, Sabbir A. Khan, Peter Krogstrup, David Pekker, and Sergey M. Frolov. Evidence of andreev blockade in a double quantum dot coupled to a superconductor, 2021.

[174] David Pekker, Po Zhang, and Sergey M. Frolov. Theory of Andreev Blockade in a Double Quantum Dot with a Superconducting Lead. *SciPost Phys.*, 11:81, 2021.

[175] Data and code for 'Evidence of Andreev blockade in a double quantum dot coupled to a superconductor'. Doi: 10.5281/zenodo.4446186.

[176] Bryan Cord, Jodie Lutkenhaus, and Karl K. Berggren. Optimal temperature for development of poly(methylmethacrylate). *Journal of Vacuum Science & Technology B: Microelectronics and Nanometer Structures Processing, Measurement, and Phenomena*, 25(6):2013–2016, 2007.

[177] Jasper van Veen, Damaz de Jong, Lin Han, Christian Prosko, Peter Krogstrup, John D. Watson, Leo P. Kouwenhoven, and Wolfgang Pfaff. Revealing charge-tunneling processes between a quantum dot and a superconducting island through gate sensing. *Phys. Rev. B*, 100:174508, Nov 2019.

[178] A. Zarassi, Z. Su, J. Danon, J. Schwenderling, M. Hocevar, B. M. Nguyen, J. Yoo, S. A. Dayeh, and S. M. Frolov. Magnetic field evolution of spin blockade in ge/si nanowire double quantum dots. *Phys. Rev. B*, 95:155416, Apr 2017.